Gravity and Centrifugal Casting of Light Metal Alloys Using Rapidly Produced Sand Moulds

Nicholas McKenna

A thesis submitted to
Auckland University of Technology
In fulfilment of the requirements for the degree
of
Masters of Engineering

July 2010

School of Engineering

Primary Supervisor: Dr. Sarat Singamneni

ABSTRACT

Traditional sand casting is a well understood method to produce metal shapes and has been used for many years in industry. It is a relatively simple method but has a significant drawback, with the requirement of a pattern to form the internal cavity. Patterns are produced at high cost through Computer Numerical Controlled machining or wood pattern making with significantly high lead times.

Rapid Prototyping is seen as a solution to this problem, with the ability to produce sand moulds directly from Computer Aided Design platforms and thus eliminate the requirement of a pattern. Through layered manufacturing, the sand mould can be produced with complex internal geometry directly, minimising labour costs and involving short waiting times. While initial research was mainly concerned with the use of Selective Laser Sintering, with the advent of 3D printing, pattern-less sand moulds can be produced more easily and cheaply. With the process gaining more and more popularity, there was a need to scientifically assess the suitability of the process for sand casting as well as, establish influences of typical process parameters on significant responses.

Critical mould properties, such as permeability and compressive strength, were investigated with respect to varying time and temperature of baking. To this end, mathematical models of permeability and compressive strength were developed. Also, the influence of mould material, mould coating, alloy type and pouring temperatures were investigated in static sand casting of light metals. Further work utilised the centrifugal casting process using these 3D printed moulds to establish links between process factors, such as rotational speed and cast strength using light metals.

Compressive strength results for the rapidly produced materials were acceptable compared to traditional values. Permeability was however lower

than commonly used foundry sand. Results showed, nevertheless, that permeability and compressive strength were both improved by baking times and temperatures. Significant model effects were established for ZP131 and ZCast501 with respect to increased compressive strength and mould permeability.

Multi-factorial experiments involving simultaneous variation of factors such as mould materials, surface coatings, alloys and pouring temperatures were conducted and static casting results in general show good as-cast mechanical properties with the factors having significant effects on surface roughness, percent elongation and hardness.

Centrifugal casting of aluminium alloys initially produced below average tensile properties, due to the large presence of hydrogen porosity. However, upon degassing, much improved tensile strengths were obtained, being superior to both static casting and traditionally sand cast aluminium. Also a Magnesium alloy was successfully trialled with the centrifugal process using 3D printed moulds in spite of numerous practical difficulties.

Substantial data relating to the process factors for mould materials and casting processes was produced. Analysis of factor influences facilitated optimum process configurations for the production of moulds and castings. These combinations of factors at optimum levels comprehensively showed that light metals such as aluminium and magnesium alloys could be successfully processed by rapidly produced moulds, both statically and centrifugally.

ACKNOWLEDGEMENTS

I would like to express my profound thanks to my primary supervisor, Dr Sarat Singamneni, senior lecturer, for his invaluable help and guidance through every stage of this project.

I would also like to thank my secondary supervisor, Prof. Darius Singh, for his overall input and commitment in helping organise the logistics for undertaking this work.

I also wish to note special thanks to the local supporting company, Centracast, for kindly allowing generous use of their casting facilities and personnel.

This project was not possible without funding from the Foundation for Research, Science and Technology, which kindly granted a scholarship to the author (contract number CCWE0901), and allowed this work to be undertaken.

Finally, I would also like to sincerely thank my partner Amie, mother Susan and father Colin for their continuous support, love, help, understanding and advice during the duration of this project.

TABLE OF CONTENTS

AUTHORSHIP

"I hereby declare that this submission is my own work and that, to the best of my knowledge and belief, it contains no material previously published or written by another person (except where explicitly defined in the acknowledgments), nor material which to a substantial extent has been submitted for the award of any other degree or diploma of a university or other institution of higher learning"

Signed: Nicholas McKenna Date: 30th July 2010

LIST OF TABLES

LIST OF FIGURES

ABBRIEVIATIONS

RP	Rapid Prototyping
CAD	Computer Aided Design
AM	Additive Manufacturing
SL	Sterolithography
FDM	Fused Deposition Modelling
SLS	Selective Laser Sintering
3D printing	Three Dimensional Printing
LOM	Laminated Object Manufacturing
UV	Ultraviolet
ABS	Acrylonitrile Butadiene Styrene
D	Dimensional
IC	Investment Casting
CNC	Computer Numerically Controlled
CMM	Co-ordinate Measurement Machine
SEM	Scanning Electron Microscope
ZCorp	ZCorporation
TDS	Thermal Distortion Testing
IT	International Tolerance
HCP	Hexagonal Closed Package
SDAS	Secondary Dendrite Arm Spacing
CAST	CAST CRC
OA	Orthogonal Array
S/N	Signal to Noise Ratio
MSD	Mean Squared Deviation
FCC	Face Centred Cubic
Seq	Sequential
Adj	Adjusted
T	Value from T-Test

NOMENCLATURE

T	Temperature	°C
t	Time	hrs
L	Length	m
P	Pressure	Pa
P value	Probability value	%
Q	Flow Rate	m^3/s
Ra	Average surface roughness	µm
UTS	Ultimate Tensile Strength	MPa
A	Cross-sectional area	m^2
F	Fisher F value	
MCS	Mould Compressive Strength	MPa
MP	Mould Permeability	mD
HB	Brinell Hardness	
σ_{Yield}	Yield Stress	MPa

CHAPTER 1 INTRODUCTION

1.1 Rapid Prototyping

Rapid prototyping (RP) is a relatively new methodology established in the late 1980's, by which material parts can be constructed directly from Computer Aided Design (CAD) files. Essentially this is accomplished by a virtual slicing of continuing cross-sections of the parts, thus creating a multi-layer model of any given part. This continued repetition of the slicing leads to the final shape of the part being reproduced. This process is also known as Additive Manufacturing (AM).

Currently, parts are produced in a range of many different materials. These materials include certain polymers, plaster, starch, foundry sand, powdered metals, wax and ceramics. Each of these materials can be combined with various, specific processes, each possessing their particular processing principles. Nevertheless, the essential layered manufacturing steps remain more or less the same. The most commonly used RP systems include Sterolithography (SL), Fused Deposition Modelling (FDM), Selective Laser Sintering (SLS), Three Dimensional Printing (3D printing) and Laminated Object Manufacturing (LOM). An initial description of the operation and capability of these common RP systems first follows first.

Sterolithography (SL)

In 1986, the SL process was patented and the first RP technique was born [1]. This process, shown below in Figure 1.1, uses a photosensitive liquid resin to form a solid polymer when ultraviolet (UV) light is applied onto the resin surface [2]. This reaction to the UV light takes place near the surface, creating solid three dimensional pixels [2]. The UV light is directed by a laser over each individual layer from information contained in the solid CAD. Once the layer has been competed the platform containing the resin is lowered to apply the resin thoroughly and then raised back up so that exactly one layer

thickness remains above the scanned surface [2]. The part is then lowered by one layer after the liquid has settled so that the next layer can be scanned and so on.

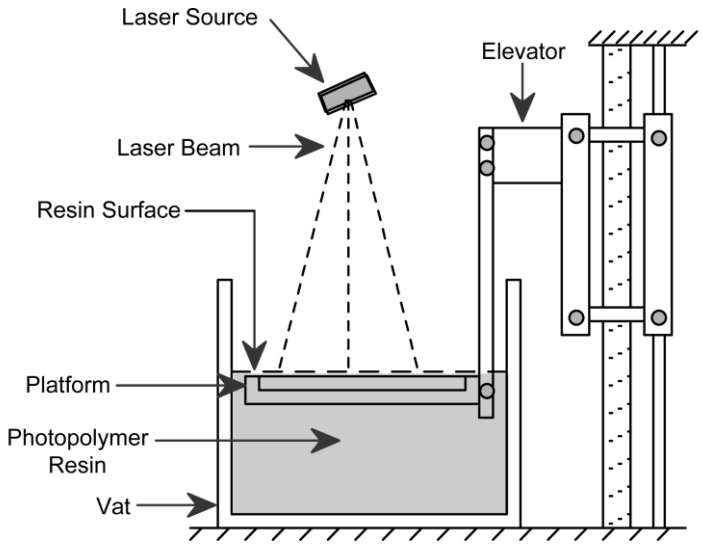

Figure 1.1 The Depiction of the SL process [3]

Fused Deposition modelling (FDM)

The FDM process is an extrusion technique where molten material, usually Acrylonitrile Butadiene Styrene (ABS) plastic, is passed through a heated nozzle. The nozzle moves in two dimensions (x, y directions) to print the individual layer, whilst the build platform is moved in the third direction (Z direction) after each layer is printed. The material is usually heated near or just above the melting point and once it is deposited the material 'cold welds' [2] itself to the previous layer. Unlike the SL process, FDM machines have to build a support material to hold the deposited material in place. This is usually by way of a separate nozzle which deposits a relatively cheaper material which can be dissolved or broken away from the part [2]. Figure 1.2 below shows the operation of a FDM machine with both the build material nozzle and the support material nozzle.

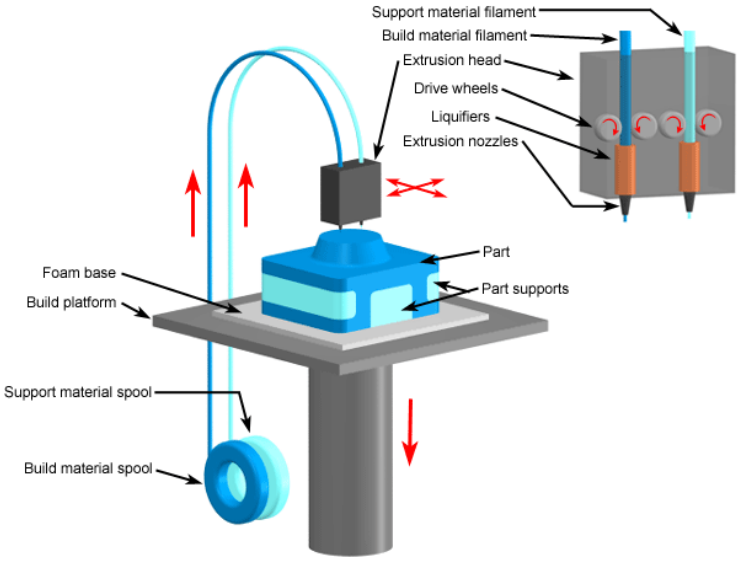

Figure 1.2 The FDM process [4]

Selective Laser Sintering (SLS)

The SLS process typically uses a high powered CO_2 laser to fuse particles together. The process was originally patented by the University of Texas with the DTM Corporation commercialising the process in 1992. Figure 1.3 below shows the overall process setup in which, the particles are fused together by a laser heating them above their melting point and allowing the particle liquid phases to mix and fuse [2]. To prevent any thermal distortion, the bed of the SLS machine is heated to just below the melting point of the material [2]. The operation of the SLS process is similar to the SL process, with the un-sintered material acting as the support structure. After each 2D layer is sintered, the platform is lowered one layer, for the next layer to be sintered. SLS machines are capable of sintering many different materials such as nylon, polystyrene, metal powders and suitably coated foundry sand.

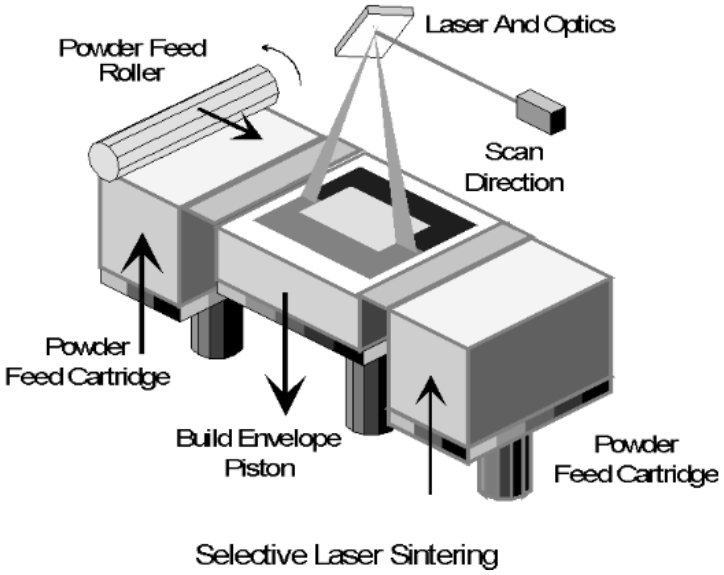

Figure 1.3 SLS machine process [5]

Although able to sinter most materials, SLS machines are often relatively expensive and slow to produce parts when compared to 3D printing. Further, SLS machines tend to use much more energy to operate and powdered metals suitable for sintering are often expensive.

Laminated Object Manufacturing (LOM)

LOM uses a slightly different technique whereby solid sheets construct the layered model. The build material is actually a roll of material which is bonded layer over layer. Figure 1.4 below illustrates the process, where a hot roller activates a heat sensitive adhesive to fuse the layers together [2]. The shape of each layer is cut out by a laser, with a careful control over the layer thickness [2]. The LOM process has several advantages such as relatively cheap materials and the ability to produce at a much faster speed than other RP machines. However, this process does produce large amounts of waste and suffers from an inability to create hollow parts.

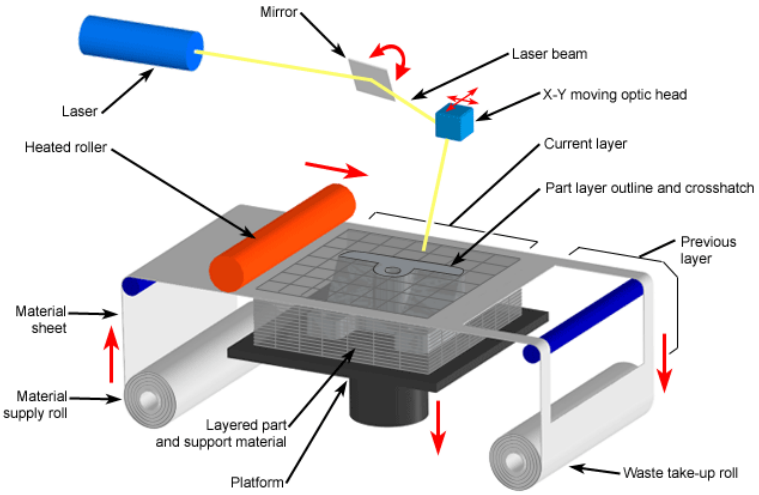

Figure 1.4 LOM process showing passing build sheet and build platform [4]

Three Dimensional Printing (3D printing)

The 3D printing process consists of a liquid binder that is printed on each layer, using a standard ink jet print head (based on ZCorporation 3D printers). Figure 1.5 shows how the process prints each layer in two dimensions, commonly using a plaster or ceramic powder. Once each layer is printed, the build platform drops by the thickness of one layer and the feed piston rises by the same thickness. The roller sweeps across the build platform and distributes a fresh layer of powder on the build platform. These steps are repeated until the part is complete.

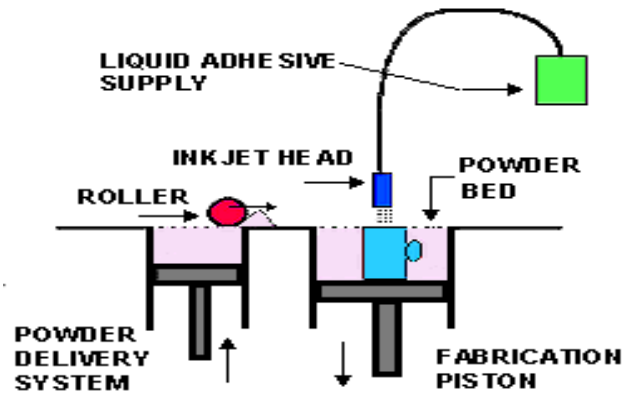

Figure 1.5 Schematic of 3D printing process showing piston and binder application [6]

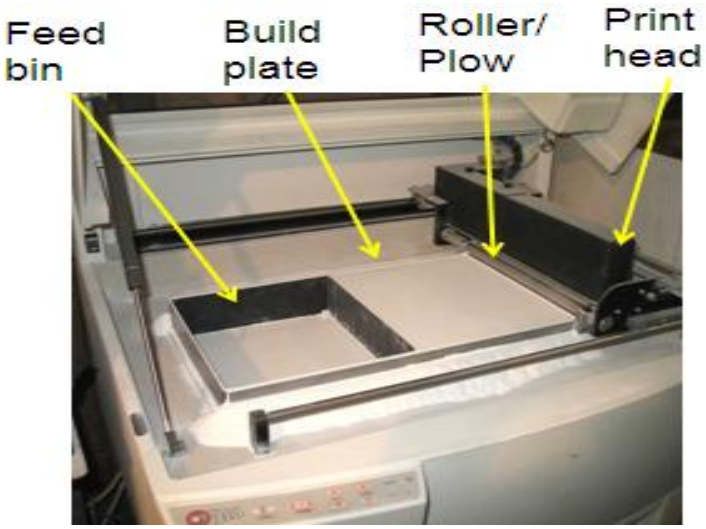

Figure 1.6 AUT's ZCorporation Z310 3D printer

Figure 1.6 gives a closer look at the actual arrangement of different components of the ZPrinter 310 produced by the ZCorporation. This is the machine used at AUT. The figure shows a standard print head which is capable of depositing a liquid binder on both powder materials such plaster (ZP131) or special casting materials (ZCast501). The part is built in layers of 0.1mm, at a speed 20mm per hour, with a maximum build volume of 203X254X203 (all mm).

1.1.1 Evolution of RP towards Rapid Manufacturing

The establishment of the first RP systems manufacturer, 3D Systems Limited in 1987 was quickly followed by other notable companies such as Stratasys, EOS, ZCorporation, Pro Metal and DTM between 1988 and 1992 [1]. The ability to create complex parts quickly and easily from CAD files made this a popular technology. Since then, these techniques have become valuable tools for shortening and improving the product design process and avoiding costly mistakes in pre-production processes. They are also now an inherent feature of concurrent engineering processes.

The potential of RP techniques has been realised in many engineering disciplines, and it is likely that these techniques will continue to be integrated into comprehensive manufacturing processes. The ability to increase part complexity without necessarily increasing product lead times and cost has now allowed design engineers much greater freedom in product design [7]. This allows the customisation of parts without undue constraint in manufacturing. The benefits in cost reduction, optimal design and verification of tooling are all available before full scale manufacturing commences. Profit margins may increase due to lower fixed operating costs [7] and, equally, labour resources in manufacturing are also reduced or directed elsewhere. Essentially, the automatic production of the parts by this technology saves labour, time and inspection and enhances quality control.

Considering all these advantages, the interest in RP processes has quickly grown from being used to just produce prototype models with inferior materials, to rapid tooling applications for direct production of end use parts using extensive engineering materials. This approach is referred to Rapid Manufacturing [7]. By definition, rapid manufacturing means the production of end use parts direct from CAD files, without the need for any complex tooling, and by means of one or more of the RP technologies. While processes such as FDM are already competing with traditional injection moulding selective laser sintering of ceramic and metal powders to produce complex 3D objects is opening up new areas of application.

Rapid manufacturing however, is also attempted by indirect means, using RP techniques together with some traditional processes, aiming at an overall reduction in the total manufacturing lead time. Use of polymer parts produced by one of the RP techniques as patterns for the Investment Casting (IC) process is one of the early developments that allowed reducing considerable time savings in the making of complex patterns. Further use of RP patterns to save time in production of dies and other tooling has been successfully applied in many cases. SLS and 3D printing technology has also been applied to the production of pattern-less sand moulds directly from CAD files for the casting of light metals.

1.2 Rapid Prototyping and Casting

The ability to produce complex shapes and patterns directly from CAD files as a method to reduce costly and time consuming traditional pattern making processes stimulated interest from the casting industry. The production lead time in terms of the fabrication of traditionally made mould patterns by Computer Numerically Controlled (CNC) machining or woodworking is typically weeks or months, depending on the complexity of the part to be produced. The tensile testing mould cavity (pattern), shown below in Figure 1.7, was sent to a local pattern maker and was quoted at $NZ1800 (2009) for the pattern alone, which was said to take forty hours to complete. This pattern was relatively basic as the mould comprises of a couple of dog bone shaped tensile test bars and the sprue and riser system. The pattern making process alone takes one week and typically work is backed up for a number of weeks, to have the pattern produced, and from there the mould still has to be created and then metal cast.

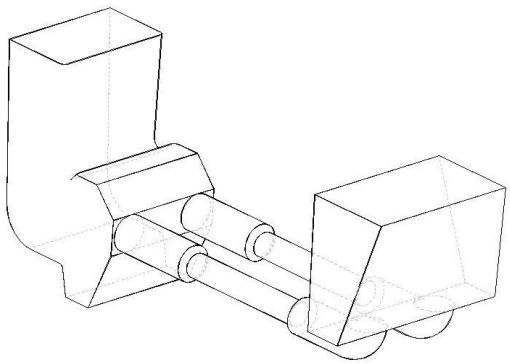

Figure 1.7 SolidWorks computer model showing the internal cavity of a test mould

Utilising CNC machinery, and a quote from a local CNC machinist, completion took up to 2 to 3 months in busy periods, down to about 2-3 weeks in quieter periods to fabricate this pattern. The high demand for the use of CNC means that lead times can also be highly variable and this could lead to problems if a part has to be made within a specific time frame. Moreover, the lead times of

the mould maker who constructs the mould has also to be considered. So, typical times to produce the cast part, in terms of traditional pattern making range from about 3 weeks for wood pattern and anywhere from 3 weeks to 3 months if CNC machining is utilised.

1.2.1 Rapid Casting

RP processes have found wide application in the casting industry, with the earliest applications being in the IC process, where RP patterns have been extensively used to create sacrificial patterns for investment in a ceramic material. SL, FDM, and SLS are all capable of producing patterns for the IC process, while LOM finds its application in the rapid production of complex patterns, for processing in a traditional sand casting way.

The lead times of foundries for producing new parts are significantly determined by the time in which the pattern can be produced. Furthermore it is common that once a casting is produced, the customer may wish to alter the design, requiring pattern modification or an entirely new pattern. The demand to produce patterns suitable for casting by RP therefore became an attractive option for foundries, starting with prototype modelling and through to complex completed moulds. As mentioned above, the RP process has allowed foundries to create expendable patterns that can be used in the IC process.

The advantages of RP manufacturing processes have led to an increasing interest in their application to the metal casting sector. This has resulted in significant research regarding the suitability of different RP technologies in the IC process. Thus, work was first directed at determining surface roughness, pattern burn out, accuracy of cast parts and tolerance ratings of printed patterns. RP techniques produced patterns in a shorter time than traditional methods as noted above. However, there remained problems with thermal expansion causing the ceramic shell moulds to crack [8]. Production of the actual mould therefore continued to be made by traditional means.

To overcome problems with pattern burnout and pattern expansion defects, RP manufacturers began to create materials especially suited for use in the IC process. 3D Systems created the Quickcast material to be used on SL machines. This material comprises a hollow internal structure principally for creating patterns for IC parts. Stratasys Inc subsequently produces parts suitable for IC by the FDM process. The FDM parts are now produced in a wax material which is suitable as a pattern in the IC process. SLS machines soon followed with the introduction of the CastForm material from DTM [2]. CastForm is a specially designed polystyrene material for IC patterns. The material features a low ash content and is compatible with traditional foundry practices [2]. The porous CastForm patterns can then be infiltrated with traditional foundry wax to produce adequate IC patterns comprising of 45% polystyrene and 55% wax [2]. DTM also produced the TrueForm SLS material, which is utilised for producing casting patterns. TrueForm however, is an acrylic-based powder and is not as effective in terms of residual ash after pattern burnout as the CastForm material [2]. All major RP systems outlined above have a material capable of being used in the IC process and traditional IC has benefited from RP patterns. TrueForm however, is an acrylic-based powder and is not as effective in terms of residual ash after pattern burnout as the polystyrene/wax based CastForm material [2]. These enhancements in RP pattern production for IC, resulted in material improvement in pattern burnout and degradation.

The next stage of development was for RP processes to extend their application towards the direct production of moulds, making pattern production redundant. Subsequent to the work on RP patterns as above, it was realised that RP techniques such as SLS and 3D printing also have the ability to construct sacrificial moulds directly from CAD files. These technologies are able to create complex internal geometries and gating systems for direct mould production. The 3D printing process for production of moulds in ceramic materials was first achieved in the early 1990’s with the commercial licensing of research generated at the Massachusetts Institute of Technology (MIT). Soligen marketed the jetting of binder onto ceramic materials for the construction of moulds for investment casting [1]. Other MIT

patents associated with 3D printing were commercialised by the ZCorporation (ZCorp) and Extrudes Hone's ProMetal system 1998 and 1997 respectively [1].

Despite these advances, the overall effectiveness of these rapidly produced moulds in terms of quality and application, were largely unknown. Similarly, little work had been done regarding the combinations of the different variables involved, such as mould characteristics and the mechanical properties of various cast metals. Furthermore, little comparative analysis had been undertaken regarding RP and traditional sand casting techniques. The following literature review is aimed at establishing what has been done in the casting sector with RP techniques with special emphasis on the 3D printing process and rapid casting in the context of light metals, such as Aluminium (Al) and Magnesium (Mg) alloys.

1.3 Literature Review

The establishment of Rapid Prototyping (RP) technologies in the late 1980's and their evolution since then has both led to new applications and significant changes in specific processes in the engineering industry. Metal casting is one of the main targets for the application of RP technology. The ability to produce prototypes quickly from Computer Aided Design (CAD) programmes has been a valuable tool for design and foundry engineers in eliminating design flaws before committing to full scale production. The advantages of using layered manufacturing in the metal casting sector has lead to production of reusable and sacrificial patterns to reduce both time of production and tooling costs for short to medium volumes.

The majority of applications of RP patterns have been in the Investment Casting (IC) sector for sacrificial wax patterns. These patterns are burnt out over time to leave the internal pattern. Recent research however has utilised direct printing of sand and ceramic materials for the fabrication of sacrificial moulds for metal casting. Three dimensional Printing (3D printing), and Selective Laser Sintering (SLS) techniques have been at the forefront of creating moulds for casting. The production of broad research in the

application of RP technology to the casting sector is reviewed below. This is followed by a discussion on specific developments in the application of magnesium and its alloys in gravity casting. Finally there is an introduction to the specific characteristics and the practical application of centrifugal casting process. This is the background to the formulation of the research question that this report addresses.

Constructing new patterns for sacrificial moulds requires both time and skill. Patterns such as those used in the IC process often have thin sections with complex shapes, which require further skill and resources to produce. The RP process is able to create custom made complex shapes and sections, and its application to create patterns for IC was an obvious use of the technology. Early use of RP techniques centred on the production of patterns for sacrificial use in the IC process. IC moulds are either produced indirectly or directly with RP technology. Indirect production involves using sacrificial RP patterns as the wax pattern. This also extends into silicone rubber moulding, where the RP pattern is moulded into the silicone mould to create a cavity for further fabrication of wax positives. Direct mould production involves the fabrication of thin ceramic shells by SLS or 3D printing (Direct Shell Production Method, DSPM) in which metal is cast. Much of the earlier work used indirect approaches (i.e. sacrificial patterns), with later work focusing on direct mould production (sacrificial shell moulds).

Use of RP Patterns

Tromans [9] presented an early overview of the various RP processes. Foundation work with casting and RP was completed with the SL process, which produced sacrificial patterns for use in IC process. The sacrificial pattern was made from a non-engineering plastic, which was coated in wax. This process was widely used and cast parts possessed a good surface finish. Pham and Dimov [10] showed that other RP processes were also suitable for producing sacrificial patterns, being; SLS and FDM.

Increasing use of sacrificial RP patterns highlighted problems such as shell cracking upon burnout and promoted investigation into the suitability of sacrificial RP pattern by Dickens, et al. [11]. The aim was to determine the suitability of different RP processes in creating sound IC shells from sacrificial patterns in the IC process. Accuracy of patterns and castings were also investigated, together with the cast surface quality. The RP systems applied were LOM, SLA and FDM, all of which created sacrificial wax patterns directly from CAD files. SLS process created a porous structure which needed further sealing with wax before being shelled. To test these RP technologies three foundries were each given the same set of patterns for a window wiper mechanism for a German automobile, to convert to castings.

All results reported significant time reductions from the avoidance of traditional prototypes and small scale tooling costs. These traditional costs were quoted as being between £1,000- £50,000 (1995) with lead times varying from 1-16 weeks. This did not include the related high commitment of staff for new projects and products. However, this did not factor in the costs of skilled operators using RP equipment and subsequent CAD drafting work. It was thus unclear whether the time and cost saving of using RP technologies in the IC process outweighed the extra cost of the RP machine and operator in large scale production. Results of testing from Co-ordinate Measurement Machine (CMM) revealed large standard deviations in accuracy with inadequate tolerances found in both the patterns and the castings. Lower variability was observed in the surface roughness values, with acceptable figures ranging from 4-25µm. Foundry experience was evidently a critical factor in the conversion of RP patterns to sound investment castings. More recent research has suggested that SLA, SLS and FDM technologies are suitable RP processes for investment and vacuum casting [10].

Lee, et al. [12] tested the FDM process as an aid in reducing tooling costs and lead times associated with a typical IC process. High tooling costs for master dies is not usually justifiable for small run production unless it has a special application, e.g. defence industry, or is unable to be made by other processes. A benchmark model consisting of common shapes and profiles

was created to assess the effectiveness of the FDM process for indirect IC mould production with sacrificial RP patterns. The FDM process was shown to be [12] effective for the economic mass production of complex metal parts which may otherwise be difficult to produce.

RP patterns were also seen [12] as ideal substitutes, as they can be melted and burnt out from the ceramic shell. Early RP wax patterns exhibited cracking due to excessive thermal expansion when melted [11]. It was discovered [12] that plastic ABS RP patterns chemically attacked the cavity surface of the ceramic shell, due to corrosive degradation during pattern burn out. This was overcome by simply creating patterns with a hollow internal structure so that upon melting the pattern expanded inwards. Indirect ceramic IC shells were then made by the FDM process, using ABS plastic on a FDM3000 (Stratays Inc.) system. Both sacrificial FDM patterns and multiple pattern production, using silicone rubber moulds poured over the FDM pattern, were investigated. Thermogravimetric analysis for the residual ash content was used to show how well the FDM patterns burnt out of the shell. Testing conducted under O_2 atmosphere at 900°C gave a residual ash content of 2.218% for the FDM pattern compared to 0.04% for traditional foundry wax material. However, Lee noted that actual burn out temperatures for the latter was above 1000°C and, a lower residual ash content was to be expected. Surface testing gave slightly lower values than that those presented earlier [11]. The surface testing conducted on the cast Aluminium A356, gave 4.63-4.69µm average roughness. Indirect mould production through silicon rubber moulds was also analysed. The cast surface roughness was found to be 5.79µm, which was slightly higher than the sacrificial pattern method. In terms of other defects, misruns were seen at 0.5mm wall thicknesses as well as metal penetration. These two defects could be due to residual ash content but misruns and metal penetration can be caused by incorrect filling and bad formation of the ceramic shell respectively. Dimensional accuracy of the sacrificial RP patterns was acceptable, with differences from actual dimension to design dimension ranging from 0.75%-1.42% (dimensions ranged from 0.5-110mm). Production costs were halved in both sacrificial and rubber mould techniques. Overall, hard tooling was eliminated with the use of RP patterns,

which led to significant time and cost savings in small run production. However, for large scale production, traditional methods were still preferred, due to the ability to offset large initial tooling costs by the sheer volume of parts produced.

Use of RP Moulds

Much of the early work on RP applications involved a variation in the IC process by direct printing of thin ceramic shells. Elimination of sacrificial patterns led to direct shell production of the ceramic shells and cores. Direct Shell Production Method (DSPM). was pursued by Sachs, et al. [13]. Potential applications for 3D printing were considered and moulds for metal casting were assessed at an early stage as a high, potential production target. Dimensional control and part strength were seen as the critical factors. Initial investigation of 3D printed parts produced good dimensional control but low part strength.

The traditional IC process produces high precision complex castings, but with commercial disadvantages. These centred on high tooling costs to create new dies, which produce the wax positives, and upon subsequent tooling changes which increase lead times. The dies for wax positives can be made simply from aluminium but those for abrasive ceramic cores must be made of harder material such as carbide [13]. Figures of US$5,000-US$50,000 (1990) for die sets were quoted as common [13]. This increases tooling costs, which are further strongly linked to mould complexity. By using the 3D printing of ceramic cores and shells, initial tooling costs for ceramic dies were eliminated, making small to moderate production profitable. Sachs et al. cited lead time as a critical factor in production.

Use of thin ceramic 3D printing moulds was developed by Curodeau, et al. [14], to cast Cobalt-Chromium (CoCr) alloy to create the bony in-growth surfaces for a medical application. The objective was to efficiently produce a surface texture optimised for bone growth application. Orthopaedic prostheses, e.g. knees and hips, require high precision metal parts which are

then implanted in the body. Standard production methods involved IC of the complex pattern or pattern fabrication by five axis CNC machines. 3D printing was incorporated to produce ceramic shells in hours without the need to create a complex wax pattern. CoCr was then cast directly into the printed alumina ceramic shell. Overall dimensional accuracy was found to be ±5-10µm in all three build directions. The 3D printing process quickly created fast complex metal parts, with intricate surface features. More significant research was later undertaken to adapt the process for production of different textures suitable for orthopaedic prostheses.

Notwithstanding developments in the 3D printing process [13], early attention was more focused on the SLS process to produce moulds for metal casting. By passing a laser over individual sand grains, localised high temperatures result in the fusing of the material and binder to create moulds for casting. Advantages were apparent [9] for design and design alterations using CAD programmes. SLS processes reduced lead times and costs of design and increased design complexity, with no significant increase in cost. The castings produced from SLS moulds were found to be accurate and repeatable but possessed poor surface finish and contained step patterns reflected from the mould surface. Significant out gassing problems were present and further testing and experience with the process was evidently needed to understand these problems.

Direct production of sand moulds using SLS was also researched [10]. The SLS SandForm process utilised Zircon sand and silica sand materials to directly fabricate sand moulds from CAD files and eliminating the need for a pattern. Laser sintering of moulds and cores was found to have equivalent accuracy and properties to moulds and cores produced by traditional methods. It was concluded that direct mould production methods such as SLS reduced production lead times. Direct methods were shown to as increase accuracy levels as intermediate replication stages such as pattern making were eliminated.

Using SLS technology Gibbons [15] produced moulds for an intake manifold for a KTM 525cc single cylinder engine. The moulds were produced from an EOSint S700 SLS machine using silica Croning Sand (Phenolic resin coated). Parts for this application were traditionally fabricated from sheet metal and then welded. The traditional production process was expensive and suffered from long lead times and limited design freedom. Total lead time for producing the mould was 33 hours. The RP moulds were flame hardened on the surface and then baked at 180°C to achieve full strength. The benefits of using RP for sand moulds were: complete design freedom, true CAD to manufacture and rapid design realisation. Also an adequate casting was produced for the application and the mould had adequate permeability. Limitations reported were poor surface roughness, which was assumed to be caused by a lack of sand particle alignment and some geometrical limitations resulting from the need to remove support structures from the mould.

Rooks (Rooks 2002), used the EOS S700 SLS machine at the Warwick Manufacturing Group (WMG) and produced sand moulds and cores for three V6 cylinder blocks. Casting was with aluminium and grey iron and compacted graphite iron. The objective was to evaluate the cylinder heads for noise, heat release and emissions and then compare findings to traditional prototypes. It was found that the cylinder heads produced in the sintered sand moulds were similar in all aspects to traditional prototypes but were completed in much shorter times. WMG stated that this process reduced lead times from 4-6 months to 2-4 weeks and established a breakeven point of 100 RP castings versus traditionally made prototype castings. They concluded that SLS for the production of moulds was viable and ideal for complicated mould and cores for small volume castings.

Tang, et al. [16] investigated the method of strengthening during SLS of silica sand. This research focused on the solidification mechanism of the sintered sand and the effects on accuracy, surface finish and strength, with scanning speed and laser power as the primary variables. With the use of a Scanning Electron Microscope (SEM), comparisons of un-sintered and sintered sand grains were made to determine the strengthening mechanism of the mould

material. The binding mechanism was linked to the surface of the sand particle, which was easily melted due to the presence of inclusions such as Al_2O_3, which create a salt like eutectic with the SiO_2. This reduced the melting temperature of the sand allowing the sand particles to bind together through the liquid surfaces and then solidify once the laser moved away. This process was observed at different scanning speeds and laser powers. It was found that the surface roughness and the compressive strength were proportional to the laser power and inversely proportional to the scanning speed. The sintered sand parts had good compressive strength and surface roughness, with the accuracy of the moulds parts ranging from 0.1mm to 0.5mm. However, the thermal nature of laser sintering created a heated zone which caused shrinkage and distortion of sand grains, which was detrimental to the accuracy of the mould dimensions.

Casalino, et al. [17] identified the influence of the main process parameters on sand properties, permeability and compressive strength. These were measured as primary responses with variables again being speed and laser power settings. Experimental planning and analysis made use of a Taguchi experimental design. LASER-CRON resin coated quartz sand particles (96.8 % quartz and 3.2 % resin) were cured at different times and temperatures in a post heat treatment process on an EOSINT S 700RP SLS machine. Compressive strengths were equal or better in terms of traditional mould making processes and suitable for steel and aluminium casting with the limits being stated to be between 50-150 KN/m^2 for steel casting and 15-25 KN/m^2 for aluminium casting. Permeability (represented in this case as a flow rate) was also suitable for steel and aluminium casting, ranging from 160-190 cm^3/min. This was considerably higher than referenced industry standards for synthetic sand, which were 20-60 cm^3/min for aluminium casting and 160-220 cm^3/min for steel casting. The process variables of laser power settings and post curing time were also influential in the fracture of sand specimens. Rupture surfaces of sand specimens were observed to be angular, cone and skin type. Shorter baking times produced skin type failures for lower strength and cone type fractures for higher strength. Considering all of the variable parameters, baking time was found to be the most significant variable on the

fracture type when evaluating the differences between skin and cone type fractures.

Direct fabrication of moulds from CAD files for metal casting can be achieved either by SLS or 3D printing. SLS sand sintering machines cost about NZ$1,380,100 (based on EOS S700). The largest 3D printers cost around NZ$120000. However, the SLS sand sintering machines are much larger and can create larger shapes. Against that build times of 3D printers are quicker, with the ability to cover entire areas rather than sintering of a single line laser. Further, energy consumption is high with SLS technology due to the use of high powered lasers. Even smaller SLS machines such as the EOSINT M 270 require 32 Amp's with a maximum 5kW of power needed. Large ZCorp 3D printing machines consume around 1.8kW (based on the ZCorp 650).

As the 3D printing process increased in popularity, there was a renewed research interest in establishing the advantages and feasibility of applying the process to sacrificial mould production. Kochan [18] examined the cost effectiveness of various RP processes, with particular focus on 3D printing. It was found that limitations of 3D printing centred on the actual speed of production itself, which was slow when compared to traditional moulding. The size limitation of 3D printing machines to produce larger moulds was also cited. It was noted there was an increasing use of RP systems, especially in the automotive sector and especially with the use of low cost 3D printers. The advantage of faster part production of ink jet 3D printing technology resulted in some manufacturers (ProMetal) claiming larger build sizes and speeds ten times that of common SLS machines.

Use of 3D printers for Part and Mould Production

Before the start of the 21st century, ZCorporation (ZCorp) 3D printing machines had only offered plaster and starch based powders, which were not seen as entirely suitable for metal casting. In the early part of the last decade ZCorp developed a ceramic material which was produced specifically for casting non-ferrous alloys. The ZCast 'direct pour method' is an effective

method for production of aluminium and other non ferrous castings at high speeds and low costs. The direct pour method produces pattern-less printed moulds suitable for casting. Waurzyniak [19] noted that small production runs of 10-20 parts can be achieved by using the ZCast process. The advantage of the ZCorp process is that the prototype is created in the final material unlike other RP systems which use plastic or sintered metals.

Research by Bak [20] showed the 3D printing technique to be a superior process to other RP processes for producing components by single line SLS technology. It was shown that 3D printing method allowed users to produce tooling locally, either on site or at a local foundry to facilitate short run production. Tolerance testing and surface testing of the printed moulds were reported to be ± 0.38mm and 200-300µm respectively (100µm when a mould wash was used). The use of the ZCast process was found to need at least a 3mm mould wall thickness in direct pour casting applications. Additional information [20] on run size was also presented, and production of a dispensing manifold was achieved with fewer than 50 production units needed to break even. It was thus cheaper to purchase a 3D printer and use the ZCast process rather than use traditional methods such as creating a pattern and then creating a mould. The use of 3D printing technologies was seen to be increasing sharply, perhaps at the expense of SLS and other RP processes associated with the casting process.

Rebros, et al. [21] undertook research (on a rival 3D printer, ProMetal) which focused on the thermo-mechanical properties of 3D printed moulds. Due to the increasing focus on production processes to produce near net shaped parts, with thin wall and tight dimensional controls, he investigated distortions in chemically bonded 3D printed sand. Thermal Distortion Testing (TDT) was used to evaluate changes produced by the thermo-mechanical reactions of the chemically bonded sand. It was shown that when molten metal comes in contact with shaped sand the heat transferred from the hot metal causes thermo-mechanical reactions, which result in dimensional changes to the sand. The TDT was conducted on 3D printed Silica sand using a furan binder, printed on a ProMetal S15 rapid casting machine. For comparison, chemically

bonded silica sand using the Phenolic-Urethane Cold box (PUCB) process was studied. TDT showed thermo-mechanical and thermo-chemical changes at elevated temperature (760°C) for both sand systems. Mass loss and surface cracking were observed in all 3D printed sand and PUCB material specimens. In all cases it was found that the specimens showed signs of cracks and elevated pressures and temperatures resulting in distortions of both 3D and PUCB sand systems. The cracking witnessed in all specimens was explained by expansion and contraction differentials in the sand composite. Overall, the testing showed that after 90 seconds, there was no significant difference in the two sand systems regarding mass loss (%). However, for shorter high temperature exposure the 3D printed sand lost less mass than the PUCB sand. More importantly, larger total magnitudes of thermo-mechanical changes were seen in the PUCB sand in the 3D printed sand. This was attributed to a higher level of thermo-chemical reactions in the PUCB sand system.

More recent primary research on the 3D printing process was mainly been concerned with the mould accuracy and mould properties for casting. Bassoli, et al. [22] researched the feasibility and accuracy of the 3D printing process with two similar techniques. These were included a printed sacrificial ZCorp starch pattern for further use in IC and a directly printed ZCast mould. An automotive part was chosen for casting and subsequent dimensional analysis was carried out on a Coordinate Measuring Machine (CMM). Printed starch patterns used in IC were infiltrated with wax and once removed Al-Si (aluminium–silicone) 304 steel was cast. Printed ZCast501 moulds were used to process Al-Si10% alloys. The printed moulds were heat treated at 6 hours and 200°C. Surface roughness measurements were carried out on both the internal and external surfaces of the cast part. The casting obtained from the invested starch pattern exhibited good surface quality with average roughness values (R_a) of 4µm. Surface porosity and filling of the mould was said to be acceptable. However, the cast part produced in the printed moulds showed both signs of micro-porosity and a parting line causing an edge on the outer surface. The average surface roughness was found to be 10µm. Results from the overall accuracies of both the starch pattern and cast parts were similar.

External International Tolerance grades were IT15 for the starch pattern, IT16 for the IC and IT15 for the ZCorp Al casting. It was concluded that both methods were effective in that castings could be produced quickly and adequately. The ZCast process provided satisfactory results but was limited to the range of light alloys. It was found that geometrical freedom was increased in the ZCast process, with the surface roughness noted as the only limitation.

More analysis followed [23-25], researching the capability of the 3D printing process to create wax patterns for further use in IC. Difficulties in creating complex parts were experienced, such as the warping of starch patterns. However the alternative CNC machining of a wax mould cavity was seen as more difficult, expensive and time consuming. The relative strengths of 3D printing process were found to be high speed, ability to print in colour, geometric freedom, and large build sizes (3D System printers). Disadvantages were inaccuracy when compared to other RP systems, poor surface finish of the mould material, limited material options and secondary epoxy and baking processes.

Further in depth analysis of the dimensional accuracy of the printed ZCorp parts was conducted with a CMM on different RP materials [25]. Various distances were evaluated and comparisons were made in the x,y and z axes of the same part. Starch (ZP14) and plaster (ZP100) materials were trialled on a Z400 3D printer. In order to quantify the accuracy of the printed parts a benchmark model was created to assess accuracy indicators. A second part, a differential housing, was also printed. Accuracy indicators included surface profile, circularity, concentricity and angular tolerance. Results showed that primary factors responsible for deviation in measured accuracy were material type, build axis and magnitude of measurement. Measurement tolerance of this 3D printer was IT9-IT16. Plaster based powders were found to yield higher accuracy. The probable reason for this is the finer grain size allowing for finer layers of 0.1mm over that of 0.18mm for the starch material. With both materials parts were found to be printed slightly larger than the CAD models but skilled selection of scaling was reported to reduce this problem.
Further research by Dimitrov, et al. [24] looked into improving design and

manufacturability of foundry equipment by using 3D printing to produce moulds and cores for casting. An evaluation of directly 3D printed shell moulds with ZCast501 and printed sand cores for use in traditional moulds was undertaken. Ten moulds were produced with a mixture of traditional foundry methods, using ZCast cores and ten directly printed ZCast501 ceramic shells. Surface roughness testing was made on ten different surfaces for each casting. Results showed that surface roughness (Ra) was 13.6μm for traditionally made castings and 14.9μm for castings produced in ZCast ceramic shells. The layered production technique led to steps on the printed mould surface, which was reflected in the castings. However, surface roughness tolerance was found to be acceptable for sand cast parts. Overall, it was found the use of 3D printing allowed greater flexibility than traditional foundry mould production by allowing quick manufacture of moulds and cores.

Mould properties such as permeability and compressive strength of the ZCorp ceramic material (ZCast501) were researched by the current author, [26] as part of undergraduate project work. Also, the suitability of mould coatings and their effects on surface finish of the castings were investigated. Basic mechanical data was first gathered to compare to traditional foundry data. Initial testing was conducted on grain size distribution. It was stated [27] that common foundry sands have average grain sizes of around 220-250μm, whereas the average grain size distribution of the ZCast501 material was about 100μm. The latter has a detrimental effect on the surface quality of the castings. Due to the large range of the grain size 50-300μm there was metal penetration into the moulds giving a poor surface finish to the cast specimens. The effect of mould baking on ZCast501permeability and compressive strength was examined. Time and temperature was varied from 3.33-8.8 hours and 130-275°C for the investigations, based on a two factor central composite experimental design. Optimum permeability and compressive testing of the mould samples gave 8cm^2/s and 1MPa respectively. Permeability was low and this was attributed to the large grain size distribution. Compressive strength was found to be acceptable. Further analysis by SEM of the fracture surfaces from compressive testing, revealed decomposition of the bonding strength of the gypsum plaster to the larger

sand grains. The smaller gypsum particles acted as a solid binder much like clay in traditional green sand moulding. It was suspected that additional time and temperature curing removed excessive water, embrittling the gypsum and liquid binder. This sharp reversal in trend with increased heat energy was initially thought to be due to some of the material melting, fusing or changing phase. This would mean that the intergranular pathways would become blocked or at least partially blocked, thus decreasing permeability. From the SEM work conducted, specimens baked at higher temperatures showed a significant change in terms of the gypsum structure and morphology.

Bassoli and Atzeni [28] experimented with direct metal casting into ZCast moulds to optimise the mechanical properties of the cast products and calculate suitable tolerance grades of the cast parts. Cylindrical specimens were printed out and cured with varying times and temperatures. The baked parts then underwent compression testing and the rupture surfaces were evaluated with SEM. Time and temperature varied from 160-250°C and 4-8 hours respectively. A benchmark pattern was produced for further evaluation of dimensional tolerances. Upon baking, the printed part colour was found to change from white to dark brown. Changes in dimensions resulted from the times and temperatures of baking showed small insignificant changes. The green parts (before baking) were seen to be the most inaccurate. In compressive strength testing the green parts were seen to have the highest strength but strength decreased as time and temperature of baking increased. Compressive strengths of the baked samples ranged from 2.6-6.2MPa, which is a much higher order of magnitude than the current author found from his own testing (around 1MPa). Thermogravimetric analysis showed temperature as the primary influencing factor for compressive strength. Samples were seen to lose 6-7% weight after baking at 4hours at 150°C. The current author however found the opposite, with exposure time more significant than baking temperature. Differences in testing and experimental design may account for some differences along with natural variation. An international tolerance (IT) grade of 15 was assigned, which was consistent with foundry applications. This tolerance grade was also in line with other findings [23] who quoted IT9-IT16. After completing accuracy tests it was concluded that the moulds were

described as ‘fundamentally the same’ in terms of dimensional variation both before and after baking. Dimensional accuracy was said to be the same in all three build directions with all tolerances calculated with 95% confidence.

In casting Zinc (Zn) alloy in printed ZCast501 shell moulds, Kaplas and Singh [29] found similar tolerance grades to that of Al (IT13-15). Tolerances were found to be acceptable and shell thickness could be reduced from 12mm to just 2mm. Radiographic testing of the castings showed decreased shrinkage and gas levels in the casting at lower shell wall thicknesses. Cost and times savings of 41 and 37 percent respectively were observed when using the 2mm wall thickness over the recommended 12mm. In a further report, Gill and Kaplas [30] compared printed shell moulds using the ZCast501 powder and the 3D printing technique for the creation of sacrificial starch and plaster patterns to be used in the IC process. Moulds and sacrificial patterns were printed on the ZCorp 310 Plus 3D printer. Sacrificial patterns once printed, were infiltrated with liquid acrylate material. Al was cast and finished casting dimensions were examined for accuracy by a CMM. The thickness of the printed shells was also varied from the recommended 12mm down to 2mm. Accuracy of the cast parts produced by IC and printed moulds were similar. The investment cast sacrificial patterns had an IT of 14, with printed shells ranging from IT13-16. This was similar to previously reported tolerance ratings, [25, 28] indicating that this tolerance rating is appropriate for ZCorp 3D printers. Results from surface testing showed that the surface roughness (Ra) values of sacrificial patterns ranged from 3.99-4.21μm and that of samples from the printed shells ranged from 6.78-6.98μm. These figures are in line with other surface roughness values presented [11, 12] when using sacrificial patterns. Results from reducing shell thickness showed that reducing from 12mm thickness to 6mm gives better dimensional and mechanical properties (with lower thicknesses showing more variability in dimensional accuracy). Likely reasons for this were increased rate of heat transfer due to reduced wall thickness of the shell.

In similar research, Singh and Singh [31] looked into the accuracy of the printed ZCast shell mould for casting lead. A thrust pad for a two stroke petrol

engine was used as the pattern to be cast. Shells were built on a ZCorp 510 printer and cured at 110°C for one hour. Tolerance grades varied from IT10-13 with an optimum shell wall thickness of 1mm. This reduction in wall thickness leads to decreased costs (material reduction) of around 45.75% and a 43% decrease in production time when compared to the 12mm shell thickness. Evidence of improved dimensional accuracy and increased mechanical properties was shown by CMM measurements and photomicrographs respectively. The refined grain structure was most likely due to faster solidification resulting from decreased shell thickness, and the consequent higher heat transfer rate.

From the examined literature it is clear that the use of three dimensional printing of moulds and cores has been researched mainly to investigate the accuracy and properties of printed moulds. Mechanical properties, accuracy and quality of the castings have been looked at to a lesser extent. However the data on the casting quality is primarily limited to aluminium prototypes.

Magnesium Casting

Due to the presence of gypsum in the moulding material, which has a low melting temperature, there has been no research into applying 3D printed moulds to ferrous metals and alloys. Further, there is also little evidence of research into other non-ferrous metals. In particular, there has been renewed interest in Magnesium (Mg) and in recent years. Global warming and sustainability issues have meant that engineers and scientists incentive have to create more efficient, sustainable and recyclable processes to avoid excessive energy consumption and pollution. One of the largest contributing sectors to overall world CO_2 levels is the transport sector. Burning of fossil fuels not only produces CO_2 which contributes to the greenhouse effect, but also other harmful emissions. These include Carbon Monoxide (CO), Oxides of Nitrogen (NO_x), Hydrocarbons (HC) and Oxides of Sulphur (SO_x). Several directions of research to reduce these emissions have lead to the development of bio-fuels from waste, hybrid engine technology and hydrogen fuel cells. One of the major targets in current car production is reduction of

mass. Small reductions of 5-10 % for each vehicle would result in very large reductions of CO_2 if implemented worldwide.

Since the early 1960's the use of Al in automotive applications has slowly replaced steel due to large weight savings and increased performance. Mg is now being assed as a possible replacement for Al, with increasing research into the mechanical properties and limitations of Mg alloys, specifically in the context of processing by sand casting. The International Magnesium Association (IMA) reports that use of die casting Mg in automotive industry is increasing at an unprecedented annual rate. Eliezer, et al. [32] underlines this claim, explaining increased demand has arisen from the automotive sector. Further, large supplies of Mg exist with an estimated 22000 tonnes (t) year supply in the Dead Sea alone available based on current production rates [32]. A periodical article by Eigenfeld, et al. [33], highlights the known advantages of Mg, particularly weight reduction. He reported that 40000t of metal was used in die casting alone in 1995 and by 2001 this figure had increased to 125000t.
The potential of Mg to reduce weight and increase efficiency has lead research into the applications and advantages of Mg alloys.

Bronfin and Aghion [34] presented several reasons to use Mg rather than other metals. Mg alloys are the lightest structural metallic material, and therefore of attraction for automotive and aerospace applications. With increasing emphasis on reducing emissions and sustainable transport, many car manufacturers are moving to use 40-100kg of Mg alloy in each vehicle [34]. This means significant weight savings when compared to traditional steel engine blocks and housings and to a lesser extent Al. Reduction of weight in turn reduces fuel and energy consumption. In one example [34], the block, wheels, front cradle and gear housing were constructed in Mg which led to a fuel saving of 0.25 litres/100km when substituting steel and 0.1 litres/100km when substituting Al. Additionally, Mg alloys have good electromagnetic interference shielding properties making it an attractive material in audio and electronic equipment. High strength to weight ratios and thin wall casting capabilities also lend Mg of use to the electronics industry. Further

characteristics [34] are good heat dissipation, dimensional stability, Radio Frequency Interference (RFI) shielding capabilities, damping capabilities and recycling capacity.

Mg also has very good machinability due to its Hexagonal closed package (HCP) structure with a limited number of slip planes. The HCP crystal structure and favourable atomic size allows Mg to form a solid solution with various elements especially commercial elements such as Al, Zn, Li, Ce, Ag, Zr and Th. 'Workhorse' alloys such as those based on the Mg-AL-Zn system alloys such as AZ91 have excellent strength and acceptable short term elevated temperature properties. It has been noted [34] that creep strength and bolt load retention were poor properties of Mg-Al-Zn alloys but these issues were then overcome by Volkswagen AG and Audi AG for die cast gear box housing by design modification. Inadequate creep properties of Mg have also led to use of Rare Earth (RE) alloys to allow for higher temperature applications. Mg-Al–Si alloys are high creep resistant alloys (e.g. AS21 and AS41) and potentially able to provide good castings. Low Al content has led to casting difficulty and poor corrosion resistance. To ensure good fluidity Mg must have a significant amount of Al but Al also leads to the formation of the eutectic $Mg_{17}Al_{12}$ intermetallic, which has lower hardness and an adverse affect on creep properties. Corrosion is another issue for Mg use, especially problems with galvanic corrosion but good design is cited as a means to overcome this. Generally Mg alloys such as AZ91 have good corrosion in atmospheric conditions but chloride environments are a concern to the wider application of Mg [32].

Casting is the primary manufacturing process for producing Mg in particular, die casting which offers many advantages. These advantages include a high fluidity (good castability), and low specific heat which reduces die wear. Iron also has low solubility in Mg which reduces sticking to metal dies. Higher in-gate pressures can also be achieved at lower overall pressures due to low density of Mg. However some recent research with sacrificial moulds such as sand (green and chemically bonded), plaster and IC shells has been undertaken. Much of this work has focused on how to increase the quality of

the cast parts. An important component of Mg casting in a sacrificial mould is mould-metal reaction. Severe oxidation of Mg in air has lead to research of inhibitors and coatings for refractory mould materials to reduce mould metal reaction. Inhibitors such as Teflon (C_2F_4), sulphur (S) and boric acid (H_3BO_3) and potassium borofluoride (KBF_4) have been successfully tried by Hanawalt and Okada [35] in low water and oil (2-3%) bonded green sand when casting AZ91C. Further work [33] saw the use of sulphur acid, boric acid, potassium tetrafluorborate and ammonium fluorosilicate used as inhibitors to prevent reactions. Green sand mixtures of 6% bentonite clay and 1.5-2% moisture content and 3% inhibitor were found to be optimum ratios [33]. Further, optimum compactability of green sand moulds was 40% and increasing water content was found to strongly increase mould metal reactions. It was also shown [33] that for chemically bonded furan/acid nobake sand system comprised of silica sand, mould metal reaction was inhibited by the spaying of an alcohol based coating containing iron oxide.

Fantetti, et al. [36] working with Mg and plaster moulds showed that for adequate results, moulds have to be thoroughly dried and moisture free. Lun Sin, et al. [37] showed that when molten Mg enters the mould, any water present will result in steam which will produce hydrogen and ignite in oxygen. Sufficient baking times and temperatures are outlined in order to minimise free water content and a minimum temperature of 105°C was recommended for plaster moulds. It was found however, that increasing the mould pre-heat temperature led to more severe mould-metal reaction. This was attributed to the decrease in the temperature gradient between the molten metal and mould material. This therefore increased the time period at which the molten metal was exposed to higher temperatures, promoting reactions to occur, similar to those found by Idris and Clegg [38].

Expanding further on mould metal reaction, a recent report by Takamori, et al. [39] looked at the reaction of Mg with silica green moulds. When Boron Nitride was used as a mould wash on the silica mould, no reaction was seen. The effect of pouring temperature was also found to have an effect on the cast surface with higher temperatures promoting blacker and rougher cast surface

finishes. Observed reactions were however most likely due to the moisture present in the moulds when the moulds were cooled down to room temperature [38].

The study of mould metal reaction has also been reviewed with respect to IC Mg. The use of more thermodynamically stable oxides such as Mg oxide (MgO), Calcium oxide (CaO), Calcium carbonate ($CaCO_3$), Aluminium oxide (Al_2O_3), Zirconium Orthosilicate ($ZrSiO_4$) and Calcium Zirconate ($CaZrO_3$) have been experimentally trialled [37, 40, 41]. Lun Sin et al. [41] however found that grading of oxides by free energy change was not entirely accurate and that mould pre-heat temperature was again a critical variable in the reactions that occur at the mould metal interface. Testing on stable oxides by Cingi, et al. [40] showed large differences in free energy change between the reactions involving no free oxygen and with free oxygen. The free energy change is over 3.5 larger when free oxygen is available. It was concluded [40] that oxygen is not just necessary for initiation of mould metal reactions but also for their continuation and formation of other products of reaction.

The increasing use of light metals, led by Al, highlights their ability to reduce weight and energy consumption whilst still satisfying mechanical demands. The unique ability of light alloys to provide high strength to weight ratios has seen increasing use in many engineering sectors notably the transport and aerospace industry. In addition, light metal applications worldwide are also vital for reducing emissions and achieving a more sustainable society. There has been an increase in research towards improving the processability of light metals. The foregoing literature looked at the use of rapidly produced moulds, clearly highlighting the improvements in design freedom, time and cost savings in small and medium volume production and in particular, paving way for rapid casting. A number of studies have identified that the tolerance limits attainable by the 3D printing process were within the normal limits generally obtained in traditional foundry processes. The relative advantages of using the 3D printing process over SLS in terms of speed and cost, have led to an increased use of 3D printing in mould and core production. Results from the preliminary analysis of the ZCorp ZCast501 material, showed that grain shape

and distribution led to slightly higher cast surface roughness and reduced permeability. However, with the application of mould coatings the surface roughness was improved to adequate roughness values. Further, mould compressive strengths were found to be adequate and tensile properties of the castings were acceptable when compared to traditional sand casting. Overall, the experimental results showed that a proper combination of process parameters and use of a suitable coating material will bring the mould characteristics close to the values recommended for traditional foundry practices for light metals.

Once the mould material characteristics are identified and standardised, it becomes important to experiment, analyse and understand how different metals would react with these moulds when cast. Light metals like Al and Mg are of particular interest due to their advantages noted above. While there is evidence of Al being researched with some of these techniques, other light metals have attracted very little or no attention. One probable reason for this is that quite a few of these RP techniques are relatively new. Renewed research interest in metals like Mg processed by sand casting is a relatively new development and there are obvious gaps in the literature. Interesting research questions arise as to what happens if metals like Al and Mg are processed to produce castings using 3D printed moulds. What are the mould metal reactions? What are the mechanical characteristics of the cast parts? What is the optimum combination of process parameters for the best performance of the rapid casting process in general?

Pressure Filling Techniques

Better mechanical properties can be achieved for light metal castings by using a pressure filling, as in the case of high pressure die casting. This produces thin complex sections which have superior mechanical properties. Gjestland and Westengen [42] showed that grain size and Secondary Dendrite Arm Spacing (SDAS) are strongly related to the solidification rate in Mg and less so in Al, which is usually high in die casting due to the rapid cooling effect of the metal dies. Fast solidification from the chilling die materials yield a fine

grain structure and improved SDAS giving the optimum mechanical properties. More importantly, the application of high pressure allows filling of complex and thin sections. Tensile yield strength of Mg follows a Hall-Petch relationship, meaning that with decreasing grain size, grain boundaries are strengthened through reduction of dislocation movements of individual grains [42]. The characteristics of castings produced by HPDC are thus improved ductility and increased tensile properties with a refined grain structure. Also, solidification shrinkage is reduced due to the high pressure, which facilitates feeding during solidification.

Gravity casting processes such as IC and sand casting cannot attain the pressures created in HPDC. However, Centrifugal Casting (CC) offers a possible solution, to bridge the gap between gravity filling of a traditional sand casting process and the pressure filling of the die casting process. This results in more sound and dense castings. Since the metal experiences pressure, conventional casting defects such as internal shrinkage, gas porosity and non metallic inclusions are less likely to occur in CC. Improved mould filling in CC also leads to a reduction of rises and runners, reducing scrap rate and secondary fettling processes. Also natural directional solidification occurs as the solidifications starts from the outside and moves inwards to the central in-gate. Sacrificial moulds and cores can be also used in the CC process with green or dry sand, plaster and graphite moulds. This opens up a new avenue for experimentation with RP moulds. Combining 3D printing as a mould making process and CC as a filling technique may produce advantages from pressure filling, paving way for sound RP castings. Current research is therefore aimed at the feasibility of CC in rapid prototyped moulds. A brief review of the CC process and related matters follows next.

Specific variables in the CC process include melting practices, mould and pouring temperatures, rotation speed and alloys. Most importantly, rotational speeds can be varied greatly. With respect to green sand moulding, low speeds are recommended for initial pouring with gradual increases up to the rated speed after partial filling of the mould. This is combined with the application of a mould coating or wash to green sand mould to ensure a dry

mould surface. Strieter and Maonner [43] looked into CC of light metals like AZ92 Mg alloy into steel dies using a vertical CC process as early as 1946. The use of Mg alloys in CC was very limited, due to rapid oxidisation upon melting and severe mould metal reactions. Furthermore, density of molten Mg is lower than that of Mg oxide, which means that oxide entrapment is common and difficult to remove. Test results showed several problems including pits, micro-porosity and cold shutting. Pitting was found to be due to excessive turbulence of the molten metal. In an attempt to reduce this effect, metal was initially poured at low rotational speed and then after filling with increased speed. No significant improvements were seen. The creation of oxides and other defects were also said to be due to excessive turbulence, especially at increased temperatures. Despite these defects, optimum process variables were found to be around 1000rpm and 700-760°C. Mould temperature was 315°C. Cost and mechanical properties of the castings were of equal or better quality than static permanent mould castings. Ultimate Tensile Strength (UTS) properties ranged from 252-255MPa compared to that of 206-215MPa for the equivalent static casting. Grain size was found to vary from 76.2-114μm when compared 228-279μm for the equivalent static casting. Ductility was found to vary from 1-1.8% compared to 1-1.3% for the static casting. All mechanical properties tested showed improved properties with the CC method.

Mechanical property improvement in CC was also observed by Chirita [44] in relation comparison to a static gravity casting model. During cooling, the first nucleation sites for solidification in CC come back into the melt, thus increasing the number of solidification sites due to excessive movement of lower temperature particles. This leads to quicker solidification and a refined grain structure when compared to gravity casting. This was similar to vibration of a static mould during solidification. Photomicrographic evidence [45] suggested that increasing rotational speed significantly refined the coarse α-aluminium grains to fine equiaxed α-Al grains. Higher rotational speeds also meant uniform distribution of secondary phases, leading to improved mechanical properties and increased wear resistance.

Mathematical modelling of the whole centrifugal process is important as this provides insight into the mechanics of the process where pure experimental

techniques become more difficult to test. Most recent work is centred on the application of numerical models to analyse fluid flow and thermal fields in CC. While most analytical work was on the mechanics of functional grading of materials using CC, Howson [46] analysed horizontal and vertical centrifugal casting to considering the fluid dynamics of the process. His model considered forces acting on a liquid particle in contact with the mould wall and excessive turbulence and particle separation were shown as possible defects in CC. In 2007, Mesquita et al [47] developed an analytical model considering an infinitesimal element of liquid under the action of centrifugal and friction forces, after experiencing an initial velocity due to gravity filling through the down gate. A governing differential equation was developed taking into account the friction force and the centrifugal force as functions of time, to determine the radial position and velocity of the molten metal from the central down gate at different time intervals.

Summary of Literature

From the above literature, the application of RP in the casting industry has led to significant research, primarily into RP pattern use and its suitability in the IC process. This research related to pattern accuracy and the ability of patterns to be invested and burnt out. Later use of RP techniques utilised sacrificial moulds produced by the SLS and 3D printing processes and this prompted investigation into achievable tolerances of printed moulds. Some work was also conducted on the cast part quality, with studies focusing mainly on the surface quality and cast part accuracy. Little work was conducted on the actual mechanical properties of the castings produced in 3D printed moulds with Al alloys and the author found no literature available on casting other light metals such as Mg. Further, the suitability of RP moulds in pressure filling applications such as centrifugal casting is unknown, with little literature quantifying the effects of process variables when using the this technique.

Project Objectives Identified from Literature

Initial investigations looked to quantify the effect of varying temperatures and time baking factors on ZCorp material (ZP131) to establish optimum mould compressive strength and permeability. These values were then compared to work previously completed on ZCast501 material.

Further investigation is aimed at metal filling under gravity (static) pressure to test the impact on subsequent cast mechanical properties.

Investigation into Centrifugal Casting (CC) follows, to show that increasing pressure filling of liquid metal is practically feasible with these moulds. This will then permit combining the advantages of 3D printing technology with the benefits of pressure filling.

The research then progresses to the actual response of RP moulds to both static and centrifugal pressures, mould erosion, metal-mould reactions and gas porosity. The significance of static and CC parameters on the mechanical properties will be examined using these RP moulds and processes.

This work will thus identify the best combination of mould material, alloy type, mould coating and pouring temperatures to produce acceptable castings. These optimum parameters will then be used for processing centrifugally cast parts in RP moulds. Influencing factors such as rotational speed, cavity angle and in gate ratio will be investigated. A statistical design of experiments will be employed to facilitate conclusions on the effects of multi-process variables upon the mechanical properties of castings produced.

1.4 Research Questions, Hypotheses and Project Objectives

Broadly, the current research comprises experimental testing to establish the properties of 3D printed moulds and light metal castings when used in the static and CC processes. Specifically, the proposed research questions are:

(i) What happens to the moulds and metals utilised like Al and Mg when static and centrifugal processes produce castings using 3D printed moulds. Specifically, what are the mechanical characteristics of cast parts and the optimum combination of process parameters for the best performance of the cast parts?

(ii) What would be the response of these moulds and castings to increased centrifugal pressure? More specifically, what effect does rotational speed, cavity orientation and runner-cavity ratio have on the mechanical properties of the castings, and how do these castings compare to traditional static castings?

The following are the proposed hypotheses:

(i) It is postulated that each 3D printed mould material has an optimum set of process parameters for the best combination of mould characteristics.
(ii) It is also thought that an optimum set of process variables exist for each casting process, from which the best mechanical properties will result.

Specific Project Aims

- Establishing the critical properties of 3D printed moulds
- Establishing the suitability of these moulds to process light metals, such as Al and Mg and the differences that exist when compared to traditional sand castings
- Establishing the mechanical properties of the castings produced in these moulds
- Determining the key influences in both static and centrifugal casting process and quantifying their effect on the mechanical properties of the castings

1.5 Methodology

Much of the work conducted throughout this project consisted of experimental trials and interpreting their significance within a statistical model. The objective was to produce quantitative information and the optimum combination of process factors to be used for further experimental work. This methodology is divided into three sections covering the experimental testing conducted on the mould materials and the work involved in the static and CC trials.

The first methodology was to analyse the suitability of 3D printed moulds for producing metal castings by introducing time and temperature baking variables. Tests were conducted on the moulds to evaluate mould permeability and strength of the rapid prototyped materials, namely ZP131 plaster material and ZCast501 material (previous work). These experiments were conducted in the context of a central composite experimental design which was able to fit an experimental model to determine the significance of different factors and establish an optimum combination of these factors for the mould responses.

After these initial mould properties were established and the optimum combination found, static casting trials involving two magnesium alloys and one aluminium alloy were cast in these mould materials and also in a traditional silica foundry sand material. A basic mould design consisting of a central inlet, pattern and riser was created, in which the pattern consisted of cylindrical specimens which were machined down to the appropriate tensile test sample. This mould design and the castings produced were then analysed using a Taguchi L9 experimental technique. These static casting trials involved varying a number of process factors to establish their influence on the mechanical properties of the cast metals, and the suitability of these moulds to process these castings. The factors included the pouring temperature of the alloys, the mould coating, the mould material and the alloy type. Signal to noise ratio analysis was then undertaken using the Taguchi technique, which resulted in the ranking of factors and their influence on the

mechanical and microstructural responses. A subsequent Analysis of Variance (ANOVA) was then undertaken to establish the level of confidence for the significance of these factors. Finally, the most influential process factors were correlated, so that further casting trials could utilise these settings.

Following the static casting trials, the suitability of these moulds in the centrifugal casting process was examined. The ability to create increased filling pressures in the centrifugal process was used to determine its influence upon the mechanical properties of the cast parts. From the previous work on static casting trials, the optimum mould material and process factors were used in the centrifugal castings. The lack of experience in this process led to some initial trials being conducted at the supporting company, Centracast. After these initial castings were completed, and suitable centrifugal process variables identified, an experimental was designed in which process factors such as the speed of rotation and geometry mould cavity were evaluated. This was to determine their influence on the as-cast mechanical and microstructural properties of test specimens. The completion of the experimental analysis and ANOVA on the resulting model established the relationship of process factors to the mechanical properties of the castings in the centrifugal process.

CHAPTER 2 CHARACTERISTICS OF 3D PRINTED MOULDS

2.1 Mould Materials

The mould materials supplied by the ZCorporation (ZCorp) are proprietary materials and little information is available regarding their essential characteristics for metal casting. The critical properties of moulds are:

- Mould Compressive Strength (MCS)
- Mould Permeability (MP)

In this study less important characteristics such as refractoriness and loss of ignition are not analysed. MCS and MP need to be optimised in order to ensure that adequate castings are produced. Optimisation of both variables is obtained by determining the baking times and temperatures of the mould for the highest MCS and MP. Thus experimentation proceeds by way of quantifying the mould behaviour with respect to time and temperature of baking so as to develop models to predict MCS and MP for use in future mould design. The mould materials used are plaster (ZP131) and a specially formulated ceramic, (ZCast501), with the latter being recommended by the manufacturer for light non-ferrous castings. These materials are chemically bound by the relevant binder, being ZB60 for ZP131 and ZB58 for ZCast501. These are baked in a furnace to achieve its dry strength[1].

2.1.1 Basic Ingredients of the Mould Materials

Basic ingredients of the ZCorp mould materials and binders used have to be established either by independent testing or from the data specified in Materials Safety Data Sheets (MSDS).

[1] Dry strength refers to mould strength obtained after subsequent baking and curing

Mould Materials

Independent testing of ZP131 by X-ray diffraction revealed the following ingredients as the basic constituents of this material:

$CaSO_4 \cdot 0.67H_2O$

This composition is partially Calcium Sulphate Hemihydrate [48].

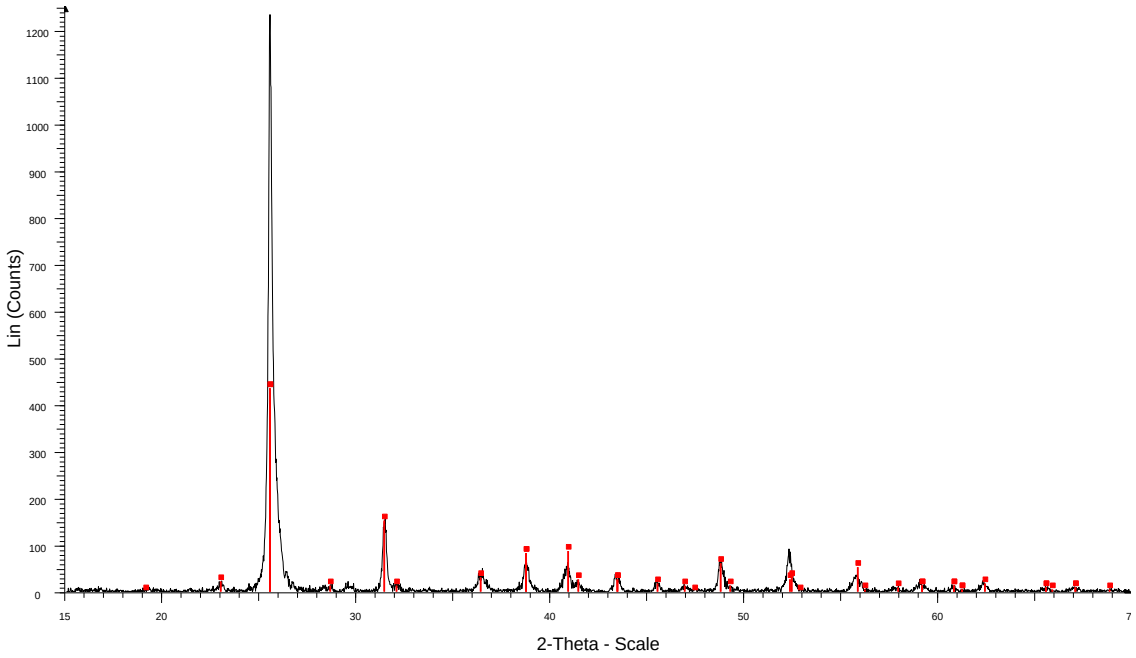

Figure 2.1 Spectra of ZP131 mould material by X-ray diffraction

XRD testing of ZCast501 also revealed the following ingredients as the basic constituents of this material:

1. $CaSO_4 \cdot 0.67H_2O$ (50 wt. %)
2. $MgSiO_4$ (50 wt. %)

The first composition is partially dehydrated Calcium Sulphate, known as Calcium Sulphate Hemihydrate [48], commonly referred to as gypsum plaster or Plaster of Paris. The second composition is Olivine Sand.

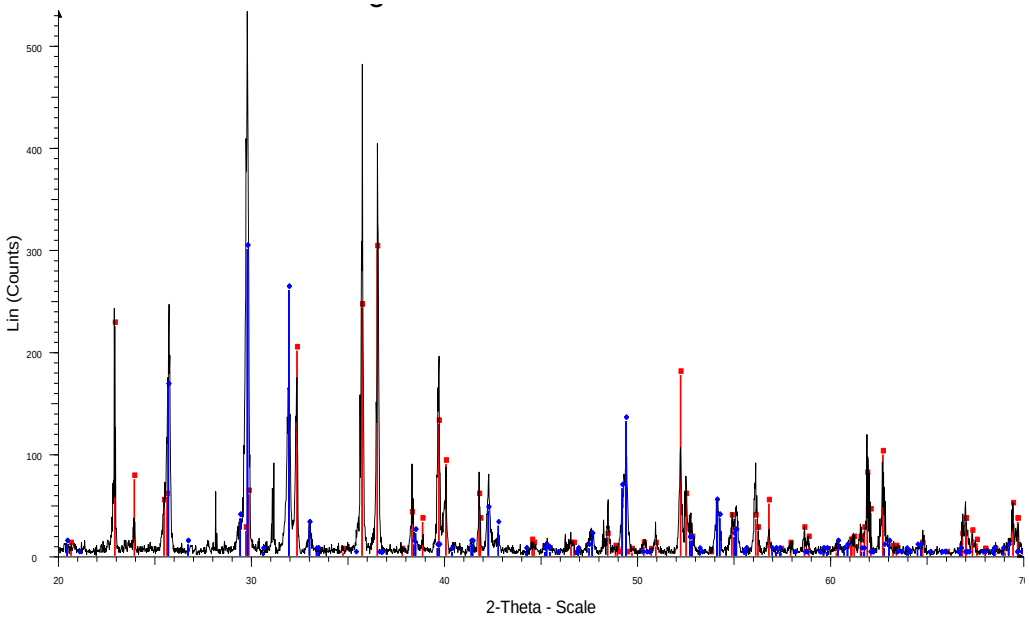

Figure 2.2 The XRD spectra graph showing the refraction angles of the ZCast 501 material

Comparative Manufacturer MSDS of Liquid Binders

To bind the 3D printer mould materials together, a proprietary binder produced by ZCorp is applied as an adhesive between each material grain. Analysis of binders is not amenable to powder X-ray diffraction but MSDS gives a good indication of the binder composition. Table 2.1 and Table 2.2 show the basic ingredients and compositions of the binders used for ZP131 ZCasy501 respectively.

While the basic chemistry and bonding mechanisms in each of these material-binder systems are important, there is little existing literature on the effectiveness of the ingredients and the proportionalities of the materials used. In this research, however, these aspects are not considered, and attention is mainly focussed on the overall characteristics and response of the mould material aggregates under varying process conditions for metal casting.

Table 2.1 The ZB60 binder ingredients for the ZP131 material [49].

Ingredient	Approximate amount (% mass)
Homectant 1	<10
Homectant 2	<8
Polymer	<4
Water	85-95

Table 2.2 ZB58 binder composition for the ZCast501 material [50].

Ingredient	Approximate amount (% mass)
Glycerol	1-10
Preservative (Sorbic acid salt)	0-2
Surfactant	<1
Pigment	<20
Water	85-95

2.2 Experimental Design for Mould Material Analysis

The mathematical model used to gauge responses to combinations of baking time and temperatures is governed by statistical variance analysis. The objective is to show the relationship of changes in the independent variables of time and temperature to the outcomes (responses) MCS and MP. Experiments proceeded by way of creating a matrix of varying time and temperature combinations, followed by a regression analysis of these outcomes. The results of the regression analysis for MCS and MP each devolve to a second order polynomial expression with two independent variables.

The experimental design used is a Central Composite Design (CCD) which yields a classical quadratic equation. This design, shown below in Figure 2.3, has sampling points at evenly spaced intervals from the central point. This is undertaken on the basis that it is not known in advance how the response surface will be orientated around the x-y axes and there is no presumption that the standard error will be greater in some directions rather than others

[51]. This provides the maximum information on each response with fewer trials than by using standard factorial experimental designs. This is important as the mould materials are relatively expensive.

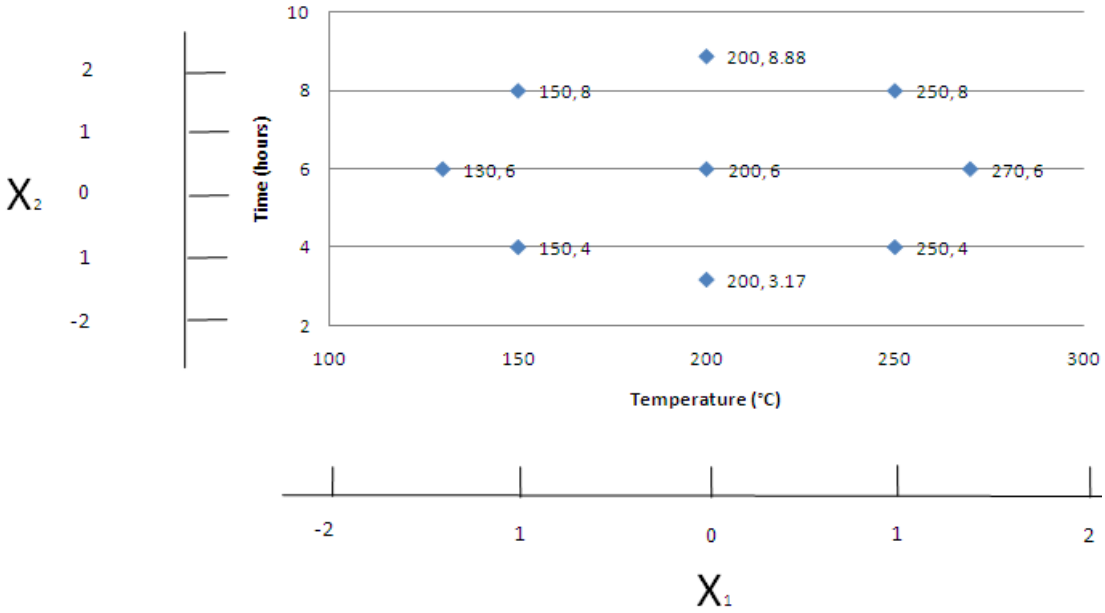

Figure 2.3 Data plot of the points showing the different sampling combinations of the central composite experimental design.

Figure 2.3 shows temperatures (X_1) and times (X_2) at which the mould is baked in a furnace. The CCD allows variation of baking time from 3.17-8.88 hours and temperature from 130-270°C, with the sampling points as shown, at equal distances from the central point. Each variable is labelled with both natural and coded values. For example 200°C is transformed into a coded variable which in this case is 0 at X_1.

The natural points of temperature and time, namely (130,6), (200,8.88), (200,3.17) and (270,6) form the star points of the model. The star points are those points at a distance α from the centre point and these points establish new extremes for the factors. In a CCD design α is equal to $\sqrt{n}$, where n is the number of factors; in this case two. Thus $\alpha = \sqrt{2} \cong 1.414$.

The CCD for outputs of MCS and MP proceeds in three separate parts. The first part is a basic two level factorial segment of the design, which allows the estimation of the linear terms [52].

For the factorial segment, the basic form is:

$$v^n \qquad (2.1)$$

Where:

v = number of levels at which factors is varied

n = Number of factors; e.g. time and temperature

In this case, the linear portion is 2^2 as there are two factors, time and temperature, and the factorial experiment only considers the maximum and minimum of each factor, as shown in Table 2.3 below.

Table 2.3 The Factorial part of CCD

	Levels	
	-1	+1
X_1 (T,°C)	150	250
X_2 (t, hrs)	4	8

The second segment of the CCD consists of the number of experimental repetitions at the centre, which is at the zero level of each factor or in this case (0,0) = (200°C,6 hrs). The third segment of the design consists of axial or star points as shown in Table 2.4, which contribute to the estimation of the quadratic portions of the model. These points are denoted distance α from the centre. This distance is defined through the following equation.

$$\alpha = (n_f)^{\frac{1}{4}} \qquad (2.2)$$

Where: n_f = number of experimental runs in the factorial portion.

This means that: $\alpha = (n_f)^{\frac{1}{4}} = \sqrt{2} \cong 1.414$ (2.3)

Table 2.4 Experimental design table showing (a) the x matrix of the time and temperatures as coded variables and (b) showing the design table with the natural and coded variable combinations

$$\begin{bmatrix} x_0 & x_1 & x_2 & x_1^2 & x_2^2 & x_1x_2 \\ 1 & -1 & -1 & 1 & 1 & 1 \\ 1 & 1 & -1 & 1 & 1 & -1 \\ 1 & -1 & 1 & 1 & 1 & -1 \\ 1 & 1 & 1 & 1 & 1 & 1 \\ 1 & -\sqrt{2} & 0 & 2 & 0 & 0 \\ 1 & \sqrt{2} & 0 & 2 & 0 & 0 \\ 1 & 0 & -\sqrt{2} & 0 & 2 & 0 \\ 1 & 0 & \sqrt{2} & 0 & 2 & 0 \\ 1 & 0 & 0 & 0 & 0 & 0 \\ 1 & 0 & 0 & 0 & 0 & 0 \\ 1 & 0 & 0 & 0 & 0 & 0 \\ 1 & 0 & 0 & 0 & 0 & 0 \\ 1 & 0 & 0 & 0 & 0 & 0 \end{bmatrix}$$

(a)

Trial No	Factors			
	Natural values		Coded values	
	T (^{0}C)	t (Hours)	X1	X2
1	150	4	-1	-1
2	250	4	1	-1
3	150	8	-1	1
4	250	8	1	1
5	130	6	-1.414	0
6	270	6	1.414	0
7	200	3.17	0	-1.4141
8	200	8.88	0	1.4141
9	200	6	0	0
10	200	6	0	0
11	200	6	0	0
12	200	6	0	0
13	200	6	0	0

(b)

Table 2.5 The CCD experimental design with additional star points

	Levels				
Coded variable	-1.414	-1	0	1	1.414
X_1 (T°C)	130	150	200	250	270
X_2 (t hrs)	3.17	4	6	8	8.88

This is translated into the X matrix and the design table, as shown in Table 2.4.

Actual experiments are conducted as per the design table, using the combinations of different factors. Using the responses measured and the matrix multiplication, polynomial expressions are developed for both MCS and MP, in the following general form:

$$y = \beta_0 + \beta_1 X_1 + \beta_2 X_2 + \beta_{11} X_1^2 + \beta_{22} X_2^2 + \beta_{12} X_1 X_2 \qquad (2.4)$$

Where:

y = Is the response at X_1 and X_2 (for both MCS and MP with their respective co-efficients).

2.2.1 ANOVA Calculations

The two equations for MCS and MP as per equation (2.4) must now be analysed:

(A) To test the overall model significance in fitting the experimental data.

(B) To test the linear, quadratic and interaction contributions of the model to results achieved.

First, the ANOVA examines the suitability of the regression analysis of the model in terms of its accuracy and its confidence (A). Then, ANOVA tests the significance of the linear and quadratic segments of the model and the overall residual term (B). This is accomplished through the use of difference of sum of squares.

Sum of Squares Regression Term (A)

$$SS_R = \sum_{i=1}^{n} (\hat{y}_i - \bar{y})^2 \tag{2.5}$$

Where:

$\hat{y}_i$ = The calculated result from the model at interval i

$\bar{y}_i$ = Average of experimental results

Sum of Squares Residual Term

$$SS_{RES} = \sum_{i=1}^{n} (y_i - \hat{y}_i)^2 \tag{2.6}$$

Where:

y_i = The experimental result at interval i

$\hat{y}_i$ = The calculated result from the model at the interval i

Pure Error (PE) Term and Lack of Fit (LOF)

$$SS_{RES} = SS_{PE} + SS_{LOF} \tag{2.7}$$

$$SS_{PE} = \sum_{i=1}^{n} (y_{ij} - \bar{y}_i)^2 \tag{2.8}$$

Where:

y_{ij} = Experimental result at centre at interval I of that group, j

$\bar{y}_i$ = Average of calculated results from model of group j

Thus $SS_{LOF} = SS_{Res} - SS_{PE}$

This describes the lack of fit of the model to the experimental data.

Sequential Sum of Squares (B)

This analysis establishes the effect of the linear, square and interaction terms separately and quantifies their individual contribution to the overall residual sum of squares. To establish these separate effects the model equations need to re-fitted to the experimental values to create separate new linear, quadratic and interactive equations. Thus, considering only the linear terms of equation (2.9) the equation then becomes:

$$y = \beta_0 + \beta_1 X_1 + \beta_2 X_2 \tag{2.9}$$

From here, the residual sum of squares is calculated using the following equation.

$$\sum_{1}^{n}(y_{xx} - \hat{y})^2 \tag{2.10}$$

Where:

y_{xx} = Predicted value using equation (2.9)

$\hat{y}$ = Predicted value using entire model

So the difference between the case of the linear effect and quadratic effect is shown below.

$$SS_{seq;linear} = ESS\ \ \beta_0\beta_1\beta_2 \mid \beta_3\beta_4 \tag{2.11}$$

Where: $$ESS = \sum_{1}^{n}(y_{\beta_0,\beta_1,\beta_2} - \hat{y})^2 - \sum_{1}^{n}(y_{\beta_0,\beta_1,\beta_2,\beta_3,\beta_4} - \hat{y})^2 \tag{2.12}$$

The values in parentheses in equation (2.11) refers to the constants in the separate linear and quadratic equations. Equation (2.12) shows that the sequential sum of squares is equal to the difference of the error sum of squares between linear terms and quadratic terms of the model. This process is further repeated for the remaining part of the polynomial, i.e. the interaction component[2].

Degrees of freedom (DOF)

The DOF for the ANOVA is the number of independent parameters to describe a particular component in a model, here the components being MCS and MP. For the overall model there are six parameters, resulting in five DOF. The linear, quadratic and interaction DOF are listed below, followed by the other terms in the ANOVA table.

[2] Appendix B details the relevant details.

DOF linear: Terms $\beta_o, \beta_1, \beta_2$ form the linear part thus DOF = 3-1 = 2

DOF Quadratic: Terms $\beta_o, \beta_{11}, \beta_{22}$ for the Quadratic part thus DOF =3-1 = 2

DOF Interaction: Terms $\beta_{0,}\beta_{12}$ for interaction part thus DOF = 2-1 =1

DOF Residual: This is the total DOF for both pure error and lack of fit and is in the form of the equation:

$$DOF_{RES} = N - P \tag{2.13}$$

Where:

N = Total number of experiments

P = Number of parameters (constants) in equation

DOF Pure Error is:

$$DOF_{PE} = \sum (N_{replicate} - 1) \tag{2.14}$$

Where: $N_{replicate}$ = The number of experimental runs at the centre

DOF Lack of Fit: $DOF_{LOF} = DOF_{RES} - DOF_{PE}$ (2.15)

F test

The F test or F statistic determines the significance of the amount of variance explained by each of the linear, quadratic and interaction terms when sequentially added to the model for determination of MCS and MP. The F test is based on the following equation:

$$F_o = \frac{SS_R / DOF_R}{SS_{RES} / DOF_{RES}} \tag{2.16}$$

If this number, F_o is less than the number found from standard tables, the Null Hypothesis is true and the significance of the model or lack of fit of the model

to the data is statistically due to chance. If F_o is higher than the standard reference the null hypothesis is rejected and the model correlation is said to be statistically significant at the chosen probability level. If a probability (P) value is <0.1 (confidence level 1-P) then 0.1 (10%) is used and the null hypothesis is rejected. This means that the there is a no greater chance of 10% of the result being due to chance.

2.3 Experimental Methodology for Testing Mould Materials

Experimental testing was conducted on 3D printed mould materials to determine MSC and MP. As noted above, statistical design of experiments was applied to ensure that the variability in the results was quantified in a scientific manner. The other primary use of statistical experimental designs was to reduce the number of experimental trials to decrease the consumption of the 3D printer materials.

Mathematical models for critical mould properties were developed as above, section 2.2. The ZCorp materials utilised were a plaster (ZP131) and plaster sand mixture (ZCast501), with the latter supplied with guidelines for a post print baking process. The general baking guidelines for ZCast501 is specified as 4-8 hours and 200°C.

The critical characteristics of sand moulds are MCS and MP [53]. High MCS is required to produce suitable moulds for metal casting. High MP allows relief from gas pressure build up during casting. The baking times and temperatures of the mould materials were varied to established their effects on responses (MCS and MP) in a two factor central CCD.

After printing and baking, all printed mould specimens were kept in a controlled low humid environment in a dessicator, shown below in Figure 2.4, to ensure consistant low humidity of the specimens. This was done to remove any complex influence that moisture may have on the MCS and MP and ensure results are only due to the influences of varying time and temperature of baking.

Figure 2.4 Photograph of the desiccator used to prevent moisture formation

All specimens were baked in electric furnaces at various temperatures and times. Each furnace was tested with a CHY K-type thermocouple to ensure that the temperature control was accurate to ±10°C. In all cases the curing temperature was reached first before the samples were placed into the furnace. Once the specimens had cooled down after baking, to room temperature, they were placed in desiccators to minimise any moisture effects. Testing was conducted on both mould materials used by the ZCorp 310 printer.

2.3.1 Mould Compressive Strength (MCS)

Compression tests on the mould samples were conducted using the Hounsfield equipment at AUT University, shown below in Fig. 2.4, using a length to diameter ratio of 2:1. The specimen shape was based on the ASTM D7012 – 10 standard [54].

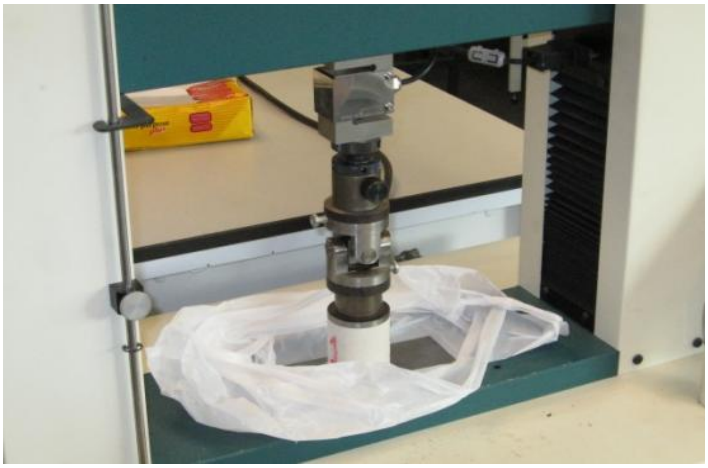

Figure 2.5 Photograph depicting the compressive test of the mould material.

The testing methods were those outlined in [54] which state that the loading rate should be at such a rate that will cause the specimen to fail within 5-10 minutes. This corresponded to a loading rate of 0.1 mm/min. However it is noted that compressive strength testing on rock like materials can compress onto themselves after initial fracture, giving values higher than the true value. To allow for this, each specimen was also observed visually for cracks at the time of initial failure. The significant drop in strength and visual sign of a crack were utilised as the true indicators of ultimate compressive failure.

2.3.2 Mould Permeability (MP)

Permeability measurements were made at the Geo-mechanics laboratory of the Civil Engineering Department of the University of Auckland. Printed cylindrical ZCast501 and ZP131 specimens, 78mm in length and 38mm in diameter, were tested. Each specimen was applied with a silicone sealant shown below in Figure 2.6a The sealant was applied around the outside longitudinal surface of the cylinder and then fitted with an impermeable rubber membrane. The specimen was then allowed to dry for 12 hours before being placed in the load cell, with rubber rings placed on the top and bottom steel seats. The role of the sealant was to prevent any air escaping outside the cross section and around the specimen's outer surface. Once the specimens were sealed, each specimen was contained in water to ensure that the rubber

membrane would not expand radially outwards. Any air passing over the outer cylindrical surface of the specimen, rather than only through the cross section, would result in inaccurate readings.

(a)

(b)

(c)

Figure 2.6 The Permeability set up showing (a) the sealant used to adhere the membrane to the specimens (b) rubber rings and specimen with membrane applied and (c) load cell apparatus ready for testing

The pressure from the air tank was set at 16KPa. Once the pressure had stabilised, an inline float type flow meter, located on the outlet side of the specimen, was read every two minutes from zero to thirty minutes. The permeability of materials changes over time but testings related to steady state permeability values only. The flow rate of the passing fluid (air) was subsequently plotted against time to establish when the permeability value had stabilised. In most cases the flow rate stabilised after thirty minutes, but

some specimens stabilised after twenty minutes. Stable conditions were assumed when six minutes had passed, with no further increase in the flow rate. The flow readings were then coupled with atmospheric pressure data sourced from the National Institute of Water and Atmospheric research (NIWA) to calculate permeability values using Darcy's equation[3]. An Auckland weather station was chosen as reference station, and instruments present in the geo-mechanics lab were used to reference the ambient temperature and relative humidity.

Figure 2.7 Photograph of the Tri-axial cell set up for the permeability testing

[3] See Appendix A1

Figure 2.8 Close up of tri-axial cell test apparatus whilst testing

2.4 ZP131 Material Results and Discussion

2.4.1 MCS Model

Earlier casting trials by the author showed that ZP131 gives better results in terms of cast surface roughness, dimensional stability and strength than castings produced in ZCast501 moulds. As a result, it was decided to use ZP131 as a moulding material, and a full analysis of the moulding characteristics of this material was considered. The testing procedures described above were used to analyse the variation of MCS and MP of this material. The regression model developed for MCS are shown in equation (2.17).

$$\sigma_{MCS}(T,t) = 1.64802 - 0.00025T + 0.19267t - 0.00001T^2 - 0.00151t^2 - 0.00091Tt \quad (2.17)$$

The ANOVA below in Table 2.6 showed that the MCS regression analysis was significant. The overall regression of the MCS was found to be statistically significant at a 96.5% confidence level. The low P value for the regression term meant that a significant portion of the total variance was

accounted for by the regression model and this was confirmed with a high R^2 value, showing that 78% of the variation was explained by the regression model. Thus an adequate representation of the overall relationship between MCS and the temperature and time of baking was established. The fact that no significant linear, square or interaction effects were found indicates that no individual effect was significant, rather the combination of all of these. This can also be observed in the response surface plot shown in Figure 2.11, which shows the linear nature of the surface but also the curved square effect. Also the surface plot revealed the optimum levels to be 150°C and 8 hours for maximum MCS.

The pure error Sum of Squares (SS) term accounted for roughly two thirds of the overall residual SS. This led to a low value for the lack of fit of SS, showing that the model was fitting the data adequately. The large error term reflects the deviations among the repeated centre points trials and shows that there was a large standard deviation.

Table 2.5 ANOVA of compressive strength model of ZP131

Source	DF	Seq SS	Adj SS	Adj MS	F	P
Regression	5	1.71474	1.714745	0.342949	5.28	0.025
Linear	2	1.67845	0.019296	0.009648	0.15	0.865
Square	2	0.0033	0.003298	0.001649	0.03	0.975
Interaction	1	0.033	0.032995	0.032995	0.51	0.499
Residual Error	7	0.45438	0.454376	0.064911		
Lack-of-Fit	3	0.11972	0.119724	0.039908	0.48	0.715
Pure Error	4	0.33465	0.334653	0.083663		
Total	12	2.16912				

R^2 = 79.05%

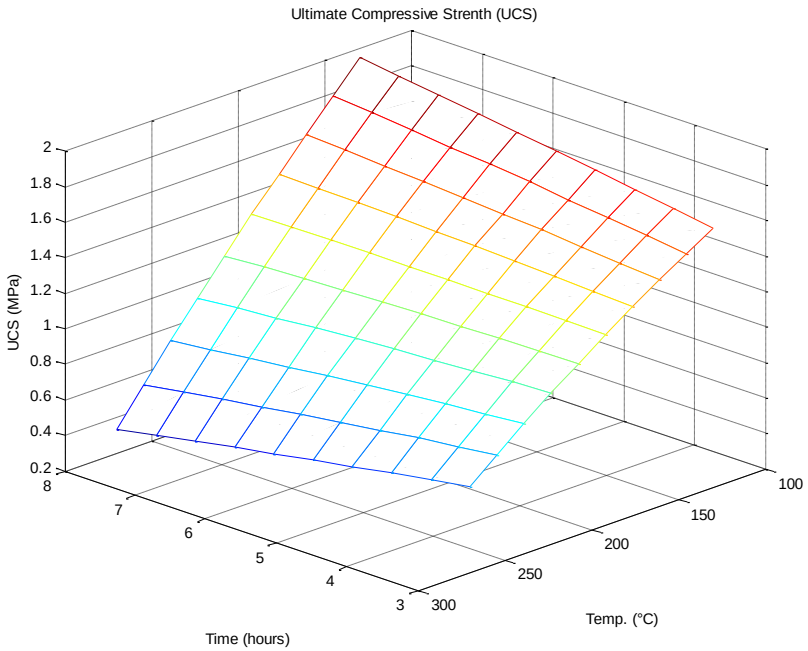

Figure 2.9 Compressive strength Vs baking time and temperature for ZP131

Variation of MCS model in Figure 2.9 shows that the best results were obtained at the lowest temperatures and highest time exposures. Increasing the baking temperature resulted in an almost linear decrease in the MCS over the entire time range, as shown in Figure 2.10a. By increasing the time interval however, this linear relationship to strength remained, but the slope gradually became more negative as time increased. This was most likely due to the removal of moisture from the gypsum plaster particles. This increased heat energy resulted in lower strength values, obviously affecting the bonding strength of the gypsum material. Increased baking temperatures removed water of crystallisation present in the gypsum microstructure [48], which results in weakening the microstructural strength of the plaster.

With respect to varying time (Figure 2.10b), the effect of increasing the temperature level was a decrease in the MCS response. However, there was a small interaction effect, with increasing temperatures changing the slope of the MCS expression from positive to negative over time. The ANOVA table shows that this interaction effect was the most significant individual model effect in the MCS analysis.

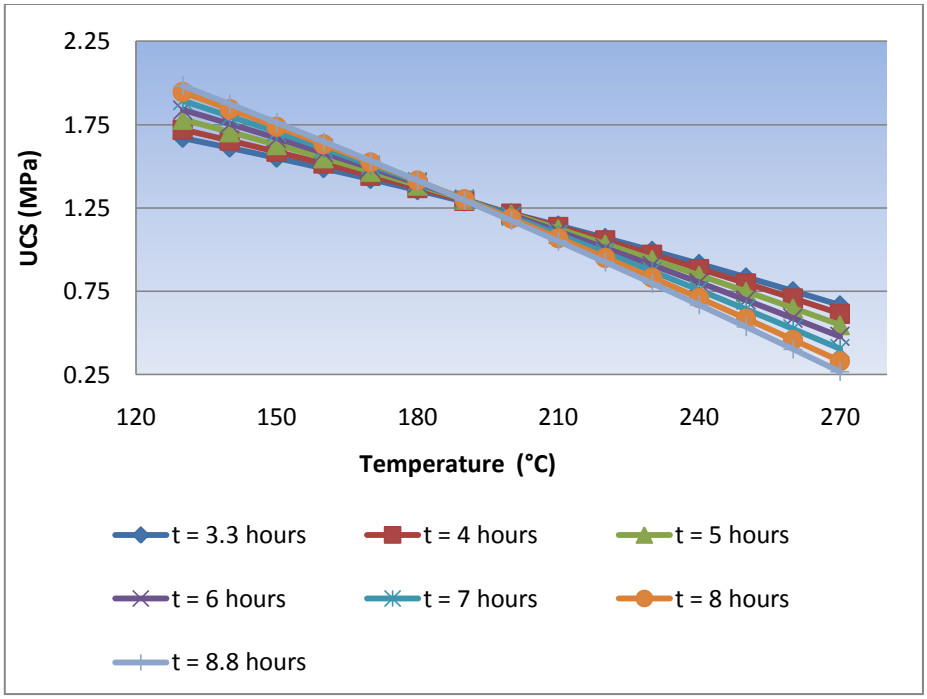

(a) MCS Vs Temperature

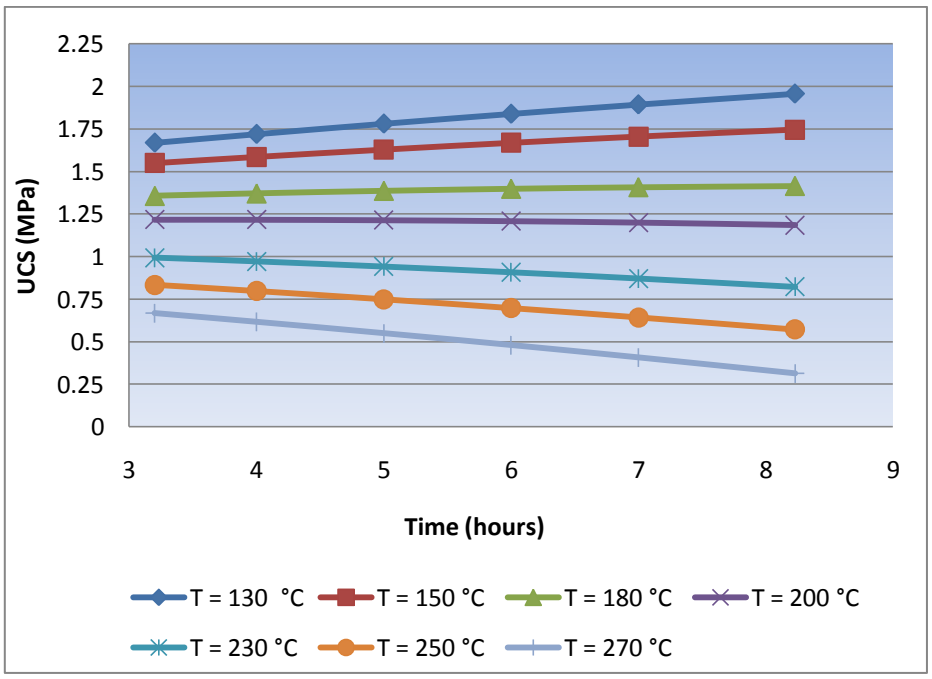

(b) MCS Vs Temperature

Figure 2.10 The Variation of Mould Compressive Strength of ZP131 with (a) baking temperature and (b) baking time

2.4.2 MP Model

The ANOVA of the MP model is given in Table 2.6 and revealed no statistically significant model effects with respect to varying time and temperature of baking. The coefficient of determination (R^2) reveals that only 38% of the total variance was accounted for by the chosen factors. The R^2 value was low, due to the large residual variance not explained by the model. This variance was comprised of pure error and model lack of fit. The pure error term was found as the majority of the total residual SS. This indicates that there was considerable variation in the trials that were repeated under the same conditions. The model lack of fit also accounted for just below half of this overall residual, highlighting the inadequacy in modelling the data. The model shows that the best MP values were achieved at low temperatures and baking times, shown below in Figure 2.11. The response surface (Figure 2.11) showed that increasing baking time and temperatures resulted in decreasing MP of ZP131 samples, with an optimum point established at 150°C and 3.2 hours. The model however, was able to fit the data, with no statistical lack of fit found. This all suggests that MP was not significantly affected by the time and temperature baking process over the chosen intervals.

$$MP\ T,t = 6199.86 - 18.16T - 635.65t + 0.03T^2 + 41.78t^2 + 0.41Tt \quad (2.18)$$

Table 2.6 ANOVA of permeability model of ZP131

Source	DF	Seq SS	Adj SS	Adj MS	F	P
Regression	5	414756	414756	82951	0.86	0.55
Linear	2	181393	189423	94712	0.98	0.421
Square	2	226773	226773	113387	1.18	0.363
Interaction	1	6590	6590	6590	0.07	0.801
Residual Error	7	674977	674977	96425		
Lack-of-Fit	3	303285	303285	101095	1.09	0.45
Pure Error	4	371692	371692	92923		
Total	12	1089734				

R^2 = 38.06%

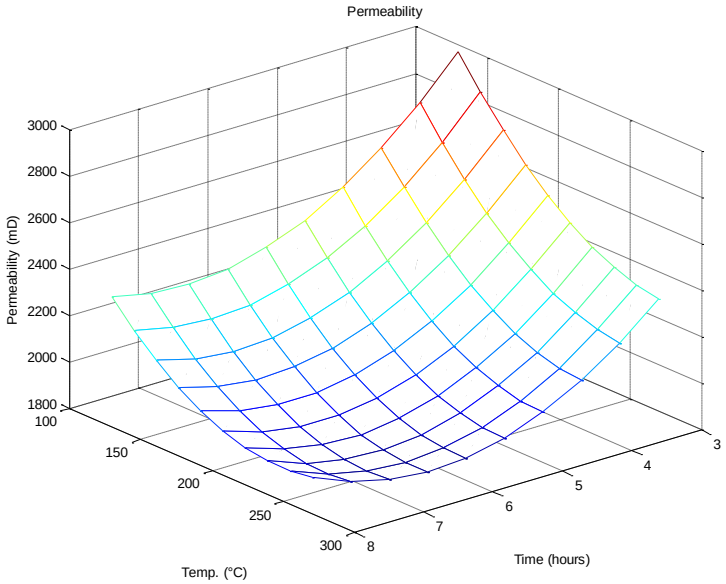

Figure 2.11 Permeability Vs baking time and temperature in the case of ZP131

The permeability plots in Figure 2.12 below show that the material was found to be more permeable at conditions closer to the green state, i.e. not baked. The effect of increasing baking temperature, shown in Figure 2.12a, resulted in a lower permeability curve. This trend continued at baking times from 3.3-6 hours but longer exposures from 7-8.8 hours resulted in a slight increase in the permeability curve. Also little interaction effects were observed, with changing factor levels resulting in a shift in the MP curve, rather than altering the slope of the curve. This relationship was quantified in the above ANOVA table with low P values for the interaction term.

With respect to time (Figure 2.12b), permeability decreased as time was increased. However after around 7 hours, Figure 2.12b shows the MP began to rise slightly. The lower permeability curves were unusual as it was expected that the permeability would slowly increase as the moisture was removed from the sample. It was possible that as the baking temperature was increased bonding strength was lowered, which may have led to some blocking of intergranular pathways. This would account for the initial decreasing trend, with the prolonged heating effect removing some binder constituents and slightly raising permeability.

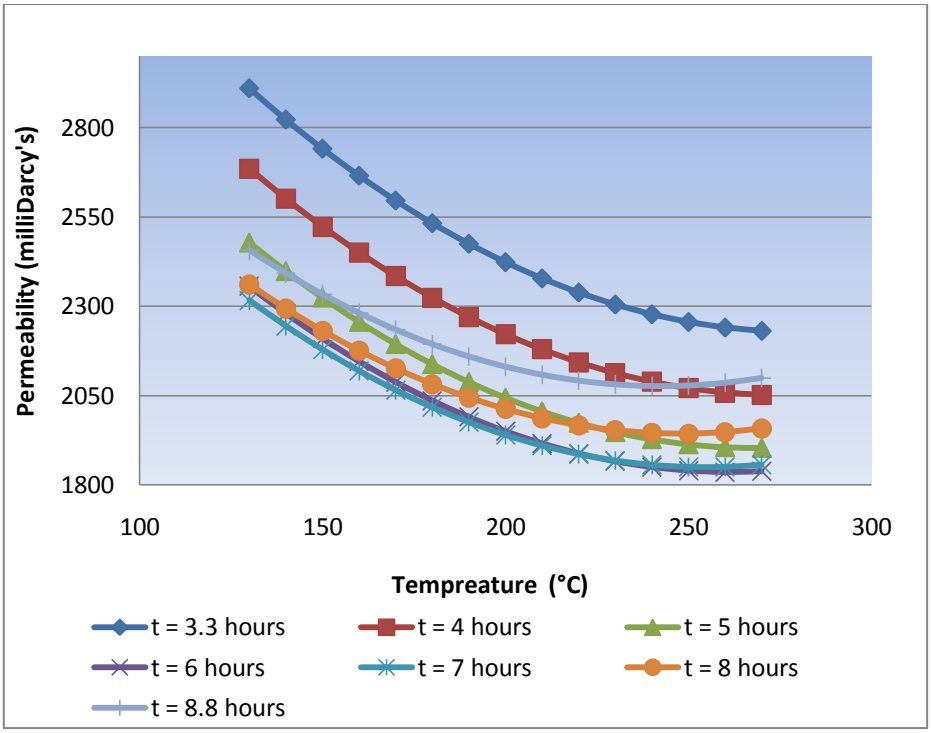

(a)

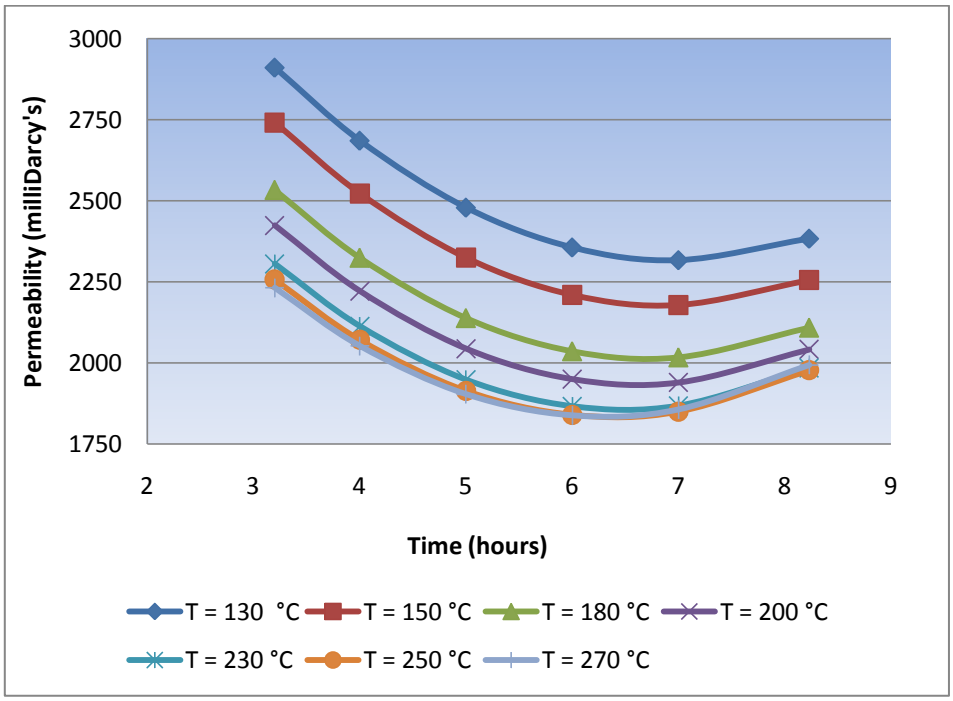

(b)

Figure 2.12 Permeability plots with respect to (a) varying temperature and (b) time

2.5 ZCast501

2.5.1 ZCast MCS

The same analysis for ZCast501 was earlier undertaken by the author in the final year of the undergraduate study. The response models, essential results and discussion, are presented here for the sake of continuity. The regression models for MP and MCS are given by equations 2.19 and 2.20 respectively.

$$MP(T,t) = -2962.12 + 10.94T + 1231.25t + 0.01T^2 - 57.6t^2 - 2.24Tt \quad (2.19)$$

$$\sigma_{MCS}(T,t) = -3.535 + 0.03205T + 0.694t - 80\times10^{-6}T^2 - 0.0514t^2 - 7.7\times10^{-4}Tt \quad (2.20)$$

The response surface for the MCS of the ZCast501 samples are shown in Figure 2.13 and the ANOVA of the model is given in Table 2.7. The ANOVA shown in Table 2.7 showed that all model parameters were significant with all parameters above the 90% confidence level, with the exception of the interaction term. The addition of the square term was the most significant with a confidence of 94.8 percent. The linear SS term was also significant at 90.8 percent confidence.

The overall regression model had 96.8% confidence level and accounted for a significant portion of the total variance in the experimental results. The model also fitted the experimental data adequately. A small residual term meant that most of the variance was accounted for by the varying baking time and temperature factors. The repeated centre point trials in the experiment were found to be consistent and close to the grand average of the experimental results.

Table 2.7 ANOVA table of the MCS model

Source	DF	Seq SS	Adj SS	Adj MS	F_{ratio}	P
Regression	5	1.00818	1.00818	0.20164	6.35	0.032
Linear	2	0.62379	0.25341	0.1267	3.99	0.092
Square	2	0.36092	0.36092	0.18046	5.68	0.052
Interaction	1	0.02348	0.02348	0.02348	0.74	0.429
Residual Error	5	0.15883	0.15883	0.03177		
Lack-of-Fit	3	0.09757	0.09757	0.03252	1.06	0.519
Pure Error	2	0.06126	0.06126	0.03063		
Total	10	1.16701				

R^2 = 86.39%

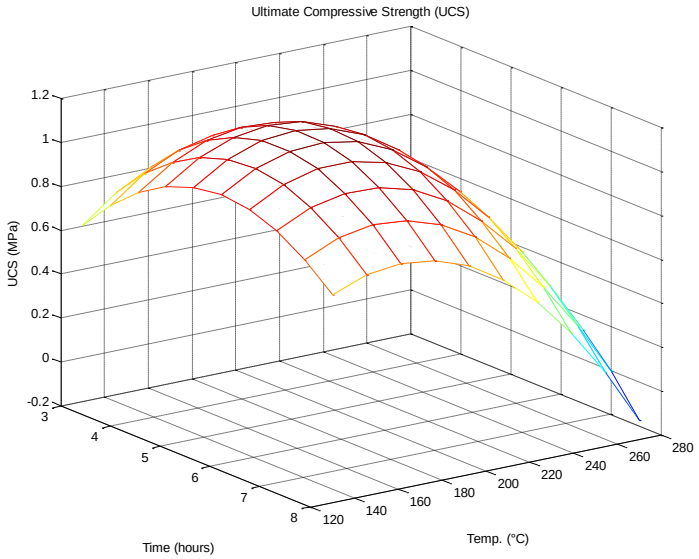

Figure 2.13 Mould Compressive Strength Vs time and temperature of baking for ZCast 501

At times ranging from about 3-6 hours, the MCS was seen to increase with temperature, reach a maximum and then sharply fall with further time and temperature exposure. The initial rise in the compressive strength is substantial and in most cases about 0.2 MPa. This behaviour was attributed to the temperature acting as a catalyst on the liquid binder.

From Scanning Electron Microscopy (SEM) work, conducted at the Department of Environmental Science of University of Auckland, high definition and high magnification pictures of the fractured specimens, from the MCS, were able to be collated. The liquid binder forms a bond between the two different materials, i.e. the gypsum and the olivine sand. This curing of the binder subsequently strengthens intermolecular bonds, leading to the initial rise in compressive strength.

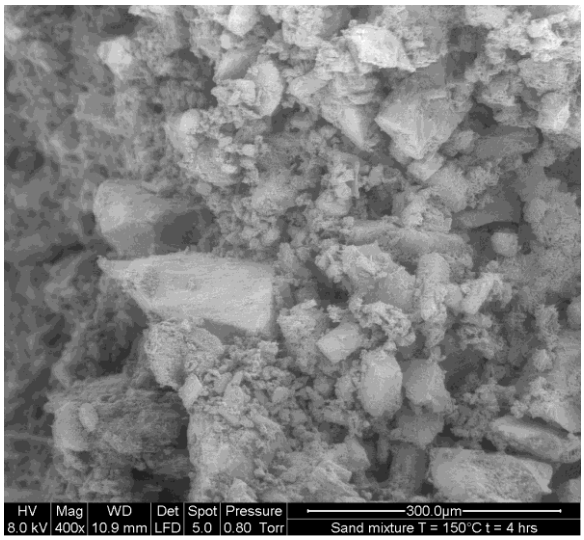

Figure 2.14 ZCast501 mould sample baking temperature was 150°C and time equal to 4 hours

The SEM photograph shown above in Figure 2.14 shows the gypsum particles adhering well to the larger sand grains, acting as a solid binding material in the overall structure. This better adhesive quality of the gypsum was seen at the lower temperatures and thus provided a strengthening structure, producing more resistance to the dislocation movement of the larger sand particles.

With further heating, however, the MCS was seen to drop rapidly after variable changes to time temperature above 6 hours and 200°C respectively. This was possibly caused by the removal of the water from the gypsum material, as water is vital for the gypsum to retain its crystal structure and strength. High temperatures and baking times produced severe dehydration of

the gypsum particles, as shown in the SEM photographs (Figure 2.15). This resulted in highly disorganised and weakened gypsum. The liquid (mainly water) binder present in the gypsum was effectively removed and as expected the MCS reduced dramatically.

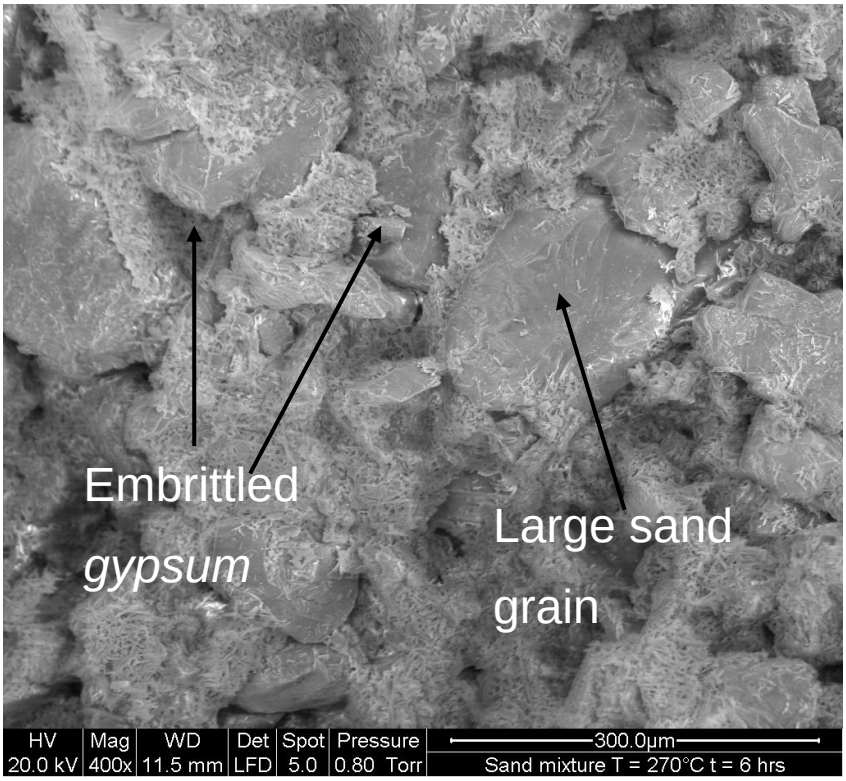

Figure 2.15 SEM photograph showing the embrittled gypsum at the grain boundary

As a result, the gypsum became embrittled and upon application of load the brittle gypsum at the grain boundaries was easily broken and classic intergranular failure resulted. The force of the dislocating sand grains fractured the relatively weak brittle gypsum.

This sudden fall of strength could explain some of the variability in the results. Also, the mechanics of aggregates is not an exact science and their behaviour under load is much more difficult to quantify than for metals. Furthermore, there are two distinctly different materials present in one bulk structure. This means that the overall material is complex. The results of MCS testing show large variations for experiments conducted at the same temperature and baking time, indicating a high sensitivity to the consistency of samples. It

appears there may be a dramatic impact on MCS results from small changes to the composition and proportions of the sample materials. This conclusion cross-references with the large material grain size distribution found by the author during the undergraduate work.

2.5.2 ZCast MP

The MP response surface model shown bellow in Figure 2.16, allowed the estimation of the optimum temperature and time of baking as 209.3°C and 7.70 hours respectively for the maximum MP. Table 2.8 below shows the ANOVA conducted for the permeability model, which showed significant reductions of the residual SS in the linear, square and interaction portions of the model. These reductions were all significant at >90% confidence, suggesting that each term reduced the residual SS. The interaction effect showed that there was a positive impact on permeability when temperature was held constant and time was varied at different levels (and vice-versa).

Table 2.8 The ANOVA table of the permeability model

Source	DF	Seq SS	Adj SS	Adj MS	F_{ratio}	P
Regression	5	856932	856932	171386	3.37	0.072
Linear	2	259770	685311	342656	6.73	0.023
Square	2	396040	396040	198020	3.89	0.073
Interaction	1	201121	201121	201121	3.95	0.087
Residual Error	7	356384	356384	50912		
Lack-of-Fit	3	7067	7067	2356	0.03	0.993
Pure Error	4	349317	349317	87329		
Total	**12**	1213316				

R^2 = 70.63

With reference to the surface plot, the MP of the ZCast material increased with time from 3.3-6 hours. It is conjectured that the initial heat energy removed some of the binder material in the mould by evaporation. This initial drying out or possible burn off of some of the minor constituents would result

in an increase in permeability, as the dynamic viscosity of the passing air increased with moisture reduction, allowing easier access of air through the material. Further, this initial heat energy was acting as a catalyst on the binder present in the mould material. The smaller Gypsum material that bonds to the larger sand grains acts as the glue in the bulk of the material. If the binder is subjected to heat energy the catalyst effect of the temperature will cause a stronger structure to be developed as the inter material bonds are strengthened. This would mean increasing more intergranular pathways, increasing MP.

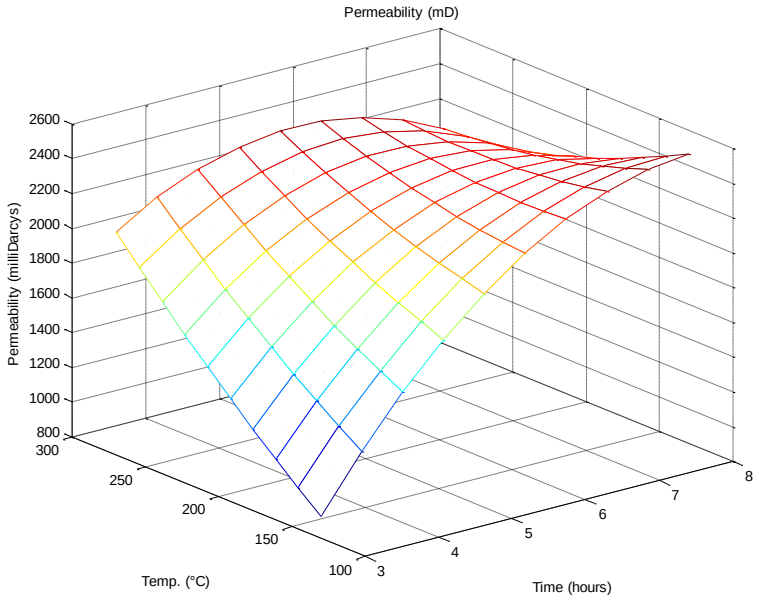

Figure 2.16 Permeability Vs baking time and temperature in the case of ZCast501

SEM photography in Figure 2.17 below shows specimens which were baked at lower times and temperatures. It is noted that the fine needle like gypsum particles adhere well to the sand particles at these lower heating intensities. Upon further heating, however, from 6-8 hours, the permeability reached a plateau and then started to decrease as shown in Figure 2.17b. This sharp reversal in trend was thought to be due to some of the material melting, fusing or changing phase. This would mean that intergranular pathways would become blocked or partially blocked, thus decreasing permeability.

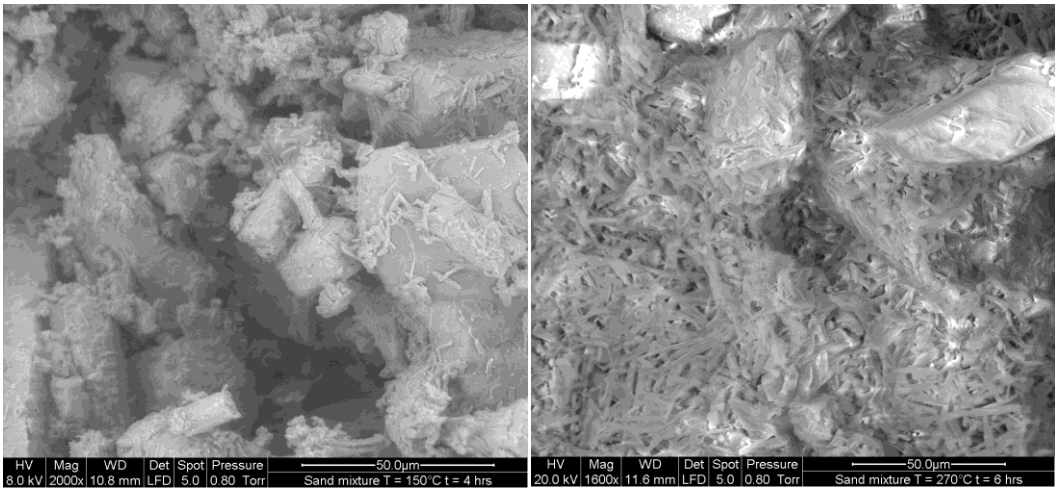

(a) **(b)**

Figure 2.17 SEM photographs showing the gypsum structure of a mould baked at (a) 150°C and 4 hours and (b) modified structure of a mould baked at 270°C for 6 hours

Figure 2.17 confirms the significant change in the gypsum structure on fractured surfaces of ZCast specimens. At high baking times and temperatures (Figure 2.17b) the gypsum structure was loose and its bonding strength reduced, resulting in a collapse of the intergranular pathways, thus blocking the passageways to flowing air.

2.5.3 A Comparison Between the Two Materials

The regression models constructed for both the ZCast501 and ZP131 materials differed in that the ZCast501 regression models had more significant coefficients that were able to explain a significant portion of the total variance from the experimental results.

In both the ZCast models the majority of model effects were significant, with considerable reductions in the SS of the residuals when each term was added to the model. The MCS and MP responses were able to be adequately modelled with the quadratic polynomial expression created by the CCD. The effect of the time and temperature of baking had significant linear and square components for both MCS and MP, with a significant interaction contribution effect to MP.

The MCS ZP131 regression model was able to explain a significant portion of the total experimental variance. However, in the MP ZP131 regression model there was no statistically significant relationships found. There were no significant reductions in the linear, square or interaction residual SS when added to the model. Nevertheless, the overall fit of the models was found to be adequate, with no significant lack of fit. The inability of the model to account for MP variance indicates that the ZP131 material was not affected by the temperature and time of baking unlike the ZCast501 material.

With respect to the actual MCS and MP values obtained, the two material systems were similar in magnitude. The repeated centre points in the experimental design (T=200°C and t=6hours) were the basis of comparisons of the MCS and MP and the results are presented below. The MCS for ZP131 was higher than for ZCast501 material. This result was predicted as the material has a finer and more uniform particle distribution, providing a more homogenous structure. The difference in the average MCS was confirmed with a T-Test between the ZCast501 and ZP131 material. The P value from the T-test was 0.2678. This value was not significant at generally accepted confidence intervals ($P<0.1$).

ZCast501 material was found to produce higher MP values. The mean permeability of the ZCast501 and ZP131 materials was 2116.77mD and 2099.1mD respectively, (based on centre point trials). The magnitude of the average permeability and the standard deviation were unexpectedly similar. It was expected that the much more closely packed gypsum material in ZP131 would produce lower MP values. Similarly, it was thought that the ZCast material, being both more porous and of larger average grain size, would produce larger MP values. However the T-Test on permeability showed a high P value of 0.9914, which meant that the two population variances were not statistically different.

From the statistical testing for MCS and MP, using the two materials, it is clear that no significant differences were found. However, on a practical basis ZP131 seemed stronger and showed superior definition regarding the mould

faces and edges. Also the ZP131 material had smoother surface finish, which was reflected in the initial castings involving the plaster material.

CHAPTER 3 CHARACTERISTICS OF STATIC CASTINGS PRODUCED IN 3D PRINTED MOULDS

3.1 Casting in Printed Moulds

Following evaluation of 3D printed materials in Chapter 2, the next procedure was to conduct casting trials to establish the suitability of these moulds for casting light metals such as Aluminium (Al) and Magnesium (Mg). As little work has been undertaken in casting light metals into these moulds, scant information is available on the effects of varying the constituent parameters. Typical experimental parameters are mould materials, mould coatings, alloys cast and process parameters such as pouring temperature. However, with the simultaneous variation of all these factors, an experimental design was required to establish in a statistical manner, the effects of these parameters, both individually, and in combinations, on the mechanical characteristics of the castings. These trials were also aimed at attaining practical experience with rapid casting of Al and Mg alloys. The following sections present the experimental design used, together with the relevant mould design used in the static casting trials.

Using the optimum mould material conditions developed in Chapter 2, the main aim of these static casting trials was to establish the combination of process variables which would yield the optimum mechanical responses for light metal casting in 3D printed moulds. The properties of the castings produced from these moulds would then be studied and compared to each other and to traditional sand casting values. Many other mechanical properties could have been chosen but given time and other constraints, the following mechanical variables were evaluated and studied by analysing the cast specimens:

Properties to be measured

- Surface roughness
- Ultimate Tensile strength (UTS)
- Percent elongation
- Brinell Hardness (HB)
- Microstructural examination

Surface Roughness

The surface roughness of a casting is an indicator of the quality of the cast surface produced from the 3D printed moulds. Surface quality needs to be high as this reduces post production machining. Cast specimens also need to have low surface roughness to ensure that good surface contact is able to be made in joining applications.

Ultimate Tensile Strength

Knowledge of the strength is one of the most important properties of a material, which has to function inside this limit to avoid failure. Also, the tensile strength gives a good indication of the overall quality of the material and its subsequent properties such as elastic limit or yield strength, and modulus of elasticity.

Hardness

The hardness gives the measurement of how resistant a material is to permanent deformation. This allows comparison of material hardness to established values found in the literature.

Microstructural Examination

Photomicrographic analysis allows the establishment of any similarities or differences between cast microstructures. Also the actual results of the tensile strength and microstructure can then be connected by carefully studying the microstructure of each specimen. These effects can also be quantified by visual examination of the grains and grain counting.

3.2 Experimental Plan

Factorial or fractional factorial design of experiments, as used in Chapter 2, could not be used here. There were two reasons for this: firstly, it is difficult to model qualitative factors, e.g. mould coatings, in traditional design of experiments. Secondly, the static casting trials required the variation of four factors each at three separate levels. This number of factors and levels would require too many trials if a traditional experimental design was used.

To achieve an efficient experimental design a Taguchi L9 Orthogonal Array (OA) was chosen. The Taguchi L9 technique allows up to four factors to be varied at three levels of each factor. The result is only nine experimental trials compared to eighty-one if a traditional factorial design was to be utilised. The four factors chosen were:

- Mould material
- Mould coating
- Alloy type
- Pouring temperature

Mould Materials

The effect of the mould type and coating used in metal casting is a primary factor affecting the quality of the cast parts. The mould itself needs to be capable of processing reactive hot metals and should possess suitable strength and permeability. The mould materials used were the two 3D printed

mould materials (ZP131 and ZCast501) and a resin bonded Silica foundry sand.

Mould Coating

The application of a mould coating to the mould surface will also have an effect on the cast surface roughness and the nature of the mould metal reaction. Three mould coatings with different base ingredients were utilised: Graphite (Isomol 200), Zirconium (Zircoat) and Magnesium Oxide (Magcoat).

Alloy Type

The alloys used in these trials were varied to establish the suitability of these moulds to process different light metals, namely Al and Mg alloys. The Mg alloys[4] chosen were AZ91HP (Al9%Zn1%, Mg base) and AM-SC1 (SC1) (Nd1.9%Ce0.7%Zr0.5%, Mg base). Firstly, the AZ91HP (High Purity) alloy was chosen primarily as it is a widely used alloy grade and is suitable for sand casting applications [55]. The SC1 alloy is a newly developed sand cast alloy aimed at being used in the production of automotive components, such as engine blocks [56]. The Al grade used was A356 (Si7%Mg0.4%, Al base), which is a common sand casting alloy used in a variety of applications [56].

Pouring Temperature

The temperature at which these metals are poured was tested over the range of 690-770°C, as specified by relevant literature [53, 55, 57]. The pouring temperature used provides data on the metal fluidity and mould metal reaction, especially when using reactive alloy such as Mg.

Table 3.1 below shows the completed L9 OA for the static casting trials, followed by the relevant levels of each factor, shown in Table 3.2. In Table 3.1, the four factors used in the static casting trials are displayed in each

[4] Refer to Appendix B for alloy composition

column, with the actual level of each factor shown in the row below. The actual experimental work commences with the chosen combinations of the levels at each experimental trial.

Table 3.1 Taguchi L9 experimental design table with natural variables

Trail	Mould	Coating	Alloy type	Temp (°C)
1	ZP131	ISOMOL	AZ91HP	690
2	ZP131	ZIRCOAT	SC1	730
3	ZP131	MAGCOAT	A356	770
4	ZCAST	ISOMOL	SC1	770
5	ZCAST	ZIRCOAT	A356	690
6	ZCAST	MAGCOAT	AZ91HP	730
7	SILICA	ISOMOL	A356	730
8	SILICA	ZIRCOAT	AZ91HP	770
9	SILICA	MAGCOAT	SC1	690

Table 3.2 Factor and level combinations for static casting trials

	Factors			
	Mould material	**Mould coating**	**Pouring temperature**	**Alloy**
Level 1	ZP131	Isomol 200 (graphite based)	690°C	Mg : AZ91HP
Level 2	ZCast501	Zircoat W (Zirconium Silicate based)	730°C	Mg: AM-SC1
Level 3	Resin bonded Silica sand	Magcoat S (Magnesium Oxide based)	770°C	Al: A356

3.2.1 Taguchi Response and ANOVA[5]

The Taguchi methodology proceeds mainly by analysis of the Signal to Noise (S/N) ratio. This measures the robustness of a specific process, i.e. the sensitivity of a process to changes in the chosen factor levels. The S/N ratio is able to measure the amount of variation due to uncontrolled (noise) factors. Therefore the S/N ratio is a variance indicator of the power of the signal (strength of response) to the noise (changes in process factors). This technique ensures both signal optimisation and minimum variation around the chosen signal level [58]. The S/N ratio is the transformation of the Mean Squared Deviation (MSD) which measures both the average and standard deviation. Depending on the application (desired signal level), the following formulas may be used when processing the S/N ratio:

'Higher the better'

The higher the better equation shown below in equation (3.1), is used when the response is desired to be as high as possible.

$$S/N_{HB} = -10\log_{10}\left(\frac{1}{r}\sum_{i=1}^{r}\frac{1}{y_i^2}\right) \qquad (3.1)$$

Where:
S/N_{HB} = Higher is Better (HB) Signal to noise ratio
y_i = Experimental response value
r = Response repetition

'Lower the better'

If a process response is desired to be reduced to a minimum (e.g. surface roughness) the following equation is used:

[5] For specific calculations of terms in the ANOVA table refer to Appendix A

$$S/N_{LB} = -10\log_{10}(\sum_{i=1}^{r} y_i^2) \quad (3.2)$$

Where:

S/N_{LB} = Lower is Better (LB) Signal to noise ratio

y_i = Experimental response

r = Repeated response

In all cases the greater the S/N ratio, the lower the variation of the measured variable is around the target value [58].

3.2.2 Pooling of Factors

Pooling of experimental factors means assigning insignificant factors utilised as the experimental error in the experiment. This can be accomplished by different methods and specific criteria which avoid arbitrarily pooling factors. Pooling is generally done to increase the error sum of squares by pooling an insignificant factor. Using Taguchi OA, such as in L9 static casting trials, all the column (factor effects) are occupied, meaning that the error DOF is zero, which then disallows the calculation of F ratios, variance and confidence levels. To create an error term, small column effects are pooled together to create a larger error term (known as pooling up strategy) [58]. This technique of pooling was used in the current experiments, with factors pooled if the contribution of an effect was around 10% or less of the total variance present in the experiment.

3.3 Mould Design

A mould to contain the molten metal was created, so that cast specimens could be subsequently machined and tested. Mould design is a highly differentiated area of expertise and sound mould design often requires significant practical experience of what works and what does not. Much of the current mould design knowledge utilised some empirical geometric relationships and experiences from prior testing. A simple mould design was

considered, comprising of a top gated inlet, cylindrical specimens (the final casting) and a feeder situated at the end of the cylindrical cavities to allow for metal shrinkage upon solidification. The mould itself was horizontally parted to form two halves, the upper half (cope) and lower half (drag) The mould halves were located together by aligning studs located at each corner of the mould and when casting a central clamp was applied to prevent any movement due to the buoyant forces of the molten metal. Along the length of the cylindrical specimens some vent holes were also added to improve permeability and help release any pressure built-up inside the cavity.

The actual casting samples produced in these moulds consisted of four 15mm diameter cylindrical specimens, to be machined down to produce tensile test specimens[6] for testing. The mould also consists of a ceramic pouring cup which was placed at the inlet to provide better metallostatic pressure. At the bottom of the pouring cup was also a ceramic foam filter with ten Pores Per linear Inch (PPI), to help remove any impurities and oxides in the metal, and also to laminate the metal flow.

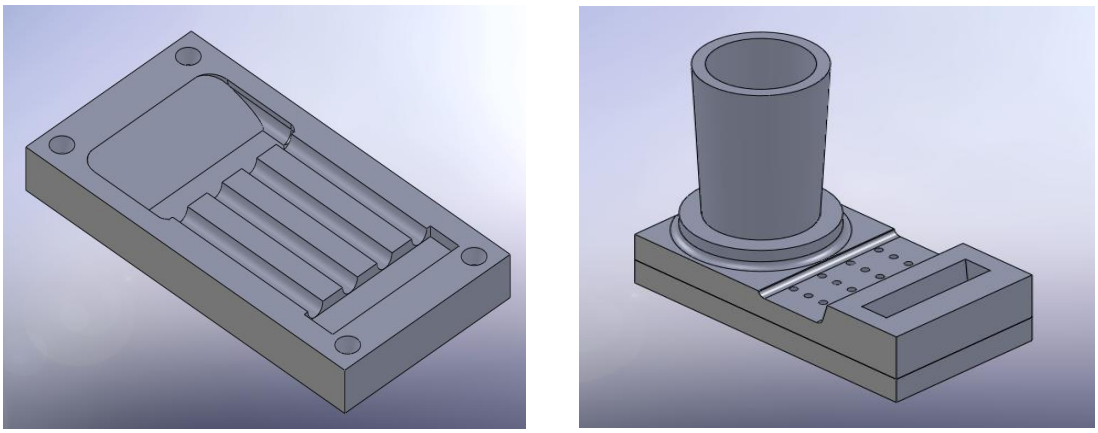

(a) **(b)**

Figure 3.1 CAD drawings of the initial static mould design, showing (a) Bottom half of the mould and (b) 3D view of completed mould design.

[6] Refer to Appendix B for tensile test part dimensions.

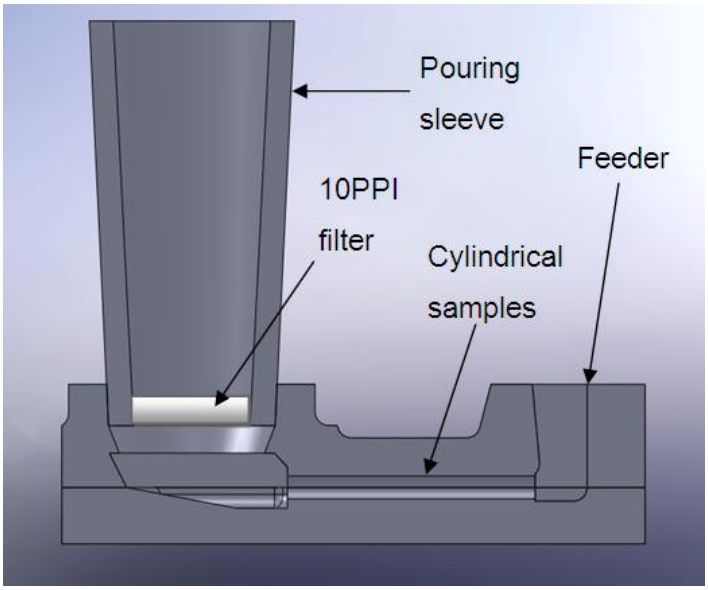

Figure 3.2 Sectional CAD drawing initial mould design, showing pouring entrance cup, cylindrical cavity and riser

3.4 Static Casting Experiments

The casting trials were conducted using AUT's induction furnace. A custom made 1040 carbon steel crucible was constructed to fit the furnace dimensions to contain the molten Mg alloys (AZ91HP and AM-SC1) due to the severe reactions when in contact with refractory crucibles. The same crucible was also used to heat the A356 Al. For each trial the melt temperature was read off a CHK500 K-type thermocouple just prior to pouring. Each 3D printed mould was baked at the optimum time and temperature. Prior to baking a mould dressing was applied with a brush over the entire cavity. For a general comparison castings were produced in silica sand bonded by an ester hardened alkaline phenol-formaldehyde polymer resin.

The casting of the metals involved transporting the steel crucible and carefully poring directly into the printed moulds. In the case of Mg castings, the molten Mg was covered by gas mixture to purge out any potentially reactive oxygen. A mixture of CO_2 and refrigerant r134a was used in conjunction with Foseco MAGREX 36 flux to prevent any violent oxidation once the metal was heated to its melting point.

Figure 3.3 Photographs showing AUT University induction furnace setup (left) during casting of Mg alloy (right)

A small quantity of flux was applied to the crucible prior to charging the crucible with the alloy. In all melting trials, alloy in the form of commercially pure ingots was melted to ensure the melt was of a high quality. The molten metal was filtrated with the use of a 10PPi ceramic foam filter placed near the bottom of the ceramic pouring cup. When casting Al, the melt was degassed with Nitrogen with a degassing lance shown in Figure 3.4. Degassing was performed for about 3-5 minutes for each melt. The pouring cup was also coated with the mould dressing to avoid any reactions with the molten Mg.

Figure 3.4 Degassing lance used in casting trials

3.4.1 Mechanical Testing of Castings

The cylindrical cast specimen surface was tested for surface roughness. This was conducted at AUT University with a Taylor Hobson Form Talysurf50 surface testing machine, shown below in Figure 3.5.

Figure 3.5 Taylor Hobson Talysur50 surface testing machine

Each tensile test specimen was tested on an arbitrary side of the cylindrical specimen in the longitudinal direction and rested on finely ground, level V blocks. A Gaussian filter was used to filter out any waviness effects of the surface profile and the average surface roughness, R_a was found. On the chosen testing side, three readings were taken to obtain an overall average surface roughness. Suitable cut offs of 8mm and 0.8mm were used in conjunction with the surface testing standard ISO 4288-1996.

Once each casting was completed, the riser and sprue sections were cut off with a hacksaw and each cylindrical specimen was turned down to form the tensile test specimen[7]. This was conducted at low speeds and feed rates to avoid excessive heating of the alloy. Whilst turning the specimens, coolant was applied to prevent excessive heating and local changes in the microstructure. The tensile testing was carried out on the Hounsfield Tensile testing equipment at AUT University shown below in Figure 3.6. The loading rate was 1 mm/min in all cases. The diameter of the critical cross-section was measured with a micrometer to obtain an accurate cross–sectional area.

[7] CAD drawing of specimens is detailed in Figure B.10, Appendix B.

Figure 3.6 Photographs of the tensile testing performed at AUT with (a) showing the testing machine set up and (b) showing close up the stressing of a tensile specimen

Sprue and riser sections were then machined flat on a milling machine to prepare specimens for hardness testing. Samples were tested in accordance to AS 1816.1-2007 on an Avery Brinell hardness tester with 10mm indenter at AUT University (Figure 3.7). The indentation diameter resulting from the hardness tests was measured with a hand held optical measurement device.

Figure 3.7 Brinell Hardness testing apparatus

After the mechanical testing, the transverse sections of the fractured tensile specimens were examined with SEM at Auckland University to determine the cause and method of fracture. Further light microscopic analysis was conducted at AUT University metal research laboratory. A transverse section was cut with a hacksaw at the midpoint of the tensile test specimen. After subsequent filing to bring the surface smooth and level, each specimen was mounted in a Struers LaboPress mounting machine at a temperature of 150°C and with a force of 30 KN. Once this was competed each specimen was sanded on a Metaserv rotary grinder on the following sand grades; 180, 320, 500, 800, 1200, 2500 grit. Water was used to lubricate and prevent heating of the specimen surface and after each specimen was completed it was finely polished on a Metaserv universal polisher with the use of a 0.2µm cloth and 1µm diamond paste. To provide lubrication a Fumed Silica lubricant was used. After polishing the specimens were then etched with Wrecks reagent[8] [59] in the case of the Al castings for 15 seconds and then dried. The Mg castings were etched in a Glycol based etchant[9] [60]. The mounted specimens were submerged for around 5 seconds, then washed in water and alcohol and then dried. The photomicrography was done on optical microscope at magnifications of X50, X100 and X400. The microstructure was characterised by grain counting to determine the average number in accordance with ASTM E 112 – 96 [61]. The Planimetric method was used to determine the number of grains within a given area. In this case the area was a rectangular photomicrograph, which was measured with a calibration measurement indicator.

3.5 Static Casting Results and Discussions

3.5.1 Surface Roughness

With the exception of the mould material factor, the ANOVA table (Table 3.3) showed that the variance in the other factors accounted for only a small

[8] See Appendix B for composition.

[9] Refer to Appendix B for composition.

proportion of the total variation in surface roughness. The mould material was found to account for over two thirds of the total variance in the experiment and at a 95% confidence level.

Table 3.3 ANOVA table of the surface roughness response

Rank	Source	DOF	SS	Variance	F_{Ratio}	P value	Percent contribution
1	Mould	2	68.43	34.21	26.33	0.04	68.97
2	Coating	2	16.12	8.06	6.20	0.14	16.25
3	Alloy	2	12.07	6.03	4.64	0.18	12.16
4	Pool Temp	2	2.60	1.30			2.62
	Total	8	99.22				100.00

Upon examining the S/N ratios in Figure 3.8 below, the ZP131 mould material was found to give the highest ranking level of the mould material factor. This was followed by the Silica foundry mould and the ZCast mould respectively.

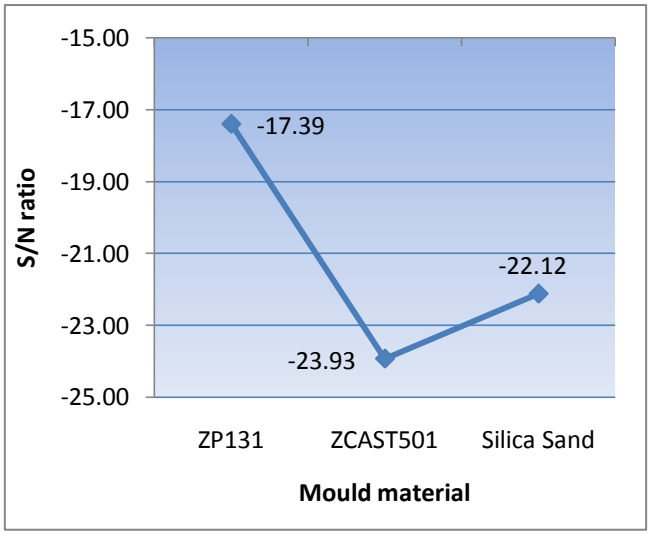

Figure 3.8 S/N ratio of mould material in the surface roughness results

The low surface roughness values achieved by the ZP131 moulds can be explained by considering the small size of the gypsum particles and their uniform grain size distribution. This meant that the mould surface had a lower roughness than the other trialled moulds, which was reflected in the castings. The presence of smaller gypsum grains decreases the mould roughness

profile, resulting in lower peaks and valleys on the mould surface. Further, the dimensional form was enhanced, providing a sharp reproduction of the overall shape and dimensions.

The highest values of surface roughness were observed in the ZCast501 moulds. The poor surface finish of the castings produced in the ZCast moulds was a combination of the inherent mould properties. Primarily this was due to the poor grain size and the shape and distribution of the ZCast mould material. Previous work by the author, noted in Chapter 2, showed that there was a large grain size distribution in the ZCast material, and disproportionate larger sand grains in relation to the gypsum particles. To compound matters, the mould surface was easily eroded due to the low bonding strength present in the ZCast moulds. Also, the degree of spherical curvature of the added Olivine sand, which is basically a crushed rock, [62] was detrimental to the as-cast surface roughness. As a result, the grains were highly angular, which created greater intergranular cavities where the metal could penetrate [55].

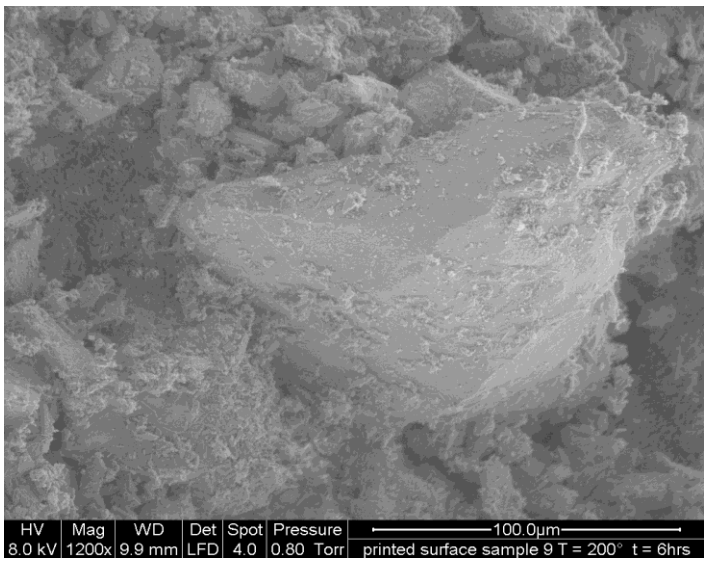

Figure 3.9 The SEM close up photograph of an angular Olivine sand grain present in the material

SEM work showed highly angular grains, as indicated in Figure 3.9. Also from this photograph, the difference in size of the Olivine sand grains relative to the surrounding gypsum was evident. This size difference leads to a decrease in

surface quality, even with the application of the mould coating. Further, the mould surface was quite fragile with surface grains easily dislodged. When applying the mould coating this led to relatively poor surface quality before metal was cast, as the act of brushing removed the surface particles.

The confidence levels of the mould coating parameter in Table 3.3 was almost significant with a P value of 0.14, which was slightly higher than commonly accepted confidence levels (P value <0.1). When considering the S/N ratios of the individual mould coating levels, shown below in Figure 3.10a, it was found that Magnesium Oxide (MgO) based Magcoat product was the best suited coating in achieving the minimum surface roughness. It was noted that Mg castings produced rougher surfaces, due to mould metal reaction, with Figure 3.10b showing that the two Mg alloy grades resulted in the lowest S/N ratios, with the less reactive Al alloy resulting in the highest S/N ratio (best surface finish).

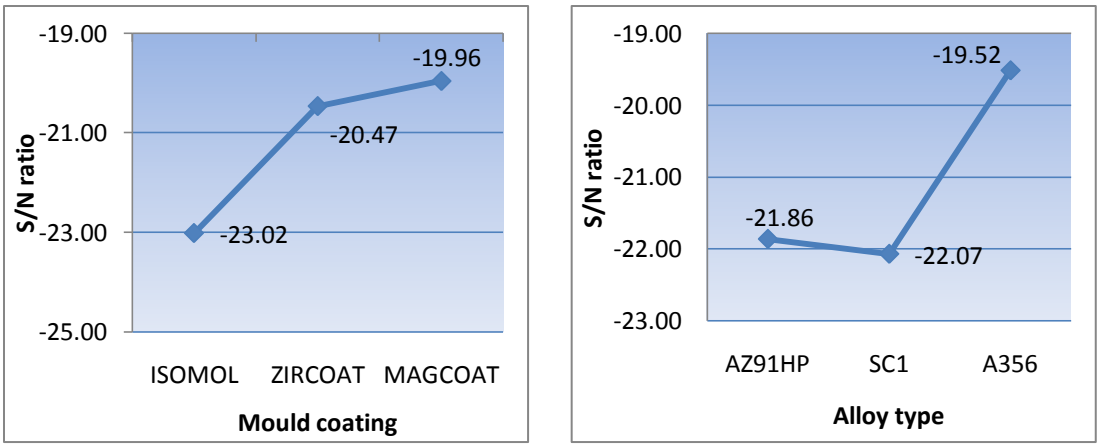

(a) Mould coating **(b) Alloy type**

Figure 3.10 S/N ratios of (a) Mould coating and (b) Alloy type levels in the surface roughness response.

The use of the different alloys in these experiments resulted in a P value of 0.18 slightly higher than the mould coating (0.14) and also outside the range of accepted P values. The reactive nature of the Mg alloys on surface roughness was significant. The propensity of Mg alloys to oxidise is governed by the Gibbs free energy change of [63].When the alloy changes phase into a liquid, the alloy begins to oxidise and revert to its stable oxide form. The application of a mould coating can reduce this reaction by providing a stable

exterior material, which facilitates a decreased ability for the alloy to oxidise. The MgO coating proved to be a very stable coating material, relatively unaffected by the molten Mg due to its large Gibbs free energy change.

The pouring temperature was shown to have a very insignificant effect, leading it to be pooled as the error term. This result indicated that the effect of pouring temperature did not affect surface roughness. Increased temperatures over this range might have been expected to produce higher surface roughness due to increased reaction but this was not observed. It is noted, however, that this outcome was only over a total temperature variation of 80°C. Moreover, temperature measurement was restricted to a thermocouple probe in an open crucible. These qualifications could produce measurement error of perhaps 10-20%, but this is not considered significant in assigning pouring temperature as the experimental error.

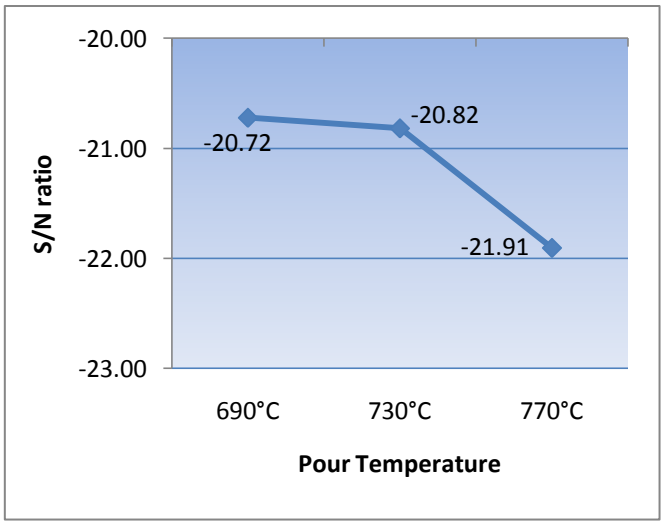

Figure 3.11 S/N ratio of the pouring temperature factor levels on the surface roughness values

All experimental results are presented in Table 3.7, while the overall rankings of the factors are listed in Table 3.8. Cast specimens surface roughness were 23.6µm for AZ91, 11.4µm for A356 and 14.33µm for SC1 for castings produced in the ZCast moulds. Surface roughness testing conducted on the castings produced by ZP131 moulds showed better surface finishes, due to the smooth surfaces of the ZP131 moulds. This was because ZP131 was not

mixed with any foreign material. The surface roughness values were seen in the ZP131, with 9.5µm for AZ91, 7.3µm for A356 and 5.8µm for SC1. These values were acceptable with typical sand cast surface roughness values ranging from 6-13µm [64].

Table 3.4 Static L9 experimental design table

Factors				Responses			
Mould	**Coating**	**Alloy type**	**Temp (°C)**	**UTS (MPa)**	**Strain %**	**Ra (µm)**	**HB**
ZP131	ISOMOL	AZ91	690	156.42	2.17	9.49	56.82
ZP131	ZIRCOAT	SC1	730	130.02	2.56	7.33	48.17
ZP131	MAGCOAT	A356	770	127.13	0.75	5.84	60.54
ZCAST	ISOMOL	SC1	770	127.99	2.28	23.66	48.87
ZCAST	ZIRCOAT	A356	690	132.05	0.85	11.47	65.70
ZCAST	MAGCOAT	AZ91	730	150.87	1.52	14.33	60.54
SILICA	ISOMOL	A356	730	93.27	0.73	12.63	52.63
SILICA	ZIRCOAT	AZ91	770	127.11	1.54	13.98	56.82
SILICA	MAGCOAT	SC1	690	157.39	3.36	11.79	47.48

Table 3.5 Overall ranking of factors and their level from static casting trials

	Factors			
Response	**Mould material**	**Mould coating**	**Alloy type**	**Pouring temp.**
UTS	(ZP131) :4th	(Magcoat):3rd	(AZ91HP):1st	(690°):2nd
Strain	(ZP131):3rd	(Magcoat) :4th	SC1: 99.99%:1st	690°C:90%: 2nd
Ra	ZP131:95%: 1st	(Magcoat) :2nd	(A356):3rd	(690°C):4th
HB	(ZCast501):2 nd	(Zircoat):3rd	A356: 90%:1st	(690°):4th

* Brackets denote highest ranked level of non-significant factors

3.5.2 Ultimate Tensile Strength (UTS)

The ANOVA in Table 3.6 showed no significant factors at any of the tested confidence levels. This result indicates that no single factor from the chosen variables was influencing the UTS and the variation observed is due to a combination of effects of all constituent factors. The ANOVA shows that the total variance was comprised of similar magnitudes, with the mould coating contributing 19.8%, the alloy 38.77% and the pouring temperature 30.21%. The mould material was seen to have a very small effect (11.21%) and was pooled as the error term. The negligible effect of the mould material perhaps is due to a minimal variation in the cooling rates, as both moulds are coated with the same materials.

Table 3.6 ANOVA of UTS response

Rank	Source	DOF	SS	Variance	F_{Ratio}	P value	Percent contribution
1	Alloy	2.00	5.92	2.96	3.46	0.22	38.77
2	Temp	2.00	4.61	2.30	2.69	0.27	30.21
3	Coating	2.00	3.02	1.51	1.77	0.36	19.80
4	Pooled Mould	2.00	1.71	0.86			11.21
	Total	8.00	15.26	1.91			100.00

The alloy type accounted for the largest variations in the experimental results. However, the end results were somewhat skewed because the UTS is directly related to the alloy system itself. In the present case, the Mg alloy AZ91HP scored better than the others as seen from the S/N ratios presented in Figure 3.12. The Al alloy was found to have the lowest strength values. The probable reason for this was the presence of hydrogen porosity, which weakened the as-cast structure. These aspects are covered more closely in section 3.5.2.

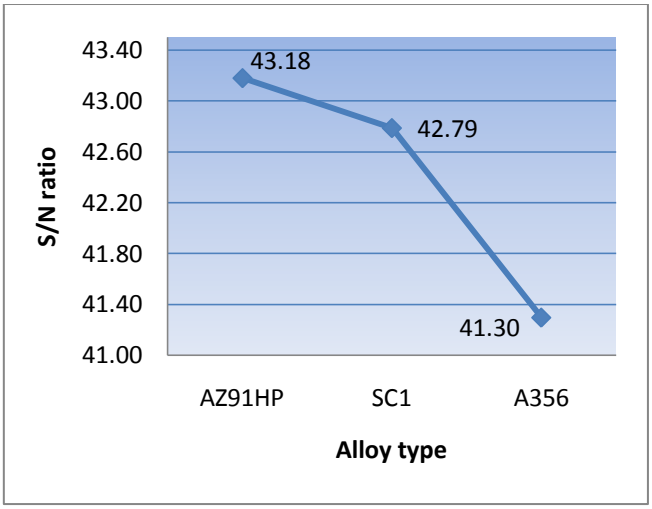

Figure 3.12 S/N ratio of the Alloy type factor levels in the UTS response

The second ranking factor in the ANOVA table was the pouring temperature, which returned a P value of 0.27. This result was perhaps linked to the reduction in the solidification time when lower casting temperatures were utilised. An examination of the S/N ratio of this factor, in Figure 3.13, shows that the best UTS can be obtained at the lowest temperature, 690°C. The reduction in the solidification time in theory should result in smaller dendrite grain sizes and a more refined grain structure. Coarser grain structures are particular important in Mg and Al alloys for the UTS of the cast material [58, 65-67].

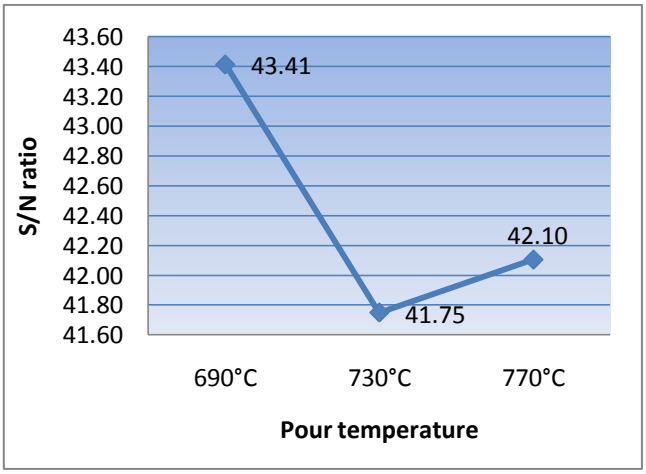

Figure 3.13 S/N ratio of the Pouring temperature Factor levels in relation to the UTS response.

The significance of the mould coating was not expected considering the small layer thickness. When considering the S/N ratios of mould coatings, the Magcoat product performed much better than the other two coatings trialled. The Magcoat product also gave the optimum surface roughness values, as noted above, indicating that lower surface roughness values may be linked to the better than expected UTS response of Magcoat.

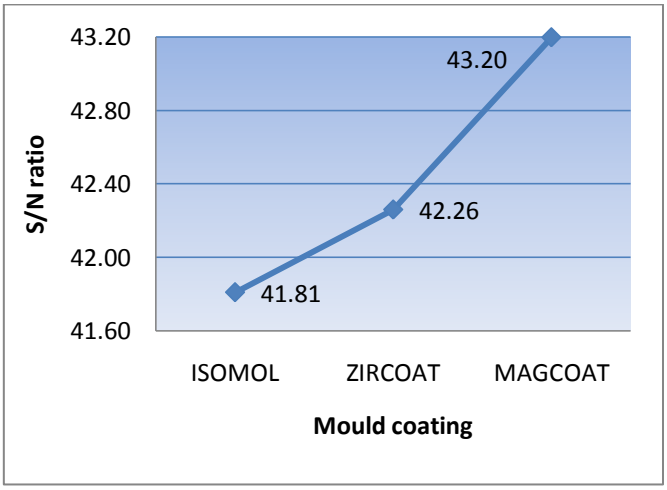

Figure 3.14 S/N ratio of the mould coating factor levels in relation to the UTS response.

The mould material was found to be the least significant factor in achieving the maximum UTS values. The thermal conductivity of plaster material was much lower than that of the Olivine sand [68]. It was thought that a casting produced in a ZCast501 mould may have slightly improved mechanical properties compared to that from a mould made of plaster (ZP131) only. This reflects the ability of ZCAST material to transfer heat at a higher rate, allowing the casting to solidify faster and permit a finer grain structure. However, S/N ratio analysis in Figure 3.15 below, showed that the ZCast mould material had a negligible effect and actually the best mould in terms of strength was the ZP131 plaster mould. It was possible that the very low thermal conductivity of ZP131 material was improved by the application of the mould coating, and that this produced an improved heat transfer performance for ZP131. Thus the cooling rates of ZP131 and ZCast501 were similar, and the differences were statistically insignificant.

While the castings produced in the ZP131 and ZCast moulds were similar in as-cast strength, the castings produced in the Silica foundry sand gave the lowest UTS values in the case of AZ91 and A356. This result was related to the mould design and dimensions used. The RP moulds were constructed to the constraints of the 3D printer with a specially designed sprue and riser. To construct a similar mould in traditional sand required a unique pattern to be constructed for the moulds. Limited time and resources meant that a pattern could not be made exactly to the dimensions of the 3D printed mould. The larger mould thickness of the foundry sand mould resulted in lower thermal gradients and metal flow velocities. This would produce a longer solidification time, resulting in more grain growth. The grain size and Dendrite Arm Spacing (DAS) is inversely related to the UTS and cooling rate in Mg and Al alloys [65, 67, 69, 70], thus meaning a lower UTS.

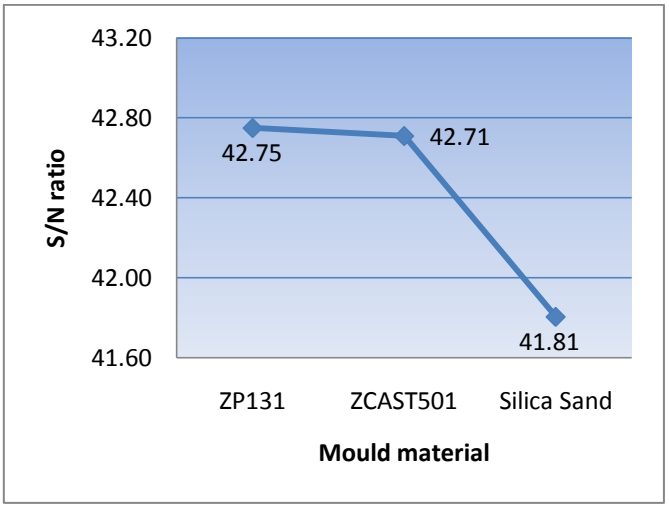

Figure 3.15 S/N ratio of the mould material factor levels in the UTS response

The actual tensile strength results from the Al and Mg castings produced in the 3D printed moulds were similar in magnitude. Generally the strength values in both RP moulds were very similar with all three alloys. The silica foundry mould however produced lower tensile properties for AZ91 and A356 alloys, with improved values of SC1 to those obtained in the RP moulds. The following is a general overview of the achieved strengths of the different alloys used.

Magnesium

Overall, the UTS of the cast Mg averages of AZ91 were of 156 MPa and 150 MPa achieved with AZ91 from ZP131 and ZCast moulds respectively. The maximum values achieved with AZ91 were 170.63 and 150.87 MPa in the ZP131 and ZCast moulds respectively. Castings produced in the silica sand moulds were slightly lower with an average of 127 MPa with AZ91. The SC1 Mg grade produced consistent results, with 130 MPa and 127 MPa for castings produced in ZP131 and ZCast moulds respectively. However, the best results were achieved with the SC1 alloy in the silica sand mould with an average as-cast strength of 157 MPa.

Typical values for sand cast AZ91 alloys obtained in traditional sand moulds reveal that the minimum as-cast UTS should be around 160 MPa [27, 71]. Though the average UTS values achieved when casting into the ZP131 and ZCast moulds were slightly lower, in some cases this was exceeded. From this perspective, the RP moulds were capable of producing adequate casting properties in terms of UTS. Furthermore an in-depth evaluation of AZ91 alloy cast in traditional plaster moulds, showed that RP plaster moulds gave higher UTS of the as cast samples. Work into the effects of grain refinement and increased cooling rate led to higher strengths. However the AZ91 magnesium castings produced in traditional plaster moulds were found to have an average as-cast UTS of only 110MPa [36] compared to 156 MPa in ZP131 plaster moulds.

The SC1 Mg alloy was not able to be compared to values found in the relevant literature directly, as no as-cast data could be soured. Typical values found in literature [56, 72] however, were after the samples had undergone a solution heat treatment and precipitation hardening. The heat treated SC1 samples found in the literature [56], have a 0.2% Proof stress of 130MPa with a UTS of 202MPa. The samples prepared in the 3D printed moulds attained an average UTS value of around 130MPa as-cast, with a maximum of 138MPa, 153MPa and 164.73MPa achieved in the ZP131, ZCast moulds and Silica moulds respectively.

Aluminium

The tensile results were lower than those achieved with Mg alloys but were close to the values achieved in traditional sand casting. Typical as-cast strength of A356 alloy (Al-Si7%) was 130-150MPa [73] and castings produced in the ZP131 moulds averaged 127MPa but did achieve a maximum of 141 MPa. The castings processed in the ZCast moulds improved on this with an average of 132 MPa, and a maximum of 138 MPa. Unfortunately, the castings produced in the Silica sand were poor and averaged only 93 MPa with a maximum of 102 MPa. The large presence of hydrogen porosity present in the cast samples meant that the microstructure was significantly weakened leading to low UTS and elongation percent properties. This was perceived a function of the melt treatment and casting setup, rather than that of the RP or foundry sand moulds, with inefficient lance degassing unable to remove dissolved hydrogen.

Tensile testing conducted from A356 tensile test parts, produced at the supporting foundry, Centracast, attained 142 MPa. These underwent correct melt treatment, which involved rotary degassing, reduced pressure testing on the molten metal and the use of cleaning fluxes. This can be considered a benchmark, as rotary degassing is considered the most efficient method of reducing hydrogen from Al melts.

3.5.3 Percent Elongation

Table 3.7 shows the ANOVA conducted on the percent elongation values from the tensile testing. This table shows that only the alloy factor was significant, with a P value less than 0.001. This low P value results in a confidence value at the 99% level. When considering the S/N ratio (Figure 3.16a) of the alloy factor, the SC1 Mg alloy achieved the maximum percent elongation. This was followed closely by the AZ91 alloy, with the A356 aluminium alloy giving the lowest S/N ratio. Traditionally, AZ91 and A356 have close values of as-cast ductility [55]. In this case, the fact that A356 was not effectively degassed, producing hydrogen embrittlement, could have

accounted for the variation obtained.

Table 3.7 ANOVA table for percent elongation response model

Rank	Source	DOF	SS	Variance	F_{Ratio}	P value	Percent contribution
1	Alloy	2	180.84	90.42	101.39	0.00	92.42
2	Pool Temp	2	11.27	5.63			5.76
3	Pool Mould	2	1.58	0.79			0.81
4	Pool Coating	2	0.21	0.10			0.11
	Pooled Error	6	1.78	0.89			
	Total	8	195.68				100.00

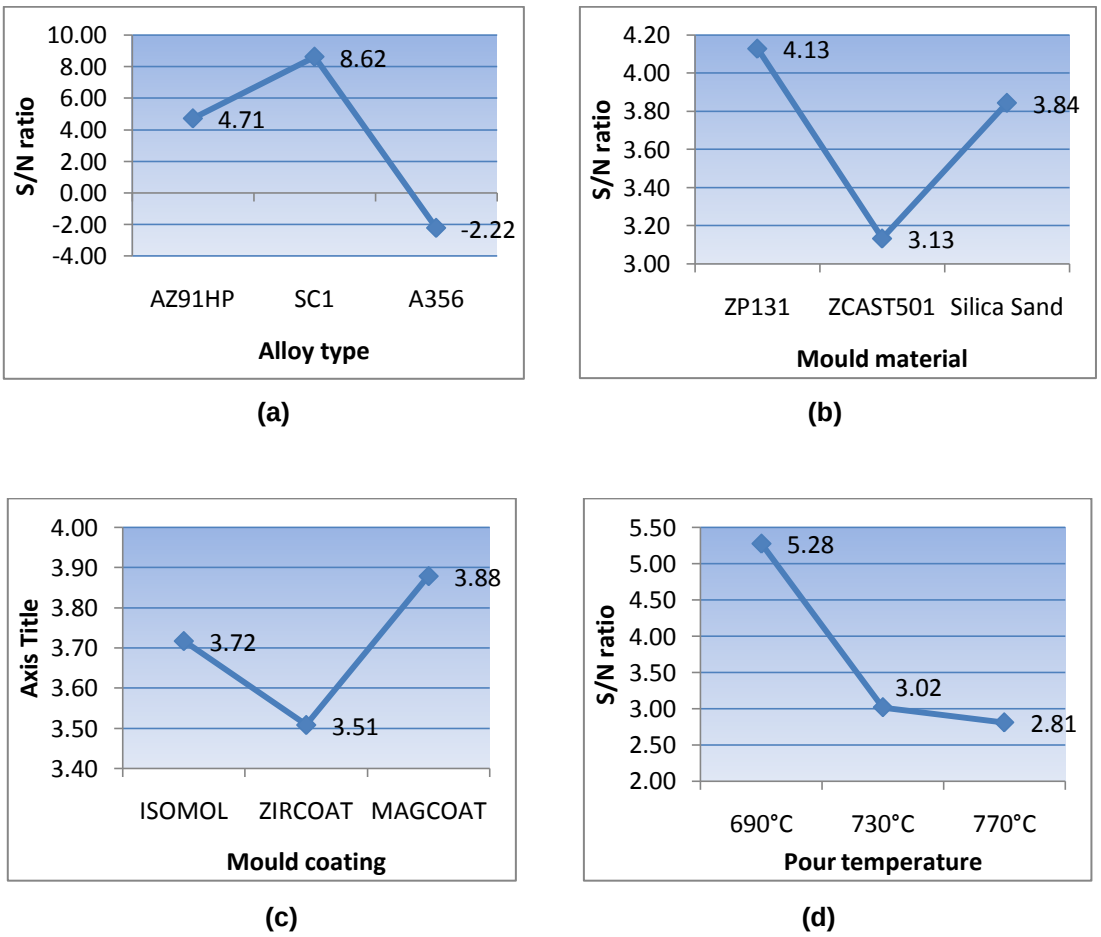

Figure 3.16 S/N ratios relating to the percent elongation values at factors (a) Alloy type (b) Mould material (c) Mould coating and (d) pouring temperature

In comparison to the alloy factor, the overall variance accounted for by the other factors was negligible. These factors were subsequently pooled as the

experimental error. In particular, mould coating and mould material both contributed minimally to the overall variance. For completeness however, the S/N ratios of these factors are shown above in Figure 3.16b-d. The highest S/N ratio for each factor was the ZP131 for the mould material, Magcoat for the mould coating and 690° for the pouring temperature.

In terms of percent elongation, interestingly SC1 outperformed AZ91 and the A356 alloy. The HCP structure of Mg would tend to indicate a lower ductility when compared to A356 and in practice A356 has been found to be more ductile due to its Face Centred Cubic (FCC) crystal structure, especially after a heat treatment. However, SC1 is a special alloy developed by the Australian research institute CAST, to increase the creep properties of magnesium in high temperature applications. The addition of special alloying elements such as Zinc (Zn), Lanthanum (La), Cerium (Ce) and Zirconium (Zr) create a completely different secondary phase which is intended to act as a more rigid interlocking medium to resist grain movement [74]. This increased ductility was most likely a result of this interlocking nature of the secondary phase. Usual alloys of Mg with Al and zinc such as the AZ series alloys create the well established secondary phase, $Mg_{17}Al_{12}$. This intermetallic created what many researchers have described as a brittle and weak phase unable to provide much resistance to grain movement when under load, especially at elevated temperatures [75]. However, the addition of Al in Mg alloys has been a requirement due to the Al increasing important casting properties such as fluidity and corrosion resistance.

Temperature of pouring was also established as a significant variable with respect to elongation percent. In addition to this it can be seen that in all the other responses, the lowest casting temperature, 690°C, gave the highest ranking level of the temperature variable. This is probably due to the reduced solidification time when casting the metals at lower temperatures. This would have resulted in less time for dendrite growth, and ultimately grain size, which has a significant effect on the mechanical properties of Al and Mg casting alloys [65-67, 70, 76]. Also, the solubility of hydrogen increases [77] when the melt temperature is increased and this may have resulted in more porosity in

castings poured at higher temperatures.

3.5.4 Brinell Hardness

The variance analysis of the Brinell hardness presented in Table 3.8, showed that the alloy factor accounted for a significant portion of the variance. This significance was tested at the 95% confidence level. When examining the individual levels of the alloys used, the A356 alloy had the highest hardness value, which was followed by the AZ91 alloy grade.

Table 3.8 ANOVA of Brinell hardness response

Rank	Source	DOF	SS	Variance	F_{Ratio}	P value	Percent contribution
1	Alloy	2	5.96	2.98	6.69	0.05	73.66
3	Mould	2	1.24	0.62	1.39	0.35	15.33
3	Pool Temp	2	0.27	0.13			3.30
4	Pool Coating	2	0.62	0.31			7.71
	Pooled Error	4	0.89	0.45			11.01
	Total	8	8.09				100.00

The mould material factor was the second ranking factor in the ANOVA table. This factor had an influential effect and the S/N ratio showed that the ZCast501 moulds produced the optimum hardness values. This was followed by the ZP131 and Silica foundry sand moulds respectively.

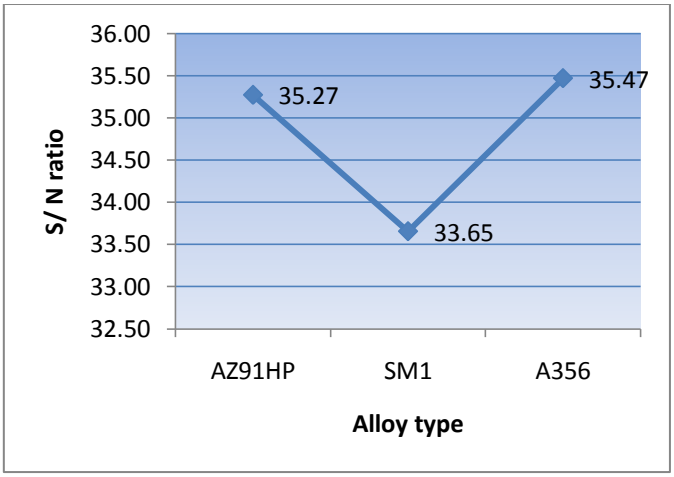

Figure 3.17 S/N ratio of the alloy type factor levels in the Brinell hardness response.

The ANOVA in Table 3.8, shows that the effects of mould coating and pouring temperature on the hardness were insignificant. The lowest pouring temperature of 690°C produced its highest S/N ratio, but the contribution to overall variation in hardness values was low. Disregarding the large influence of the alloy factor in the ANOVA table, little variance was accounted for by the remaining factors.

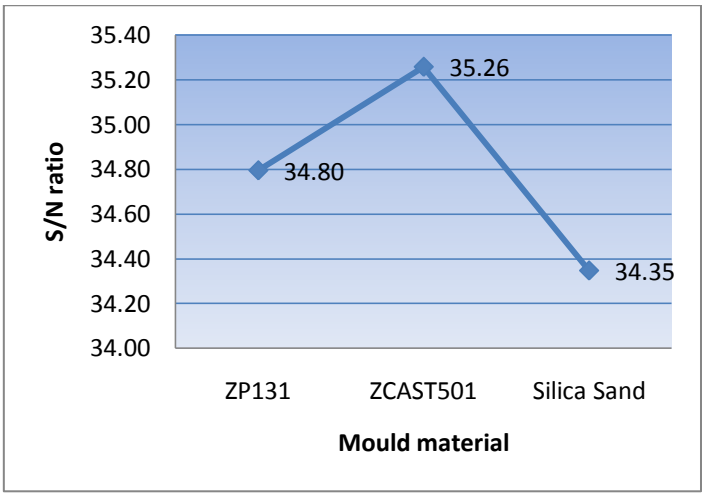

Figure 3.18 S/N ratio of the Mould material factor levels in the Brinell hardness response.

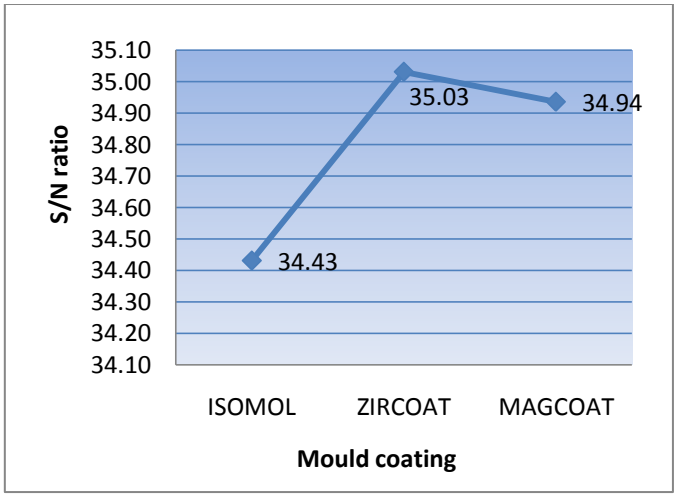

(a)

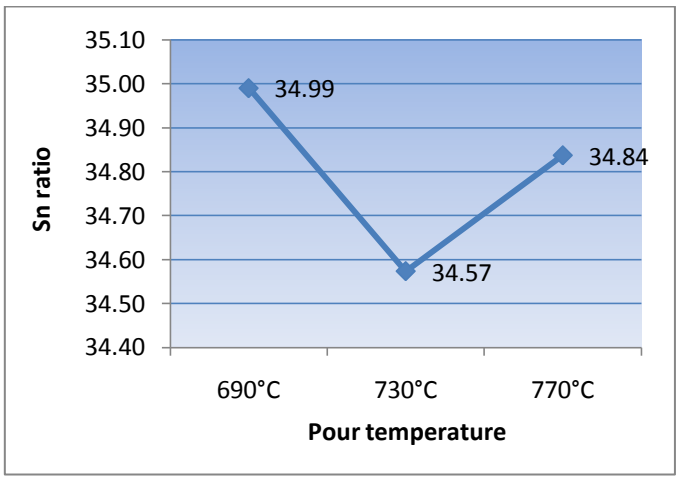

(b)

Figure 3.19 S/N ratios relating to the Brinell hardness values at factors (a) Mould coating and (b) pouring temperature.

The Brinell hardness response was actually an obvious result with the predictably harder aluminium receiving some significance in terms of alloy type. Ignoring the alloy type in the ANOVA table however, it can be seen that there were no other factors that were even remotely significant and the pouring temperature and mould coating variables were pooled as error terms due to their relative size to the much larger alloy effect. The only other variable having some effect on the hardness was the mould material, however even this effect was only accounting for 5% of the total variation.

In terms of actual hardness values, the A356 alloy gave an average Brinell hardness value of 59.62 with AZ91 a close second with 58.06. SC1 was the

softest alloy with only a BH value of 48.17. These values were in close comparison to values obtained in literature. These were 60 for A356 and 50-65 AZ91HP [55].

3.6 Metallographic Analysis

All cast samples were subject to metallographic analysis subsequent to mechanical testing. The following sections describe the metallurgical and metallographic aspects of the cast alloys. Attempts were made to compare results with existing literature and to correlate the microstructures and mechanical properties observed.

3.6.1 ASTM Grain Number

Grain counting was conducted using the relevant ASTM standard [61]. The counting of grains quantified the number of grains present within a specific area and with the use of reference charts the ASTM grain number can be calculated. The grain number is the inverse of the grain size and allows the average values of grain size and shape to be determined.

Figure 3.20 below shows the calculated ASTM grain numbers of the static castings produced in the various moulds. The grain number was similar when the three alloys were cast in the RP moulds. However, the castings produced in the Silica foundry sand gave slightly higher values with respect to the two Mg alloys. Interestingly, the Al castings gave similar grain numbers when produced in each mould, although lower than for Mg alloys.

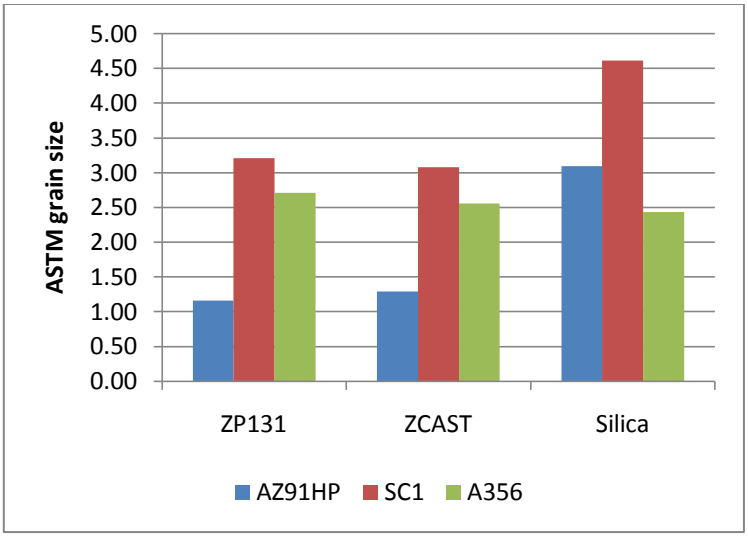

Figure 3.20 Average ASTM grain number produced in different moulds

The grain numbers for each alloy quantifies their microstructural granular size and is directly related to the tensile properties of the castings. Microscopic analysis of each alloy follows, utilising light microscopy and SEM.

3.6.2 Magnesium alloy: AZ91

The equilibrium phase diagram for Magnesium-Aluminium alloy systems is shown in Fig. 3.17 and is a typical binary system with solid solutions, displaying an intermetallic phase and an eutectic reaction. Photomicrographs of Figure 3.22 the microstructures of different grades of magnesium alloys obtained while casting into moulds under varying conditions as per the Taguchi L9 design. In all cases the white areas represent the pro-eutectic α Mg phase, and the darker areas represent the eutectic mixture of the α phase and the intermetallic phase, $Mg_{17}Al_{12}$.

The cast structures produced by the ZP131 mould have the coarsest primary grain structure, which is probably due to the poor heat transfer characteristics of the plaster mould material. This slow cooling rate promotes a more homogenous dispersion of the intermetallic phase, $Mg_{17}Al_{12}$. The Hexagonal Close Packed (HCP) structure of the Mg crystals results in a limited number of slip planes and resistance to fracture is primarily provided by the grain

boundary phase [75]. The intermetallic phase in AZ91 alloys is a Body Centred Cubic (BCC) structure which is incompatible with the HCP Mg structure. This difference results in the segregation of the intermetallic around the α-Mg grains. It has been shown that the bond between the $Mg/Mg_{17}Al_{12}$ interface is fragile and the intermetallic itself is a relatively soft phase. This results in a perfect location for cracks to propagate from, with the formation of micro cracks commonly observed at the $Mg/Mg_{17}Al_{12}$ interface.

Intermetallic Phase in Al-Mg Alloys

The role of the intermetallic in the microstructure has a large effect on the mechanical characteristics of the AZ91 alloy. Also, the relative volume and morphology of the intermetallic phase influences the mechanical properties [75]. The formation of the cast microstructure of AZ91 clarifies the role of the intermetallic phase. Commercial Mg casting alloys typically contain a small eutectic volume fraction of Al to avoid increasing the concentration of the intermetallic phase described above [70]. With reference to the equilibrium cooling diagram shown below in

Figure 3.21, the eutectic reaction should only occur when the Al content is about 13 percent weight [70]. However, eutectic structures were observed in alloys with an Al content much lower than this, and this is shown in the results in Figure 3.22. The eutectic structures commonly seen in Mg-Al alloys are known as partially or fully divorced eutectic structures. The difference between the partially and fully divorced structures is that the partially divorced eutectic structures tend to contain islands of the eutectic in the intermetallic phase; whereas, the fully divorced structures surround the primary Mg dendrites with the intermetallic phase existing as separate phase or layer between the primary dendrites.

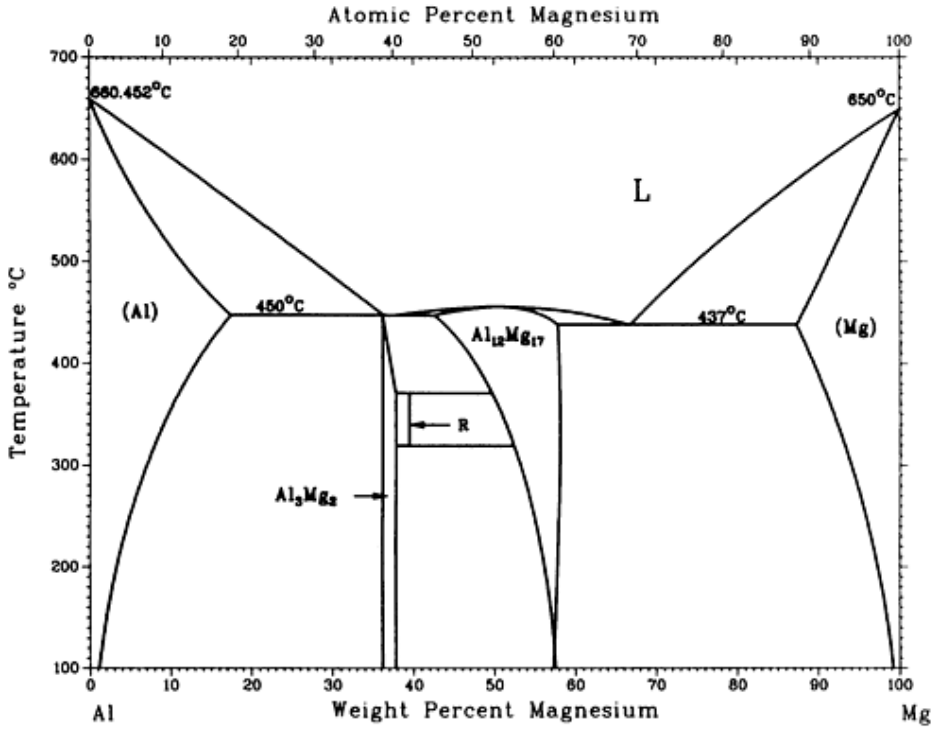

Figure 3.21 Magnesium-Aluminium binary phase diagram [78]

The larger volume fraction of the primary dendrites results in the eutectic mixture solidifying in small inter-dendritic regions [70]. When the alloy solidifies, small trapped pockets of the intermetallic phase exist, which require only a small amount of undercooling for nucleation and growth. This is said to be sufficient to cause the remaining liquid between the primary dendrites to solidify. When a large number of pockets are formed by the dendritic structure, each isolated pocket requires this nucleation for the intermetallic phase. This causes partially and fully divorced eutectic structures to form as the undercooling required is larger for nucleation than it is for growth.

Higher cooling rates also assist in the formation of more divorced structures as dendrite structure becomes more ‘branched’. This branched structure then isolates the eutectic into smaller volumes, which require a higher amount of undercooling for the nucleation of the intermetallic phase, which results in divorced eutectic structures. The resulting divorced eutectic structures in slow cooling castings (such the ZP131 material), results in a more homogeneous dispersion of the intermetallic phase, leading to increased resistance to deformation under load [70].

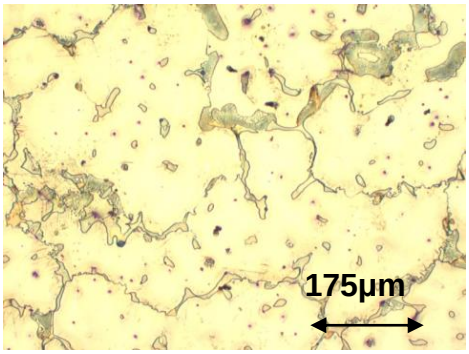

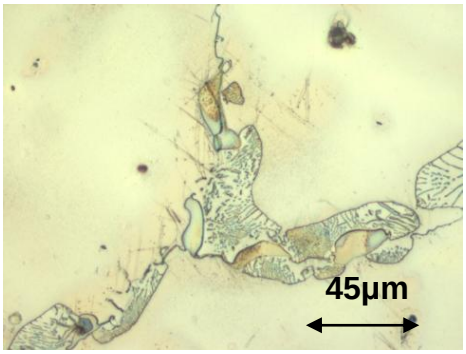

(a) X100 **(b) X400**

AZ91, ZP131 mould, at 690°C, Isomol 200 coating (σ_{UTS} = 156.4MPa δ = 2.17% HB = 56.8 Grain size: 1.11)

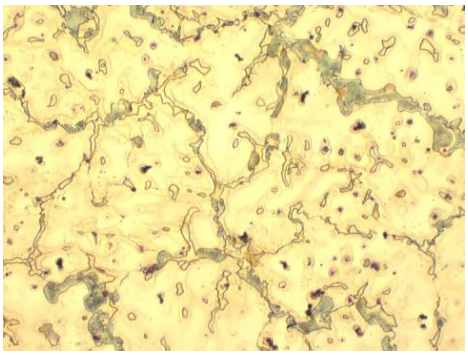

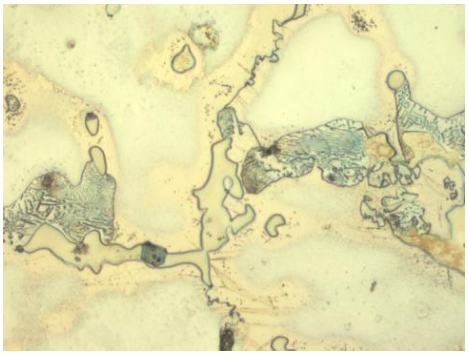

(c) X100 **(d) X400**

AZ91 casting produced in ZCast501 mould cast at 740°C. The mould was coated with Magcoat. (σ_{UTS} = 150.87 MPa δ =1.51% HB = 60.53 Grain size: 1.29).

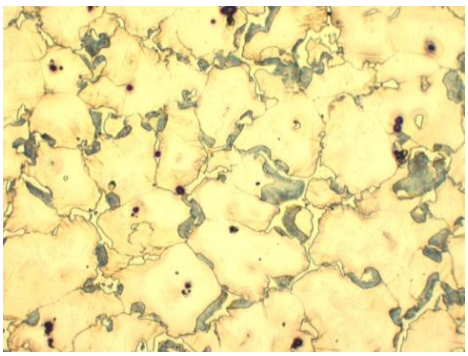

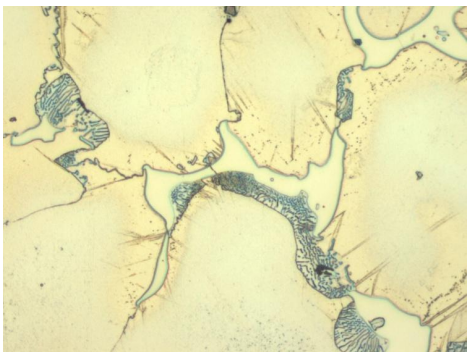

(e) **(f)**

AZ91 casting produced in Silica sand foundry mould, cast at 770°C. The mould coating was Zircoat (σ_{UTS} = 127.1MPa δ = 1.54% HB = 56.82 Grain size: 3.09)

Figure 3.22 AZ91 microstructures in (a&b) ZP131 (c&d) ZCast and (e&f) Silica foundry moulds

This may explain the increased tensile properties of the slower cooling castings produced in the ZP131 moulds over those from the ZCast and silica sand moulds.

Although the average grain number of the castings produced in the silica foundry sand was considerably higher (smaller grains), this effect may be negated by the isolated dispersion of the intermetallic phase. This non-homogenous dispersion may have resulted in a weakened structure due to lower resistance to grain boundary movement. This has also been promoted [70] as a problem of divorced eutectic structures (higher cooling rates e.g. silica sand) in structural applications because of a decrease in the ductility of the alloy. This result was also seen in the above results, with a clear drop in the elongation percent of the casting produced in the silica sand moulds. Thus, it appears that to obtain a Mg casting with suitable tensile properties, the intermetallic phase must be evenly dispersed to resist grain boundary movement [36].

The photomicrographs below in Figure 3.23 show both partially and fully divorced eutectic structures. It has been shown [79] that faster cooling rates tend to form fully divorced eutectic structures in Mg-Al alloy systems. Castings produced in RP mould resulted in partially divorced (low cooling rate) structures whilst those produced in silica foundry moulds produced fully divorced structures (high cooling rate).

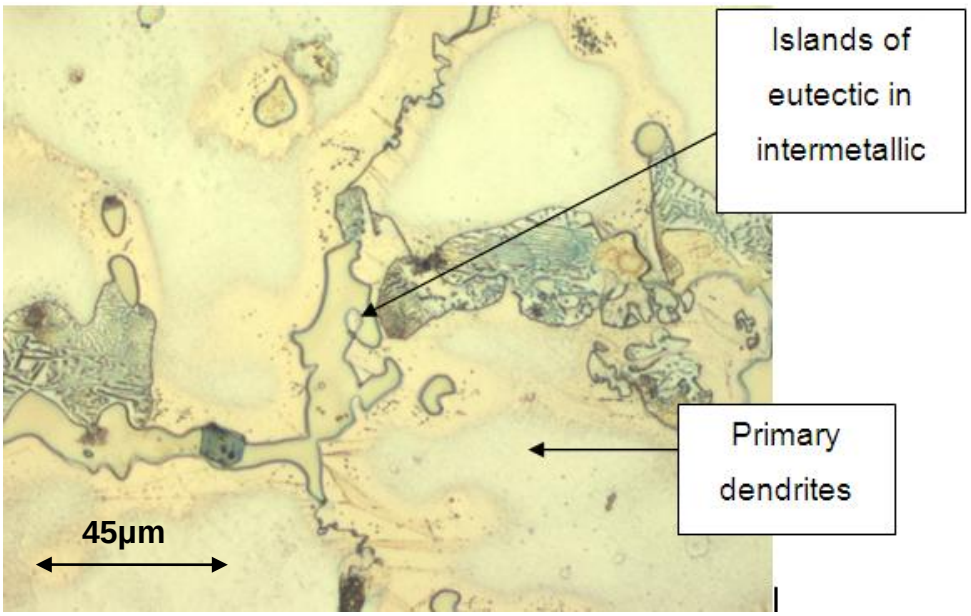

(a) Partially divorced – slow cooling (plaster)

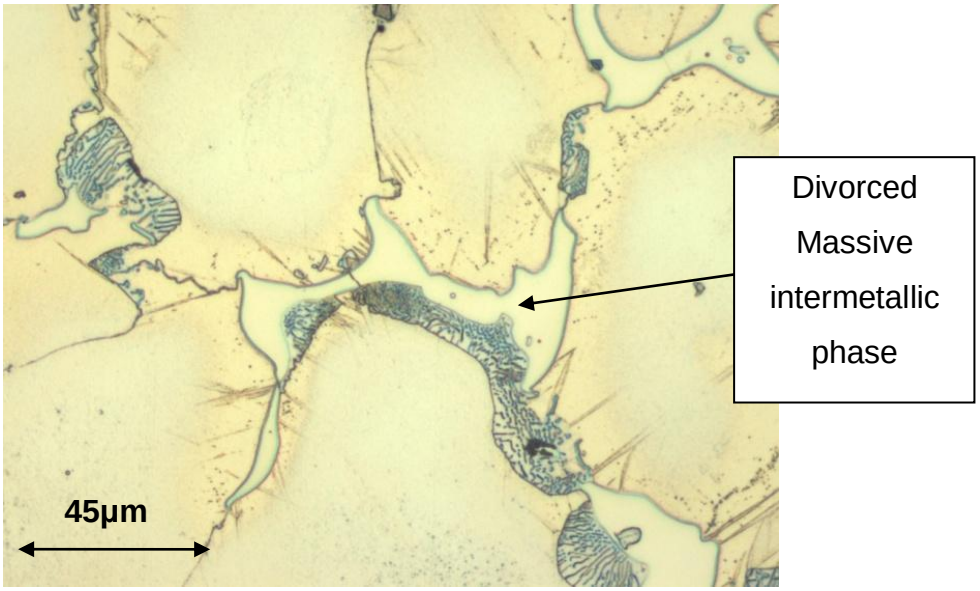

(b) Fully divorced - Fast cooling (silica sand)

Figure 3.23 Micrographs showing (a) partially divorced and (b) fully divorced eutectic structures in AZ91 magnesium alloy

Overall Microstructure of Mg Alloys

The overall structure of the primary Mg dendrites revealed a globular, coarse grain structure with no evidence of secondary arm growth in RP moulds.

Microporosity was also present in the microstructure of the cast AZ91.Figure 3.24 below shows suspected microporosity from Hydrogen present in the atmosphere, resulting in small levels of hydrogen dissolving into the melt. Upon solidification, the dissolved hydrogen is trapped, which forms micro-voids in the cast structure.

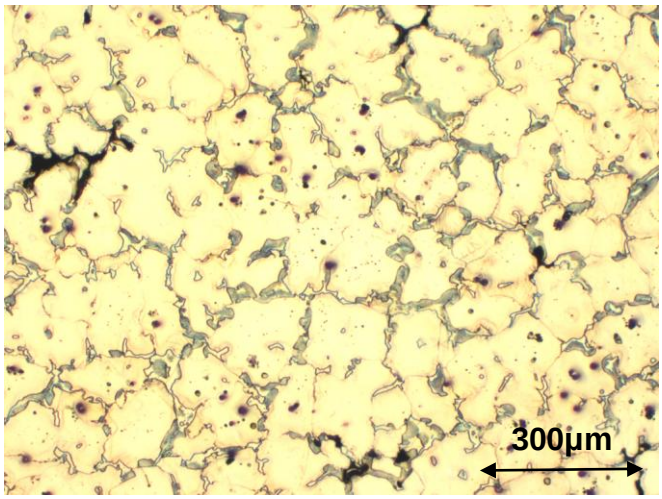

Figure 3.24 Photomicrograph of AZ91 casting showing areas of micro-voids (X50 magnification)

The presence of this porosity has been linked to a decrease in the mechanical properties of cast Mg alloys. The level of porosity (% of cross sectional area), has a linear dependence with yield strength in permanent mould cast AZ91 alloys [80]. Non linear and power law relationships of porosity were also established for UTS and % elongation of the tensile test specimens [67, 80].

Further quantification of the cast structure by SEM in this study revealed small levels of porosity located on the fracture surface of the tensile test specimens as shown below, in Figure 3.25. There was little evidence of the ductile dimple structure found in plastically deformed fractured surfaces. The fractured surfaces appear to have been caused by transgranular brittle fracture (cleavage) [81]. Other observations from tensile testing, such a relatively flat fractured surface, limited ductility and audible fracture confirmed the brittle fracture mode. Literature [81] also supported this finding, with the fracture of Mg alloys explained as being brittle in a cleavage or quasi-cleavage mode

due to limited ductility. The photomicrograph of the fractured surface obtained by Zeng et al is reproduced in Figure 3.26a, which is similar to the current results shown in Figure 3.26b.

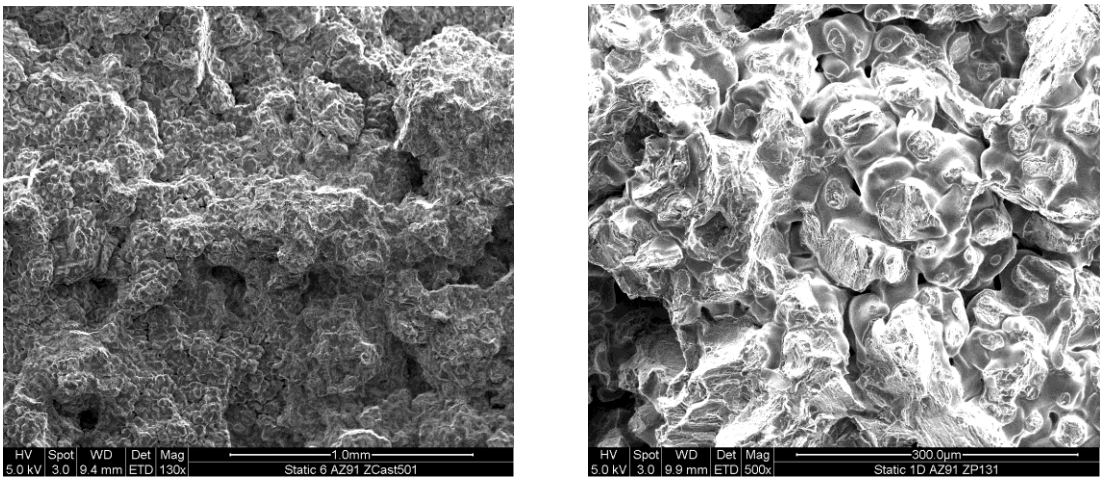

Figure 3.25 SEM photographs showing porosity present on the fractured surfaces of the AZ91 Castings (X130 (left) and X500 (right) magnification respectively).

.

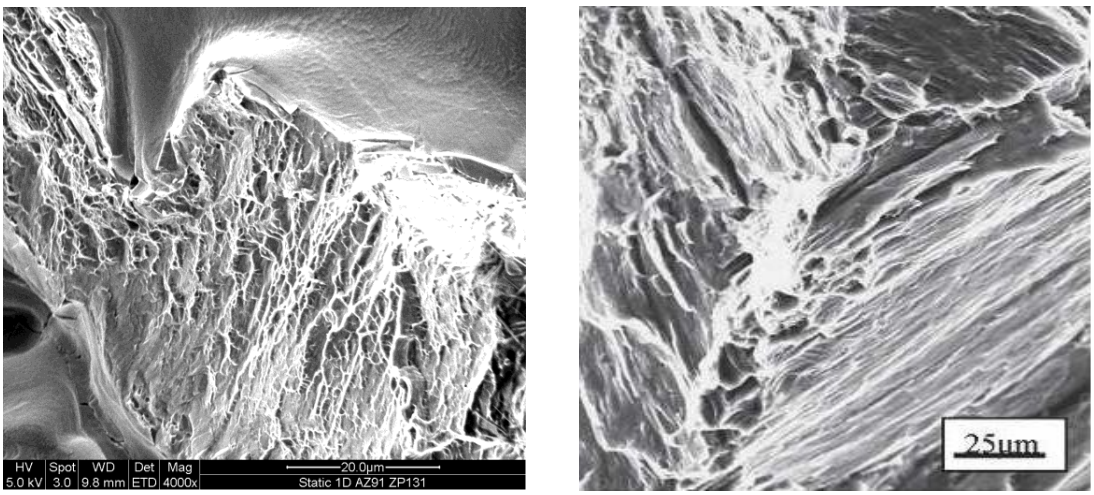

(a) From current work **(b) Zeng et al [81]**

Figure 3.26 SEM fracture surface showing quasi-cleavage fracture surface in (a) current work and (b) Literature

3.6.3 Magnesium alloy: AM-SC1

Unlike the AZ91 alloy system which utilises Al as the primary alloying addition to the base Mg, SC1 comprises rare earth elements such as Nd, Ce, La, plus Zn, Zr and Mn. Zn, Zr and La contain about 0.5% of the total weight, with higher concentrations of Nd (1.7%) and Ce (0.7%). Al is not present and this alloy system falls under the umbrella of Zr containing alloys. SC1 was developed at the CAST Metals Institute with the objective of developing a high temperature, creep resistant alloy capable of being cast into sand moulds for automotive applications, primarily engine blocks and gearbox housings [82]. This alloy has an intermetallic phase which is located around the grain boundaries, which reduces grain boundary sliding at higher temperatures.

The grain number of SC1 alloys was larger (smaller grains) in the silica sand when compared to those used in RP moulds. The silica moulds produced both increased the UTS and percent elongation. The absence of the $Mg_{17}Al_{12}$ intermetallic reaction, shown to be a relatively weak strengthening phase, is a probable reason for this improvement. The RP moulds produced lower UTS and percent elongation when both compared to the AZ91 alloy and to the SC1 castings produced in the Silica sand.

Overall Microstructure of SC1

SC1 alloys were observed to have globular primary dendrites, surrounded by the Mg-RE intermetallic phase, as shown below in Figure 3.27a-f. The castings produced in silica moulds showed consistently higher UTS and elongation values compared to the RP moulds, being 157MPa and 3.35% respectively. On the other hand, the castings showed in the ZCast and ZP131 moulds, showed consistently lower UTS and elongation values of 132 and 130MPa, and 2.28 and 2.56% respectively. The microstructure of castings produced by 3D printed moulds was similar to traditional produced SC1 castings, as noted in the literature [56, 72], supporting the results of this work. The literature samples showed typical α-Mg dendrites with a surrounding intermetallic phase, chemically reported as $Mg_{12}La_{0.43}Ce_{0.57}$ [56].

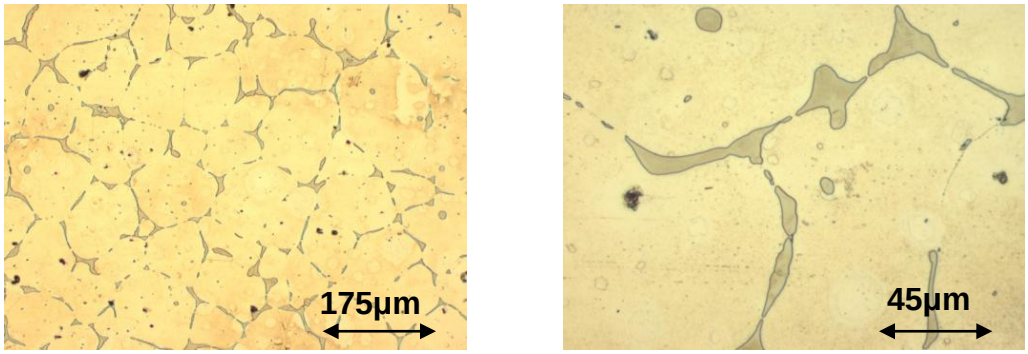

(a) **(b)**

SC1 magnesium alloy cast in ZP131 plaster moulds at 730°C. The mould was coated with Zircoat (σ_{UTS} = 130.02 MPa δ = 2.56% 48.87 Grain size: 3.08)

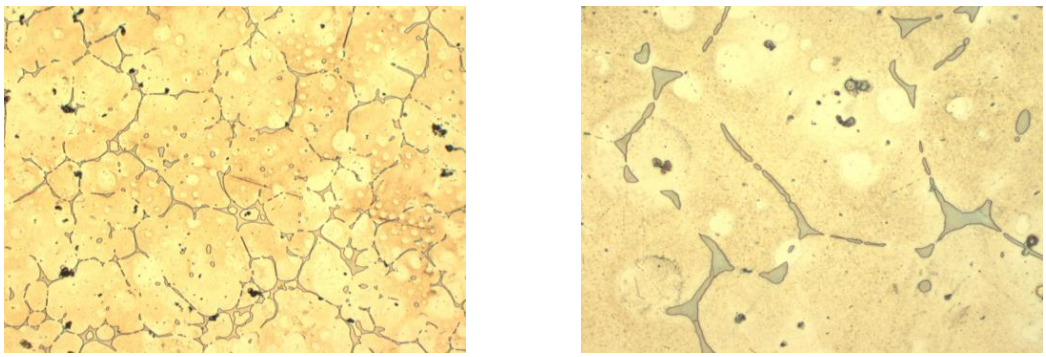

(c) **(d)**

SC1 casting poured into ZCast501 moulds at 770°C. The mould was coated with Isomol 200 (σ_{UTS} = 128 MPa δ =2.28% HB = 48.16 Grain size: 3.21)

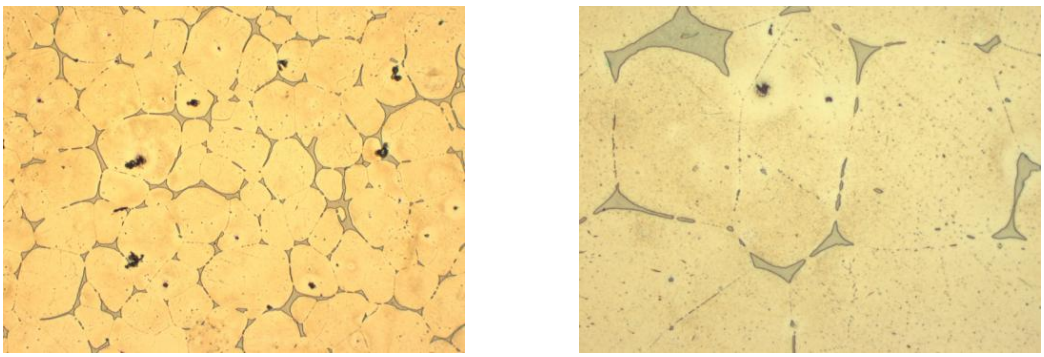

(e) **(f)**

SC1 casting produced in Silica foundry sand moulds at 690°C. The mould was coated was Magcoat (σ_{UTS} = 157.38MPa δ = 3.35 HB = 47.47 Grain size: 4.6).

Figure 3.27 Photomicrographs of SC1 produced in (a&b) in ZP131 and (c&d) ZCast501 and (e&f) Silica foundry sand moulds

Overall, the SC1 grain numbers were higher (ASTM E112), than those of AZ91, due to the grain refining properties of Zn. However, this only translated into increased tensile properties compared to AZ91 using silica sand moulds and not the RP moulds. This suggests that to achieve equivalent tensile properties to AZ91 with SC1 a significant increase in the cooling rate must be achieved (even smaller grain size). This reversal in performance using SC1 as against AZ91 may also be due to additional RE intermetallic phase contributions in SC1.

Subsequent SEM analysis suggests transgranular failure as the mechanism of fracture of this magnesium alloy. SEM photographs clearly show fracture surfaces that are consistent with transgranular failure, as shown in Figure 3.28. Similar to AZ91, small microporosity can be observed on the fracture surface.

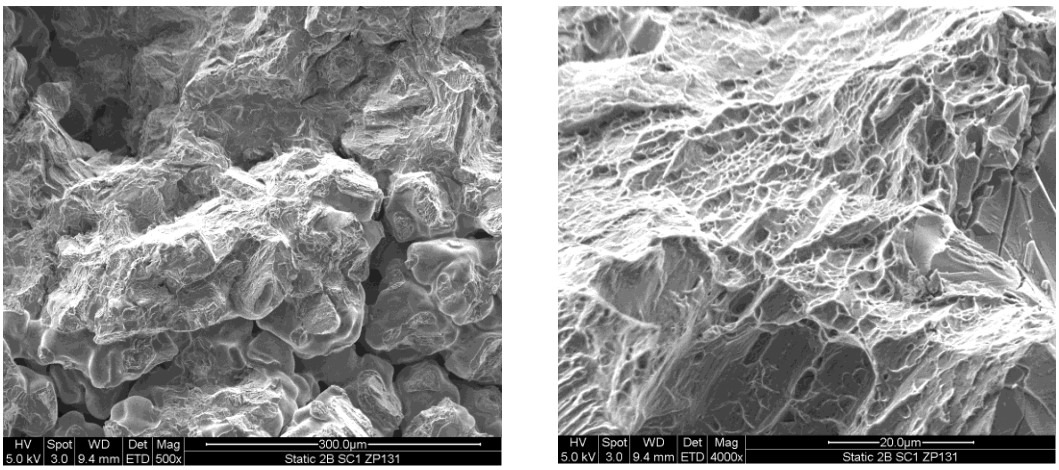

(a) **(b)**

Figure 3.28 SEM photographs showing fracture surface on the primary (a) Mg dendrites and (b) more ductile regions on the same sample (magnifications are X500 and X4000 respectively).

3.6.4 Aluminium: A356

The photomicrographs obtained with A356 cast under different conditions are shown below, in Figure 3.29a-e. Inspection of the microstructure showed unusual plate like Silicon (Si) eutectic morphologies, coarse grain structures and large porosities in the Al-7%Si castings. Also, the photomicrographs

showed the presence of Iron (Fe) intermetallics in the cast alloys. Subsequent SEM photographs of the fractured surface showed large pores. The presence of coarse Si eutectic particles, iron intermetallics and porosity in cast Al alloys all have adverse effects on the material quality and strength [57, 65, 69, 76, 83, 84].

These properties of A356 must be placed in the context of Al casting alloys. This alloy is a widely used hypoeutectic alloy, which includes primary Si around 7% weight and 0.03% Strontium (Sr). The microstructure of this alloy consists of Al dendrites, and an Al-Si eutectic. A356 has a modified eutectic structure because of Sr content. An unmodified eutectic structure results in silicon particles which have a plate like morphology.

The modification of these plate-like Si particles to rounded particles results in improved strength and elongation values. Permanent mould casting demonstrates the influence of the eutectic modification [83] on the mechanical properties of Al-7%Si alloy. It was shown that in unmodified castings the UTS was 77MPa, whereas partially and fully modified samples were 147 and 188 MPa respectively. The eutectic modification results in a ‘composite like’ structure which increases UTS, elongation, hardness and machinability [83]. Other sources [85] have identified that the mechanical properties of Al-Si castings are dependent on the size, form and distribution of the silicon particles, together with the level of porosity, Dendrite Arm Spacing (DAS) and eutectic morphology.

The morphology of the plate like constituent Si particles appears to be a result of no Sr modification. This may have occurred because of strontium burn off which is a known phenomenon. The result was large brittle plate like Si particles which were detrimental to the mechanical properties of the cast parts [85]. The shape and size of these Si particles is important as increasing DAS has been linked to increasing size of the Si particles [86]. Modification of the Si particles was found to decrease the overall Si particle size and number of particles per mm^2 [86].

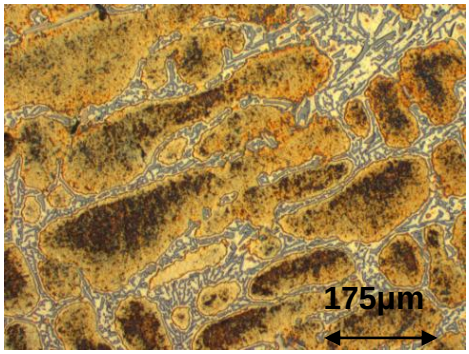

(a)

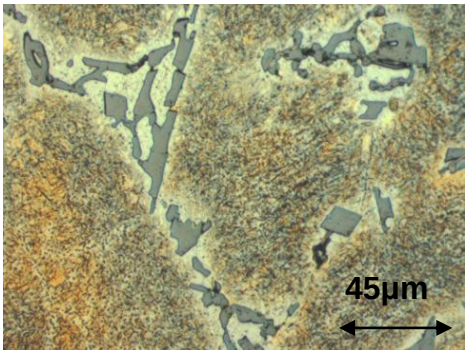

(b)

A356 Aluminium castings produced in ZP131 plaster moulds, poured at 730°C. The mould coating used was Zircoat (σ_{UTS} = 140.23MPa δ = 0.96% HB = 60.53 Grain size: 2.45).

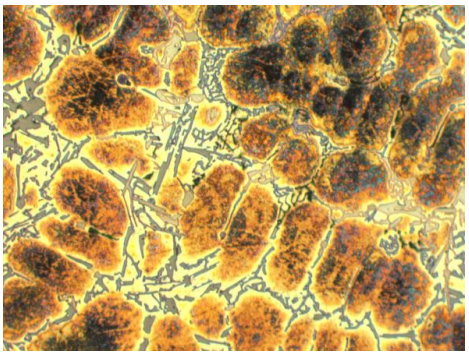

(c)

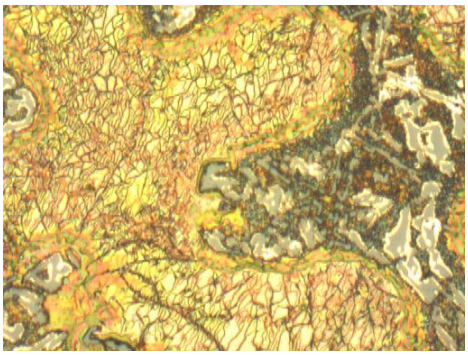

(d)

A356 castings produced in ZCast moulds poured at 770°C. The mould coating was Isomol 200 (σ_{UTS} = 134.30MPa δ = 0.74% HB = 66.70 Grain size: 2.45).

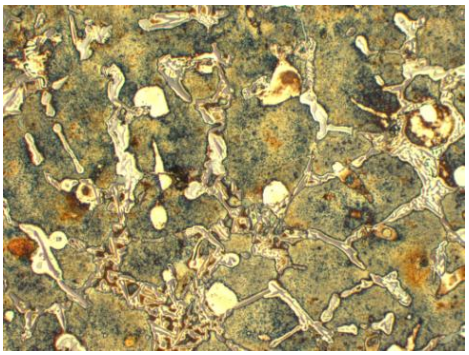

(e)

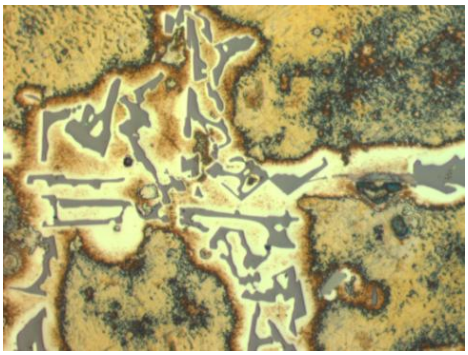

(f)

A356 castings produced in Silica foundry sand moulds, poured at 690°C. The mould coating used was Magcoat (σ_{UTS} = 102.26MPa δ = 0.89% HB = 52.65 Grain size: 2.18)

Figure 3.29 Microphotographs showing A356 cast structures in (a&b) ZP131 (b&c) ZCast501 and (d&e) Silica foundry sand

Eutectic morphology is also important inasmuch as shrinkage and porosity are adversely affected by the eutectic solidification. This proceeds through solidification of primary Al dendrites until the dendrites impinge on each other [85]. At this point, dendritic mobility is reduced. Interdendritic feeding the primary mechanism by which the contraction of the metal is compensated for, as the volume reduces upon freezing. This feeding results in the flow of eutectic fluid, which indicates that the eutectic formation and growth are important to the fluid flow and ultimately the cast mechanical properties.

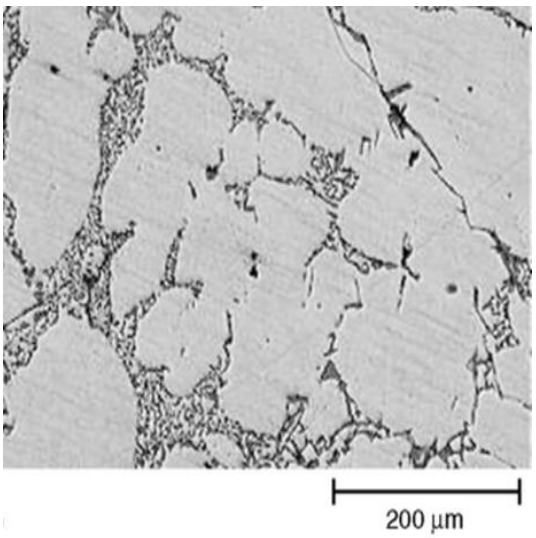

(a) Typical modified eutectic structure found from literature [60].

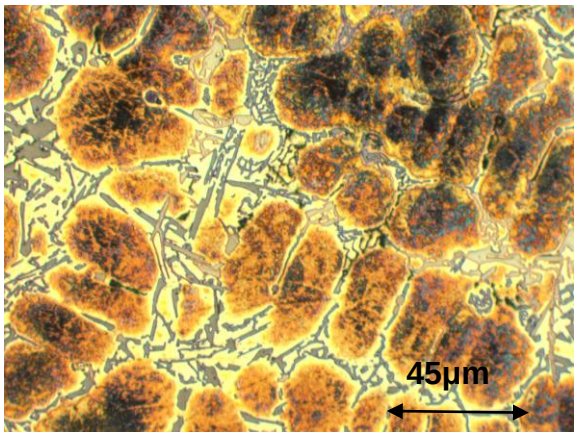

(b) Static A356 casting showing sharp silicone eutectic (X200)

Figure 3.30 Al-Si alloy, showing (a) fine modified eutectic silicon and (b) coarse eutectic silicon.

The plate morphology is detrimental to the cast alloy strength. Proper modification is shown above in Figure 3.30a, with the unmodified structures, from the current work, shown in Figure 3.30b. This mechanism has been explained by the reduction of stress concentrations present at the sharp Si needle particles. The presence of these stress concentrations reduces material toughness, leading to typical brittle fracture [84]. Further, it was found [84] that in the unmodified alloy, the damaged Si particles were present on the fracture surface of tensile tested specimens, indicating that the cracks which caused fracture initiated from these Si particles. It was concluded that in unmodified alloys the Si particles have a plate like structure, from which fracture is likely to initiate and propagate. Conversely it was determined that modified alloys have a ductile fracture mode, with considerable plastic deformation seen before fracture, and that the modified eutectic structures indeed have a strong relationship with fracture behaviour [84]. In this work, all Al alloys were seen to have a transgranular fracture mechanism, with the unmodified alloys producing intergranular fracture modes. These results indicate further that the eutectic structures are weak and are a typical source of fracture, as cracks propagates around the dendrites in unmodified alloys.

Proper modification of the eutectic has also been found to not only refine the eutectic Si particles but also the Iron plate like particles, which reduces embrittlement of the cast specimens [87]. Further research [88] showed that the size and shape of the eutectic silicon particles and Fe intermetallics affect the tensile and fracture properties of A356 alloys. In unmodified alloys (heat treated, T6), the eutectic silicon particle size and aspect ratio led to a decreased ductility, accompanied by increased SDAS. At larger SDAS in particular, ductility was low, which was synonymous with large elongated silicon particles. The tensile properties were described as very dependent on the SDAS, eutectic particle size and the aspect ratio of eutectic particles [88].

The presence of iron can also be manifested as large plate like iron particles and these are similarly harmful to the cast strength [89]. The size of Fe intermetallics in A356 aluminium alloys depends on the cooling rate and the amount of iron present in the alloy. Cooling rates decrease the intermetallic

plate size and increasing iron content increases the plate size. Inverse logarithmic relationships of Fe intermetallic particle length to percent elongation and UTS were found fro of unmodified A356 permanent mould cast samples.

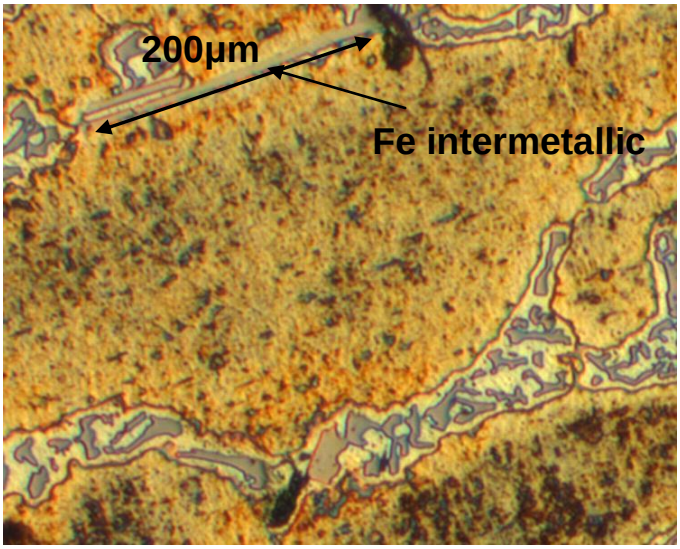

Figure 3.31 Photomicrograph showing plate like Fe intermetallics in A356 casting produced in 3D printed moulds

These Fe intermetallics were identified in the current work as β-Al_5FeSi which are detrimental to the mechanical properties of the castings and in particular, particles over 70µm in length in A356 castings [89]. From the photomicrograph obtained in the current study, and shown in Figure 3.31 an identified Fe intermetallic particle of 200µm can be seen. Fe intermetallics decrease ductility and tensile strength by 'participating' directly when fracture occurs [90]. Unmodified alloys are easily fractured under loads relative to the Al and Si phases of the alloy. This is caused by the formation of micro-cracks which provided a low resistance path for larger cracks to propagate through [90].

As well as plate like Si and Fe in porosity also affects the mechanical properties. The rounded pores observed in Figure 3.32 below, are due to the presence of dissolved hydrogen, which enters the molten Al as the alloy changes to the liquid phase. This change of phase dramatically increases

hydrogen solubility. Upon solidification, impinging dendritic networks trap the gas, leading to the formation of pores in the cast specimens.

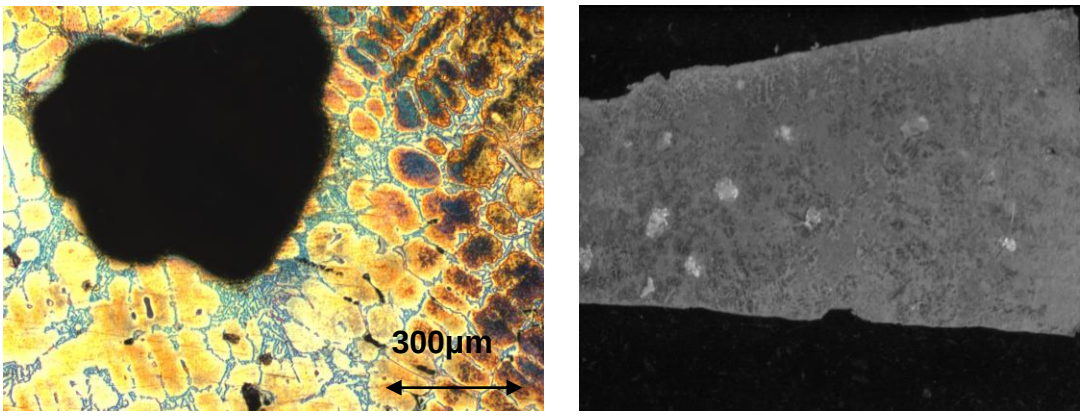

a) Microporosity **(b) Macroporosity**

Figure 3.32 Un-degassed showing typical hydrogen porosity in (a) microstructure and (b) macrostructure produced in RP moulds

The solubility of hydrogen is dependent on the partial pressure of the hydrogen in the atmosphere. This is shown below in equation (3.3).

$$H = S\sqrt{P_{H_2}} \tag{3.3}$$

Where:

H = the amount of hydrogen in liquid Aluminium, $cm^3/100g$

P_{H_2} = the partial pressure of H_2 of gas in the atmosphere

Figure 3.32a&b above, show large porosities in the un-degassed specimens. These samples un-degassed were examined to confirm that the porosity present was indeed due to hydrogen. This is required because two types of porosity form during solidification, namely shrinkage porosity and gas porosity [68]. Evidence from literature on traditional sand casting shows that hydrogen porosity formed is dependent on the solidification time as interdendritic porosity is suppressed by rapid cooling, which impairs the transfer of hydrogen into the liquid [64]. Slow cooling of the metal thus leads to interdendritically distributed voids containing hydrogen.

It is difficult to distinguish between shrinkage porosity and hydrogen porosity but hydrogen is often said to be ‘additive’ to existing shrinkage porosity. This is because the shrinkage void created upon solidification is caused by a drop in pressure and this results in a reduction in hydrogen solubility in the surrounding liquid which facilitates the precipitation of the hydrogen into the forming void [64]. From experience and the literature hydrogen voids are characterised by a round smooth surface in the defect void. Also the wide distribution of the hydrogen voids provides much of the evidence as shrinkage voids are more localised and not distributed evenly over the section being considered. The voids shown in Figure 3.32a&b were evenly distributed porosity, which is typically round in shape. This indicates that the porosity present was hydrogen driven and discussions with foundry engineers confirmed that these voids were indeed of the hydrogen type. The presence of hydrogen and subsequent porosity in the cast specimens, led to reduced tensile strength.

Literature reveals that porosity indeed produces ‘large decreases’ in both tensile strength and ductility [91]. Also, not surprisingly, porosity has a detrimental effect on the fatigue life of Al-Si cast alloys, with regions of high stress created around the pores present [92]. Other research [89] also observed inverse logarithmic relationships of porosity pore size (mm^2) with elongation and UTS values from cast tensile test bars. Similar Al alloys such as A356.2 (unmodified) were degassed and cast into permanent moulds and the presence of pores in all cases led to decreased mechanical properties. Large decreases in elongation and UTS were seen in samples with pores over 50μm in length [89].

Subsequent SEM work on the static castings showed large porosities in the Al castings obtained in the current experimental work. Typical porosities present in a SEM photograph are shown below in Figure 3.33

Figure 3.33. The pore size is about 0.30mm (longest diameter). Literature suggests that the overall porosity (represented as a percent of the fracture area) of the cast A356 samples have been found to have a negative linear relationship with UTS and an inverse parabolic relationship with elongation

percent.

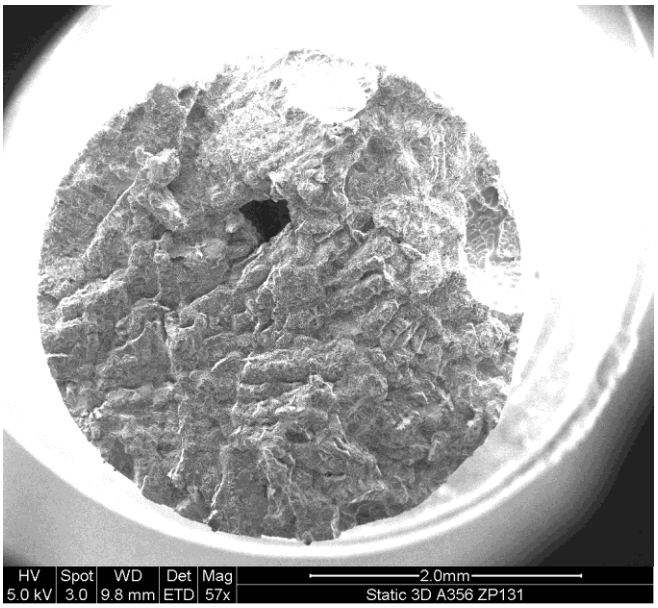

Figure 3.33 SEM photographs showing large pores from su8spected hydrogen porosity

SEM analysis of fractured Al specimens found that the fractured surfaces contained intergranular dimple type rupture. The dimples themselves were not observed to be deep and exhibited only a partial rim around each dimple. This indicated that the fracture had progressed in a specific direction. Conventional fracture mechanics shows that typically, materials fail due to crack propagation in the presence of local stress raisers in the material. In this case, casting defects such as hydrogen porosity, entrapped oxides and intermetallics, act as locations of high stress concentrations, from which micro-voids can form and cracks can propagate.

The morphologies of the fractured surfaces are also influenced by the loading type also. Fractured surfaces found from uniaxial tensile for example, results in equiaxed dimples bounded by a lip or rim [93]. The SEM photos shown below in Figure 3.34 depict this however, the rim does not extend all the way around each dimple.

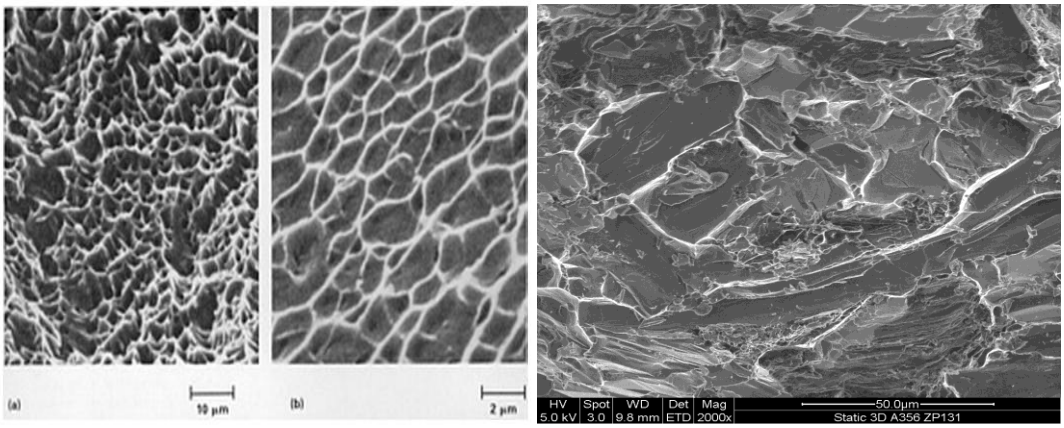

(a) **(b)**

Figure 3.34 SEM fracture surfaces showing (a) typical dimpled, ductile fracture surface [93] and (b) a sample from the current research , exhibiting a lack of a rim around each dimple.

Elongated as opposed to round dimples with an open end indicated the failure mode was a type I 'tear' fracture. This means that the crack originated at a defect near the surface or from porosity present at the surface, allowing the tearing action to propagate through the material.

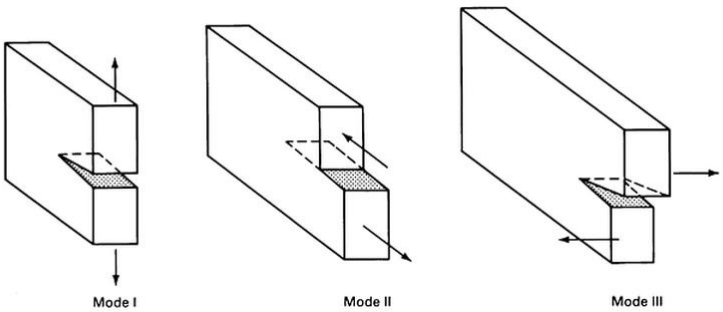

Figure 3.35 Different fracture modes, with arrows showing the direction of the applied loads [93]

Evidence of a crack path originating from porosity is shown at the bottom of the pore. Thus the SEM evidence shows that, the examined fracture surfaces appeared to be typical of brittle fracture. The specimen shown in Figure 3.36 did indeed have limited ductility with 0.74% strain measured from the tensile test and the SEM photograph shows evidence of a pore intercepted by the fracture surface. These shallow dimples were consistent with brittle fracture initiated at pores present in the material. Large pores, shown in Figure 3.36

below are likely candidates for stress raisers and crack initiation points. The absence of shear lips around the edge of the broken specimens also indicates a general lack of ductility [93].

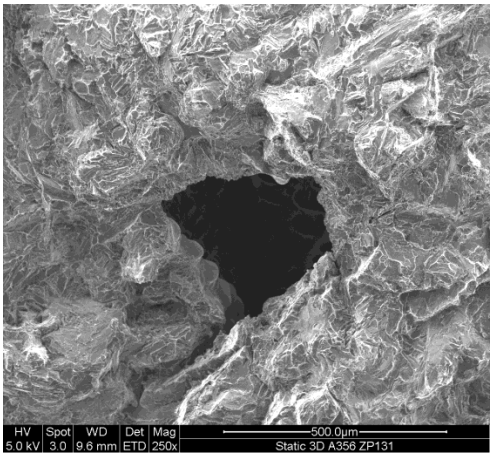

Figure 3.36 A Crack path seen to initiate from pores due to suspected hydrogen porosity.

The combination of unmodified eutectic silicon, porosity and large grain structure, resulted in brittle fracture in the Al castings produced by RP moulds. This was a function of the melt quality rather than the RP moulds used.

3.7 Summary

Static casting of light metals, namely Aluminium and Magnesium was successfully performed in 3D printed mould materials. Significant process factors were linked mechanical properties and possible reasons for their importance was conjectured. Generally, the cast mechanical properties were comparable to values found from traditional sand casting, leading to the conclusion that these RP moulds are suitable for the static processing of light metals

CHAPTER 4 CENTRIFGUAL CASTING IN RP MOULDS

4.1 Centrifugal Casting

The Centrifugal Casting (CC) process is attractive because it is able to improve cast properties by filling the mould with metal under pressure, due to the absence of the centripetal force. This process also facilitates the filling up of more complex and thin sections which may not be achieved by gravity alone. The use of CC offers several mechanical advantages, such as reduction of porosity, increased solidification rate, refined grain structure and increased cast strength. Thus there are both potential design and economic benefits with this casting process. Use of CC can also reduce the amount of scrap in symmetrical components as removal of scrap is often more straight forward, because there is only one central sprue and often only one gate to be attached to each cavity. This reduces both material and labour costs, increasing the overall casting yield. Further, the CC process can be utilised in large scale production, including creation of automated casting processes. Machines and operations can be numerically controlled and casting and mould removal become mechanical actions. Castings can be repeated with fine control over speed of rotation of the mould, pouring rates, cooling rates and casting removal.

Apart from the increased pressures generated in CC, the casting process also facilitates functional grading of materials. For example, in Aluminium-Silicon Carbide (Al-SiC) alloys, hard and heavy SiC particles present in the alloy are displaced at a greater rate than the lighter Al particles, leading to a greater concentration of the hard SiC phase at the periphery of the casting with the lighter more ductile aluminium phase located away from the outer surface. The production of car wheels is a common example where a hard surface is desired for the outer rim of the wheel to reduce wear associated with operation, whilst a ductile region is desired at the centre to avoid brittle fracture.

The ability of the 3D printing process to produce complex shapes has been noted. The advantages of the CC process offer the opportunity of creating complex strong castings in rapidly produced moulds. Also poor thermal properties of the printed moulds may be improved by use of the CC process. It is currently unknown whether in fact 3D printed moulds can be used in the CC process, and this chapter presents work to experimentally investigate the application of CC in RP moulds.

4.2 Background

The CC process is casting process whereby molten metal is poured in a central sprue in the mould cavity, which is then filled under pressure, due to the absence of the centripetal force. Filling under pressure creates castings with superior mechanical properties and increased accuracy when compared to traditional static sand casting [94].

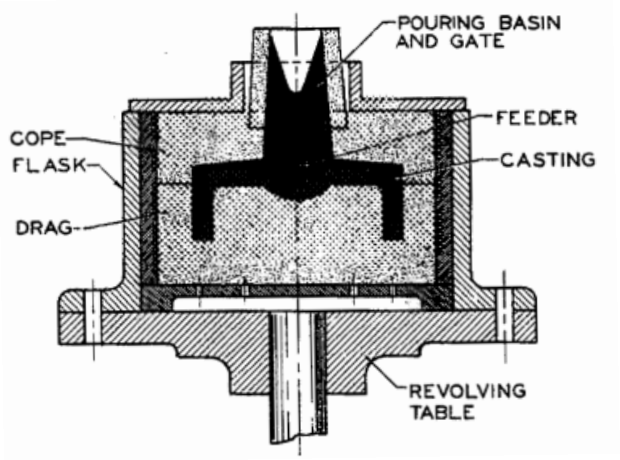

Figure 4.1 Vertical semi-centrifugal casting setup [95]

The process consists of three primary techniques, these being [95]:

- True centrifugal
- Semi-centrifugal
- Centrifuge casting

In true CC, cast iron and steel pipes, liners and sleeves were produced [95]. This can proceed around a vertical axis, as shown below in Figure 4.1, or around a horizontal axis. The metal is cast with no internal core and the molten metal solidifies in the shape of a tube. Semi-centrifugal casting usually comprises a centrally placed cavity which is supplied by a central sprue. The cast objects are typically small or medium sized castings. Finally, centrifuging is when multiple cavities are placed a specific certain distance away from the centre of the mould. The in-gates are connected to the central sprue, which supplies molten metal to the cavity under pressure.

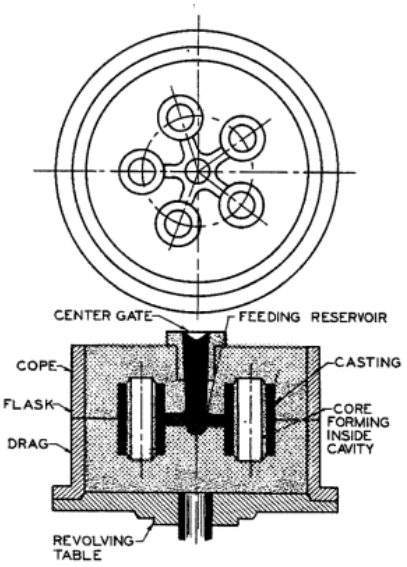

Figure 4.2 Illustration of the centrifuge technique with multiple castings placed around the central sprue [95]

These CC techniques can utilise sacrificial moulds such as traditional green sand or chemically bonded sand moulds. Other moulds used are plaster and vulcanised silicone rubber moulds [94]. The use of sacrificial moulds in CC may be applicable to creation of sand cast components comparable to those produced by high pressure die castings.

4.3 Analytical Model

The initial approach to the CC process is through the development of a mathematical model, to further understand the process on a more fundamental level. Specifically, the relationship between metal velocity and radial position with respect to pressure, is sought in a scientific manner, along with the quantification of the magnitudes of the resulting metal velocities and pressures.

The basis of using the CC technique is centred on the ability to fill a mould under pressure, resulting in improved mechanical properties. This pressure is created by increasing the fluid velocity inside the rotating mould, caused by the absence of the centripetal force (informally known as the centrifugal force). The increased fluid pressure developed, allows thin and complex sections to be filled, as the pressure present in the fluid overcomes the surface tension of the molten metal. This is advantageous to static casting, which utilises only the force of gravity, requiring a large metallostatic head to overcome the surface tension, to force the metal into thin sections.

Although the basic understanding of increasing rotational speed results in higher fluid velocities, the actual magnitudes of these velocities and pressures require investigation, into not only their quantity, but the nature of their mathematical relationship to increasing rotational speed. To gain further clarity and understanding, with respect to the current casting setup, a second order differential equation was developed to predict the magnitude of these properties at a given radius. This allowed the calculation of the pressure of the metal at given radius as a function of time. These values were then cross-referenced to the mechanical properties of the castings gained from the experimental testing, in the attempt to link improved mechanical properties to increases in rotational speed (increased filling pressures). Further, the effect of rotational speed on the microstructural features of the cast parts, such as defects and grain size, was of importance to help understand the influences of the CC process on the properties of light metal alloys (section 4.7.1). Lastly, the ability of these moulds to withstand the calculated pressures can then be formulated and their suitability assessed, in the context of CC of light metal

alloys. The resulting range of influential rotational speeds from the experimental results could then represented as a pressure and possibly used in future work. However, due to restrictions with the respect to the 3D printer build size and maximum rotational speed of the CC machine, speeds ranging from 150-450RPM were analysed with at various radii (up to 90mm) from the centre of rotation.

To quantify rotational speed, a particle with unit mass located at a fixed radius from the centre of rotation was considered. This particle was confined within a fixed channel which acted as the cylindrical portion of the rotating mould. Figure 4.3 below shows the schematic of the experimental model, with the free body diagram of the particle and the forces acting on an element of liquid during the CC process. The model assumes that the fluid is not compressible, and considers only the action of the centrifugal force. The element of liquid shown is constrained in a radial channel as designated in the mould design. Once spinning, the particle experiences acceleration due to the absence of centripetal force. This has the effect of moving the fluid radially outward for, the centre along the channel.

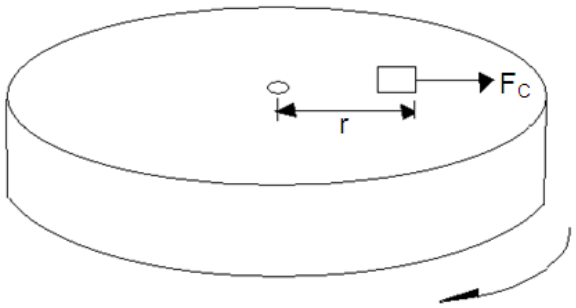

Figure 4.3 Schematic of the forces acting on an element of liquid under the absence of centripetal forces, at constant angular velocity

Initially, neglecting friction experienced at the mould wall, the following differential equation applies:

From Newton's second law of motion:

$$\sum F_x = m.\frac{d^2r}{dt^2} \tag{4.1}$$

Assuming the radial direction as the x direction, the equation (4.1) becomes:

$$\omega^2 r = \frac{d^2r}{dt^2} \tag{4.2}$$

Rearranging yields

$$\frac{d^2r}{dt^2} - \omega^2 r = 0 \tag{4.3}$$

Equation (4.3) is a homogeneous, second order, ordinary differential equation, which has the following characteristic form:

$$\lambda^2 - \omega^2 = 0 \tag{4.4}$$

Rearranging equation (4.4) gives:

$$\lambda^2 = \omega^2 \tag{4.5}$$

The roots of equation (4.5) are then $\lambda = \pm\omega$

From this the general solution shown in equation (4.7) for this differential equation is used to develop the expressions for radial position, velocity and acceleration as a function of time.

$$y(x) = C_1 e^{x_1 t} + C_2 e^{x_2 t} \tag{4.6}$$

Substituting radial position (r) for y, time (t) for x and w for λ yields the general solution.

$$r(t) = C_1 e^{wt} + C_2 e^{-wt} \qquad \text{(general solution)} \tag{4.7}$$

To determine the constants C_1 and C_2, initial and boundary conditions are implemented. From the initial condition, it is known that at time = 0, the radial position equals 0, thus:

$$r(0) = C_1 + C_2 \tag{4.8}$$

Rearranging gives:

$$C_1 = -C_2 \tag{4.9}$$

Differentiating the equation (4.7), the velocity relationship is determined.

$$\frac{dr}{dt} = C_1 w e^{wt} - C_2 w e^{-wt} \quad \text{(velocity expression)} \tag{4.10}$$

Applying the second initial condition, it is known that the initial entry speed of the molten metal is V_0. This can be determined from the falling height from the crucible to the entry of the mould (sprue). Knowing this value, and that it occurs at time equal to zero allows the constants C_1 and C_2 to be found.

Thus:

$$\left.\frac{dr}{dt}\right|_{t=0} = V_0 \quad \text{Giving} \quad V_0 = C_1 w - C_2 w \tag{4.11}$$

Rearranging gives $V_0 = C_1 w - C_2 w$ thus, (4.12)

$$C_1 = \frac{V_0}{w} + C_2 \tag{4.13}$$

Substituting equation (4.13) into equation (4.9) yields:

$$\frac{V_0}{w} + C_2 = -C_2 \tag{4.14}$$

Rearranging equation (4.14) gives:

$$C_2 = \frac{-V_0}{2w} \tag{4.15}$$

thus

$$C_1 = \frac{V_0}{2w}. \tag{4.16}$$

Substituting equations (4.15) and (4.16) into the (4.7) and (4.10) yields the final expressions for radial position and velocity of the fluid element:

$$r(t) = \frac{V_0 e^{wt}}{2w} - \frac{V_0 e^{-wt}}{2w} \qquad \text{(radial position)} \tag{4.17}$$

And

$$\frac{dr}{dt} = \frac{V_0 e^{wt}}{2} + \frac{V_0 e^{-wt}}{2} \qquad \text{(fluid velocity)} \tag{4.18}$$

From here the acceleration expression is obtained by differentiation equation (4.18) giving:

$$\frac{d^2r}{dt^2} = \frac{wV_0 e^{wt}}{2} - \frac{wV_0 e^{-wt}}{2} \qquad \text{(fluid acceleration)} \tag{4.19}$$

With these relationships were established, the analysis of the different velocities and pressures of flow can be determined at different radial positions away from the central inlet. Knowing the values of these radial positions, the time at these locations were solved iteratively in Microsoft Excel by the radial position formula (equation (4.17)). The time found from this relationship is then used in the velocity and acceleration expressions to find both these values at the chosen radius.

However, before these values are obtained, the frictional resistance of the flowing fluid over the mould surface has to be factored into the model. As the overall aim of this model is to determine the pressure setup in the fluid at the radius considered, the loss of pressure can be determined from Darcy's

equation, presented as a pressure head.

$$h_f = \frac{fLV^2}{2Dg} \quad \text{(Darcy's equation)} \qquad (4.20)$$

Where:

f = Friction factor

L = Pipe length (m)

V = Fluid velocity (m/s)

D = Pipe inside diameter (m)

g = Gravitational acceleration (m/s^2)

Here the pipe length is the runner length into the cylindrical cavity and D is the runner diameter. The friction factor is found from a semi-empirical equation which is dependent on the mould surface roughness and the Reynolds number. This equation is known as the Swamee and Jain equation [96] which can be used for Reynolds numbers ranging from 5000-10^8. In the worse case for velocity (no friction), the velocity can be computed from the analytical model. From here the Reynolds number is then computed with the following equation:

$$Re = \frac{rVL}{m} \quad \text{(Reynold's number)} \qquad (4.21)$$

Where:

Re = Reynolds's number

ρ = Density (kg/m^3)

V = Velocity (m/s)

L = Pipe length (m)

μ = Dynamic viscosity (Pa.s)

The friction factor was then computed with a surface roughness value of the mould material of 100µm. The Reynold's numbers found were in the region of

350000, which constituted turbulent flow. The following equation was used to determine the friction factor.

$$\frac{1}{\sqrt{f}} = 1.14 - 2\log\left(\frac{e_x}{D} + \frac{21.25}{Re^{0.9}}\right) \qquad (4.22)$$

Rearranging gives;

$$f = \left(\frac{1}{1.14 - 2\log\left(\frac{e_x}{D} + \frac{21.25}{Re^{0.9}}\right)}\right)^2 \quad \text{(friction factor)} \qquad (4.23)$$

Where :

f = Friction factor

ε_x = Mould surface roughness (m)

D = Runner diameter (m)

Re = Reynolds number

Lastly, with the friction factor determined, the pressure loss due to the frictional resistance of the metal flowing in the runner bar can be determined by using the Darcy-Weisbach equation shown below. This yields a pressure loss in terms of a head of the corresponding fluid.

$$h_f = \frac{fLV^2}{2Dg} \qquad (4.24)$$

Also $P_{Loss} = \rho g h_f$

Thus $$P_{Loss} = \frac{fLV^2}{2D} \qquad (4.25)$$

This pressure loss is subtracted from the pressure created from the velocity found using the velocity expression. This gives the final overall expression for

the pressure created at the end of the runner bar.

$$P_{Total_x} = P_{Model_x} - P_{Lost_x} \tag{4.26}$$

Where:

P_{Total_x} = Overall pressure created due to CC effect (KPa) (at a radius 'x' away from centre of rotation).

P_{Model_x} = Pressure from velocity determined from velocity expression (KPa)

P_{Lost_x} = Pressure lost due to friction (KPa)

The pressure developed by the rotation of the mould is then computed as a change in momentum from the entry point to the section under consideration. The following equation relates force to momentum:

$$F_x = \dot{m} V_x \tag{4.27}$$

And since

$$P = \frac{F}{A} \tag{4.28}$$

Therefore

$$P_x = \frac{\dot{m} V_x}{A} \tag{4.29}$$

Where:

P_x = Pressure at any radius 'x' from centre of rotation (Pa)

$\dot{m}$ = Mass of fluid (kg)

V_x = Velocity at radius x (m/s)

A = Cross-sectional area of duct (m^2)

The overall pressure developed at any point x was shown to be:

$$P_{total} = P_x - P_{Lost} \tag{4.30}$$

The initial velocity was evaluated to determine the actual velocity of the liquid after undergoing the 90° turn into the runner. This was found from the initial mass flow rate of the metal, which was assumed to be conserved. The initial mass flow rate was set as 0.150 Kg's/s and the vertical distance from the top of the pouring system to the mould cavity surface was 333mm (Figure 4.24). The velocity of the fluid after undergoing this vertical drop was calculated with the following equations:

The velocity at the cavity initial was found from:

$$V = \sqrt{2gH} = \sqrt{2 \times 9.81 \times 0.333} = 2.55 \text{ m/s} \quad (4.31)$$

Where:
V = Melt velocity (m/s)
g = Gravitational acceleration (m/s^2)
H = vertical fall height (m)

However, this is not the actual velocity entering the runner as compensation for the 90° turn into the runner needs to be factored in. This results in the reduction of the velocity to some value lower than 2.55 m/s, as determined above.

To determine the true velocity, the equivalent friction of the bend in the pipe is accounted for in the P_{Lost} equation. The P_{lost} equation now takes the form of:

$$h_f = \frac{fLKV^2}{2Dg} \quad (4.32)$$

Where:
K = The Equivalent loss due to a fitting

And

$$K = f\frac{L}{D} \tag{4.33}$$

Where:

f = Fiction factor of pipe

L/D = Equivalent ratio from a pipe fitting, in this case a 90° bend.

It was found that the L/D for a 90° bend was 30. Also calculations made for the friction factor was 0.033. Substituting these values into the Equivalent loss equation, K equals 0.99.

Now the Pressure head loss due to this bend is computed, giving:

$$h_f = \frac{fLKV^2}{2Dg} = \frac{0.033 \times 0.03 \times 2.55^2}{2 \times 0.016 \times 9.81} = 0.0205 \text{ m}$$

Converting this to a pressure:

$$P_{Lost} = 2680 \times 9.81 \times 0.0205 = 538.97 \text{ Pa}$$

The initial pressure resulting from the drop is calculated from the force acting over the pipe area, since the velocity due to the initial fall is known and the mass flow rate is also known, thus:

$$P_{Initial} = \frac{F}{A} = \frac{V\dot{m}}{\left(\frac{\pi D^2}{4}\right)} = \frac{2.55 \times 0.150}{0.000201} = 1902 \text{ Pa}$$

Thus the overall Pressure allowing for the pipe bend is:

$$P_{Total} = P_{Initial} - P_{Lost} = 1902 - 538 = 1364 \text{ Pa}$$

Now this result can be used to establish the force, i.e.:

$$F = PA = 1364 \times 0.000201 = 0.274\ \text{N}$$

And since we know $F = \dot{m}V$:

$$V = \frac{F}{\dot{m}} = \frac{0.274}{0.150} = 1.83\ \text{m/s}$$

Thus the initial velocity of liquid metal entering the runner is 1.83 m/s, accounting for the pipe bend.

4.4 Results from the Analytical Model

The analytical model provided mathematical insight into the effect of rotating the mould on the velocity and pressures developed in the liquid metal at different stages of filling. The model was used to predict the pressures present at the runner/cavity interface, which was situated 30mm from the axis of rotation. The reason for predicting the pressure at this junction was firstly, to obtain the magnitude of the pressure and secondly, analyse the effect of the cavity angle and the runner/cavity ratio, with respect to the mechanical properties, independently (as these effects were considered as separate variables, as they occurred after this 30mm distance).

The below results showed that at a given radius, increasing the rotational speed resulted in a velocity increase of the liquid metal and subsequently a rise in the metal pressure in the cavity. These pressures were represented as static pressure heads of the metal with the maximum pressure found to be around 300mm Aluminium, which equates to 7.88KPa.

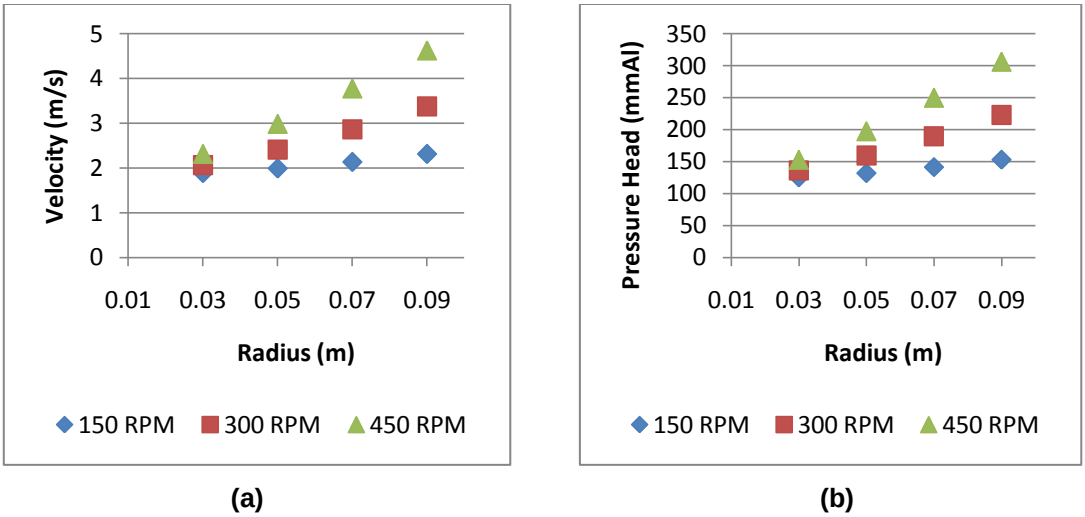

Figure 4.4 Results of the analytical model showing (a) the velocity at different radii from the centre of rotation and (b) fluid pressures developed at the same radii.

The model shows that the link between rotational speed and the melt velocity (as function of time), is exponential in nature (equation 4.18), and provides the basis for estimating the filling pressure. Also, increasing the radial position away from the centre of rotation has the effect of increasing the amplitude of the velocity (and thus pressure). The model thus indicates that to obtain higher pressures, moulds should have increased radii to fully take advantage of the CC process.

The experimental constraints present in this CC setup have been noted, however this analytical model may be further used as a tool in future mould design work, to ensure that correct rotational speeds are chosen. For instance, typical speed ranges used in CC are represented as a ratio of the centrifugal force to the gravitational force. This ratio yields the 'G factor" which is used as a general guideline for choosing the rotational speed. Values of 15-50G have been quoted [53] in the relevant literature for semi-centrifugal casting in sand moulds. Table 4.1 below lists the G values obtained in this experiment at different speeds and radii from the centre of rotation.

Table 4.1 Values of G developed at different speeds with respect to different radii

Radius (m)	150 RPM	300 RPM	450 RPM
0.03	0.75	3.02	6.79
0.05	1.26	5.03	11.32
0.07	1.76	7.04	15.85
0.09	2.26	9.05	20.37

From the above table it is clear that only at a rotational speed of 450 RPM and a radius of 0.07m or greater, was the minimum of 15G achieved in the current setup. However, the mould created in this experiment was subject to the constraints of the 3D printer build size and material cost. Typically much larger moulds are used in actual production with radii up to 250mm [94]. The analytical model is thus useful for calculating the predicted values of pressures and values of G at specific radii from the centre of rotation. This model however, constitutes only preliminary work to establish the linkage between radial position, rotational speed and resulting velocities and pressures in the mould. Other, more complex factors, such as density change (compressibility) due to cooling of the flowing metal and the formation of turbulence due were not considered, but these factors will have effects on fluid flow.

4.5 Centrifugal Casting Experimental Design and Setup

The above analytical model has quantified a range of pressures due to the effect of increasing rotational speed and radial position. To further assess the effects of these pressures on the mechanical properties of the castings, the CC trials were conducted, making use of analytical model and findings from the static casting trials discussed in Chapter 3. This involved the use of ZP131 moulds in a statistical design of experiments known as a Box-Behnken design, which uses three factors at three levels, creating a second order polynomial expression in the three factors. This design was chosen over Central Composite Design (CDD) used in Chapter 2 as only 15 trials are required, as against 20 trial required for the CCD. While a number of factors

could have been considered for the CC trials, only three critical factors were finally chosen, due to time and practical constraints. These factors are presented below:

Speed of Rotation

The speed of mould rotation dictates the pressure generated in the flowing metal. Faster rotational speeds thus result in greater pressures, which influence solidification rate and improve the cast part density [44, 94, 97]. Variation in the rotational speed is of great interest and in these experiments is the primary factor of importance for its impact on mechanical properties.

Cavity Angle

The direction at which the cavity angle is orientated with respect to the inlet is also of importance, as it has a direct effect on how the metal enters the mould cavity. There will be varying angles at which liquid metal enters different parts of the casting, and variation in the angle of entry of the liquid metal into the cavity may influence cast part properties.

Runner to Cavity (r/c) Ratio

Lastly, the ratio of the cylindrical runner diameter to the size of the final entry section at the mould cavity represents the intensity of chocking, and may result in changes in the properties of the cast parts. Relevant literature [94] mentions the importance of ensuring directional solidification in centrifugal casting, and, again variation in this factor may influence changes in the cast part quality.

The experimental work involved simultaneous variation of the three factors at three different levels, as shown in Table 4.2. The experimental design in Table 4.3 shows both the coded variables and natural variables. Much like the central composite design, this design also allows calculation of constants shown in equation (4.34).

Table 4.2 Summarised factor and level combinations for the centrifugal casting trials

Factor	Low	Medium	High
Mould rotational speed (RPM)	150	300	450
Mould cavity angle (°)	45	90	180
Runner/cavity ratio	0.8:1	1:1	1.2:1

Table 4.3 Centrifugal casting experimental design table

Run	X_1	RPM	X_1	Angle (°)	X_1	Ratio
1	-1	150	-1	45	0	1:1
2	1	350	-1	45	0	1:1
3	-1	150	1	180	0	1:1
4	1	350	1	180	0	1:1
5	-1	150	0	90	-1	0.8:1
6	1	350	0	90	-1	0.8:1
7	-1	150	0	90	1	1.2:1
8	1	350	0	90	1	1.2:1
9	0	250	-1	45	-1	0.8:1
10	0	250	1	180	-1	0.8:1
11	0	250	-1	45	1	1.2:1
12	0	250	1	180	1	1.2:1
13	0	250	0	90	0	1:1
14	0	250	0	90	0	1:1
15	0	250	0	90	0	1:1

The Box-Behnken experimental design creates response surfaces for quadratic models. The following polynomial expression is procedural methodology for establishing the responses.

$$y = \beta_0 + \beta_1 X_1 + \beta_2 X_2 + \beta_3 X_3 + \beta_4 X_1^2 + \beta_5 X_2^2 + \beta_6 X_3^2 + \beta_7 X_1 X_2 + \beta_8 X_1 X_3 + \beta_9 X_2 X_3 \quad (4.34)$$

Where y in is the response at X_1, X_2 and X_3. (Note Chapter 2, section 2.2.1 refers to for the basic information on the missing column matrix, along with the calculation of the ANOVA terms.)

4.5.1 Mould Design

A mould, consisting of four cylindrical specimens was designed to accommodate all combinations of factors, as per the above design table. The cylindrical specimens branch out from the central sprue, as shown in Figure 4.5. The mould itself was a horizontally parted mould, with a 30mm long runner, and mould walls shelled to a 5mm thickness. The mould design provided two configurations, to account for the variation of the cavity angle from the central sprue. Figure 4.5 below depicts the two configurations used. The first design below, has the cavity angled at 0° and 45°. The second configuration beneath, shows the cavity angled at 90° to the centre of rotation.

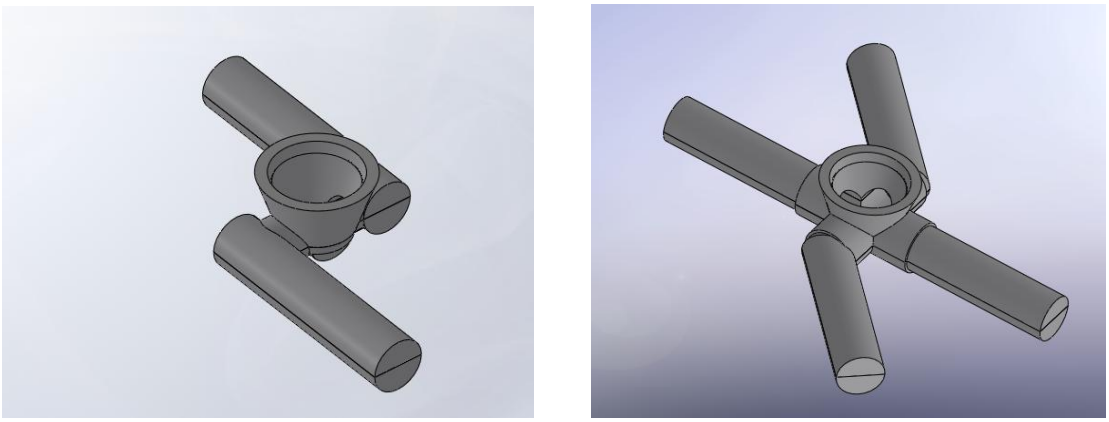

(a) **(b)**

Figure 4.5 CAD models of the centrifugal ZP131 plaster moulds used in the experimental trials, showing (a) samples angles 90°to runner and (b) samples orientated at 0 and 45° in relation to the runner bar.

4.5.2 Setup and Methodology

The CC experimental work was conducted on a custom built vertical CC machine, located at Centracast Engineering, Auckland. The machine is pneumatically operated and is able to control speed of rotation, pouring

speed, motor delay[10] and ramp rate[11]. Castings with a diameter up to 720mm and height up to 250mm can be accommodated, and the mould can be preheated to the desired temperature. The operation[12] of the machine is controlled by a Graphical User Interface (GUI), which controls the machine with the set parameters.

The original use of this CC machine was to utilise a steel die in which Al would be cast. Steel dies machine were thus to attached to the machine rotated by a connecting spindle. To incorporate a 3D printed mould into this design, a two part hollow steel die with 300mm outside diameter was fabricated from 1040 steel, inside which the 3D printed moulds could be located. Cold setting easter hardened resin polymer coated sand was placed around the 3D printed moulds to act as a rigid support for the mould and also stop any metal spillage through the parting line. The steel die (metal enclosure)[13] shown below in Figure 4.6, was fabricated at AUT University using a CNC machine.

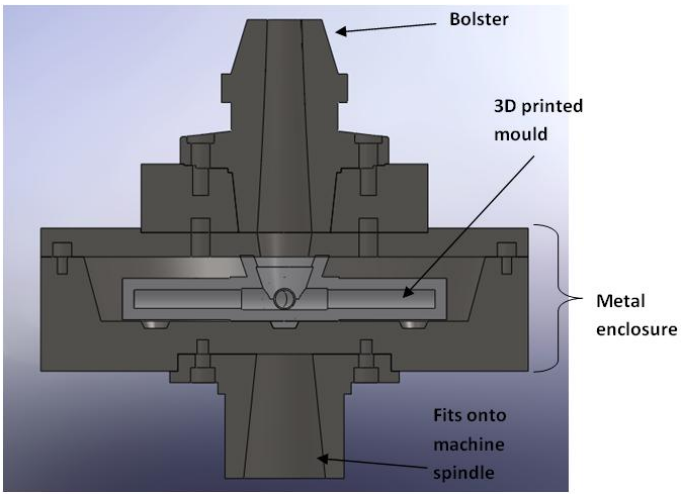

Figure 4.6 CAD sectional model of the centrifugal die and mould setup

[10] Time taken for the mould to rotate after the pouring has been completed

[11] Acceleration of the mould up to the set rotation speed.

[12] For detailed machine operation please refer to Appendix…

[13] Refer to Appendix C for the die CAD drawings of the material information

Figure 4.7 Centrifugal casting setup showing steel die, pouring cup and holding crucible

For the initial castings, Al A356 was poured at rotational speeds varying from 150RPM to 350RPM at temperatures from about 730°C. Initial testing's trialled both the ZCast and ZP131 mould materials at different shell thicknesses, baked at optimum time and temperatures. Before casting, the printed moulds were preheated in a microwave oven at a temperature of about 100°C. After two hours of preheating, the printed moulds were placed in the steel enclosure and supported with the backing sand. Before pouring, the steel die and pouring equipment were preheated with several gas torches to remove any residual moisture. The metal was then transported in small aluminium oxide crucibles from the furnace to the holding crucible on the centrifugal casting machine, and then poured automatically.

4.5.3 Experimental Procedure

Following completion initial trials, the experimental trials were conducted in accordance with Table 4.3. Each 3D printed mould was baked to the optimum levels of permeability and compressive strength established from the material testing covered in Chapter 2. The moulds were preheated at a baking temperature of around 100°C for about an hour prior to casting. Before casting, the preheated mould was placed in the locating centre hole in the

steel die shown in Figure 4.3 to position it directly under the down sprue of the CC machine. Chemically bonded backing sand was then packed around the 3D printed moulds to act as a support for the mould and also prevent any turning of the mould relative to the metal enclosure. This was achieved by introducing holes into the bottom surface of the metal enclosure into which the chemically bonded sand would form. After the supporting sand had bonded to its full strength, the mould was placed on the CC machine and this was setup for mould filling under CC operations. After casting the mould was allowed to sit for twenty minutes before the casting was removed.

All castings were made in un-degassed CC601 alloy, which was melted in a small electrical resistance furnace, at about 720°C. For casting the Al alloy was melted in ceramic crucibles, which were charged with the CC601 ingot. Before each melt, the crucible was cleaned of any oxide left from the previous casting. Once the crucible was taken out of the furnace, the Al was poured into a ceramic holding crucible in the CC machine, which was preheated to around 200°C. The same pouring time was used in all the castings. The motor delay was set to one second (the lowest value) for the castings performed at 150 and 300RPM and two seconds for the castings spun at 450RPM. The desired amount of Al was poured into the holding crucible inside the CC machine casting commenced. Every casting was spun for five minutes. After this period, the top half of the metal die was lifted away, and the mould was removed and allowed to air cool.

4.6 Centrifugal Casting Results

The experimental design and the responses measured with the CC trials involving Al are presented in Table 4.4. Average values of each response are plotted against rotational speed in Figure 4.8 for ease of comparison and a detailed discussion of these results follows next.

Table 4.4 Overall results of mechanical testing of centrifugal test bars

Mould Speed (RPM)	Mould Cavity angle (°)	Runner cavity ratio	Surface roughness, Ra (µm)	UTS (MPa)	Yield strength, 0.2% offset (MPa)	Strain %
150	45	1:1	13.27	92.60	77.00	0.95
450	45	1:1	18.15	128.60	87.25	1.49
150	180	1:1	13.05	99.60	82.90	1.13
450	180	1:1	19.07	109.55	93.45	0.93
150	90	0.8:1	15.24	106.90	85.70	1.33
450	90	0.8:1	14.31	103.20	91.50	0.86
150	90	1.2:1	11.98	104.10	88.30	0.75
450	90	1.2:1	11.62	107.30	82.90	1.11
300	45	0.8:1	13.17	102.70	79.00	1.31
300	180	0.8:1	13.54	106.00	82.35	1.09
300	45	1.2:1	14.78	116.70	85.95	2.10
300	180	1.2:1	14.10	112.50	87.80	1.15
300	90	1:1	12.22	120.60	89.10	1.47
300	90	1:1	12.22	109.80	80.90	1.44
300	90	1:1	12.53	144.55	95.20	2.35

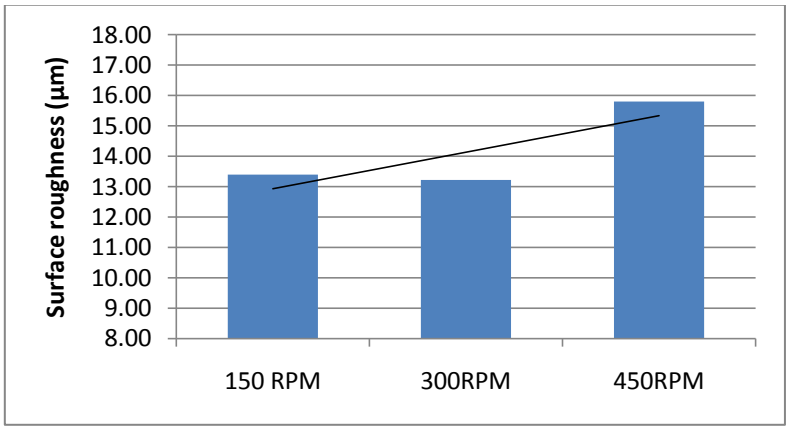

(a)

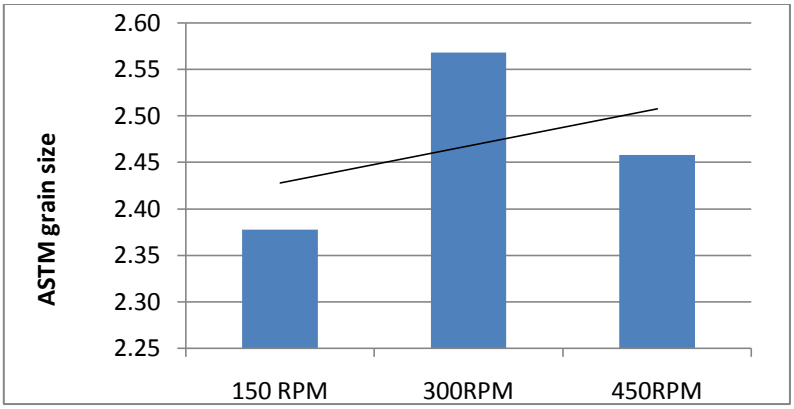

(b)

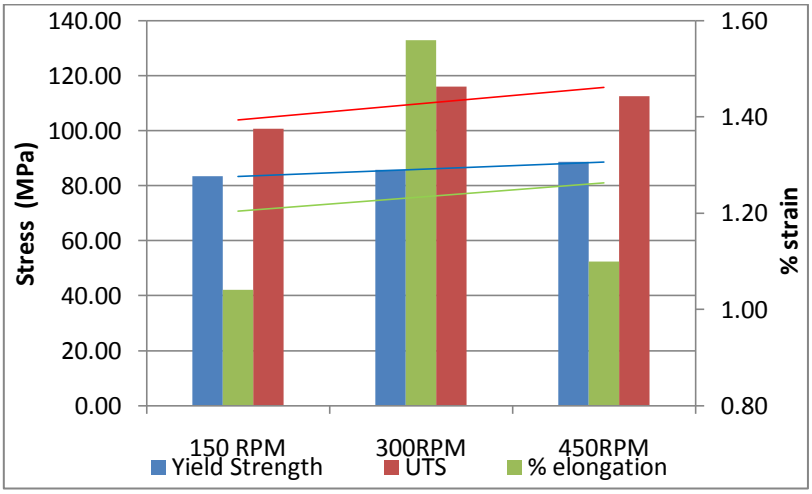

(c)

Figure 4.8 Graphical form of overall results from testing at various rotational speeds, specifically (a) surface roughness (b) ASTM grain size of primary dendrites and (c) tensile properties[14].

4.6.1 Surface Roughness

The ability of these moulds to withstand the velocities and pressures created upon spinning was not previously known and it was suspected, there may be some increase in surface roughness values due to mould erosion resulting from turbulence, or perhaps even mould cracking due to the larger forces acting. However, the moulds withstood the rotational forces in all cases and only some flash was observed between the upper and lower halves of the moulds, which is a common phenomenon in CC, due to the increased

[14] Compiled averages from each speed range

pressures developed in the metal. While the use of the rigid backing sand provided resistance to mould cracking, the internal surfaces of the cavity exhibited no visual signs of mould surface erosion. Also, there was no evidence of mould surface erosion present on the cast specimen surface, indicating that mould erosion was not a significant problem with 3D printed moulds when for CC.

In general, the overall surface roughness results were acceptable, with the averaged values ranging from 13-15.5µm over the tested speed ranges. These values appear to be slightly higher than those achieved in the static casting trials (5.84µm), but it is noted that the ZP131 plaster moulds used in the centrifugal casting trials were uncoated. This was done as the cast surfaces actually gave a more consistent finish, due to the absence of the markings induced by painting the mould coating onto the mould surface. This resulted in well defined shapes and sections with a consistent surface finish. Upon initial visual inspection and touch comparison, the cast surface roughness was very comparable to those found from Al sand castings conducted at the company using chemically bonded silica sand.

From the overall mechanical results in Figure 4.8, the surface roughness was relatively stable at rotational speeds of 150 and 300 RPM respectively. The results obtained at 450 RPM however, were elevated by around 2.5µm over those the two lower speed settings. Without testing at higher speeds, it cannot be concluded that this was due to increased mould erosion resulting from the higher rotational speeds. But given that all the other factors were relatively constant, such as mould production method, baking time, melt temperature and method of pouring, it seems likely that this increase was influenced by the higher rotational speed. The mechanism for this increase in cast surface roughness could be due to either increased mould erosion at higher speeds or increased metal penetration due to higher pressures present within the liquid metal. Figure 4.9 below depicts the effect of metal penetration at (a) low pressure and (b) high pressure.

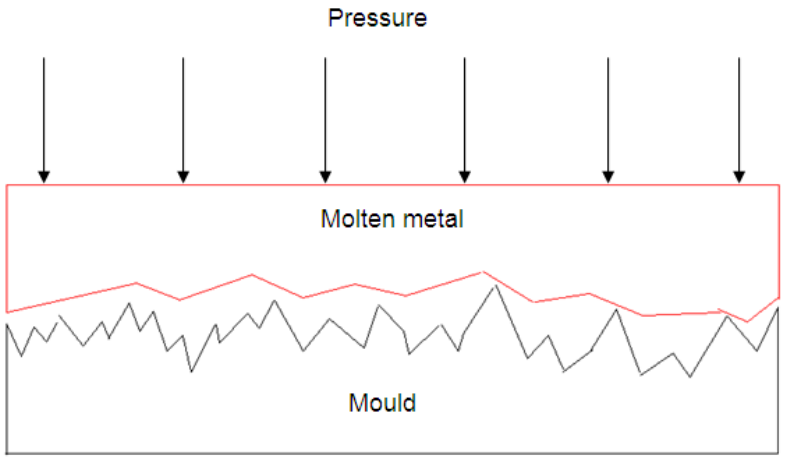

(a) Low pressure

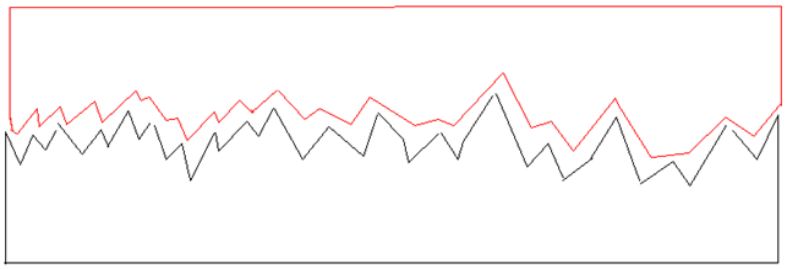

(b) High pressure

Figure 4.9 Possible influence of pressure on surface roughness at (a) low & (b) high pressures

The increased pressure forces the metal into the mould surface, overcoming the surface tension of the liquid metal. This may have resulted in the metal forming a profile closer to the mould surface profile, leading to an increase in the average surface roughness.

(a) 150 RPM

(b) 450 RPM

Figure 4.10 Typical cast surfaces at (a) 150 RPM and (b) 450 rpm

From Figure 4.10, it can be seen that the surface of the specimen cast at 450 RPM was considerably rougher than that of the casting spun at 150RPM. The presence of greater pressure was also confirmed by the occurrence of a large flash around the outer surface of the cylinder. However, this increased pressure did not seem to affect the surface roughness values of the castings conducted at 150 and 300RPM. Perhaps this occurred at only the highest rotational speeds (450RPM) as the pressure generated overcame the threshold of the surface tension force, pushing the metal into the small peaks and valleys on the mould surface.

The other mechanism which may cause rougher surfaces could be the increased velocity of the melt flowing over the mould surface. As the mould is rotated at higher speeds, the shear stress present at the mould wall (due to the flowing metal) will increase as a function of the square of the melt velocity. This shearing action may dislodge gypsum plaster particles at the surface leading to some loose mould material 'washing through' with the melt and leading to rougher cast surfaces. The equation below shows the relationship between shear stress present at the wall and flow velocity of a given fluid [96]:

$$\tau_0 = \frac{f\rho V^2}{8} \tag{4.34}$$

Where:

τ_0 = Shear stress at the mould wall (N/m^2)

f = friction factor

ρ = Fluid density ($kg's/m^3$)

V = Fluid velocity (m/s)

Equation (4.34) shows that the flow velocity is the dominating variable with respect to the shear stress experienced at the wall. Again however, there is no significant difference in the surface roughness between 150RPM and 300RPM, though there is considerable increase in the fluid velocity. There may be however a critical value of the shear stress, of the gypsum particles, which is overcome at higher rotational speeds above 300RPM. Figure 4.8 clearly shows that cast surface roughness was highest at 450RPM with respect to lower speeds of 150 and 300RPM.

The empirical model built based on the surface roughness values measured in the experiment is given below as equation (4.35). Figure 4.11 presents plots showing variation in surface roughness with varying factors and it can be seen that the effect of increased cavity angle results in reduction of the overall surface roughness over the tested speed range (150-450RPM). As the cavity angle increases the surface roughness reduces because of reduced melt velocity. As the fluid flows around a bend, this acts as an obstruction to flow,

reducing the fluid velocity. The sharper the angle the greater this loss becomes, resulting in a reduction in the surface roughness. The effect of the runner to cavity ratio (r/c) seems to be constant for ratios ranging from 0.8-1.2. Although changing the runner diameter should result in velocity change (as the flow rate is the product of area and velocity) this does not seem to have any effect on the surface roughness of the cast parts. However, the total variation in the r/c ratio was small and might not have had a significant effect on velocity of filling of the liquid metal, both generally and in particular on the outer layers, where surface roughness is affected.

$$Ra(X_1, X_2, X_3) = 15.7924 - 0.0436X_1 - 0.142X_2 + 1.3237X_3 + 0.0000656X_1^2 + 0.000511X_2^2 - 0.498X_3^2 + 0.0000739X_1X_2 + 0.000293X_1X_3 + 0.000344X_2X_3 \quad (4.35)$$

Where:

X_1, X_2, and X_3 are rotational speed, cavity angle and r/c, respectively

The angle and the square of the cavity angle (X_2 and X_2^2) were the most significant parameters at 73.9 and 85.5% confidence respectively (Table 4.5). For the squared cavity angle this confidence level was close to the standard level and is a near statistically significant result. The square of the speed term was meaningful with a 73.8% confidence level. The other model terms, specifically the interaction terms and linear and square runner diameter had little influence on the overall model output. These effects however may be significant at other levels outside this experiment and it cannot be assumed that these effects vary linearly.

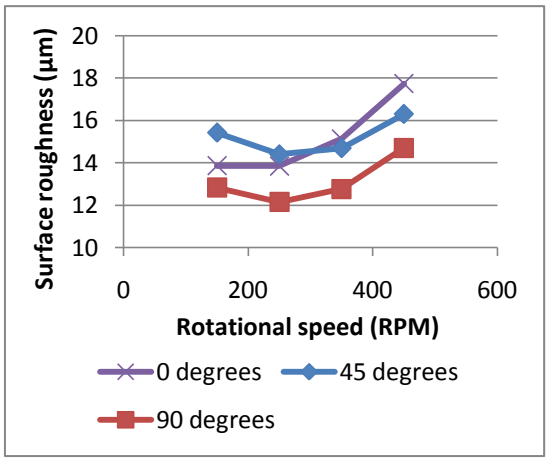

(a) 0.8:1

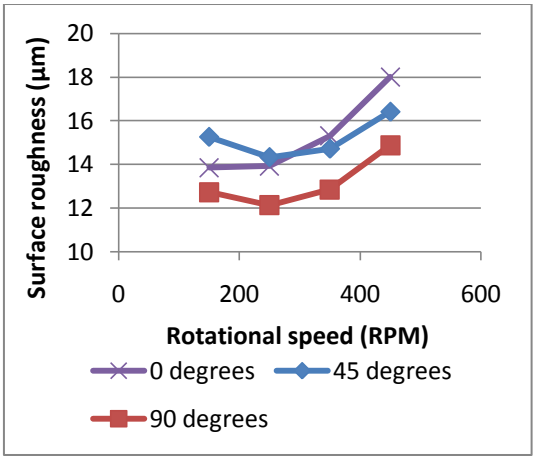

(b) 1:1

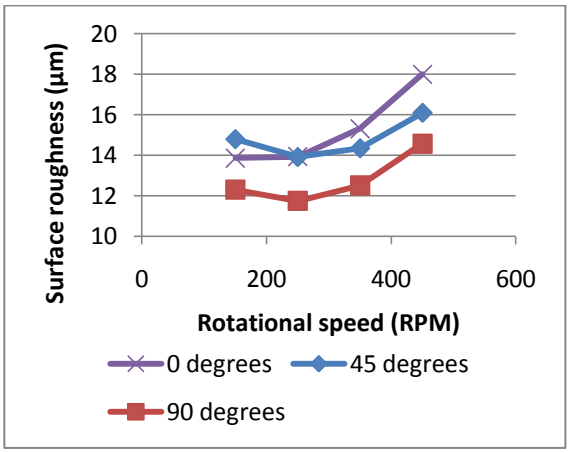

(c) 1.1:1

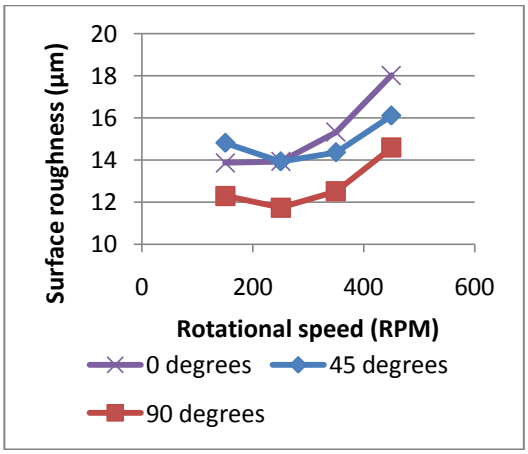

(d) 1.2:1

Figure 4.11 Graphical plots of surface roughness model results at runner-cavity (r/c) ratios of (a) 0.8:1 (b) 1:1 (c) 1.1:1 and (d) 1.2:1.

Table 4.5 Contribution and significance of individual terms for the surface response model

Term	Co-eff.	SE Co-eff.	T	P
Constant	15.7924	33.2018	0.476	0.654
Speed	-0.0436	0.0502	-0.867	0.426
Angle	-0.142	0.112	-1.268	0.261
Runner diameter	1.3237	3.7651	0.352	0.739
Speed ^{2}	0.0000656	0.0001	1.263	0.262
Angle^2	0.000511	0.0003	1.727	0.145
Runner diameter ^{2}	-0.0498	0.1142	-0.436	0.681
Speed x Angle	0.0000739	0.0001	0.685	0.524
Speed x Runner diameter	0.000292	0.0023	0.125	0.905
Angle x Runner diameter	0.000311	0.0051	0.068	0.948

Table 4.6 ANOVA table showing linear, square and interaction model effects

Source	DF	Seq SS	Adj SS	Adj MS	F	P
Regression	9	40.5064	40.5064	4.50071	0.89	0.586
Linear	3	14.3204	13.3357	4.44523	0.88	0.511
Square	3	23.7147	23.7147	7.9049	1.57	0.308
Interaction	3	2.4713	2.4713	0.82377	0.16	0.917
Residual Error	5	25.2535	25.2535	5.05069		
Lack-of-Fit	3	25.19	25.19	8.39667	264.68	0.004
Pure Error	2	0.0634	0.0634	0.03172		
Total	**14**	65.7598				

R^2 = 61.6%

The ANOVA presented above in Table 4.6 revealed no significant factors at 90% confidence or above. The ANOVA table revealed that the regression analysis conducted was not significant and only 61.6% (R^2 term) of the variation in the surface roughness was accounted for by the variation in the experimental factors, in this case rotational speed, cavity angle and runner

diameter. The square portion of the regression accounted for the largest variation, with smaller effects seen from the linear terms and especially the interaction term.

The low R^2 value was accompanied by a significant lack of fit test. This showed that at a confidence level of 99.6 %, polynomial expression was not an adequate model for the surface roughness response. The inability to fit the data highlights that the varying factors were not affecting the response in a way that a second order model could predict.

4.6.2 Yield Strength

The yield strength model developed is given in equation (4.36). The averaged yield strength results (0.2% strain), shown below in Figure 4.12, showed a slight increase at higher rotational speed. In particular, values increased 2.28MPa from 150-300RPM and 3MPa from 300-450RPM. This was a significant result as the experimental values increased with rising rotational speed. The yield strengths were however lower than those typically found in traditional sand castings (90 MPa) [55].

$$\begin{aligned}\sigma_{yield} &= 8.31601 + 0.10124X_1 + 0.201272X_2 + 6.00576X_3 \\ &+ 0.00000166667X_1^2 - 0.000989712X_2^2 - 0.130615X_3^2 \\ &+ 0.0000865497X_1X_2 - 0.0058383333X_1X_3 + 0.00171784X_2X_3\end{aligned} \quad (4.36)$$

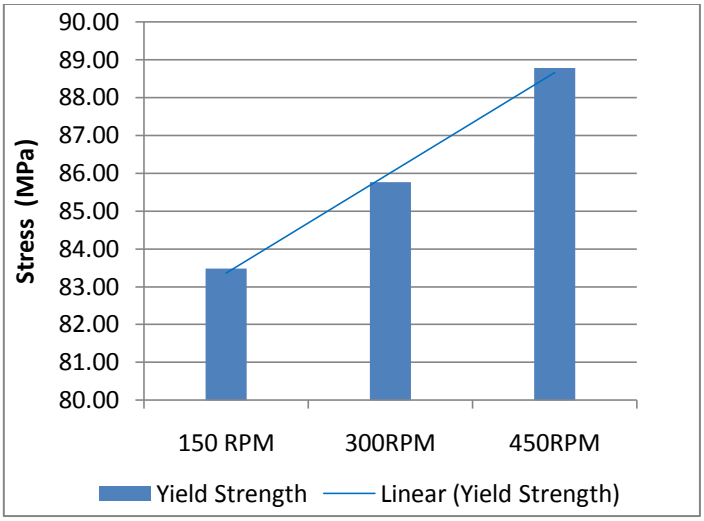

Figure 4.12 Yield strength variation with rotational speed

The reasons for these lower values were attributed to larger grain sizes and hydrogen porosity of the cast Al. In particular, the cooling rate of Plaster (ZP131) moulds with their characteristic poor thermal conductivity, result in grain growth and coarse grain structures at lower speeds. Further, the dendrite cell size and spacing are linked with the yield strength through the Hall-Pitch equation. Increases in grain size and DAS, thus decrease yield strength of the cast parts.

For grain sizes to be decreased, and yield strength enhanced, increased pressures during filling are necessary as this forces the metal against the mould walls, achieving greater surface area of contact. This increases the rate of heat transfer, resulting in a decrease in the solidification time and giving slightly smaller dendrites. Also the eutectic structure is refined by the increase in the cooling rate and this results in a change in morphology of these particles, resulting in a more fibrous eutectic [88]. Figure 4.13 below shows the differences in the dendritic and eutectic phases in static and centrifugally cast A356 alloy. The static casting photomicrograph shows coarser grain growth, whilst the centrifugally cast specimen shows a more refined structure.

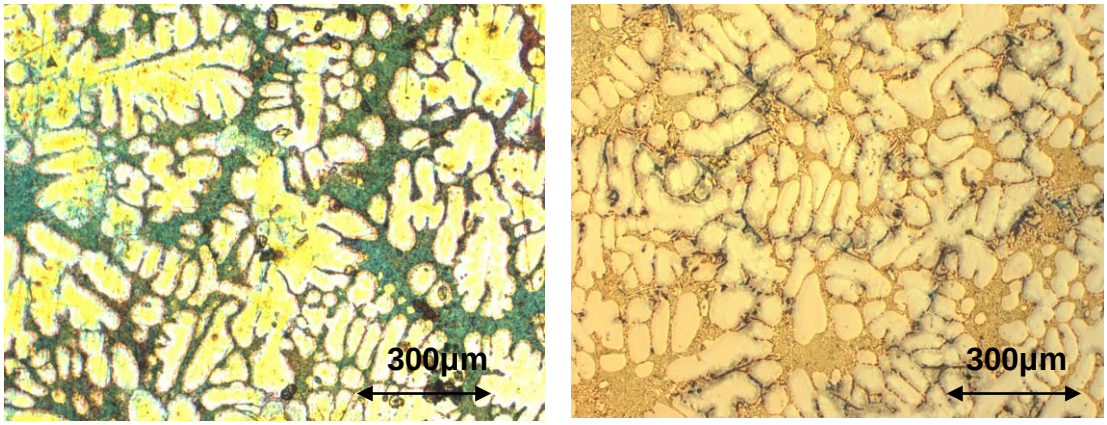

(a) Static ZP131 casting **(b) Centrifugal ZP131 casting**

Figure 4.13 Comparison between (a) Static casting and (b) Centrifugal castings produced in ZP131 plaster moulds (both X50)

The other possible reason for increase in yield strength at higher speeds was increased pressure filling of the mould cavity. As highlighted in section 3.6.4, Fe intermetallics influence the solidifying structure of Al castings, which has a detrimental effect on cast strength. In static casting, these intermetallics block the liquid eutectic mixture being fed through the dendrite network, resulting in poor formation of dendrite cells and random placement of these particles [98]. Feeding has also been found to be drastically reduced when Fe intermetallics are longer than a critical value [98]. In addition, the β phase Fe intermetallics have severe effects on feeding ability and can often lead to porosity formation. These β type partials were observed in the CC in the current work.

Perhaps under increased pressure at higher rotational speeds, the eutectic liquid was able to be forced through the dendrite network more effectively, resulting in fewer defects and a more sound grain structure, with little shrinkage and fewer discontinuities. However, the presence of large porosities due to hydrogen in the melt leads to below average yield and UTS compared to traditional sand casting.

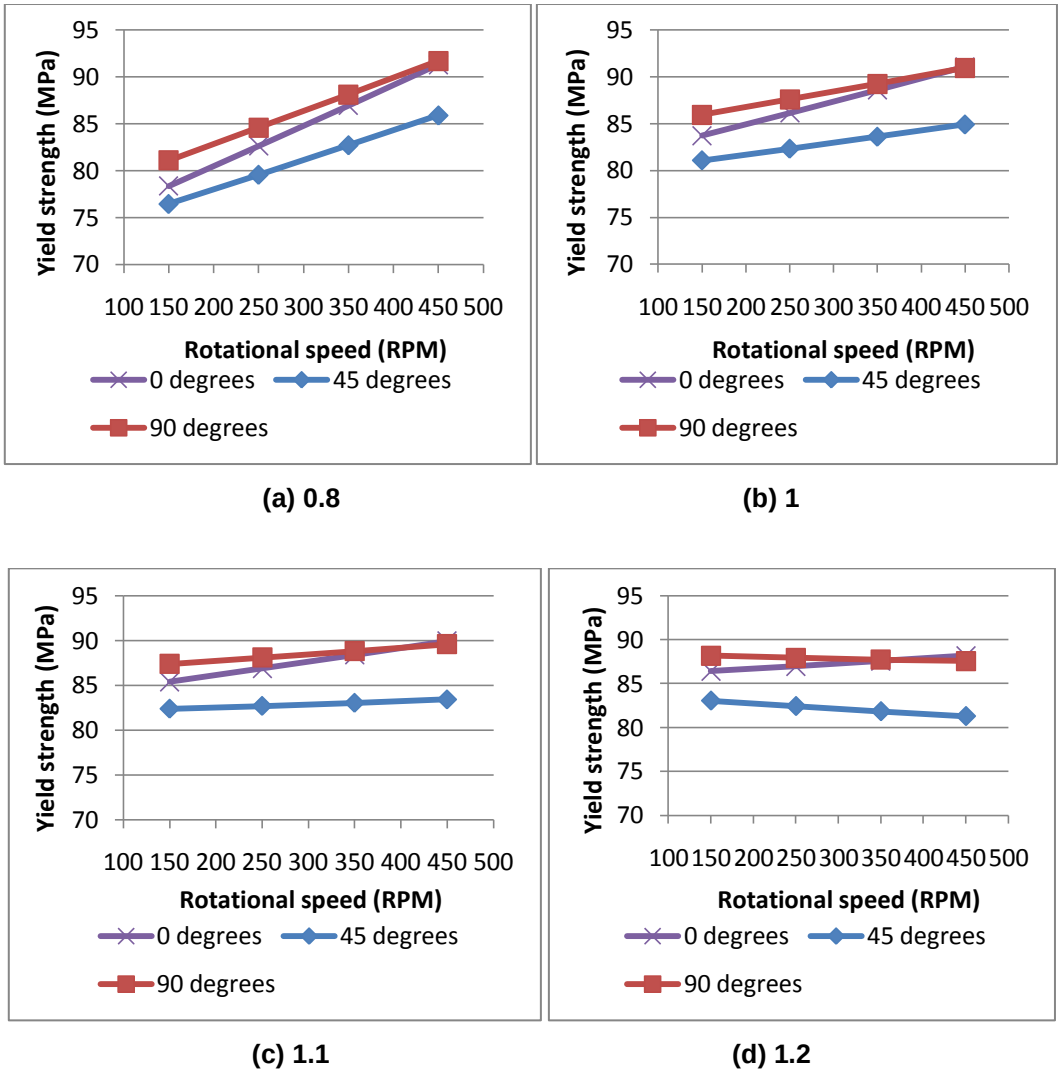

Figure 4.14 The Graphical plots of yield strength model at r/c ratios of (a) 0.8 (b) 1 (c) 1.1 and (d) 1.2

From the plots of Figure 4.14 clear trends were observed with respect to rotational speed, cavity angle and runner-cavity diameter ratio. Firstly, the rotational speed had a positive linear effect on the yield strength over the entire speed range at each cavity angle, for r/c ratios ranging from 0.8-1.1. For r/c ratio of 1.2 however, yield strength was seen to plateau and then decrease with respect to all three cavity angels. Secondly, increasing cavity angle resulted in increased yield strength, with 45° and 90° angles giving the lowest and highest values of yield strength respectively, with the 0° angle between these two results.

Table 4.7 Breakdown of model parameters in the yield strength model

Term	Co-eff.	SE Co-eff.	T	P
Constant	8.31601	93.4441	0.089	0.933
Speed	0.101237	0.1414	0.716	0.506
Angle	0.201272	0.3151	0.639	0.551
Runner diameter	6.00576	10.5966	0.567	0.595
Speed ^{2}	1.66667E-06	0.0001	0.011	0.991
Angle^2	-0.00098712	0.0008	-1.188	0.288
Runner diameter ^{2}	-0.130615	0.3215	-0.406	0.701
Speed x Angle	0.0000865497	0.0003	0.285	0.787
Speed x Runner diameter	-0.00583333	0.0066	-0.885	0.417
Angle x Runner diameter	0.00171784	0.0143	0.121	0.909

With respect to the individual model parameters, no statistical significance, was observed

Table 4.7. The square of the cavity angle however was contributing more than any of other terms, at a confidence level of 71.2%. There was little effect from the other factors and small interaction effects highlighted the lack of any importance of factors undergoing simultaneous change.

Table 4.8 ANOVA table of the yield strength model response

Source	DF	Seq SS	Adj SS	Adj MS	F	P
Regression	9	178.67	178.67	19.85	0.5	0.830
Linear	3	82.4	39.3	13.1	0.33	0.806
Square	3	61.09	61.09	20.36	0.51	0.693
Interaction	3	35.18	35.18	11.73	0.29	0.829
Residual Error	5	200.03	200.03	40.01		
Lack-of-Fit	3	97.05	97.05	32.35	0.63	0.662
Pure Error	2	102.98	102.98	51.49		
Total	**14**	378.71				

R^2 = 47.18%

The ANOVA presented in Table 4.8 showed no significant relationships between yield strength and the linear, square and interaction effects of the model. The square terms however accounted for more variance than linear and interaction portions. The R^2 value was 47.18%, meaning, that over half of the variation in the results was not accounted for by the model effects. Despite this there was no significant lack of fit and the model was adequate in fitting the yield strength data. The regression itself was not significant as the overall residual sum of squares (SS) (values that cannot be accounted for) was relatively large (200.03) compared to the total SS (378.71). These low confidence values may indicate a large standard deviation. This leads to the conclusion that other significant variables may be involved to explain the variance, such as porosity level.

4.6.3 Ultimate Tensile Strength (UTS)

From the averaged results shown in Figure 4.8c, there was an increase in the UTS over the speed range. The tested UTS values ranged from 90.5-145.8MPa for non-degassed CC601 alloy. The averaged values showed a 16MPa increase from 150RPM to 300RPM and a 12MPa increase from 150 to 450RPM. The middle speed setting gave the highest average UTS values with an average of 116MPa. Although there was a slight decrease in the average strength from 300-450RPM, the overall linear trend was positive with respect to rotational speed. The results from the analytical model in section 4.3.2 indicate that these higher rotational speeds result in relatively higher pressures, up to 300mmAl. Simple T-tests conducted between the different speeds are shown below in Table 4.9, clearly indicating that the increases in UTS at each speed were statistically significant.

Table 4.9 Results of T-Tests conducted between each speed range.

T-Test	Confidence level from T-Test
150 and 300 RPM	97%
150 and 450 RPM	86%
300 and 450 RPM	52%

High confidence intervals were established between 150 and 300 and 150 and 450RPM in relation to the statistical difference of their averages (Table 4.9). A statistically significant result is seen when comparing speed at 300RPM with a near statistically significant result at 450RPM. (Note: the importance of these results should not be confused with the ANOVA model which takes into account linear, square and interaction effects contributing to the overall model variance).

When compared to values achieved from the static castings, much more variability in the UTS of the CC cast specimens was observed. Both the lowest and highest UTS values were achieved in the CC process, indicating considerable process influence on the final cast strength.

The UTS values relied greatly on the size and distribution of the porosity, due to the dissolved hydrogen in the melt. Due to restrictions in the casting setup used, degassing of the molten metal was unable to be incorporated, leading to high levels of hydrogen in the molten metal. When examining the tensile specimens, large pores were observed but these sizes were seen to reduce when rotational speed was increased to 300 and 450RPM respectively.

The size and distribution of these pores were dominant in reducing the strength of these cast samples. Lesser effects such as particle inclusion and oxide entrapment do provide an effect by reducing the strength developed in the microstructure (hydrogen porosity was covered in section 3.6.4). It was suspected that correct melt treatment (degassing) before pouring would yield significant improvements in cast strength. To confirm this, a final CC was conducted at 235RPM at AUT University using a modified setup, with samples angled at 0 and 45°respectively. The melt was lance degassed with Nitrogen for three minutes before pouring and the tensile properties are listed below (refer to 4.8.2 for methodology).

Table 4.10 Tensile properties of centrifugally cast degassed specimens

Sample	UTS (MPa)	Yield Strength (0.2% offset)	% elongation
0°	154	118.5	2.03
45°	151.4	121.1	1.95

This result shown above in Table 4.10 was *very* significant as large improvements in yield and UTS values resulted. It is noted that lance degassing is not very efficient at removing the dissolved hydrogen when compared with other degassing methods, such as rotary degassing [99]. Despite this, the highest tensile strength values were achieved with the degassed samples. Further, the rotational speed was not as high as previously used (Centracast trials).

For the Centracast trials, (un-degassed), the model developed for the UTS is given in equation (4.37). The plots of the UTS in Figure 4.15, showed that all three variables had an influence on UTS values. The overall trend was an initial increase of strength from 150RPM to about 250-350RPM, followed by a slight decrease up to the maximum speed, 450RPM. Again, the effect of increasing cavity angle resulted in the raising of the strength values from angle change 45° to 90°. The 0° angle however resulted in generally lower strengths obtained at higher speeds ranging from 350-450RPM.

$$\sigma_{UTS} = -184.070 + 0.310348X_1 + 0.519288X_2 + 27.9396X_3$$
$$-0.00047768X_1^2 - 0.00150283X_2^2 - 0.865275X_3^2$$
$$-0.000428265X_1X_2 + 0.00359375X_1X_3 - 0.00471491X_2X_3 \quad (4.37)$$

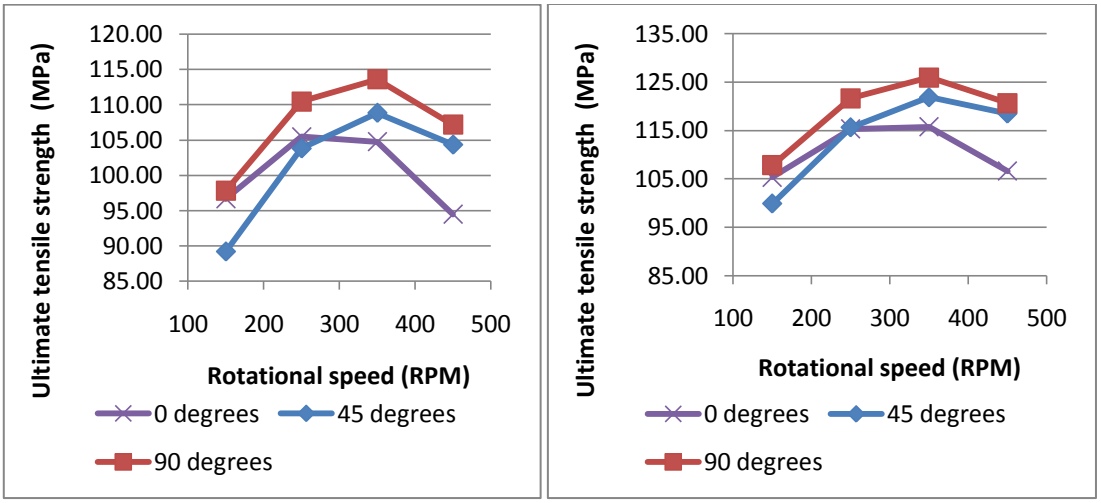

(a) 0.8:1 **(b) 1:1**

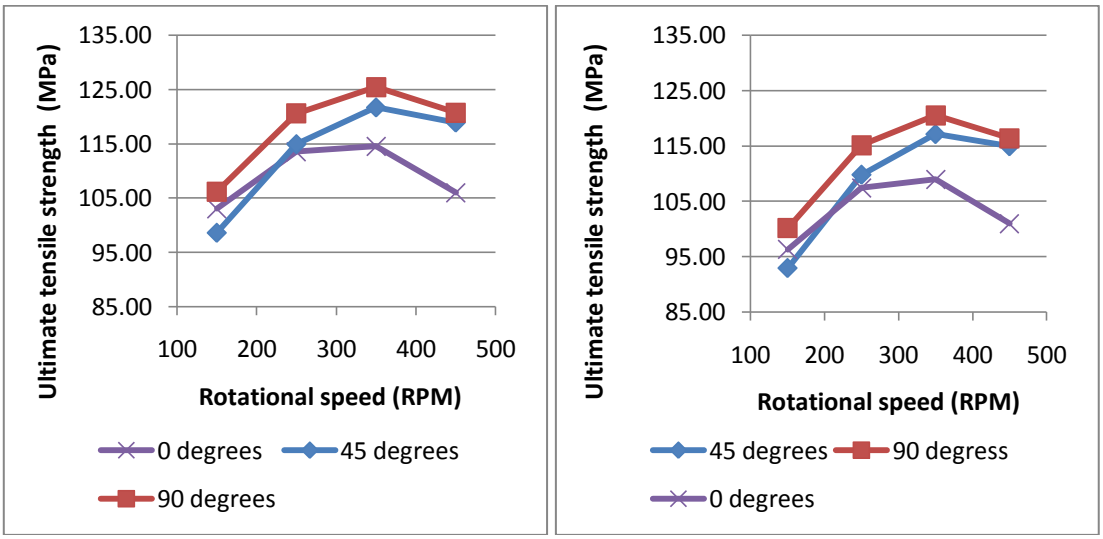

(c) 1.1:1 **(d) 1.2:1**

Figure 4.15 The Graphical plots of Ultimate Tensile strength model at r/c ratios of (a) 0.8:1 (b) 1:1 (c) 1.1:1 and (d) 1.2:1.

A decrease in UTS was observed at high rotational speeds when compared to the average value obtained at 300RPM. Although this suggests improved properties at 300RPM, this result was somewhat skewed by a large strength value in trial 15 (Table 4.4) at 300RPM, which gave UTS of 144.55 MPa. If this result was excluded, the average UTS at 300RPM and 450RPM become similar. To illustrate this, Figure 4.16 shows the average UTS values with trial 15 excluded.

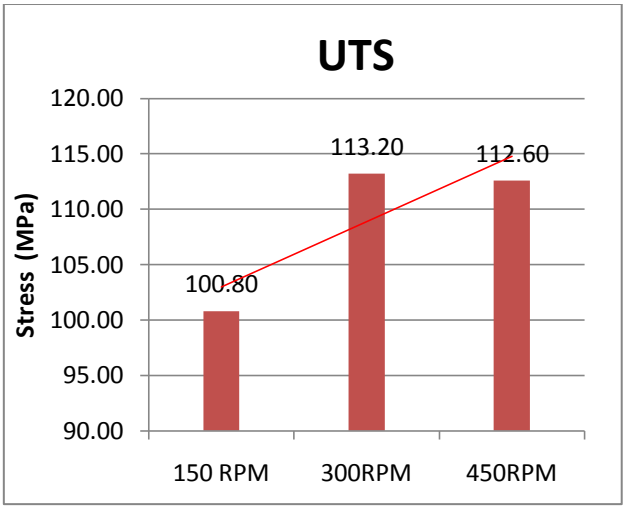

Figure 4.16 UTS values of specimens ignoring results of trial 15

Table 4.11 Contribution of individual model parameters in the UTS model

Term	Co-eff.	SE Co-eff.	T	P
Constant	-184.07	215.499	-0.854	0.432
Speed	0.310348	0.326	0.952	0.385
Angle	0.519288	0.727	0.715	0.507
Runner diameter	27.9396	24.438	1.143	0.305
Speed ^{2}	-0.00047768	0	-1.416	0.216
Angle^2	-0.00150823	0.002	-0.785	0.468
Runner diameter ^{2}	-0.865275	0.741	-1.167	0.296
Speed x Angle	-0.000428265	0.001	-0.611	0.568
Speed x Runner diameter	0.00359375	0.015	0.237	0.822
Angle x Runner diameter	-0.00471491	0.033	-0.143	0.892

With respect to Table 4.11, there were no statistically significant co-efficients found for equation (4.38) but some medium level confidence values were obtained, with the square of the rotational speed giving a 78.4% confidence level. Also, linear and square terms of the r/c ratio were confident at 69.5% and 70.4%, respectively. Lower confidence levels were observed for all interaction effects, together with linear speed and cavity angle parameters.

Table 4.12 ANOVA of the UTS model response

Source	DF	Seq SS	Adj SS	Adj MS	F	P
Regression	9	1203.29	1203.29	133.7	0.63	0.744
Linear	3	362.71	453.92	151.31	0.71	0.586
Square	3	744.91	744.91	248.3	1.17	0.409
Interaction	3	95.67	95.67	31.89	0.15	0.925
Residual Error	5	1063.87	1063.87	212.77		
Lack-of-Fit	3	431.27	431.27	143.76	0.45	0.742
Pure Error	2	632.6	632.6	316.3		
Total	**14**	2267.16				

R^2 = 53.07%

The variance analysis shown in Table 4.12 also showed no statistically significant linear square or interaction effects (P value <0.1). The square portion of the model accounted for slightly more variation than the linear model, with a very insignificant interaction effect. The sum of squares (SS) of the linear portion for example was 362.71 and with the addition of the square effects this increased to 744.91.

The overall regression model was only able to account for 53.07% of the total variation in the experiment, leaving a large experimental residual term. Nevertheless, no statistically significant lack of fit of the model was found, showing that the chosen model was able to fit the data points. This highlights that the large residual term must be due to the absence of some other influencing factor. It has already been suggested that this may be hydrogen porosity.

When conducting simple T-Test on the difference of the averages of un-degassed (Centracast) specimens at 300RPM and the degassed specimens (AUT University) at 235RPM a significance of 98.2% was observed, confirming the effect of degassing was *very considerable* on the overall UTS results.

4.6.4 Percent Elongation

The overall elongation values shown below in Figure 4.8c, were low and this is due to characteristic brittle fracture. The elongation values ranged from 0.43-2.44%, with typically larger values linked to specimens with high UTS values. The porosity present affected the ductility of the material as these voids created stress concentrations, which led to premature fracture. Also, the slower cooling rate might increased grain growth, leading to slightly coarser dendrite and eutectic structures which provide less resistance to grain boundary sliding.

Over the tested speed ranges, increases in ductility were observed with a notable increase at the 300RPM speed. Interestingly, there was only a minor difference of 0.06% strain between the samples tested at 150RPM and 450RPM, despite there being a 12MPa difference in UTS. At 300RPM the elongation was increased to an overall average of 1.56%, considerably higher than at the other two speed levels. Disregarding trial 15, which gave high tensile test results, the average elongation was still 1.43%. When a T-Test was conducted on the average elongation values over the tested speeds there was no significance between 150RPM and 450RPM. However, significant confidence levels of 94.8 and 91.8% were found at 300RPM as against 150 and 450RPM respectively.

$$\begin{aligned}\delta &= 8.31610 + 0.101237X_1 + 0.201272X_2 + 6.00576X_3 \\ &0.0000016X_1^2 - 0.00098712X_2^2 - 0.130615X_3^2 \\ &0.0000865X_1X_2 - 0.005833X_1X_3 + 0.00171784X_2X_3\end{aligned} \tag{4.38}$$

The elongation model was similar to that of the UTS model in terms of the overall relationships and trends. The elongation values tended to increase over the speed of 150-350RPM but decreased at higher rotational speeds from about 350-450RPM. For increasing r/c ratios, all elongation values at both the 45 and 90° angles increased initially from 150-350RPM, reached a maximum at about 350RPM and then dropped but to values above those at the 150RPM speed. The 0° angle at these higher r/c ratios tended to plateau

at lower speeds of about 250RPM and then proceeded to fall over speeds of 250-450RPM. At r/c ratios of 1 and 1.1, elongation values at the 0° angle dropped below those found at 150RPM.

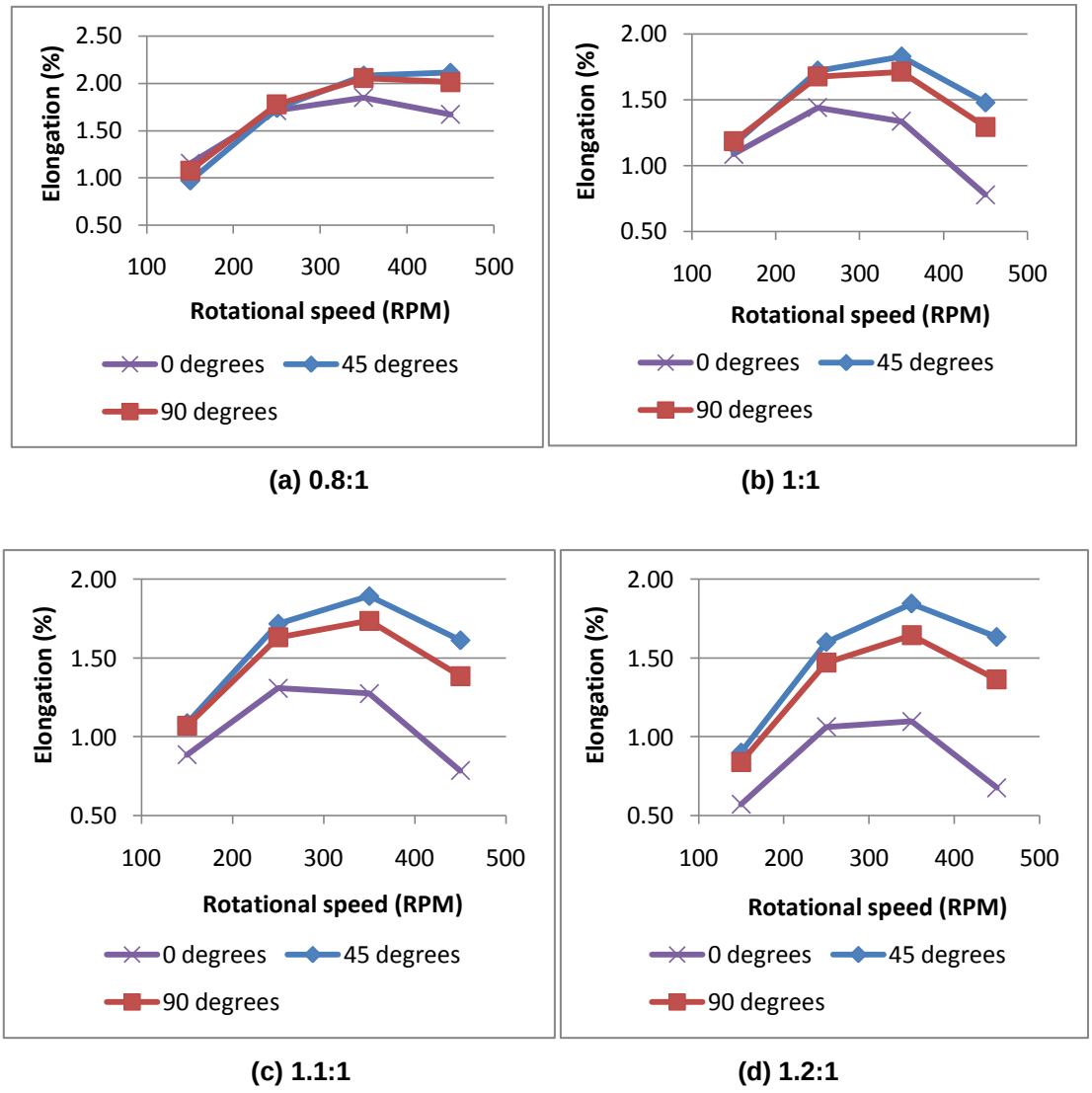

Figure 4.17 Individual plots of rotational speed and cavity angle with respect to the percent elongation model at r/c ratios of (a) 0.8:1 (b) 1:1 (c) 1.1:1 and (d)1.2:1.

Table 4.13 Significance of the individual model parameters in the percent elongation model

Term	Co-eff.	SE Co-eff.	T	P
Constant	-5.58457	6.29297	-0.887	0.415
Speed	0.00855246	0.00952	0.898	0.41
Angle	0.0140219	0.02122	0.661	0.538
Runner diameter	0.656933	0.71363	0.921	0.4
Speed ^{2}	-0.0000227889	0.00001	-2.313	0.069
Angle^2	0.0000121399	0.00006	-0.216	0.837
Runner diameter ^{2}	-0.0220459	0.02165	-1.018	0.355
Speed x Angle	-0.0000154893	0.00002	-0.757	0.483
Speed x Runner diameter	0.000430208	0.00044	0.97	0.377
Angle x Runner diameter	0.000593933	0.00096	-0.619	0.563

The parameters in the model percent elongation expression (equation 4.38) shown in Table 4.13, showed a statistically significant effect from the square value speed term. This gave a 93.1% confidence level, which is statistically significant. The other model parameters had relatively low confidence levels, mostly in the range of 50-65% confidence.

Table 4.14 ANOVA of the various effects present in the percent elongation model.

Source	DF	Seq SS	Adj SS	Adj MS	F	P
Regression	9	1.7962	1.7962	0.19958	1.1	0.484
Linear	3	0.3526	0.2964	0.09879	0.54	0.673
Square	3	1.0997	1.0997	0.36657	2.02	0.23
Interaction	3	0.3439	0.3439	0.11464	0.63	0.626
Residual Error	5	0.9072	0.9072	0.18144		
Lack-of-Fit	3	0.371	0.371	0.12368	0.46	0.738
Pure Error	2	0.5362	0.5362	0.26809		
Total	**14**	2.7034				

R^2 = 66.44%

The ANOVA presented in Table 4.14 contained no significant linear, square or interaction terms, though the addition of the square effects term did yield the highest confidence level of 77%. The elongation model was the most accurate model with a R^2 value of 66.44%. This meant that two thirds of the total experimental variation was accounted for by the regression analysis. There was no significant lack of fit of the model. Nevertheless, the chosen factors did not account for enough variation for the regression to be significant. The sensitivity of the elongation values to the random distribution of the pores present in the casting was a likely contributor to the unexplained variance present in the results.

4.7 Macro and Micro Structural Examination

4.7.1 Macrostructures

The macrostructures of CC showed severe gas porosity throughout the cross-sections of the samples. These pores were often distributed over the cross-sectional area, indicating that these were not shrinkage pores but more likely hydrogen gas entrapped by solidifying dendrites. The pore morphology in Figure 4.18 shows the effect of higher rotational speeds on pore size.

The beneficial effect of higher rotational speeds also reduced the size and distribution of these voids as increased pressures reduced pore size. The mechanism for this centres on the initial and final volumes of a bubble due to pressure change. By using Boyle's law the change in size of the bubble can be determined, i.e.:

Final bubble volume

$$v_2 = v_1\left(\frac{P_1}{P_2}\right) \tag{4.49}$$

Where:

v = Volume (kg/m^3)

P = Pressure (Pa)

(*Subscripts 1 and 2 denote initial and final conditions)

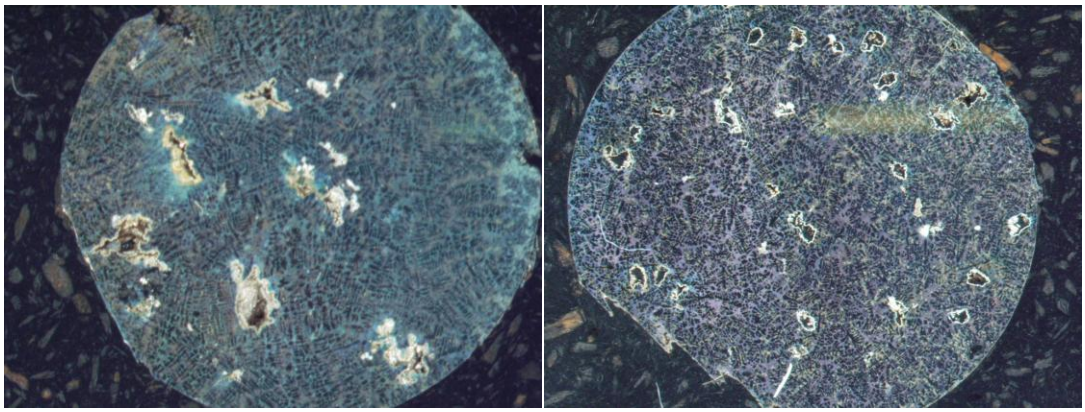

(a) 150RPM **(b) 300RPM**

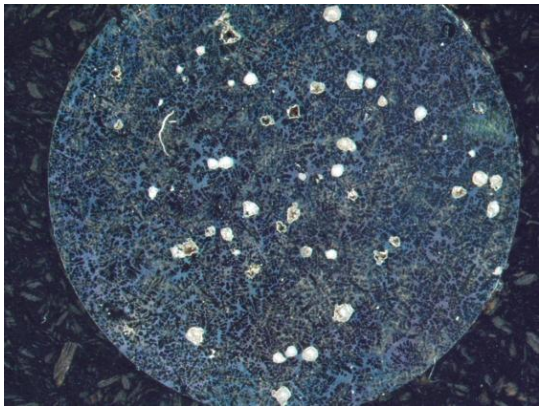

(c) 450RPM

Figure 4.18 Macrostructures of cast specimens at (a) 150 (b) 300 and (c) 450 RPM

From equation (4.49), increasing fluid pressure will result in the reduction of the final volume of the gas pore. With respect to Figure 4.18, larger and fewer pores were seen at 150RPM, whereas at 300 and 450RPM much smaller and evenly distributed pores were observed. The analytical model presented in section 4.3.1 shows that these higher rotational speeds correlate to increased pressures ranging from 150-300mmAl, as opposed to pressures of 135-150mmAl at 150RPM.

The shape of these pores was also significant and generally these pores were round, which is a characteristic of pores resulting from hydrogen porosity [100]. The round pores seen in the macrostructures, particularly at speeds of 300RPM and 450RPM form by precipitating in the liquid metal at the start of solidification [100]. This results in unrestricted bubble growth and is characterised by Al containing high levels of hydrogen [100]. It seems reasonable to conclude that the size and distribution of these pores formed during CC were reduced by higher pressures present in the molten metal and that this correlates to improved tensile properties at higher rotational speeds.

4.7.2 Microstructures

The as-cast microstructures presented in Figure 4.19a-e show typical dendrite and eutectic phases expected with Al casting alloys containing 7% Silicon (Si). Other inclusions, such as oxide skins and Fe intermetallics s also observed in the samples. On average there was a slight decrease in the dendrite grain size shown in Figure 4.8b when rotational speeds were increased from 150 to 450RPM. The average grain number at 150, 300 and 450 RPM were found to be 2.38, 2.57 and 2.46 (ASTM grain number) respectively. The lowest grain size was achieved at 300RPM, which also correlates to the highest average UTS.

The overall microstructures did not show any unusual or modified phases, indicating that the only other possible influence on mechanical properties outside of the model was due to porosity. Previous researchers [91, 92, 101] have deduced links between porosity defects and tensile properties, with their results highlighting significant decreases in strength and ductility as the level of porosity increases.

However, in the current work there was also a link between solidification time and the total porosity present in the sample. The cooling rate increases slightly with rotational speed and this reduces pore size as the dendrites restrict hydrogen mobility [76]. Research has shown that at a specific hydrogen content, the increase in cooling rate decreases both the average

pore size and the total amount of porosity present in A356 alloys [89]. Other work showed that volume percent of porosity does not define the mechanical properties in itself, rather it is the maximum pore lengths and areas which correlate to the tensile properties [102].

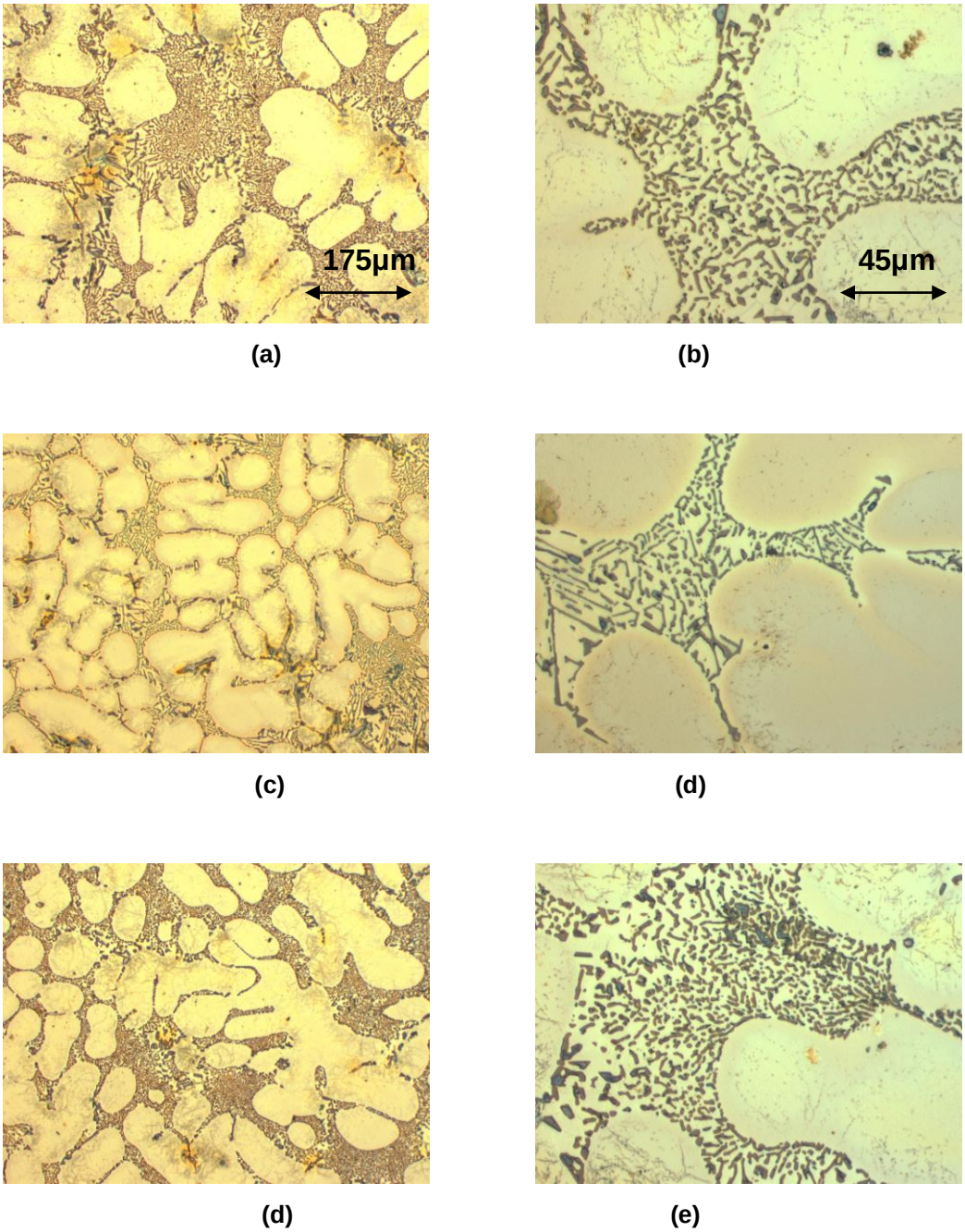

Figure 4.19 Microstructures of centrifugal castings, spun at 150RPM at X100 and X400 magnifications respectively (all) for (a & b) Trial 1 – 45°, 1:1 runner ratio (c & d) Trial 7 – 90°, 1.2:1 runner ratio and (d & e) Trial 3 – 180°, 1:1 runner ratio.

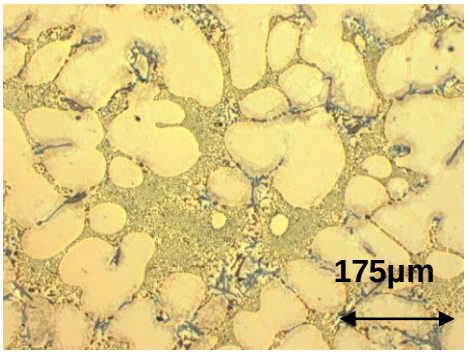

(a)

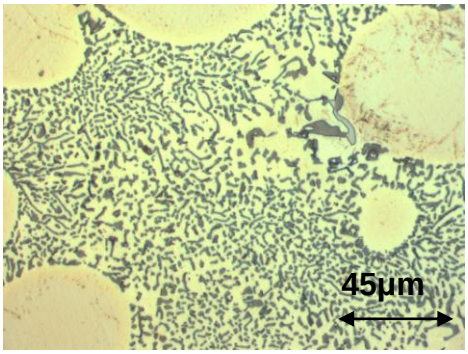

(b)

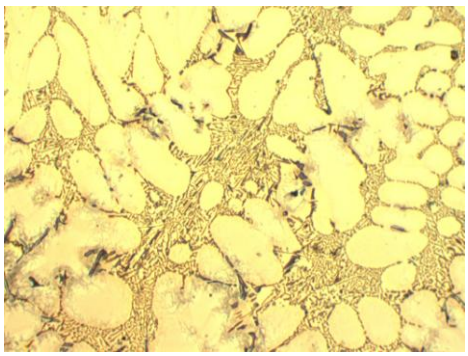

(c)

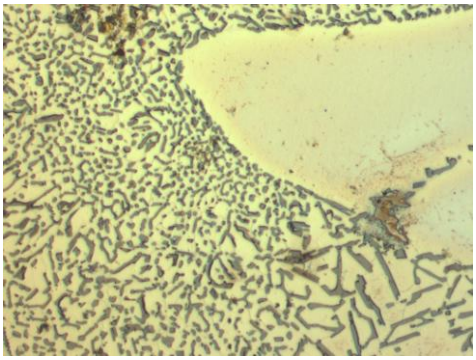

(d)

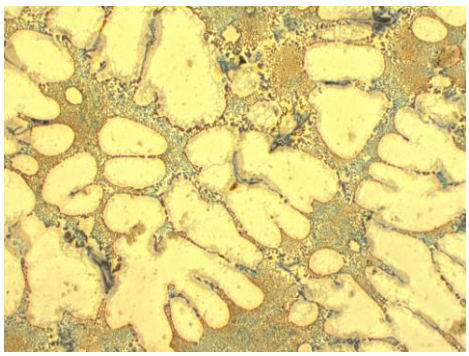

(d)

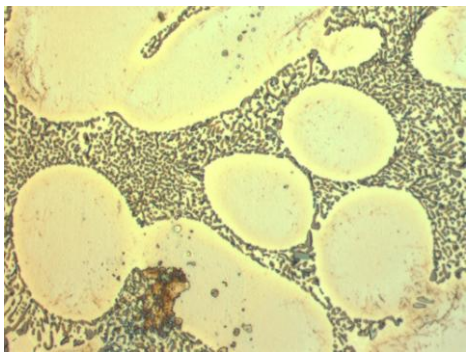

(e)

Figure 4.20 Microstructures of castings spun at 300RPM at conditions (a & b) Trial 11 – 45°, 1.2:1 runner ratio (c & d) Trial 15 – 90°, 1:1 runner ratio and (d & e) Trial 12 – 90°, 1:1 runner ratio.

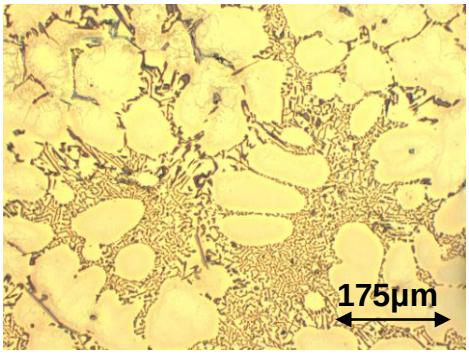

(a)

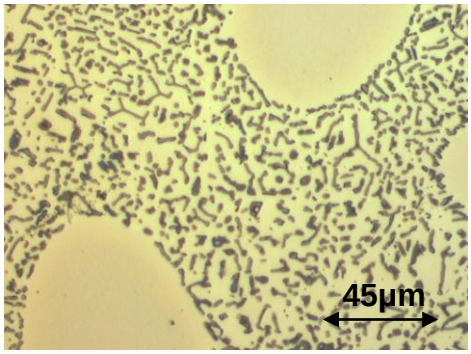

(b)

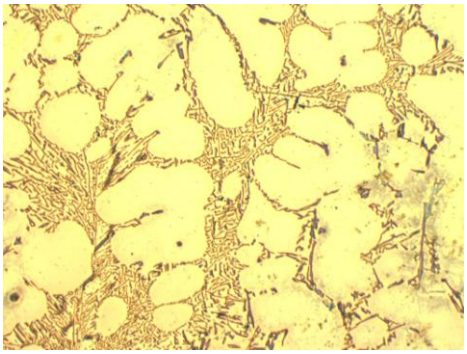

(c)

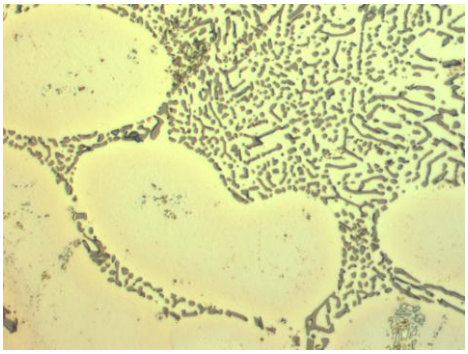

(d)

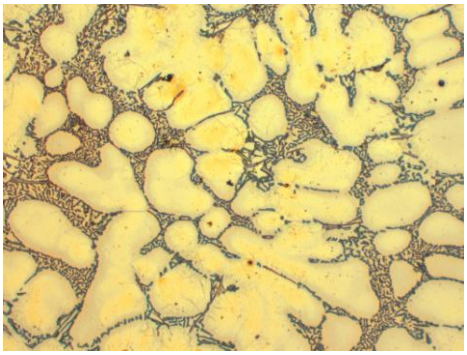

(d)

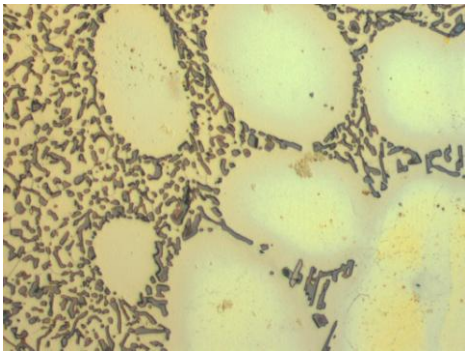

(e)

Figure 4.21 The Microstructures of castings spun at 450RPM at conditions (a & b) Trial 2 – 45°, 1:1 runner ratio (c & d) Trial 8 – 90°, 1.2:1 runner ratio and (d & e) Trial 4 – 180°, 1:1 runner ratio.

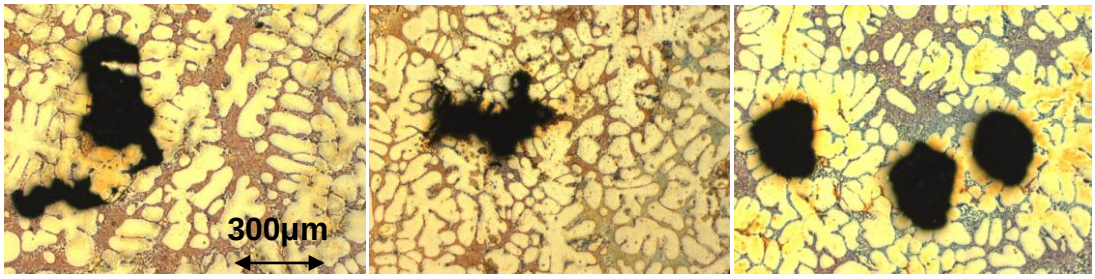

Figure 4.22 Microporosity present at the three different rotational speeds, namely (a) 150RPM (b) 300RPM and (c) 450RPM

Microporosity featured throughout the castings at different rotational speeds and these are shown in Figure 4.22. Microporosity weakens the microstructure, as noted above, and the presence of entrapped oxides also influences the strengths of Al-Si castings alloys. Significant research by Campbell [103-105] on the role of entrapped oxides during casting has led to the discovery of double oxide films (bifilms). The inclusion of bifilms in the cast structure is influential in the development of strength, as it creates locations from which cracks can propagate. Bifilms are entrained into the casting by the action of pouring, which then folds the surface film, creating two adjacent faces which do not bond together [105]. The good thermal stability of oxides is a problem in metal casting as they stay suspended in the molten metal for extended periods of time. Further, oxides are capable of unfolding themselves, resulting in a major crack in the cast microstructure. The centrifugal action itself expected to move these particles towards the axis of rotation, moving the heavier particles to the outer radius of the mould cavity. However, a large presence of oxides was still observed, resulting in a weakening of the test samples. Also, the longer cooling times associated with casting into plaster moulds may have resulted in more unravelling or unfurling of these oxide files [106]. Shown below in Figure 4.23 were several examples of entrained oxide films observed from the photomicrographs of the current investigation, which resulted in a thin planar cavity, facilitating crack initiation.

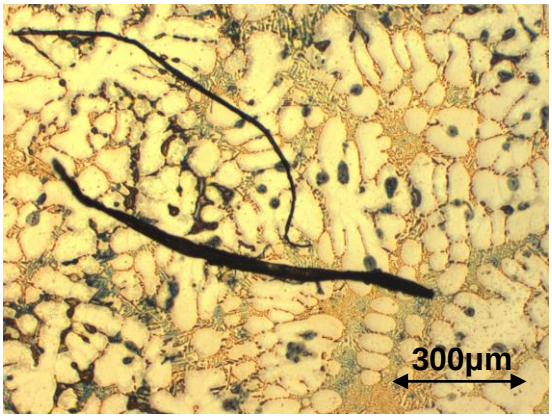

(a)

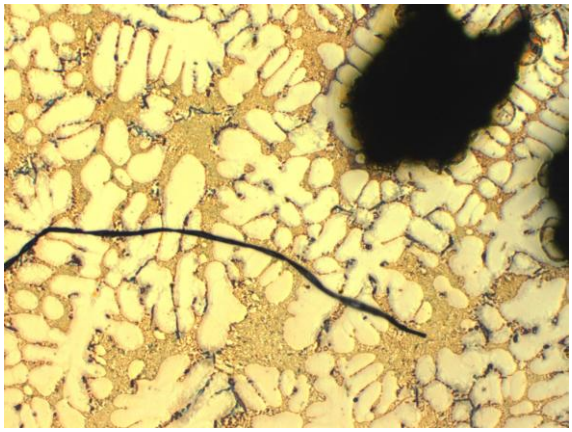

(b)

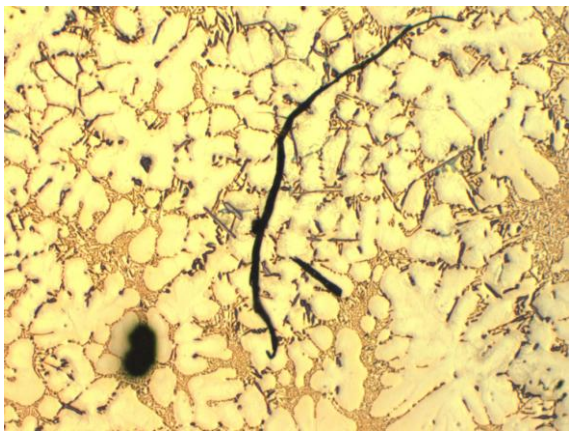

(c)

Figure 4.23 Photomicrographs of entrained oxide films in castings conducted at (a) 150RPM (b) 300RPM and (c) 450RPM (all X50 magnification)

The presence of these oxides was probably due to several reasons. The melting procedure firstly resulted in the formation of a surface layer of oxide, which in the current setup was difficult to remove. This led to oxides entering the mould. However, further issues result from large uncontrolled fall height,

shown below in Figure 4.24, which resulted in some initial oxides being entrained into the casting. This fall height however was unavoidable, due to the setup of the Centracast CC machine. Lastly, there was no filter used to remove any entrained films, resulting in these defects being carried through and subsequently trapped in the solidifying structure. To reduce the presence of these entrained films, future trials should be conducted with improved melting practices to reduce oxide formation. The use of filters specifically needs to be incorporated, not only to remove oxide films but other non-metallic inclusions.

Figure 4.24 Die and machine setup, with fall height depicted

4.7.3 Fractography of Centrifugal Castings

When evaluating the fractured specimens, it was evident that the presence of porosity was dominant on all of the fractured surfaces, indicating that failure initiated from these voids. The fracture surfaces[15] showed both regions of brittle and ductile fracture, with typical dimple fracture characterising the ductile failures and smooth featureless surfaces characterising the brittle fractures. The mechanism for fracture during tensile testing often originates from particle inclusions or from eutectic silicon particles [66]. The large

[15] Refer to Appendix B.3

presence of porosity throughout the samples resulted in the initiation of fracture at these defects. The created voids are localised areas of intense stress, with stress levels reaching up to five times greater than that of the Al-Si Matrix [107]. Further, the level of stress intensity is greater for voids located at the outer surface of the test sample. This surface porosity causes the initial fracture from which cracks would propagate and link with other internal pores in the sample. These stress concentrations affect both the primary Al dendrites but more importantly the eutectic Si, which is a much more brittle phase [107].

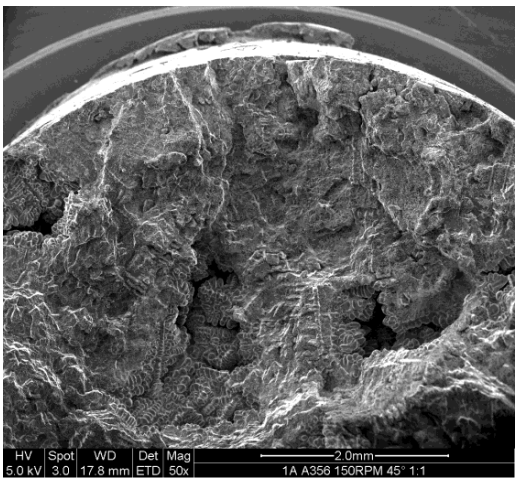

(a) 150RPM

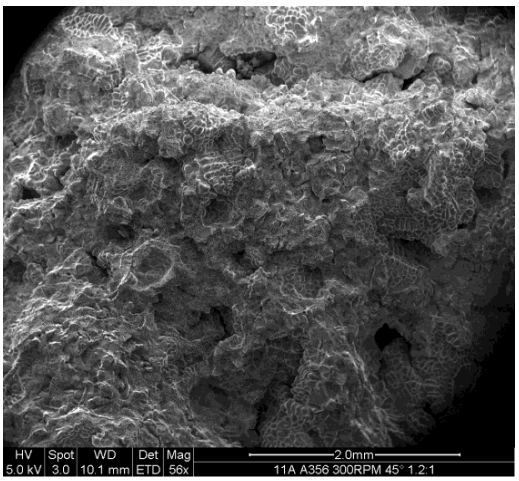

(b) 300RPM

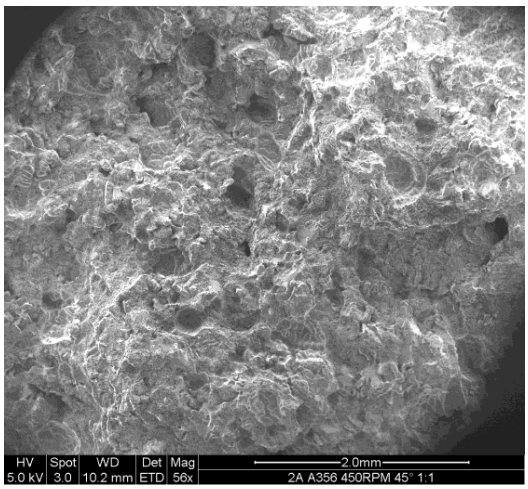

(c) 450RPM

Figure 4.25 SEM photographs of the fractured surface at (a) 150 (b) 300 and (c) 450RPM.

Evidence of porosity and other defects on the fractured surfaces was found across all tested samples. Presence of the distribution of these pores was evident from the results of the macrostructures, although SEM allowed more vivid and detailed photographs of this phenomenon. The comparison between samples cast at 150RPM, 300RPM and 450RPM is shown in Figure 4.25. Evidence of oxide films was also present on the fractured surfaces and Figure 4.26 below shows a large film present on the surface of the tensile specimen.

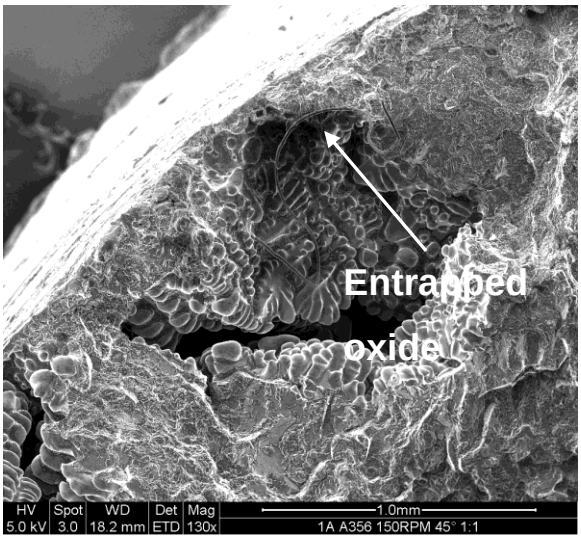

(a)

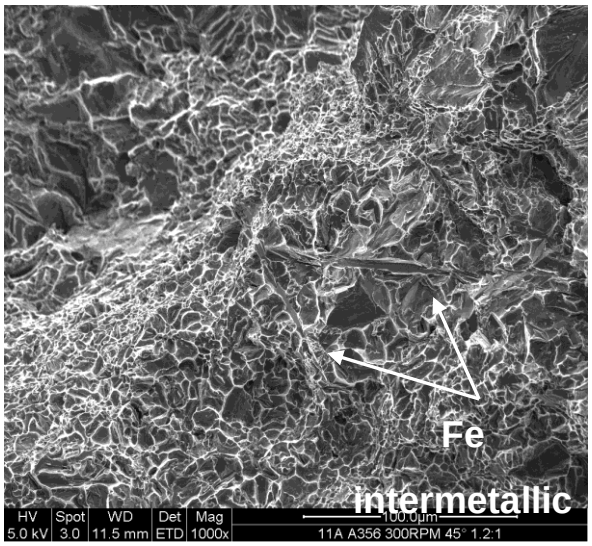

(b)

Figure 4.26 SEM photographs showing (a) long oxide film and (b) Fe-intermetallic particle

4.8 Further Centrifugal Casting

Most of the CC trials were conducted with Al alloys, as the current setup and resources were not suitable to process Mg in this CC machine. Several attempts were made at melting the Mg at Centracast, with gas fired torches used to heat small steel crucibles containing AZ91 Mg alloy. However, this was an inadequate heating method which seemed to cause excessive reaction and oxidation. As a result, no castings were produced. A new casting setup was then constructed at AUT University. An initial trial was conducted with Mg to prove that these moulds were capable of being cast centrifugally and to analyse mechanical properties of the CC Mg alloy.

4.8.1 An Improvised Centrifugal Casting Setup

The casting setup adopted an existing rotating table. An electrically controlled Frema Mini potter's wheel shown in Figure 4.27, was chosen to rotate these RP moulds. This machine was capable of rotating parts up to thirty kilograms and speed can be varied from 0-235RPM. The direction of rotation was able to be varied both clockwise and counter clock wise. The metal was poured into the moulds whilst stationary and then a protective cover, such as a steel enclosure, was placed over the mould and the machine was allowed to spin for about two minutes.

Figure 4.27 Improvised potter's wheel used for CC of Mg

4.8.2 Centrifugal Casting Trials with the New Setup

Aluminium trial

The same 3D printed moulds used in the previous CC trials were employed in this new setup. A one off trial involving CC601 Al alloy was conducted at 235RPM to first ensure the proposed method was capable of producing a casting. The 3D printed mould was held in place by a mixture of foundry green sand and hardened gypsum plaster. Before casting the metal the melt was degassed with commercially pure Nitrogen through the use of a lance. The melt was degassed for about five minutes prior to pouring and the metal was cast at 710°C. The CC trial was successful, thus allowing the equipment to be trialled with the more dangerous Mg alloy.

Magnesium trials

Two Mg casting trials were conducted with AZ91 magnesium at rotational speeds of 235RPM. The first trial was conducted at AUT University's metal casting laboratory, in which the Mg was heated to 730°C and then poured into the 3D printed mould shown in Figure 4.5b. The mould was kept stationary and the alloy was poured into the mould. Once the mould cavity was filled, a metal cover was placed over the rotating table, whilst a protective gas mixture was applied through a small opening at the top of the steel enclosure. Power was applied to the machine and the mould was spun for about two minutes. Excessive oxidation of the Mg occurred, which culminated in a sudden release of molten Mg upon removal of the pouring cup. Protective gas and flux was placed on the reacting metal, but the Mg continued to oxidise completely. The practical difficulties in containing Mg fires were apparent and it was decided that future work, would need to be conducted offsite.

A local foundry, Progressive Castings obliged, and a final trial was conducted onsite. The trial consisted of the same setup at AUT; however the Mg alloy was treated somewhat differently. This involved melting the alloy under the cover of a flux rather than a cover gas. Also, chemically bonded sand instead

of a greensand was used to hold the rotating 3D printed mould in position. This sand was very similar to that used as the backing sand in the Al centrifugal trials conducted at Centracast. The mould had a proprietary coating applied to reduce mould metal reaction. Finally, before pouring, the mould was flushed with a sulphur containing gas, and then the metal was cast. The melt was cast at about 710°C and the same protective cover was placed over the rotating mould. The casting was spun for two minutes. This proved successful and initial tensile and microstructural evaluation was conducted.

4.8.3 Results of the Modified Centrifugal Casting Trials

Aluminium castings

The tensile testing results on the cast parts produced in the modified CC machine are shown in Table 4.15. Large increases in all tensile properties were obtained with the highest UTS and yields strengths achieved, obtained, from the castings produced from this modified setup. The average strengths of these parts were 152.70 MPa and this was considerably higher than the cast strengths achieved at higher rotational speeds, conducted at Centracast. The difference in yield strength was also significant with an average of 116.95MPa, compared to 86.88MPa for the castings spun at 300RPM (optimum setting) at Centracast. The difference in percent elongation to earlier trials conducted at the company was not as pronounced, with an average of 1.99% for the aluminium trials, compared to the optimum of 1.60%.

Table 4.15 Tensile testing results from centrifugal castings, produced with CC601 aluminium

Sample		UTS (MPa)	Yield Strength (0.2% off-set) (MPa)	% Elongation
Aluminium	0°	154.00	118.50	2.03
	45°	151.40	115.40	1.95

The difference in fall height (about 250mm), and the use of lance degassing are likely reasons why these castings were significantly stronger than those trails conducted at Centracast. Although inefficient, the lance degassing would have removed some portion of the dissolved hydrogen, resulting in a less porous casting. However, upon turning down the cast samples to the required test shape, porosity was still observed throughout the samples but high strengths were obtained, indicating that efficient degassing should result in even higher cast properties. The arguments presented for the low tensile properties of the Centracast casting produced previously centred on the melt quality, with dissolved hydrogen shown as the dominating adverse factor. These arguments have been validated as lance degassing resulted in *much* higher strengths.

Analysis of the microstructure in Figure 4.28 showed the typical modified eutectic Si particles surrounded by the primary Al dendrites. Considerably fewer pores were present, and there were significantly smaller than those from un-degassed samples. The reduction in the number of pores and pore size accounted for the higher tensile properties of degassed the Al alloy. The sensitivity of the as-cast tensile strength to the quantity and morphology of these pores cannot be underestimated. Even with modest lance type degassing, the UTS were on average 10MPa higher than those samples cast in chemically bonded foundry sand which also underwent rotary degassing (best practice).

As referred to in Figure 4.24, the fall height of the metal in the Centracast CC machine probably caused excessive entrainment of metal oxides into the castings. However the lower fall height in this modified setup resulted in a lower number of oxide films being present in the cast microstructure, resulting in sounder castings.

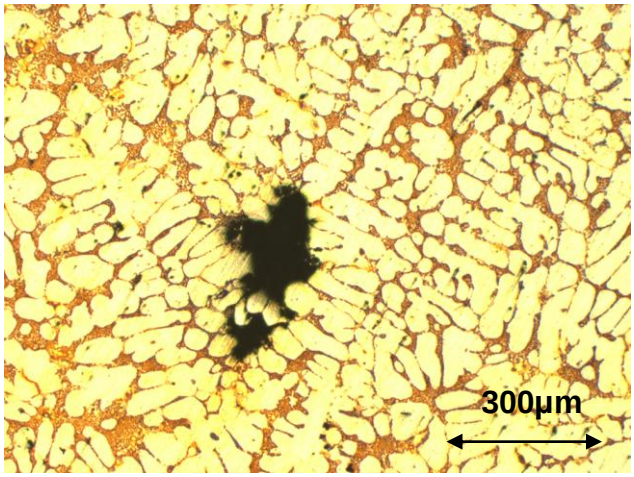

(a) X50

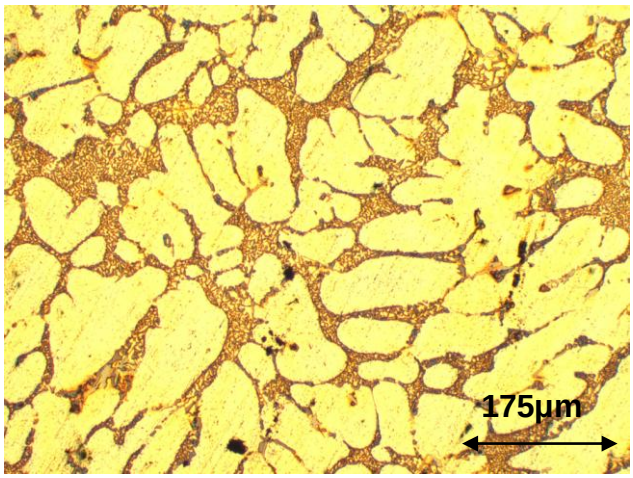

(b) X100

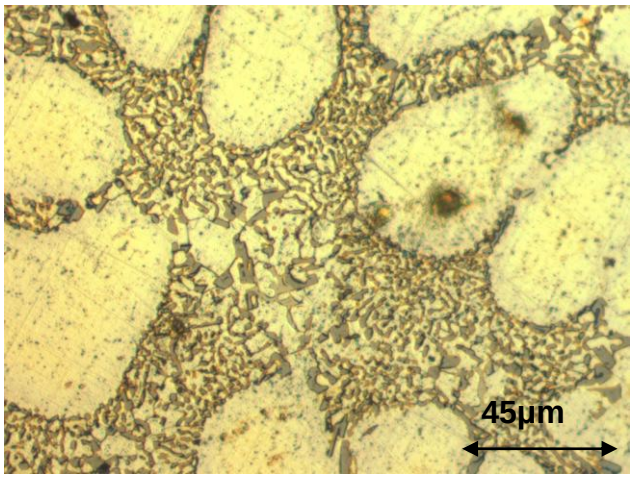

(c) X400

Figure 4.28 Al as-cast microstructure of lance degassed centrifugal castings at (a) X50 (b) X100 and (c) X400

Mg castings

These Mg castings proved that the overall concept of CC of Mg by 3D printing was a viable concept when cast with the help of industry professionals. No significant oxidation, mould-metal reaction or mould deformation was observed from this casting trial, leading the author to conclude that these 3D printed moulds were indeed suitable for processing Mg alloys. The problems faced in the initial trial at AUT University were primarily practical, relating to melting and the excessive tendency for oxidation of Mg alloys. The casting shown below is just after the Mg was poured

Figure 4.29 AZ91 CC shown in ZP131 printed mould (left) with close-up of cast surface shown on the right

Surface testing results of the as-cast surfaces gave an average roughness of 19.16µm. This was slightly higher than the static casting produced under similar conditions. The static casting produced with ZP131 mould material, AZ91 alloy gave a surface roughness of 9.49µm, whereas testing on the centrifugal cast surface ranged from 11.88-26.48µm. The application of the mould coating may be partly due to these changes in surface roughness. Before this CC trial was conducted, the 3D printed mould was coated by foundry personal. Brush coating of moulds in the static casting trials showed that much detail and care was taken to avoid surface deformation. These practices were not evident here, due to the trial nature of the casting. Also, excessive turbulence and vibration during CC may have contributed to mould metal reaction, leading to surface porosity, increasing surface roughness. The

actual cast strength of the centrifugal Mg castings were low in relation to the strengths achieved in the static Mg casting trials.

Table 4.16 Results of centrifugal magnesium castings

Sample		UTS (MPa)	Yield Strength (0.2% off-set) (MPa)	% Elongation
Magnesium	0°	113.00	100.80	1.22
	45°	93.50	N/A	0.64

These tensile properties summarised in Table 4.16, ranged from 93-113.50MPa, which was significantly lower than static casting trials, which gave 156.42MPa average using the same mould materials. The ductility of these castings was also low, with only 0.64-1.22% elongations obtained. These figures indicate that foreign materials, such as the covering flux, became entrained in the cast microstructure. On a macro level, when turning down the specimens to the tensile test shape, the castings showed no porosity or shrinkage.

The resulting lower tensile properties must be reflect by the as-cast microstructure. As a result, a tentative microstructural analysis was conducted on the cast parts and these findings are shown below. The cast microstructure shown in Figure 4.30 revealed slightly refined grains when compared to those in the static casting trials in ZP131 moulds. This refinement was a likely result of an increased solidification rate brought on by CC effect. However, as noted above, these advantages did not prevent the low tensile properties were obtained.

Upon examination, the microstructures showed shrinkage and microporosity was observed, possibly contributing to these poor tensile properties. The dark areas in Figure 4.30a&b represent microporosity weakening the cast structure. However, Figure 4.30c shows a slightly different eutectic structure, where a more fully divorced structure obtained. As noted in Chapter 3, fully divorced structures relate to higher solidification rates. In static casting results,

this did not translate to improved properties. These eutectic particles may be flux material trapped in the solidifying structure, as these particles were not observed elsewhere in the static casting Mg trials.

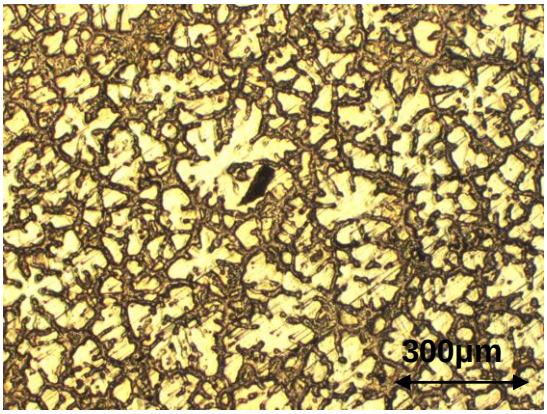

(a) X50

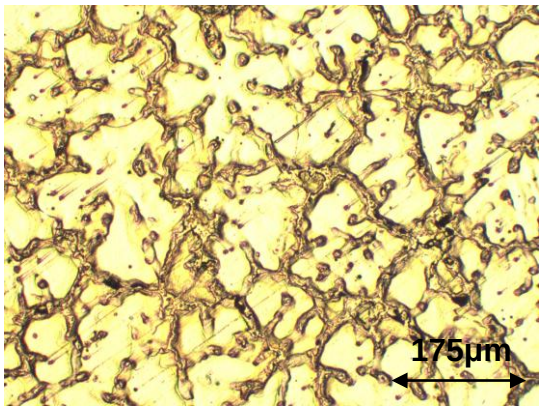

(b) X100

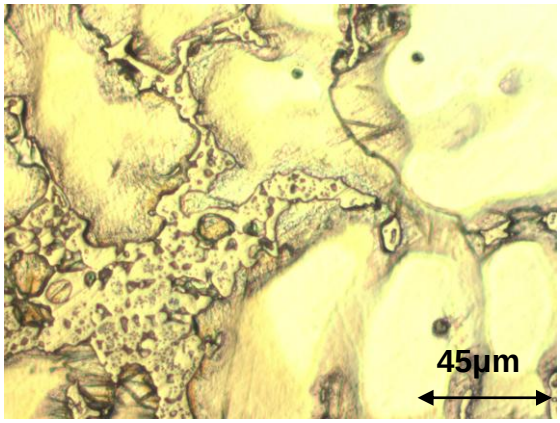

(c) X400

Figure 4.30 Photomicrographs of centrifugally cast AZ91 in ZP131 moulds at (a) X50 (b) X100 and (c) X400

Figure 4.31 below showed severe example of shrinkage.

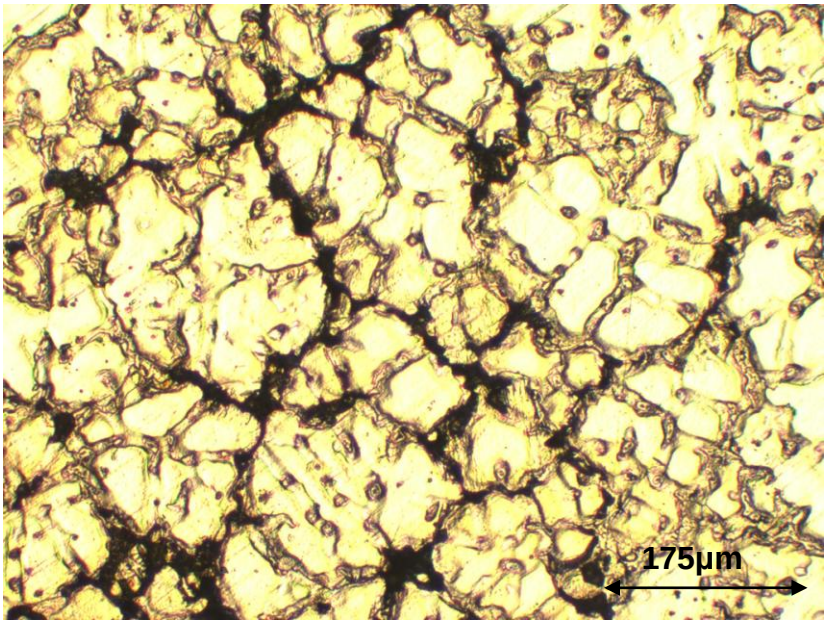

Figure 4.31 Suspected shrinkage porosity in AZ91 CC (X100)

4.9 Summary of Centrifugal Casting Trials

The CC trials using rotating moulds resulted in interesting results, which varied over a large range of values. The samples, however, were badly affected by the presence of hydrogen porosity, which became the dominant failure mechanism in Al castings. Nevertheless, increasing rotational speed was linked to increases in tensile properties such as grain number and tensile strength. Also, it was found that increasing rotational speeds resulted in a dramatic decrease in porosity pore size and distribution, which was closely linked to improved material strength.

The additional trials substantially increased Al tensile properties, giving the highest yield and UTS values in this entire work. Final trials, involving AZ91 Mg, alloy resulted in below average tensile properties. However, the suitability of these RP moulds in processing Mg alloys was successful, in that hot volatile Mg alloys were cast without mould deformation or excessive reaction.

It is conjectured that the low tensile properties of these Mg castings were a function of the melt quality and not the RP mould used.

Further, there was no evidence of mould cracking or deformation under increased filling pressures, with some castings producing superior as cast tensile properties when compared to traditional sand castings. Overall, 3D printed ZP131 plasters moulds used for CC were considered successful in the context of the experimental constraints experienced and the problematical variables not examined or not proven.

CHAPTER 5 CONCLUSIONS

It is submitted that the results of experimental investigations carried out in this research were significant, and, specifically, that the suitability of RP moulds for casting of both aluminium and magnesium was established. Critical property data for different mould materials were developed for optimum process conditions. Influences of several factors on the performance of RP moulds while casting different alloys were outlined. The rapid produced moulds were found to be suitable for both static and centrifugal casting and for both aluminium and magnesium alloys. The following are the main conclusions drawn from the results obtained:

Mould materials

- Both and ZP131 ZCast501 were found to be suitable for casting light metals namely, aluminium and magnesium.
- The experimental factors selected had varying levels of significance on performance of the RP mould materials.
- For ZP131, the compressive strength model gave a statistically significant regression analysis.
- Significant effects were found in both permeability and compressive strength models for the ZCast501 material.
- Optimum baking times and temperatures for ZP131 were 150°C and 8 hours for the best compressive strength and 150°C and 3 hours for the optimum permeability.
- Optimum baking times and temperatures for ZCast501 were 174°C and 5.27 hours for the best compressive strength and 209°C and 7.70 hours for the optimum permeability.
- Post baking compressive strengths in both materials were comparable to those using traditional sand casting materials at the optimum baking conditions.
- Permeability was low for both RP materials employed relative to values for traditional foundry sand.

Static casting trials

- Both aluminium and magnesium were cast successfully using RP moulds
- Mechanical properties such as surface roughness, tensile strength, percent elongation and hardness were optimised by selected factors, namely mould material, mould coating, alloy type and pouring temperature.
- Based on Taguchi signal processing and variance analysis, the significance and best combinations of the factors and their levels were found for each response.
- Specifically, ZP131 moulds were best suited for processing Al and Mg mechanical properties, using a combination of magnesium oxide based mould coating and a pouring temperature of 690°C.
- The mechanical properties of static castings produced using RP moulds were close to values reported in the traditional sand casting literature.
- The best surface roughness for these trials was 5.84µm, obtained in ZP131 moulds with SC1 magnesium alloy, which was better than recommended values of 6-13µm.
- The optimum percent elongation for these trials was 2.56%, obtained in the ZP131 moulds with SC1 alloy, and above the recommended value of 2%.
- The best UTS for these trials was 170MPa, which was also obtained in the ZP131 moulds with AZ91 magnesium alloy. This was larger than the recommended value of 160MPa.
- Photomicrographic evidence suggests that the metals produced from static casting were similar to those produced from traditional foundry practice.

Centrifugal Casting

- 3D printed moulds were successful in centrifugal casting of both aluminium and magnesium under varying process conditions
- Speeds ranging from 150-450RPM were used without any significant signs of mould erosion or deformation.

- The experimental factors considered for CC trials, namely rotational speed, cavity angle and runner to cavity ratio, together accounted for a large portion of the total variance in the experimental results.
- The tensile properties of centrifugally cast aluminium specimens were initially below expected levels, due to the presence of hydrogen gas and subsequent gas porosity, i.e. when the molten metal was not degassed prior to pouring.
- When lance degassing was subsequently used, the resulting UTS properties were some 10MPa higher than the recommended values.
- Microstructural observations then showed smaller grain sizes at high rotational speeds, and improved tensile properties.
- Changes to melt treatment and experimental setup were recommended to reduce porosity and oxides in the castings.

Overall, the project objectives were achieved:

- RP moulds were found to be suitable for casting both aluminium and magnesium alloys using static and centrifugal filling techniques.

- Mechanical properties and microstructural characteristics of castings varied, with process conditions and the optimum values obtained being comparable to traditional casting results.

- Specifically, magnesium alloys were successfully cast in these moulds, verifying its potential suitability for rapid casting.

The suitability of the static and centrifugal processes for functional parts to be rapidly produced with light metals was established. It is postulated that the future use of pattern-less moulding will gain momentum and that rapid casting will become standard practice in a variety of situations.

REFERENCES

1. Grimm, T., *User's guide to rapid prototyping*. Illustrated ed. 2004: SME. 404
2. Pham, D.T. and S.S. Dimov, *Rapid Manufacturing*. 2001: Springer-Verllag London Limited.
3. Zhang, G., Y.-C. Tsou, and A.L. Rosenberger, *Reconstruction of the Homunculus skull using a combined scanning and stereolithography process.* Rapid Prototyping Journal, 2000. **6**(4): p. 267-275.
4. Custom Part. *Additive Fabrication*. 2010 [cited 2010 28th April]; Available from: http://www.custompartnet.com/wu/additive-fabrication.
5. Ryall, C. and D. Wimpenny. *Rapid Prototyping for Rapid Castings*. 2008 [cited 2010 April 28th]; Available from: http://www.jharper.demon.co.uk/rptc01.htm.
6. *3D printing process*, in *ESG Associates Corporation*. 2003.
7. Chua, C.K., K.F. Leong, and C.S. Lim, *Rapid prototyping: principles and applications*, ed. C.S. Lim. 2003: World Scientific.
8. *Rapid Prototyping*, in *Foundry Management and Technology*. 2004. p. 79-81.
9. Tromans, G., *Developments in rapid casting*. 2004: John Wiley and Sons.
10. Pham, D.T. and S.S. Dimov, *Rapid prototyping and rapid tooling—the key enablers for rapid manufacturing.* Proceedings of the Institution of Mechanical Engineers Part C: Journal of Mechanical Engineering Science, 2003. **217**(1): p. 1-23.
11. Dickens, P.M., R. Stangroom, M. Greul, B. Holmer, K.K.B. Hon, R. Hovtun, R. Neumann, S. Noeken, and D. Wimpenny, *Conversion of RP models to investment castings.* Rapid Prototyping Journal, 1995. **4**(1): p. 4-11.
12. Lee, C.W., C.K. Chun, C.M. Cheah, L.H. Tan, and C. Feng, *Rapid investment casting: direct and indirect approaches via fused deposition modelling.* International Journal of Advanced Manufacturing Technology, 2004. **23**(1-2): p. 93-101.

13. Sachs, E., M. Cima, and J. Cornie, *Three-Dimensional Printing: Rapid Tooling and Prototypes Directly from a CAD Model.* CIRP Annals - Manufacturing Technology, 1990. **39**(1): p. 201-204.
14. Curodeau, A., E. Sachs, and S. Caldarise, *Design and Fabrication of Cast Orthopedic Implants with Freeform Surface Textures from 3-D Printed Ceramic Shell.* Journal of Biomedical Materials Research Part B: Applied Biomaterials, 2000. **53**(5): p. 525-535.
15. Gibbons, D.G. *Rapid Casting Using Laser Sintering Sand Moulds and Cores*. Warwick Formula Student- A Case Study 2007 [cited 2010 10th January]; Available from: http://www.imeche.org/NR/rdonlyres/1081D434-E678-4961-BDB0-99AB9877AED9/0/greggibbonssintering.pdf.
16. Tang, Y., J.Y.H. Fuh, Loha, H. T., Y.S. Wong, and L. Lu, *Direct laser sintering of a silica sand* Journal of Materials & Design, 2003. **24**(8): p. 623-629.
17. Casalino, G., L.A.C. De Filippis, and A. Ludovico, *A technical note on the mechanical and physical characterization of selective laser sintered sand for rapid casting* Journal of Materials Processing Technology, 2005. **166**(1): p. 1-8.
18. Kochan, A., *Rapid prototyping gains speed, volume and precision.* Assembly Automation, 2000. **20**(4): p. 295-299.
19. Waurzyniak, P., *Rapid metal*, in *Manufacturing Engineering*. 2003, ABI/INFORM Global. p. 49-57.
20. Bak, D., *Rapid prototyping or rapid production? 3D printing processes move industry towards the latter.* Assembly Automation, 2003. **23**(4): p. 340-345.
21. Rebros, M., S.N. Ramrattan, M.K. Joyce, and P.G. Ikonomov, *Behaviour of 3D Printed Sand at Elevated Temperature*, in *AFS Transactions*, A.F.s. Society, Editor. 2007, American Foundrymen's Society: Schaumburg. p. 341-348.
22. Bassoli, E., A. Gatto, L. Iuliano, and M.G. Violante, *3D printing technique applied to rapid casting.* Rapid Prototyping Journal, 2007. **13**(3): p. 148-155.

23. Dimitrov, D., K. Schreve, and N. de Beer, *Advances in three dimensional printing – state of the art and future perspectives.* Rapid Prototyping Journal, 2006a. **12**(3): p. 136-147.
24. Dimitrov, D., W. van Wijck, and N. de Beer, *Development, evaluation, and selection of rapid tooling process chains for sand casting of functional prototypes* Journal of Engineering Manufacture, 2007. **221**(9): p. 1441-1450.
25. Dimitrov, D., W. van Wijck, K. Schreve, and N. de Beer, *Investigating the achievable accuracy of three dimensional printing* Rapid Prototyping Journal, 2006b. **12**(1): p. 42-52.
26. McKenna, N., S. Singamneni, O. Diegel, D. Singh, and A.R. Choudhury, *Rapid manufacture in light metals processing.* Materials Science Forum, 2009. **618-619**: p. 387-390.
27. Brown, J.R., *Foseco foundryman's handbook*. 1994: Butterworth-Heinemann.
28. Bassoli, E. and E. Atzeni, *Direct metal rapid casting: mechanical optimisation and tolerance calculation.* Rapid Prototyping Journal, 2009. **15**(4): p. 238–243.
29. Kaplas, M. and R. Singh, *Experimental investigations for reducing wall thickness in zinc shell casting using three-dimensional printing.* Proceedings of the Institution of Mechanical Engineers, Part C: Journal of Mechanical Engineering Science, 2008. **222**(12): p. 2427-2431.
30. Gill, S.S. and M. Kaplas, *Comparative Study of 3D Printing Technologies for Rapid Casting of Aluminium Alloy.* Materials and Manufacturing Processes, 2009. **24**(12): p. 1405–1411.
31. Singh, J.P. and R. Singh, *Investigations for a statistically controlled rapid casting solution of lead alloys using three-dimensional printing.* Proceedings of the Institution of Mechanical Engineers, Part C: Journal of Mechanical Engineering Science, 2009. **223**(9): p. 2125-2134.
32. Eliezer, D., E. Aghion, and F.H. Froes, *Magnesium Science, Technology and Applications.* Advanced Performance Materials, 1998. **5**(3): p. 201-212.

33. Eigenfeld, K., W. Tilch, S. Erchov, and O. Podobed, *Integrated magnesium technology.* Advanced Engineering Materials, 2004. **6**(7): p. 520-525.
34. Bronfin, B. and E. Aghion, *Magnesium Alloys Development towards the 21st Century.* Materials Science Forum, 2000. **350-351**: p. 19-30.
35. Hanawalt, J.D. and M. Okada, *Oxidation inhibiting techniques for magnesium sand casting*, in *Transactions of the American Foundrymen's Society*, T.o.t.A.F.s. Society, Editor. 1972, Transactions of the American Foundrymen's Society. p. 87-90.
36. Fantetti, N., A. Thorvaldsen, and A. Couture, *Properties of Magnesium Plaster Casting.* SAE Technical Paper Series, 1991: p. 1-10.
37. Lun Sin, S., D. Dube, and R. Tremblay, *Interfacial reactions between AZ91D magnesium alloy and plaster mould material during investment casting.* Materials science and technology, 2006. **22**(12): p. 1456-1463.
38. Idris, M.H. and A.J. Clegg, *Processing and evaluation of investment cast magnesium-base alloy*, in *Transactions of the American Foundrymen's Society*. 1996, Transactions of the American Foundry's Society. p. 237-244.
39. Takamori, S., Y. Osawa, T. Kimura, L. Xinbao, and T. Muka, *Casting Surface of AZ91 Alloy and Its Reaction with Sand Mold.* Materials transactions, 2008. **49**(5): p. 1089-1092.
40. Cingi, C., J. Vainola, and j. Orkas, *Role of oxygen in mold metal reactions in investment casting of magnesium alloy AZ91E.* International Foundry Research, 2007. **59**: p. 18-27.
41. Kim, S., M. Kim , T. Hong, H. Kim, and Y. Kim, *Investment casting of AZ91HP magnesium alloy* Metals and Materials International, 2000. **6**(3): p. 275-279.
42. Gjestland, H. and H. Westengen, *Advancements in high pressure die casting of magnesium.* Advanced engineering materials 2007. **9**(9): p. 769-776.
43. Strieter, F.P. and R.J. Maonner, *Centrifugal casting of magnesium part*, in *American Foundryman*, A.F. Association, Editor. 1946, American Foundryman Association: Chicago. p. 43-47.

44. Chirita, G., D. Soaresa, and F.S. Silva, *Advantages of the centrifugal casting technique for the production of structural components with Al–Si alloys.* Materials & Design, 2008. **29**(1): p. 20-27.
45. Mukunda, P.G., A. Shailesh Rao, and S.S. Rao, *Influence of rotational speed during centrifugal casting on sliding wear behaviour of the Al-2Si alloy.* Frontiers of Materials Science in China, 2009. **3**(3): p. 339-344.
46. Howson, H.O., *Macrostructural comparison of centrifugal and static castings.* Foundry Trade Journal, 1969. **127**(2750): p. 261-272.
47. Mesquita, R.A., D.R. Leiva, A.R. Yavari, and W.J. Botta Filho, *Microstructures and mechanical properties of bulk AlFeNd(Cu, Si) alloys obtained through centrifugal force casting.* Materials Science and Engineering A, 2007. **452-453**: p. 161-169.
48. Meinecke, G., *Production, properties and processing directions for moulding and casting plasters.* Zement-kalk-Gips, Edition B, 1989. **42**(5): p. 233-235.
49. Corporation, Z. (2007) *ZB60 MSDS*. 1-9.
50. Corporation, Z. (2002) *ZB 58 Binder MSDS*. 1-8.
51. Cochran, W.G. and G.M. Cox, *Experimental Designs*. 1950: Wiley.
52. Rekab, K., *Statistical Design of Experiments with Engineering Applications*. 2005: CRC Press.
53. Beeley, P.R., *Foundry technology*. 2 ed. 2001: Butterworth-Heinemann. 719 pages.
54. ASTM International, *D7012 – 10 Standard Test Method for Compressive Strength and Elastic Moduli of Intact Rock Core Specimens under Varying States of Stress and Temperatures*. 2010. p. 9.
55. Brown, J.R., *Foseco Non-Ferrous Foundryman's Handbook*. 1999: Butterworth-Heinemann.
56. Bettles, C.J., C.T. Forwood, D.S. Jones, J.R. Griffiths, M.T. Frost , D.H. St.John, Ma Qian, G.-L. Song, and J.F. Nie, *AMC-SC1: A New Magnesium Alloy Suitable for Powertrain Applications* SAE International Technical Papers, 2003.
57. American Foundrymen's Society, *Aluminum Casting Technology 2nd edition*, ed. 2nd. 1993: American Foundrymen's Society. 368.

58. Roy, R., *Primer on the taguchi method*. 2010: SME.
59. Vander Voort, G.F., *Color Metallography*, in *MICROSCOPY TODAY*. 2005. p. 22-27.
60. ASM Handbook Committee, *ASM Handbook*. Metallography and Microstructures, ed. G.F. Vander Voort. Vol. 9. 2004: ASM International 1184.
61. ASTM International, *E 112 – 96 Standard Test Methods for Determining Average Grain Size*. 2004, ASTM International.
62. Rennie, A.E.W., C.E. Bocking, and D.M. Jacobson, *Rapid and Virtual Prototyping and Applications*. 2003: John Wiley and Sons.
63. Smallman, R.E. and R.J. Bishop, *Modern physical metallurgy and materials engineering: science, process, applications*. 6 ed. 1999: Butterworth-Heinemann. 438.
64. *Aluminum Alloy Castings*. 2004: ASM International.
65. Hong, S.J., S.S. Kim, J.H. Lee, Y.N. Kwon, Y.S. Lee, and J.H. Lee, *Effect of microstructural variables on tensile behaviour of A356 cast aluminium alloy.* Materials Science and Technology, 2007. **23**(7): p. 810-814.
66. Kobayashi, T., *Strength and fracture of aluminum alloys.* Materials Science and Engineering A, 2000. **286**(2): p. 333-341.
67. Lee, C.D., *Effect of grain size on the tensile properties of magnesium alloy.* Materials Science and Engineering A, 2007. **459**(1-2): p. 355–360.
68. Campbell, J., *Castings: The New Metallurgy of Cast Metals*. 2003: Butterworth-Heinemann.
69. Backerud, C., G. Chai, and J. Tammen, *Solidification Characteristics of Aluminium Alloys*. 1990: AFS International.
70. St John, D.H., A.K. Dahle, T. Abbott, M.D. Nave, and Qian Ma, *Solidification of cast Magnesium alloys.* TMS Annual Meeting, 2003.
71. Avedesian, M.M., H. Baker, and ASM International Handbook Committee, *Magnesium and magnesium alloys*. 2nd ed. 1999: ASM International. 314.

72. Dunlop, G., Bettles, C.J., J.R. Griffiths, K. Venkatesan, L. Zheng, and M. Qian. *The Effect of Grain Size on the Mechanical Properties of AMSC1*. in *6th International Conference of Magnesium Alloys and Their Applications*. 2003. Wolfsburg.
73. Standards, B., *Specification for Aluminium and Aluminium alloy ingots and castings for general engineering purposes*. 1988, British Standards.
74. Bettles, C.J., M.A. Gibson, and Z. S.M., *Microstructure and mechanical behaviour of an elevated temperature Mg-rare earth based alloy.* Materials Science and Engineering A, 2009. **505**(1-2): p. 1-12.
75. Lu, Y.Z., Q.D. Wang, W.J. Ding, X.Q. Zeng, and Y.P. Zhu, *Fracture behaviour of AZ91 magnesium alloy.* Materials Letters, 2000. **44**: p. 265-268.
76. Ceschini, L., A. Morri, A. Morri, Gamberini, A. , and S. Messieri, *Correlation between ultimate tensile strength and solidification microstructure for the sand cast A357 aluminium alloy.* Materials and Design, 2009. **30**(10): p. 4525–4531.
77. Totten, G.E. and D.S. Mackenzie, *Handbook of Aluminum*. Vol. 1. 2003: CRC Press. 1310 pages.
78. Committee, A.I.H., *Alloy Phase Diagrams*. ASM Handbook, ed. H. Baker and H. Okamoto. Vol. 3. 1992: ASM International.
79. Nave, M.D., A.K. Dahle, and D.H. St John, *Eutectic growth morphologies in Magnesium-Aluminium alloys*, in *Magnesium technology 2000*. 2000, TMS. p. 233-242.
80. Choong Do Lee and Kwang Seon Shin, *Effect of microporosity on the tensile properties of AZ91 magnesium alloy.* Acta Materialia, 2007. **55**(13): p. 4293–4303.
81. Zeng, X., Y. Wang, Wenjiang Ding, A.A. Luo, and A.K. Sachdev, *Effect of Strontium on the Microstructure, Mechanical Properties, and Fracture Behaviour of AZ31 Magnesium Alloy.* Metallurgical and materials transactions A, 2006. **37A**: p. 1333-1341.
82. Polmear, I., *Light Alloys*. 2005: Butterworth-Heinemann. 437.

83. Davis, J.R., Davis J. R. & Associates, and ASM International. Handbook Committee, *Aluminum and aluminum alloys - ASM specialty handbook*. 5, illustrated ed, ed. J.R. Davis. 1993: ASM International. 784 pages.
84. Fatahalla, N., M. Hafiz, and M. Abdulkhalek, *Effect of microstructure on the mechanical properties and fracture of commercial hypoeutectic Al-Si alloy modified with Na, Sb and Sr.* Journal of Materials Science, 1999. **34**: p. 3555 – 3564.
85. Hegde, S. and K.N. Prabhu, *Modification of eutectic silicon in Al–Si alloys.* Journal of Materials Science, 2008. **43**(9): p. 3009–3027.
86. Shabestari, S.G. and F. Shahri, *Influence of modification, solidification conditions and heat treatment on the microstructure and mechanical properties of A356 aluminum alloy.* Journal of Materials Science, 2004. **39**(6): p. 2023 – 2032.
87. Haque, M.M. and A.F. Ismail, *Effect of superheating temperatures on microstructure and properties of strontium modified aluminium–silicon eutectic alloy.* Journal of Materials Processing Technology, 2005. **162–163**: p. 312–316.
88. Wang, Q.G., *Microstructural Effects on the Tensile and Fracture Behaviour of Aluminum Casting Alloys A356/357.* Metallurgical and Materials Transactions A, 2007. **34**(12): p. 2887-2899.
89. Ma, Z., A.M. Samuel, F.H. Samuel, H.W. Doty, and S. Valtierra, *A study of tensile properties in Al–Si–Cu and Al–Si–Mg alloys: Effect of β-iron intermetallics and porosity.* Materials Science and Engineering A, 2008. **490**: p. 36–51.
90. Taylor, J.A., *The Effect of Iron in Al-Si Casting Alloys* in *35th Australian Foundry Institute National Conference*, C.e. al, Editor. 2004, Australian Foundry Institute (AFI): Adelaide, South Australia. p. 148-157.
91. Bourcier, R.J., D.A. Koss, R.E. Smelser, and O. Richmond, *The influence of porosity on the deformation and fracture of alloys.* Acta Metallurgica, 1986. **34**(21): p. 2443-2453.

92. Ammar, H.R., A.M. Samuel, and F.H. Samuel, *Porosity and the fatigue behaviour of hypoeutectic and hypereutectic aluminum–silicon casting alloys.* International Journal of Fatigue, 2008. **30**(6): p. 1024–1035.
93. ASM Handbook Committee, *ASM Handbook*. Fractography, ed. K. Mills. Vol. 12. 2004: ASM International 1184.
94. Janco, N., *Centrifugal casting*. 1988: American Foundrymen's Society.
95. Johnson, H.V., *Manufacturing Process*. 2 ed. 1984: DIANE Publishing. 590
96. Subramanya, K., *1000 solved problems in fluid mechanics (includes hydraulic machines)*2005: Tata McGraw-Hill. 456 pages.
97. Chirita, G., I. Stefanescu, D. Soares, and F.S. Silva, *Centrifugal versus gravity casting techniques over mechanical properties*

Anales de Mecánica de la Fractura, 2006. **1**: p. 317-322.

98. Lu, L. and A.K. Dahle, *Iron-Rich Intermetallic Phases and Their Role in Casting Defect Formation in Hypoeutectic Al-Si Alloys.* Metallurgical and Materials Transactions A, 2005. **36A**: p. 819-835.
99. Stefanescu, D.M., *ASM Handbook*. Vol. 15 Casting. 1988.
100. Monroe, R., *Porosity in Castings.* Transactions of the American Foundry Society, 2005. **113**(Silver Anniversary Paper): p. 519 - 546.
101. Choong Do Lee, *Effects of microporosity on tensile properties of A356 aluminium alloy.* Materials Science and Engineering: A, 2007. **464**(1-2): p. 249-254.
102. Herrera, A. and V. Kondic. in *Proceedings of the International Conference on Solidification and Cast Metals*. 1977. Sheffield, UK.
103. Campbell, J., *Castings*. 2 ed. 2003: Butterworth-Heinemann. 335 pages.
104. Campbell, J., *Castings practice: the 10 rules of castings*. 2004: Butterworth-Heinemann.
105. Campbell, J., *An Overview of the Effects of Bifilms on the Structure and Properties of Cast Alloys.* Metallurgical and Materials Transactions B, 2005. **37B**: p. 857-863.

106. John, K., P.R. Beeley, J.R. Griffiths, and N.R. Green, *Commentaries on 'Entrainment defects' by J. Campbell.* Materials Science and Technology, 2006. **22**(8): p. 999-1008.
107. De-Feng, M., H. Guo-Qiu, H. Zheng-Fei, Z. Zheng-Yu, C. Cheng-Shu, and Z. Wei-Hua, *Crack initiation and propagation of cast A356 aluminum alloy under multi-axial cyclic loadings.* International Journal of Fatigue, 2008. **30**(10-11): p. 1843-1850.
108. British Standard, *BS EN 10 002-1 Tensile testing of metallic materials*, in *Part 1. Method of test at ambient temperature* 1990, British Standards Institution p. 1-17.

APPENDIX A Mould Material

A.1 Experimental Design

Firstly consider a square matrix, n x n, shown in equation (A.1):

$$x \ \{\beta\} = [y] \tag{A.1}$$

Where:

[x] = X (design) matrix

$\{\beta\}$ = Unknown constants (column matrix)

$\{y\}$ = Experimental results

So in the square matrix case, shown in equation (A.1), above, the unknowns are the missing constants in the column matrix, β But this assumes that the missing column matrix is square which in this case it is not, as it contains 6 missing constants in one column i.e. 6x1 matrix.

To allow further analysis to be done the column matrix must be multiplied by its transposed matrix, shown in equation (A.2)

If, $X = a_1 \quad a_2 \quad a_3$ then its transpose;

$$X^T = \begin{bmatrix} a_1 \\ a_2 \\ a_3 \end{bmatrix} \tag{A.2}$$

Thus:

$$[X][X^T]\{\beta\} = [Y][X^T] \tag{A.3}$$

Rearranging equation (A.3) β we obtain equation (A.4):

$$\{\beta\} = ([Y][X^T]) \times ([X][X^T])^{-1} \quad \text{(A.4)}$$

$$\{\beta\} = \begin{pmatrix} \beta_0 \\ \beta_1 \\ \beta_2 \\ \beta_{11} \\ \beta_{22} \\ \beta_{12} \end{pmatrix} \quad \text{(A.5)}$$

Where:

The missing column matrix in equation (A.5) shows the constants that will form the polynomial expression, shown in equation (A.6) below.

$$y = \beta_0 + \beta_1 X_1 + \beta_2 X_2 + \beta_{11} X_1^2 + \beta_{22} X_2^2 + \beta_{12} X_1 X_2 \quad \text{(A.6)}$$

The missing column matrix was determined with the use of Matlab and Mintab software. The procedure was to establish the values missing co-efficients, based off the coded values, in Matlab then confirming these in Minitab. Also Minitab was used to confirm the values of the natural variables, obtained by hand calculations. A sample of these calculations is shown below.

Co-efficient values found from the coded variables Matlab for ZP131 permeability strength model were:

$$\{\beta\} = \begin{pmatrix} 2099.08 \\ -109.377 \\ -105.208 \\ 82.8813 \\ 166.930 \\ 40.5881 \end{pmatrix} \quad \text{(A.7)}$$

Thus, the expression in terms of natural variables becomes:

$$P\ X_1, X_2 = 2099.08 - 109.33X_1 - 105.208X_2 + 82.8813X_1^2 + 166.93X_2^2 + 40.5881X_1X_2 \quad \text{(A.8)}$$

To convert a coded variable into a natural variable, the increment of change of the natural variable and the centre point must be known, i.e.:

$$x = \frac{N - C}{i} \quad \text{(A.9)}$$

Where:

x = coded variable

N = Value of natural variable

C = Centre point of natural variable in experimental design

i = Increment of change of natural variable

The configuration of this formula is shown below for temperature and time of mould baking

$$X_1 = \frac{T - 200}{50} = 0.02T - 4 \quad \text{(A.10)}$$

and

$$X_2 = \frac{t - 6}{2} = 0.5t - 3 \quad \text{(A.11)}$$

Equations (A.10) and (A.11) are then substituted into equation (A.8), which gives the following:

$$P\ T, t = 2099.08 - 109.33\ (0.02T - 4) - 105.208\ (0.5t - 3) + 82.8813\ (0.02T - 4)^2 + 166.93\ (0.5t - 3)^2 + 40.5881\ (0.02T - 4)\ (0.5t - 3) \quad \text{(A.12)}$$

Expanding equation (A.12)

$$\begin{aligned} MP\ T,t\ &= 2099.08 - 2.1876T + 437.52 - 29.89t + 179.32 \\ &+ 0.039408T^2 - 15.7532T + 1576.32 + 29.68t^2 - 356.16t \\ &+ 1068.48 + 0.4059Tt - 2.435T - 81.18t + 487.08 \end{aligned} \quad \text{(A.13)}$$

Collecting like terms in equation (A.13) gives the final form of the model in natural variables

$$\begin{aligned} MP\ T,t\ &= 5847.32 - 20.3758T - 467.23t \\ &+ 0.039408T^2 + 29.68t^2 + 0.4059Tt \end{aligned} \quad \text{(A.14)}$$

The co-efficients in terms of the natural variables are then shown below in equation (A.14) in matrix form. These values were checked against those obtained in Minitab, which confirms that these values were correct.

$$\{\beta\} = \begin{pmatrix} 5847.82 \\ -20.3858 \\ -467.23 \\ 0.039408 \\ 39.68 \\ 0.4059 \end{pmatrix} \quad \text{(A.15)}$$

A.2 Permeability and Compressive Stress Calculations

Permeability

The permeability of the tested mould samples was calculated using Darcy's equation, shown below.

$$k = \frac{\mu \dot{Q} \Delta P L}{A P_{mean} \Delta P_{in,out} \times 1000} \quad \text{(A.16)}$$

Where:

μ = Dynamic viscosity of passing fluid air (1.82 x 10^{-5} Ns/m^2)

L = length of specimen (m)

A = Cross sectional area of specimen (m^2)

P_{mena} = Mean pressure of inlet and outlet added onto P_{atm}

$\Delta P_{in,out}$ = Inlet pressure – outlet pressure

$\dot{Q}$ = Flow rate m^3/s

ΔP = Pressure difference between atmosphere and gauge pressure

Compressive strength

The compressive strength values were calculated by using the definition of stress, shown below in equation (A.17). The ultimate compressive strength was determined when the specimen had started to crack and the force either reduced or remained relatively constant.

$$\sigma = \frac{F}{A} \tag{A.17}$$

Where:

σ = The resulting compressive stress

F = The applied uniaxial force

A = The cross-sectional area, perpendicular to the applied force

A.3 Raw Experimental Results From Material Testing

Over the next few pages the raw experimental data is presented relating to the permeability and compressive testing conducted on both the ZP131 and ZCast501 mould materials.

A.3.1 Permeability Data

Table A.1 ZP131 mould material permeability data

Temp (°C)	Time (Hrs)	Outflow rate (m^3/s)	Inlet pressure (KPa)	Mean Press (KPa)	K(m^2)	K (mD)
150	4	3.48E-05	16	110.3	2.5E-12	2496
250	4	2.92E-05	16	110.3	2.1E-12	2092
150	8	2.97E-05	16	109.2	2.1E-12	2150
250	8	2.66E-05	16	110.3	1.9E-12	1909
130	6	3.53E-05	16	110.3	2.5E-12	2533
271	6	3.22E-05	15.5	110.3	2.3E-12	2371
200	3.17	3.48E-05	16	110.6	2.4E-12	2473
200	8.23	3.53E-05	16	110.6	2.5E-12	2509
200	6	3.48E-05	15.6	110.4	2.5E-12	2541
200	6	2.86E-05	16	109.2	2.0E-12	2062
200	6	2.81E-05	16	109.2	2.0E-12	2025
200	6	2.35E-05	16	109.2	1.7E-12	1694
200	6	3.02E-05	16	109.2	2.1E-12	2173

Table A.2 Experimental permeability data for ZCast501 mould material

Temp (°C)	Time (Hrs)	Outflow rate (m^3/s)	Inlet pressure (KPa)	Mean Press (KPa)	K(m^2)	K (mD)
150	4	1.63E-05	12.5664615	108.6	1.5E-12	1500
250	4	2.05E-05	12.3406667	108.4	1.9E-12	1917
150	8	2.17E-05	10.9258043	106.7	2.3E-12	2304
250	8	1.89E-05	12.03	108.3	1.8E-12	1825
130	6	1.60E-05	9.87268182	107.2	2.1E-12	2120
271	6	1.79E-05	9.47026316	107.3	2.2E-12	2213
200	3.17	1.84E-05	14.9532263	110.0	1.4E-12	1405
200	8.23	1.69E-05	10.2588692	107.7	1.9E-12	1926
200	6	1.87E-05	12.4919192	108.8	1.7E-12	1721
200	6	2.46E-05	11.6226814	107.0	2.5E-12	2499
200	6	2.10E-05	12.5545169	107.5	1.9E-12	1948
200	6	2.30E-05	12.0973137	107.2	2.2E-12	2241
200	6	2.20E-05	11.7914585	107.1	2.1E-12	2175

A.3.2 Compressive Strength Data

Table A.3 ZP131 and ZCast501 compressive strength data

Coded units		Un-coded units		ZP131 Compressive strength		ZCast501 Compressive strength	
X_1	X_2	Temp (°C)	Time (Hrs)	Force (N)	UCS (MPa)	Force (N)	UCS (MPa)
-1	-1	150	4	871.33	1.78	1674	0.85
1	-1	250	4	401.66	0.82	988	0.50
-1	1	150	8	896.33	1.83	1803	0.92
1	1	250	8	248.33	0.51	515.30	0.26
-1.414	0	130	6	837.66	1.71	1938	0.99
1.414	0	270	6	357.33	0.73	755	0.38
0	-1.414	200	3.17	590.66	1.20	2031.30	1.03
0	1.414	200	8.88	640.33	1.30	561.70	0.29
0	0	200	6	424	0.86	2056	1.05
0	0	200	6	572.33	1.17	2431	1.24
0	0	200	6	738.33	1.50	1744	0.89
0	0	200	6	590.33	1.20		
0	0	200	6	778.33	1.59		

APPENDIX B STATIC CASTING INFORMATION

B.1 Design of Experiments and ANOVA

The L9 experimental design used in the static casting trials, is able to identify the highest ranking factor and level combinations, however, an ANOVA is also needed on the signal to noise ratio, to establish at what confidence level are these factors significant. The AVOVA table is used here to identify any significant factors at 90, 95 or 99 % confidence level. Over the following section, the individual calculations presented in the ANOVA table are presented in the context of the L9 experimental design.

Degrees of freedom

Factor D.O.F:

$$D.O.F_{factor} = \#\ levels_{factor} - 1 \tag{B.1}$$

For the L9 experiment each factor is at three levels so the D.O.F associated with factor is = 3-1 = 2 D.O.F.

Total D.O.F:

$$D.O.F_{total} = \#\ \text{exprimental trials} - 1 \tag{B.2}$$

For the L9 experiment there were 9 trials so D.O.F = 9-1 = 8

Error D.O.F:

$$D.O.F_{\boldsymbol{Error}} = D.O.F_{\boldsymbol{total}} - \sum D.O.F_{\text{Factor}} \tag{B.3}$$

I.e. for a L9 experiment = 8-(number of factors) *(2)

In this case we have 4 factors at 2 levels thus $D.O.F_{Error} = 8 - 2 - 2 - 2 - 2 = 0$

As we can see we now have used all the columns in the experiment and consequently have zero D.O.F for the error in the experiment. To account for some error the lowest factor is normally pooled according to some criteria i.e. least significant factor is assumed as the error to allow further ANOVA calculations (as they require a known amount of error).

B.1.1 Sum of squares

Each factor is considered a column in the Taguchi design. The formula below returns the value of the sum of square of each factor based on its S/N ratios.

$$SS_{Factor} = K_{f_1}\left(\bar{T}_{f_1} - \bar{T}\right)^2 + K_{f_2}\left(\bar{T}_{f_2} - \bar{T}\right)^2 + K_{f_3}\left(\bar{T}_{f_3} - \bar{T}\right)^2 \quad \text{(B.4)}$$

Where:

$T_{f_{1...n}}$ = Average of response of factor f_1

$\bar{T}$ = Average response

$K_{f_{1...n}}$ = Number of levels of factor K

Variance

Factor Variance: $$v = \frac{SS_{factor}}{D.O.F_{factor}} \quad \text{(B.5)}$$

E.g. Variance of mould coating = 3.02/2 = 1.51

F-Ratio

The calculated F value is a simple ratio of variances. When this ratio becomes large enough the two sample variances are accepted as being unequal at some confidence level. We use F-ratio to see if our value is significant or greater than the standard table value at a specific confidence level usually 90, 95 or 99 %. If the experimental value is higher than the standard value at the specific confidence interval (taking into account the D.O.F) the factor is said to be significant and that the variation in the results cannot be explained by chance alone (based on the F distribution).

$$F_{ratio} = \frac{V_{factor}}{V_{error}} \tag{B.6}$$

The critical F value, $F_{critical}$ is found from standard tables at the required confidence level and at the appropriate D.O.F.

A factor is said to be significant when the F_{ratio} is larger than the $F_{critical}$ value.

Percent contribution

Percent contribution is simply the ratio of the sum of squares of each factor to the total sum of squares i.e. how much variation does each factor contribute to the total variance.

$$\%_{factor} = \frac{SS_{factor}}{SS_{total}} \tag{B.7}$$

Pooling of factors

The following is taken from ‘Taken from A primer on the Taguchi method by Ranjit K. Roy [58]. Error terms in an experiment represent the degree of inter-

experiment error when the D.O.F is sufficiently large. When the error D.O.F is small or zero which is the case when all the columns (factors) in an orthogonal array are occupied, the small column effects are pooled to form a larger error term (known as pooling up). In terms of what has been done in the current experiment, the factor contributing the least sum of squares to the total sum of squares was pooled as the error. It is mentioned that repetition of result can provide an error term even if the experiment has all its columns used.

B.2 Mechanical testing data

Table B.1 Results of tensile testing of static castings (average values shown in bold). Testing was conducted at 1mm/min.

Trail number	Gauge dia. (mm)	Gauge Length	Extension (m)	Force at break	UTS (MPa)	Ext (%)
1A	0.0048	0.05	0.001325	3087.667	170.63	2.65
1B	0.00496	0.047	0.00111	3064.333	158.59	2.36
1C	0.00492	0.05	0.0009	2724	143.28	1.80
1D	0.005	0.05	0.000935	3007.33	153.16	1.87
					156.42	**2.17**
2A	0.00496	0.05	0.00132	2676.333	138.51	2.64
2B	0.00508	0.0479	0.00104	2582.667	127.42	2.17
2C	0.00475	0.0505	0.00129	2221	125.33	2.55
2D	0.0048	0.05	0.001438	2330.667	128.80	2.88
					130.02	**2.56**
3A	0.00416	0.05	0.00048	1906	140.23	0.96
3B	0.0041	0.0549	0.000375	1466.33	111.06	0.68
3C	0.00414	0.049	0.0003	1561.33	115.99	0.61
3D	0.00374	0.05	0.00037	1551.667	141.24	0.74
					127.13	**0.75**
4A	0.00454	0.048	0.001229	2482	153.32	2.56

4B	0.00417	0.048	0.001116	1798.667	131.70	2.33
4C	0.00503	0.0485	0.00109	2245.333	112.99	2.25
4D	0.00493	0.05	0.001	2175.33	113.96	2.00
					127.99	**2.28**
5A	0.00498	0.0505	0.000375	2616	134.30	0.74
5B	0.00506	0.0505	0.00046	2478	123.23	0.91
5D	0.00515	0.049	0.00044	2887.333	138.61	0.90
					132.05	**0.85**
6B	0.00367	0.04935	0.00075	1596	150.87	1.52
					150.87	**1.52**
7A	0.00492	0.0491	0.000285	1514.33	79.65	0.58
7B	0.00488	0.0504	0.00045	1912.667	102.26	0.89
7C	0.00492	0.0491	0.00035	1861.33	97.90	0.71
					93.27	**0.73**
8A	0.0051	0.049	0.0006	2105.33	103.06	1.22
8B	0.00504	0.0477	0.0009	2816.333	141.17	1.89
8C	0.00508	0.0468	0.00071	2778.667	137.09	1.52
					127.11	**1.54**
9A	0.00475	0.049	0.001505	2730	154.06	3.07
9B	0.00453	0.0484	0.0019	2655	164.73	3.93
9C	0.00508	0.0505	0.00155	3108.667	153.38	3.07
					157.39	**3.36**

Table B.2 Brinell hardness results, conducted on cast samples. (All samples were tested at a minimum of 4 readings. Samples were tested with 500Kg load with 10mm diameter ball, with readings 1 and 2 showing the measured diameters of the indentation)

Sample	Read 1(mm)	Read 2	Ave	Read 1	Read 2	Ave	Total Ave	HB
1A	3.4	3.3	3.35	3.3	3.2	3.25	3.3	56.82
1B	3.4	3.2	3.3	3.4	3.2	3.3		
2	3.5	3.6	3.55	3.5	3.7	3.6	3.575	48.17

3	3	3.2	3.1	3.3	3.3	3.3	3.2	60.54
4	3.6	3.5	3.55	3.6	3.5	3.55	3.55	48.87
5	3.1	3.1	3.1	3.1	3	3.05	3.075	65.70
6	3.2	3.3	3.25	3.1	3.2	3.15	3.2	60.54
7	3.4	3.3	3.35	3.5	3.5	3.5	3.425	52.63
8	3.3	3.4	3.35	3.1	3.4	3.25	3.3	56.82
9	3.5	3.7	3.6	3.5	3.7	3.6	3.6	47.46

Table B.3 Surface roughness values measured from the as-cast surface.

Trial	Surface roughness readings, Ra (μm)						Overall average
1	9.2561	11.5939	7.6289	8.4369	10.4254	9.6500	9.4985
2	3.7006	10.4743	7.4631	9.3854	5.6562	7.2831	7.3271
3	7.1392	6.2032	5.0519	4.2915	4.9427	7.4167	5.8409
4	38.1190	32.7692	20.0400	7.7737	17.9628	25.3097	23.6624
5	15.4813	8.2465	10.7501	14.0728	6.9355	13.3186	11.4675
6	13.0575	22.6259	11.6315	10.0185	12.8754	15.7890	14.3330
7	17.7029	7.9240	11.2059	13.6704	11.4595	13.8245	12.6312
8	11.6313	13.7565	16.5517	14.4340	13.4570	14.0485	13.9798
9	20.0345	9.2689	11.2082	12.7540	9.1077	8.3472	11.7868

B.2.1 ASTM grain size

To determine the average dendrite grain size of the static castings, the Planimetric method outlined in the ASTM grain counting standard, E 112 – 96 [61] was used. In compliance with this standard, five different fields were considered in each trial. To determine the average grain size, the number of grains in a given area must be counted. For this analysis, a magnification of 100 was chosen and the area of the photomicrograph was computed by a standard measurement device.

The actual counting procedure considers a whole grain inside the area as equal to one with grains overlapping at the edge of the picture considered as

a half. From square photographs, the four corners are considered as one whole grain. Once all the five samples for each field was counted the average number of grains was calculated. From here the value of Na was calculated with equation (B.8).

$$Na = f(N_{inside} + \frac{N_{intercepted}}{2} + 1) \quad \text{(B.8)}$$

Where:

$$f = \frac{magification^2}{Area(mm^2)}$$

N_{Inside} = Number of grains inside given area

$N_{Interepted}$ = Number of grains intercepted at boundary area

Area = Area of photomicrograph (allowing for magnification)

In these trials magnifications of X100 was used. The size of the photomicrograph was 70mmX53mm. Once Na is determined, the ASTM average grain size is found by the following equation:

$$G = (3.32 \log_{10} Na) - 2.954 \quad \text{(B.9)}$$

Once G has been determined, the average grain properties such as area and diameter can be found from standard tables correlating the ASTM grain size.

Table B.4 Experimental results from grain size testing

Trial	Field 1	Field 2	Field 3	Field 4	Field 5	Average	G
1	7	10	3	4	8	6.4	1.16
2	19	14	32	29	39	26.6	3.21
3	15.5	19	17	19	23	18.7	2.71
4	30	23	22	21	25	24.2	3.08
5	15.5	17	16.5	17.5	18	16.9	2.56
6	8	3	9	9	6	7	1.29
7	15.5	16	15.5	17.5	13	15.5	2.43
8	18	30	28	21	25	24.4	3.09
9	67	46	75	92	71	70.2	4.61

B.3 Microstructure Evaluation

(X100) **(X400)**

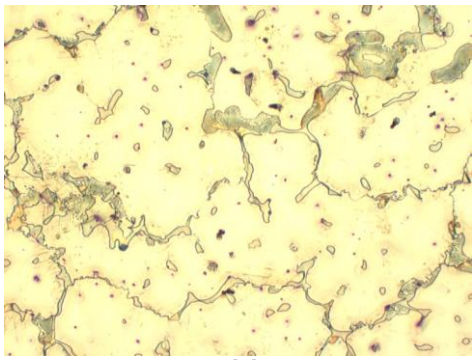

(a)

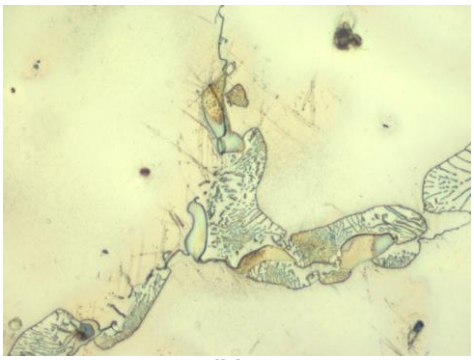

(b)

AZ91 castings produced in ZP131 plaster moulds at 690°C. Mould was coated with Isomol 200 coating (σ_{UTS} = 156.4MPa δ = 2.17% HB = 56.8 Grain size: 1.11)

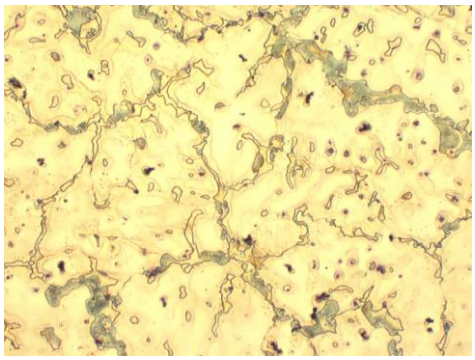

(c)

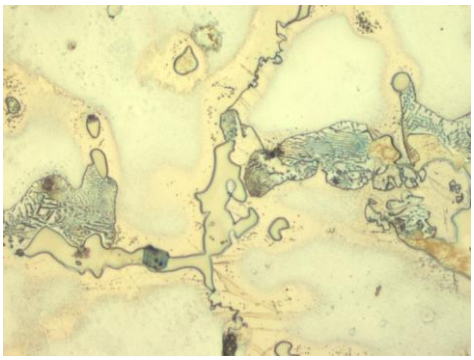

(d)

AZ91 casting produced in ZCast501 mould cast at 740°C. The mould was coated with Magcoat. (σ_{UTS} = 150.87 MPa δ =1.51% HB = 60.53 Grain size: 1.29)

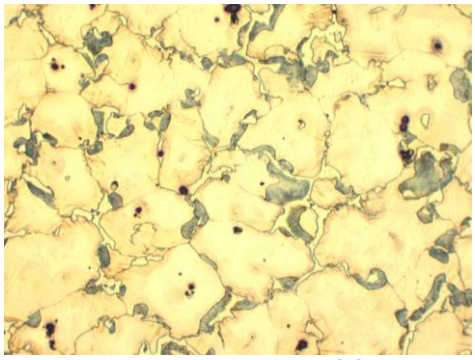

(e)

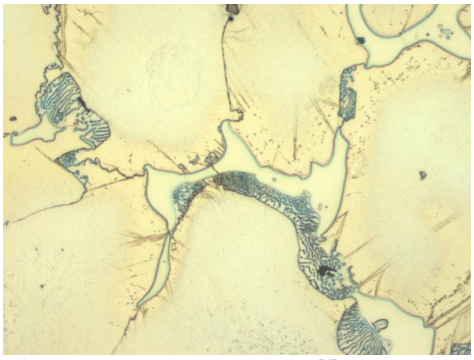

(f)

AZ91 casting produced in Silica sand foundry mould, cast at 770°C. The mould coating was Zircoat (σ_{UTS} = 127.1MPa δ = 1.54% HB = 56.82 Grain size: 3.09)

Figure B.1 AZ91 photomicrographs of (a&b) ZP131 (c&d) ZCast and (e&f) Silica moulds

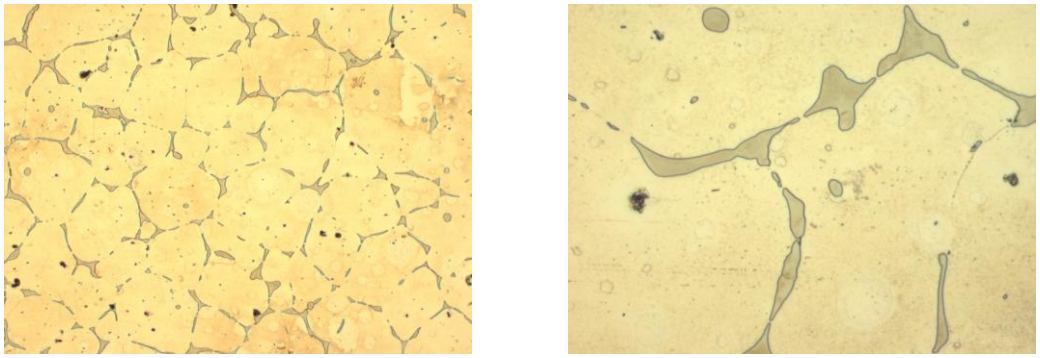

(a) **(b)**

SC1 magnesium alloy cast in ZP131 plaster moulds at 730°C. The mould was coated with Zircoat (σ_{UTS} = 130.02 MPa δ = 2.56% HB = 48.87 Grain size: 3.08)

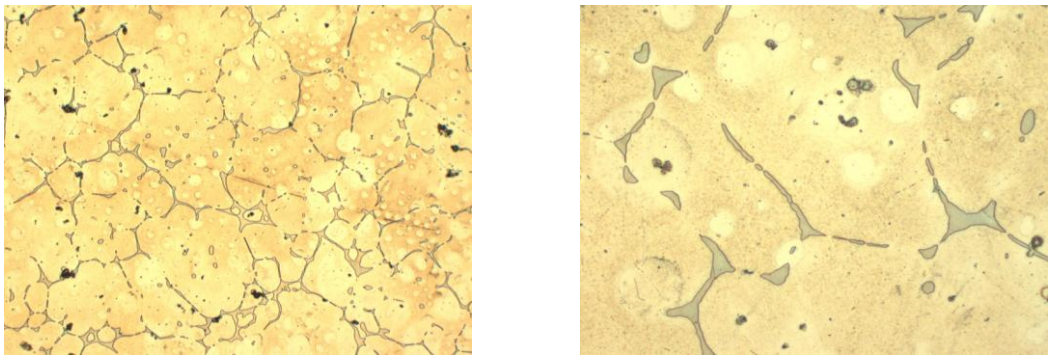

(c) **(d)**

SC1 casting poured into ZCast501 moulds at 770°C. The mould was coated with Isomol 200 (σ_{UTS} = 128 MPa δ =2.28% HB = 48.16 Grain size: 3.21)

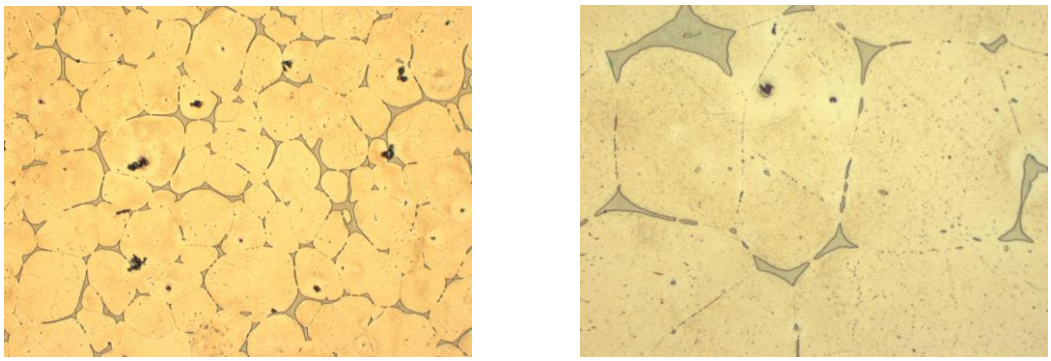

(e) **(f)**

SC1 casting produced in Silica foundry sand moulds at 690°C. The mould was coated was Magcoat (σ_{UTS} = 157.38MPa δ = 3.35 HB = 47.47 Grain size: 4.6)

Figure B.2 SC1 photomicrographs of (a&b) ZP131 (c&d) ZCast and (e&f) Silica moulds

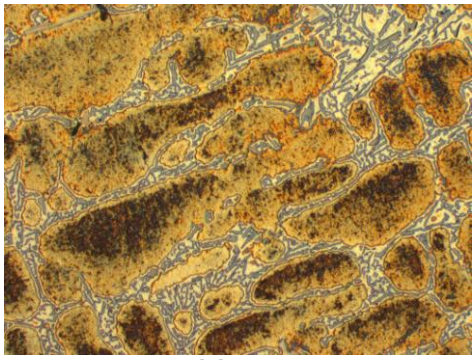

(a)

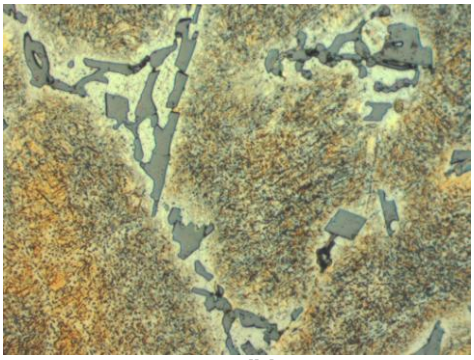

(b)

A356 Aluminium castings produced in ZP131 plaster moulds, poured at 730°C. The mould coating used was Zircoat (σ_{UTS} = 140.23MPa δ = 0.96% HB = 60.53 Grain size: 2.45)

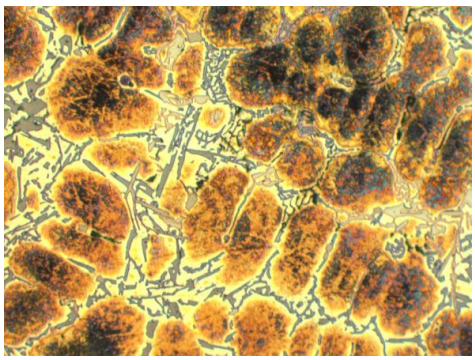

(c)

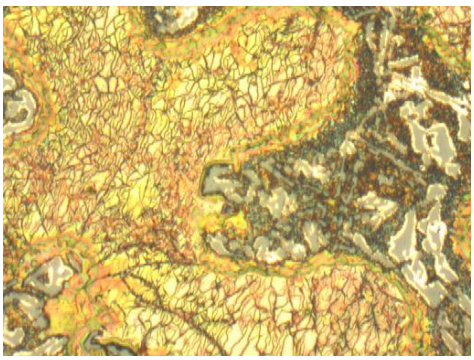

(d)

A356 castings produced in ZCast moulds poured at 770°C. The mould coating was Isomol 200 (σ_{UTS} = 134.30MPa δ = 0.74% HB = 66.70 Grain size: 2.45)

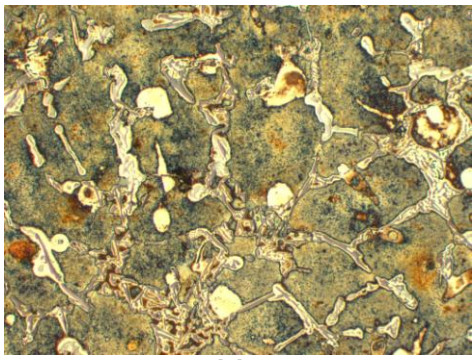

(e)

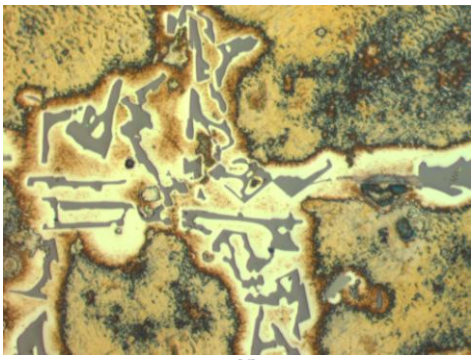

(f)

A356 castings produced in Silica foundry sand moulds, poured at 690°C. The mould coating used was Magcoat (σ_{UTS} = 102.26MPa δ = 0.89% HB = 52.65 Grain size: 2.18)

Figure B.3 Al microstructures in (a&b) ZP131 (c&d) ZCast and (e&f) Silica mould

B.4 Castings Produced in ZP131 Moulds

AZ91

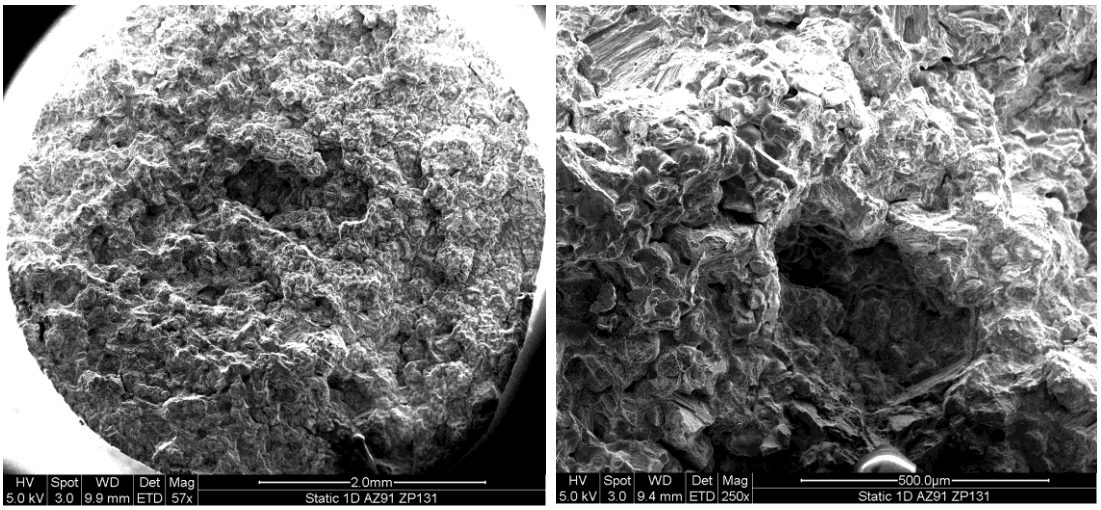

(a) **(b)**

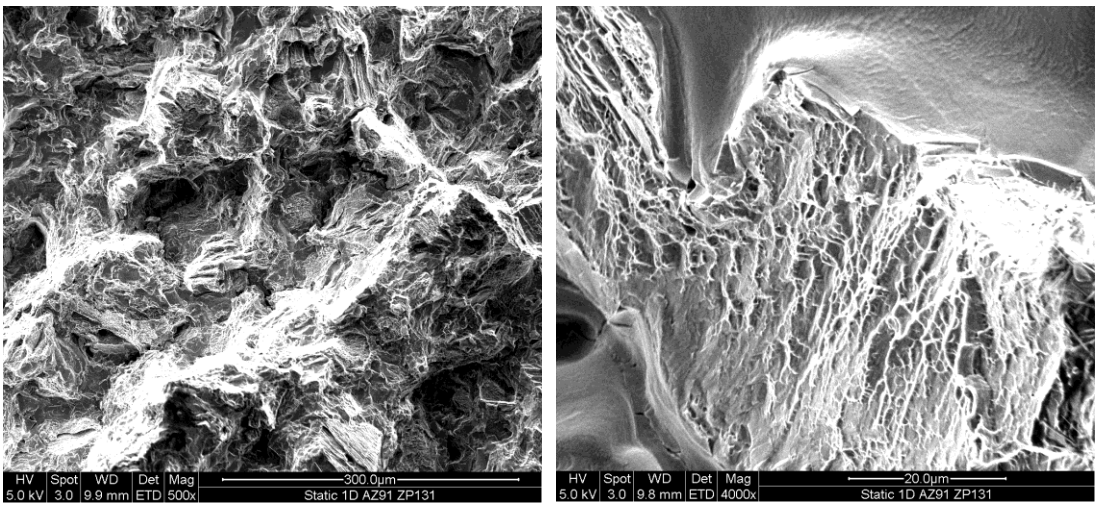

(c) **(d)**

Figure B.4 SEM photographs of AZ91 castings produced at (a) X57 (b) X250 (c) X500 and (d) X4000. (Sample properties UTS = 153.16MPa, δ = 1.87%).

SC1

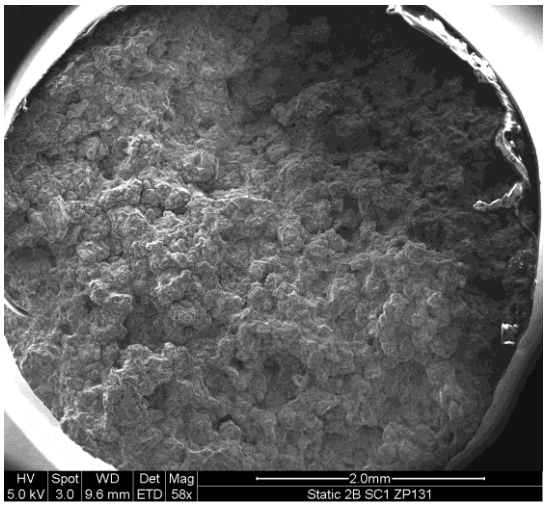

(a)

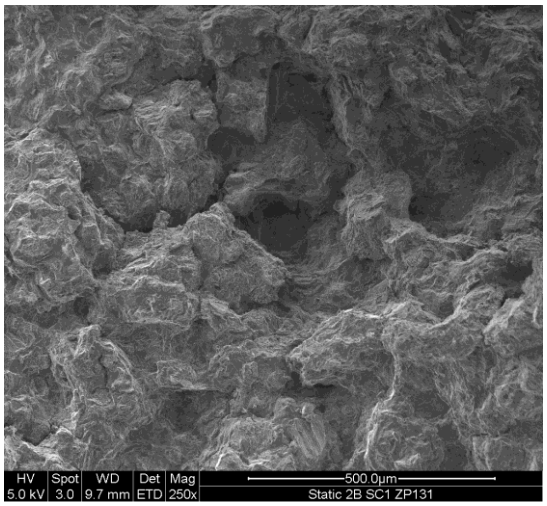

(b)

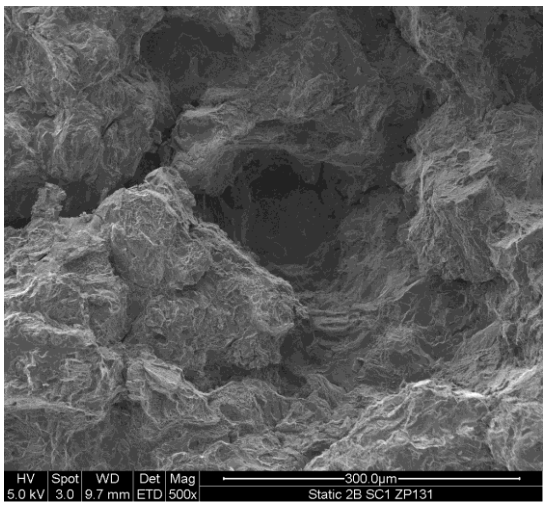

(c)

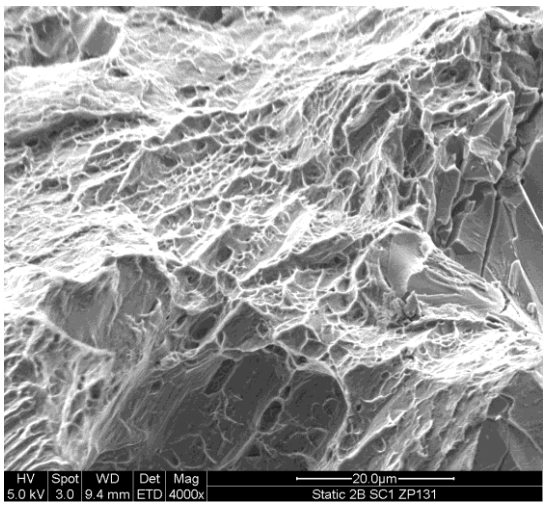

(d)

Figure B.5 SEM photos of AM-SC1 alloy at (a) X58 (b) X250 (c) X500 and (d) X4000. (Sample properties UTS = 127.42MPa, δ = 2.17%).

A356

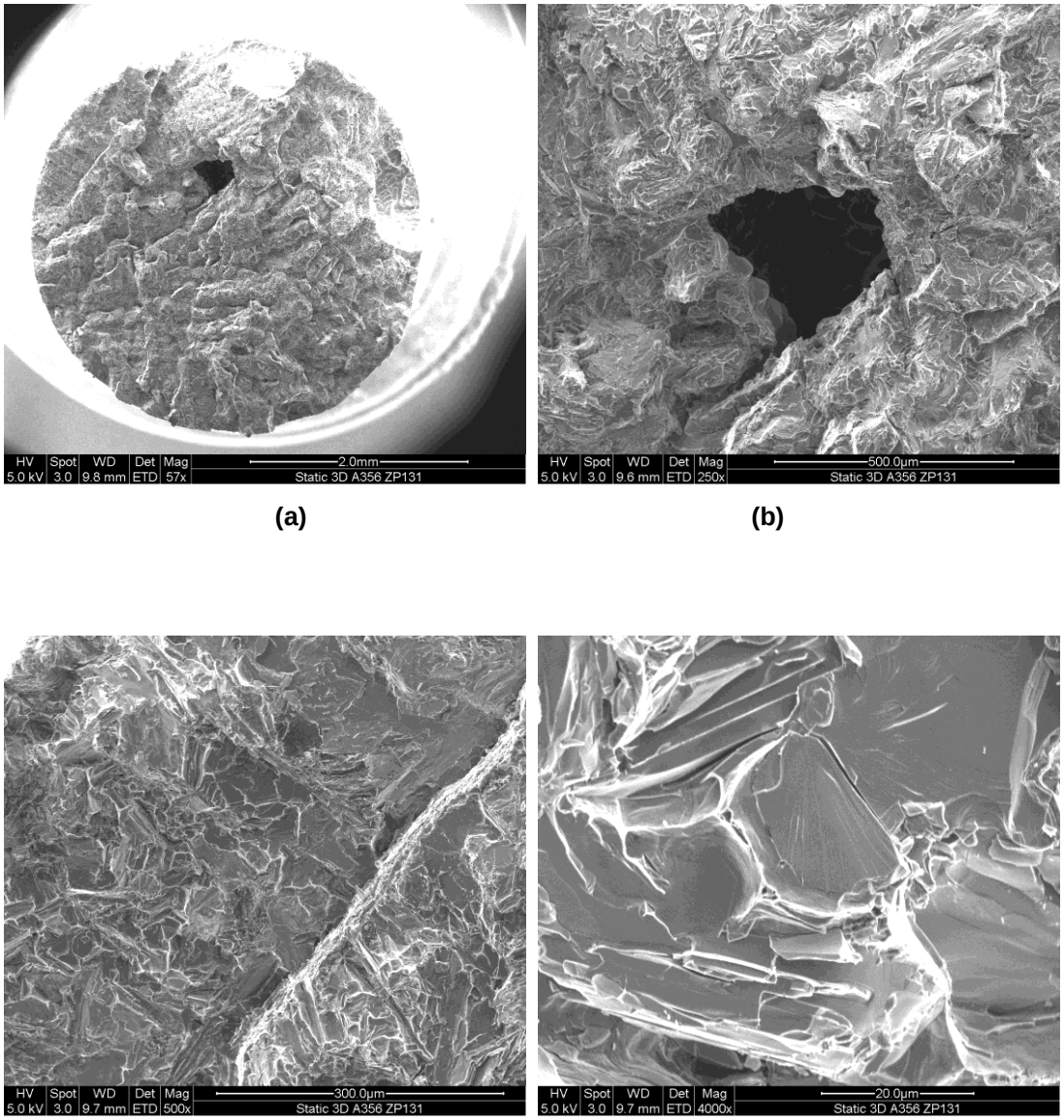

(a) **(b)**

(c) **(d)**

Figure B.6 SEM photographs of A356 castings at (a) X57 (b) X250 (c) X500 and (d) X4000. (Sample properties UTS = 141.24MPa, δ = 0.74%).

B.4.1 Castings Produced in ZCast Moulds

AZ91

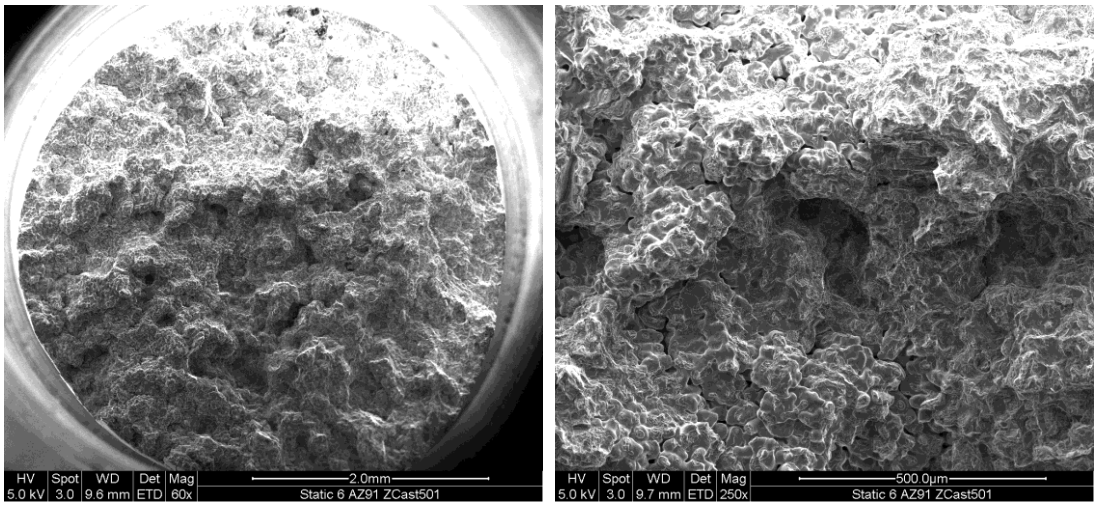

(a) **(b)**

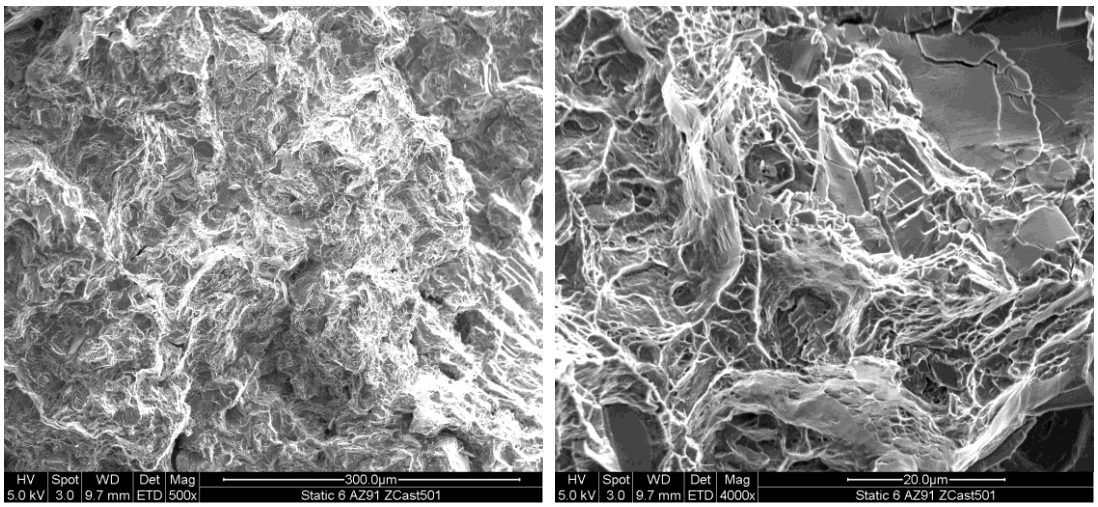

(c) **(d)**

Figure B.7 AZ91 castings (a) X57 (b) X250 (c) X500 and (d) X4000. (Sample properties UTS = 150.87MPa, δ = 1.52%).

SC1

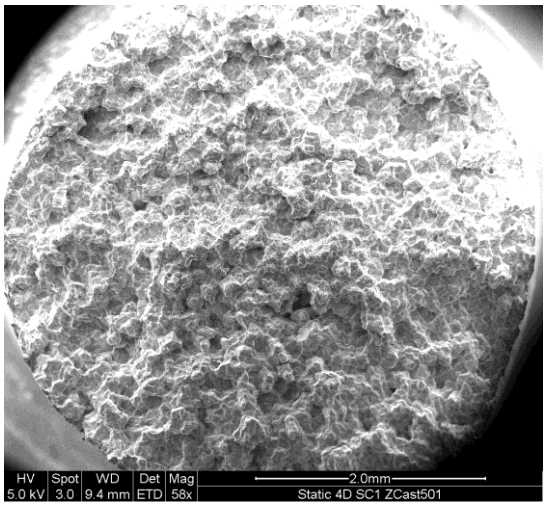

(a)

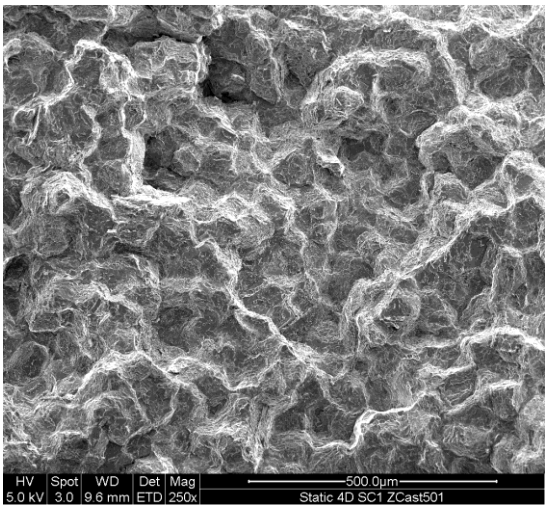

(b)

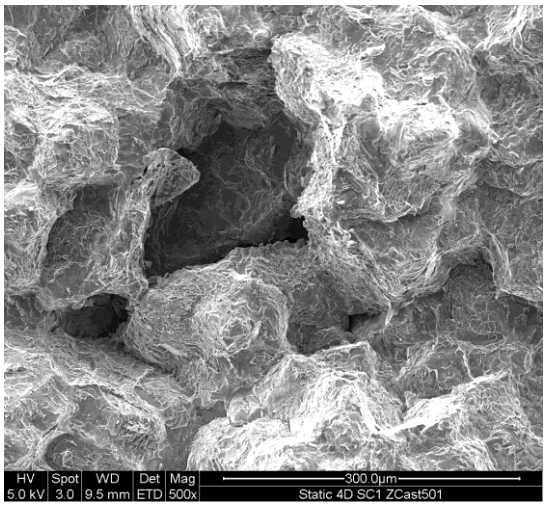

(c)

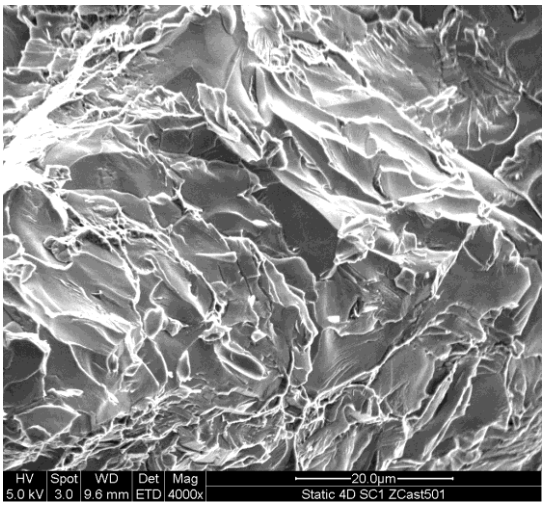

(d)

Figure B.8 AMSC1 fractured surfaces at (a) X57 (b) X250 (c) X500 and (d) X4000. (Sample properties UTS = 133.96MPa, δ = 2.00%).

A356

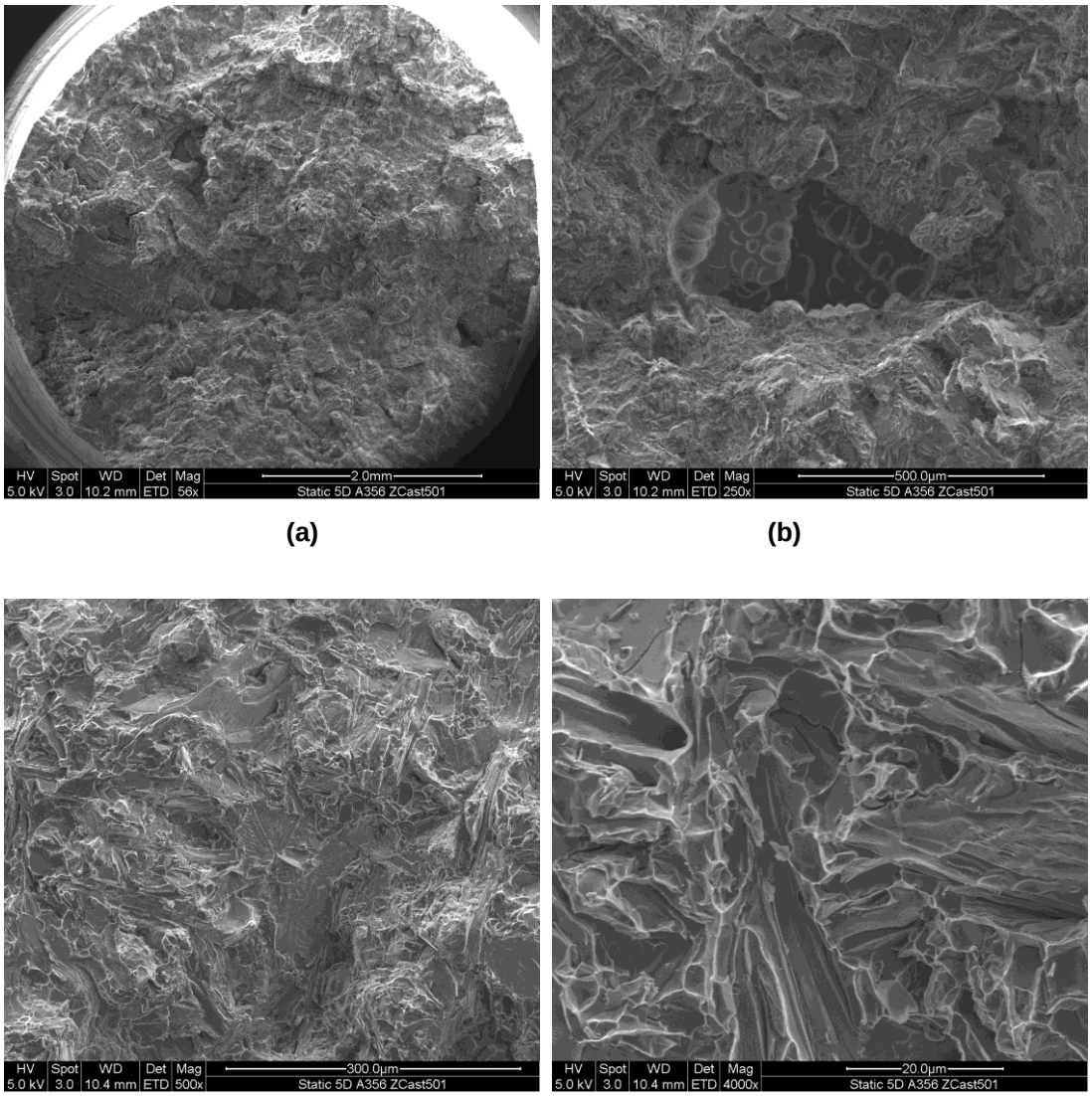

Figure B.9 SEM photos of A356 castings at (a) X57 (b) X250 (c) X500 and (d) X4000. (Sample properties UTS = 138.61MPa, δ = 0.90%).

B.5 Tensile Part Setup

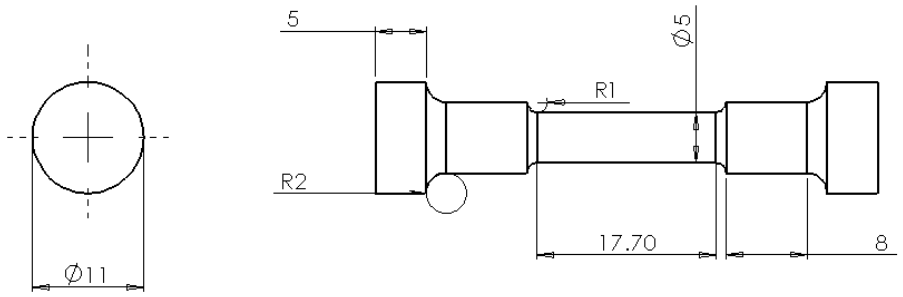

Figure B.10 Cad drawing of the tensile test part used in the static casting trials

B.6 Static Mould Design

The static mould design consisted of the pattern, detailed below in Figure B.11. This cavity was placed in the mould, shown in Figure B.12.

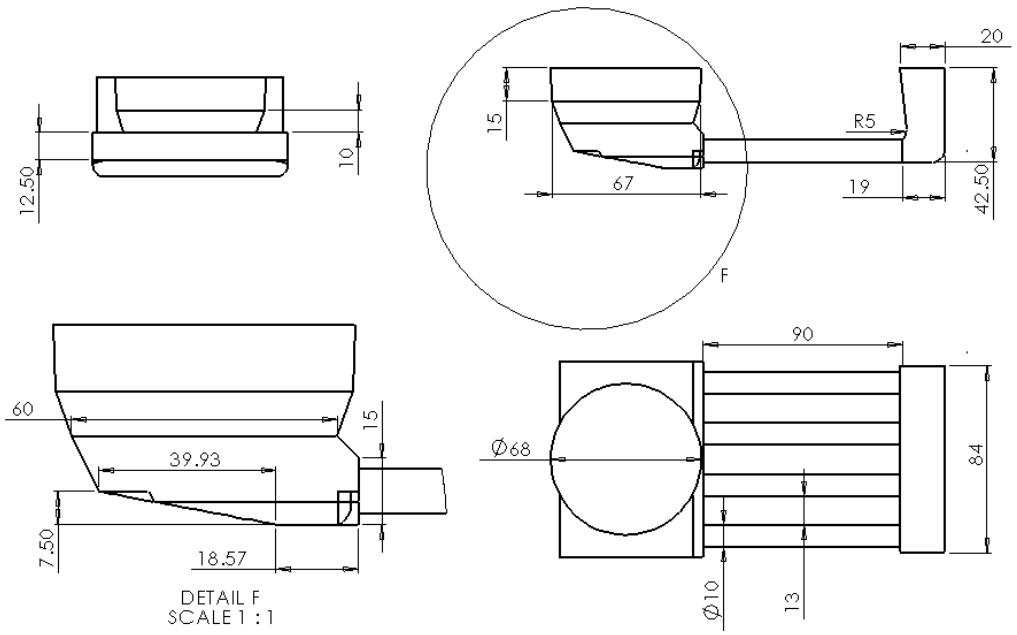

Figure B.11 CAD drawing, showing critical dimensions of mould cavity (pattern) used in the static mould design.

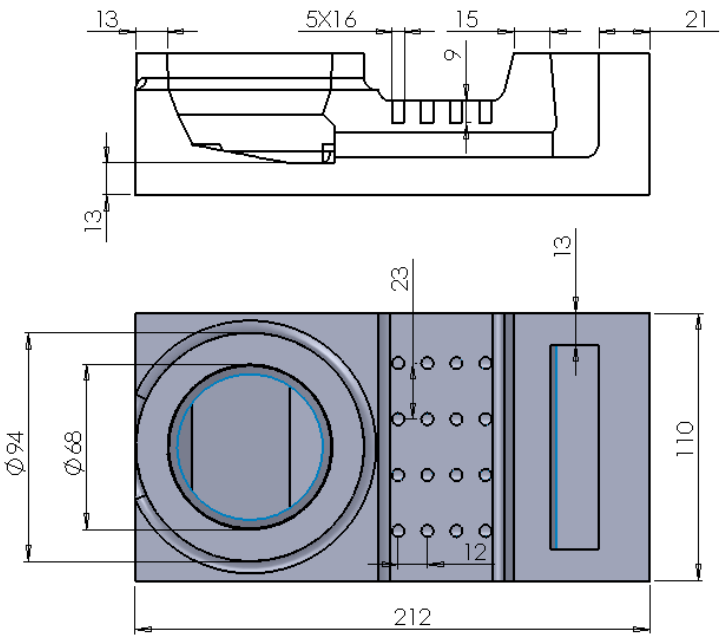

Figure B.12 – Configuration of the cavity in the mould.

B.7 Alloy Constitutes

AZ91HP:

%Al	%Zn	%Mn	%Be	%Mg
8.70	0.80	0.25	0.001	90.25

SC1:

Nd	Ce	Zn	La	Zr	Mn	Pr
1.69	0.71	0.50	0.40	0.38	0.13	0.07

Fe	Ni	Cu	Si	Mg
<0.004	<0.001	<0.002	<0.01	96.10

Al CC601

Si	Fe	Cu	Mn	Mg
6.5–7.5	0.55	0.2	0.35	0.2–0.65

APPENDIX C CENTRIFUGAL CASTING DATA

C.1 Experimental Design

The Box-Behnken experimental design analysis is very similar to the analysis covered in section A.1. The analysis is identical with the exception that the missing column matrix has some additional terms, associated with the third independent variable. The relevant missing column matrix is shown below in.

Where:

$$\{\beta\} = \begin{pmatrix} \beta_0 \\ \beta_1 \\ \beta_2 \\ \beta_3 \\ \beta_{11} \\ \beta_{22} \\ \beta_{33} \\ \beta_{12} \\ \beta_{13} \\ \beta_{23} \end{pmatrix} \qquad \text{(C.1)}$$

These missing co-efficients were then substituted in the second order polynomial expression shown below in equation (C.2).

$$\begin{aligned} y = {} & \beta_0 + \beta_1 X_1 + \beta_2 X_2 + \beta_3 X_3 + \beta_{11} X_1^2 + \beta_{22} X_2^2 \\ & + \beta_{33} X_2^2 + \beta_{12} X_1 X_2 + \beta_{13} X_1 X_3 + \beta_{23} X_2 X_3 \end{aligned} \qquad \text{(C.2)}$$

For completeness, the entire X matrix, is shown below, in coded format

Table C.1 X matrix used in Box-Behnken experimental design

$$x = \begin{bmatrix} x_0 & x_1 & x_2 & x_3 & x_1^2 & x_2^2 & x_3^2 & x_1x_2 & x_1x_3 & x_2x_3 \\ 1 & -1 & -1 & 0 & 1 & 1 & 0 & 1 & 0 & 0 \\ 1 & 1 & -1 & 0 & 1 & 1 & 0 & -1 & 0 & 0 \\ 1 & -1 & 1 & 0 & 1 & 1 & 0 & -1 & 0 & 0 \\ 1 & 1 & 1 & 0 & 1 & 1 & 0 & 1 & 0 & 0 \\ 1 & -1 & 0 & -1 & 1 & 0 & 1 & 0 & 1 & 0 \\ 1 & 1 & 0 & -1 & 1 & 0 & 1 & 0 & -1 & 0 \\ 1 & -1 & 0 & 1 & 1 & 0 & 1 & 0 & -1 & 0 \\ 1 & 1 & 0 & 1 & 1 & 0 & 1 & 0 & 1 & 0 \\ 1 & 0 & -1 & -1 & 0 & 1 & 1 & 0 & 0 & 1 \\ 1 & 0 & 1 & -1 & 0 & 1 & 1 & 0 & 0 & -1 \\ 1 & 0 & -1 & 1 & 0 & 1 & 1 & 0 & 0 & -1 \\ 1 & 0 & 1 & 1 & 0 & 1 & 1 & 0 & 0 & 1 \\ 1 & 0 & 0 & 0 & 0 & 0 & 0 & 0 & 0 & 0 \\ 1 & 0 & 0 & 0 & 0 & 0 & 0 & 0 & 0 & 0 \\ 1 & 0 & 0 & 0 & 0 & 0 & 0 & 0 & 0 & 0 \end{bmatrix}$$

C.2 Mechanical Testing Data

Over the following section the experimental results from the mechanical testing conducted on the centrifugal castings is presented. These results included, Ultimate Tensile Strength (UTS), Yield Strength, percent elongation to fracture and grain counting conducted on the microstructures, cut from the tensile test parts. In the UTS and Yield strength testing, two samples at each condition were tested, denoted by A and B respectively.

Table C.2 UTS results from centrifugally cast test bars

Trial	UTS (MPa)	Average	Trial	UTS (MPa)	Average
1A	90.5		8B	110.3	110.3
1B	94.7	92.6	9A	104.5	
2A	131.4		9B	100.9	102.7
2B	125.8	128.6	10A	105.5	
3A	104.9		10B	106.5	106
3B	94.3	99.6	11A	116.6	
4A	107.8		11B	116.8	116.7
4B	111.3	109.55	12A	109.3	
5A	108.9		12B	115.7	112.5
5B	104.9	106.9	13A	117.7	
6A	101.2		13B	123.5	120.6
6B	105.2	103.2	14A	110.2	
7A	98.0		14B	109.4	109.8
7B	110.2	104.1	15A	145.8	
8A	104.3		15B	143.3	144.55

Table C.3 Yield strength experimental data obtained from centrifugally cast test bars.

Trial	Yield Strength (MPa)	Average	Trial	Yield Strength (MPa)	Average
1A	78.0		8B	85.7	80.1
1B	76.0	77.0	9A	73.3	
2A	84.5		9B	84.7	79
2B	90.0	87.25	10A	73.6	
3A	84.5		10B	91.1	82.35
3B	81.3	82.9	11A	85.9	
4A	90.7		11B	86.0	85.95
4B	96.2	93.45	12A	89.6	
5A	90.7		12B	86.0	87.8
5B	80.7	85.7	13A	90.8	
6A	90.0		13B	87.4	89.1
6B	93.0	91.5	14A	75.9	
7A	93.7		14B	85.9	80.9
7B	82.9	88.3	15A	97.9	
8A	80.1		15B	92.5	95.2

Table C.4 Surface roughness experimental results conducted on centrifugally cast test bars

Trial	Reading 1	Reading 2	Ave. (µm)	Trial	Reading 1	Reading 2	Ave. (µm)
1A	15.26	12.19		8B	11.73	10.62	12.06
1B	12.62	12.99	13.27	9A	12.02	12.22	
2A	15.54	18.25		9B	14.77	13.68	13.17
2B	16.00	22.82	18.15	10A	12.63	14.20	
3A	16.08	9.80		10B	15.43	11.89	13.54
3B	13.41	12.92	13.05	11A	15.13	15.66	
4A	14.96	21.80		11B	14.67	13.66	14.78
4B	20.51	19.00	19.07	12A	14.44	14.11	
5A	11.53	16.38		12B	14.12	13.75	14.10
5B	17.21	15.84	15.24	13A	12.08	13.98	
6A	15.97	15.81		13B	11.29	11.54	12.22
6B	10.19	15.28	14.31	14A	11.58	11.21	
7A	12.25	11.17		14B	14.76	11.32	12.22
7B	11.15	13.37	11.98	15A	15.20	9.65	
8A	12.68	11.44		15B	14.94	10.32	12.53

C.3 Etchants Used for Cast Alloys

Aluminium Etching (Wrecks) reagent

- 100ml H_2O,
- 4g $KMnO_4$
- 1g NaOH

Magnesium Etching reagent

- 20ml Acetic acid
- 1ml HNO_3
- 60ml Ethylene glycol
- 20ml H_2O

Table C.5 Percent elongation values from tensile testing on cast specimens

Trial	% Elongation	Average	Trial	% Elongation	Average
1A	0.97		8B	1.08	1.15
1B	0.93	0.95	9A	1.54	
2A	1.47		9B	1.08	1.31
2B	1.51	1.49	10A	1.54	
3A	1.47		10B	0.65	1.09
3B	0.79	1.13	11A	2.05	
4A	0.86		11B	2.15	2.10
4B	1.01	0.93	12A	1.22	
5A	1.47		12B	1.08	1.15
5B	1.18	1.33	13A	1.44	
6A	0.86		13B	1.51	1.47
6B	0.86	0.86	14A	1.54	
7A	0.43		14B	1.33	1.44
7B	1.08	0.75	15A	2.26	
8A	1.15		15B	2.44	2.35

Table C.6 ASTM grain size results from centrifugal casting trials

Trial	Field 1	Field 2	Field 3	Field 4	Field 5	Average	G
150RPM	12.5	14.5	17.5	17.5	12.5	14.9	2.38
300RPM	14	16.5	20	12	22.5	17	2.57
450RPM	6	17	16.5	14	25.5	15.8	2.46

C.4 As-Cast Macrostructures

150 RPM

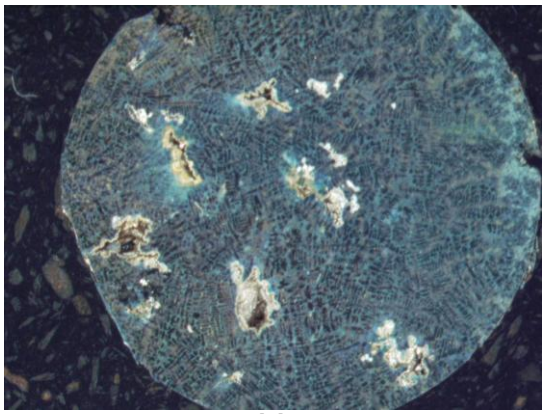

(a)

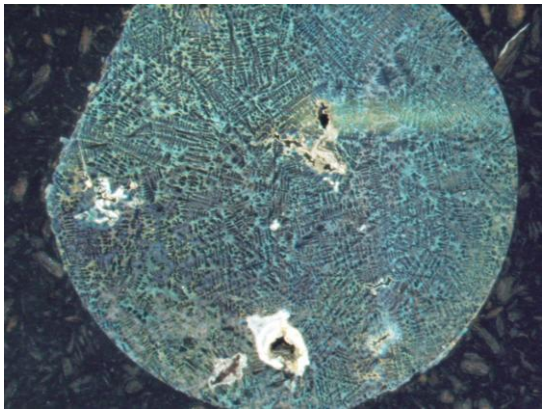

(b)

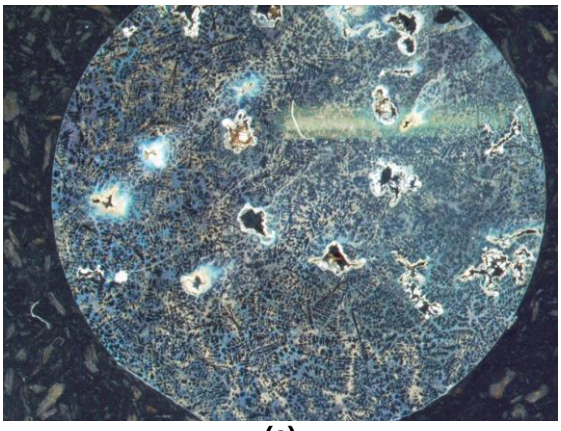

(c)

Figure C.1 Cross-sectional macrostructures of tensile specimens at 150RPM at (a) Trial 1 – 16mm runner, 45° cavity angle (b) Trial 3 – 16mm runner, 180° cavity angle and (c) Trial 7– 19.2mm runner, 90° cavity angle

300 RPM

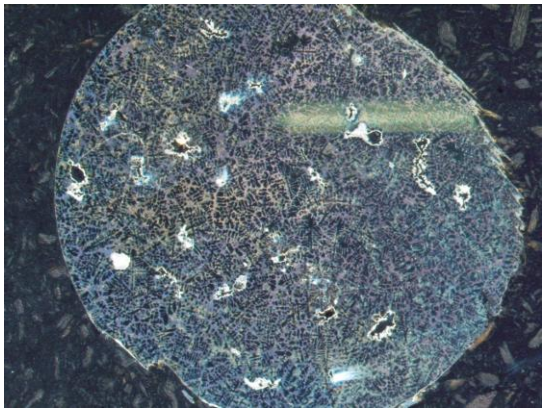

(a)

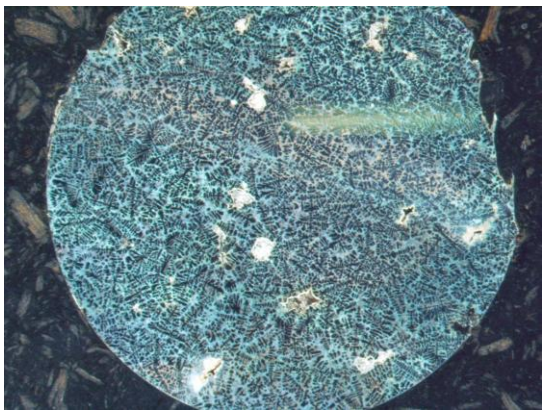

(b)

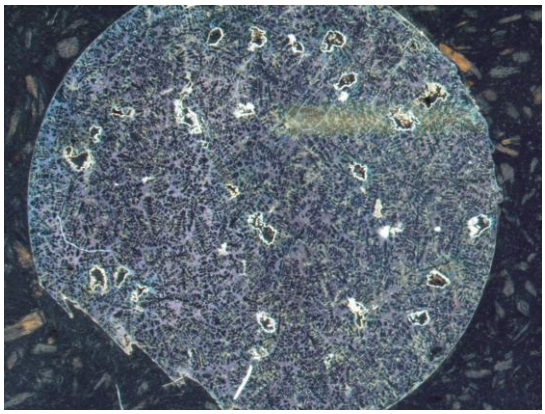

(c)

Figure C.2 The macrostructures of tensile specimens at 150RPM at (a) Trial 11 – 19.2 mm runner, 45° cavity angle (b) Trial 12 – 19.2mm runner, 180° cavity angle and (c) Trial 15 – 16mm runner, 90° cavity angle.

450RPM

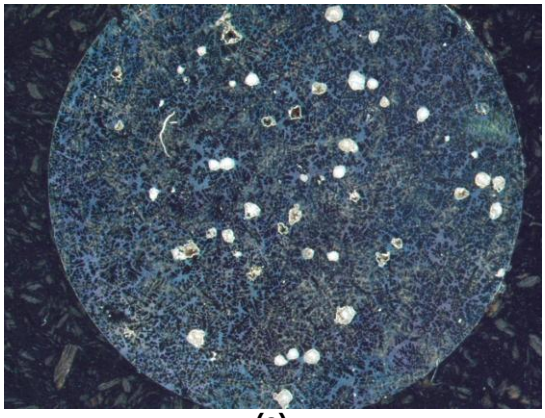

(a)

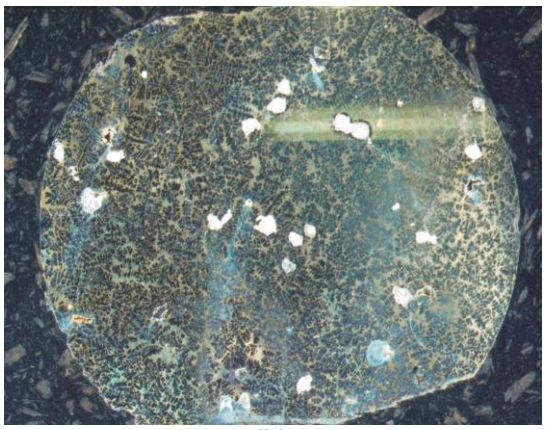

(b)

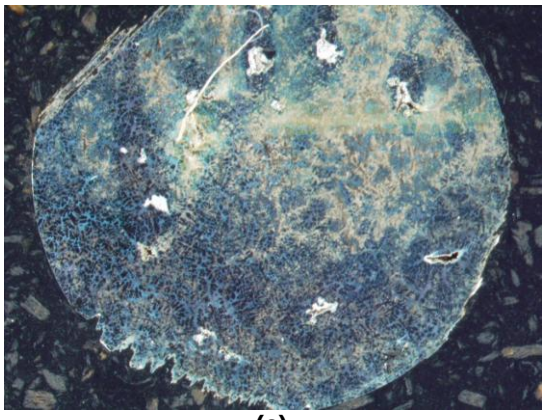

(c)

Figure C.3 The macrostructures of tensile specimens at 150RPM at (a) Trial 2 – 16mm runner, 45° cavity angle (b) Trial 4 – 16mm runner, 180° cavity angle and (c) Trial 8 – 19.2mm runner, 90°cavity angle.

C.5 SEM Photographs

150RPM

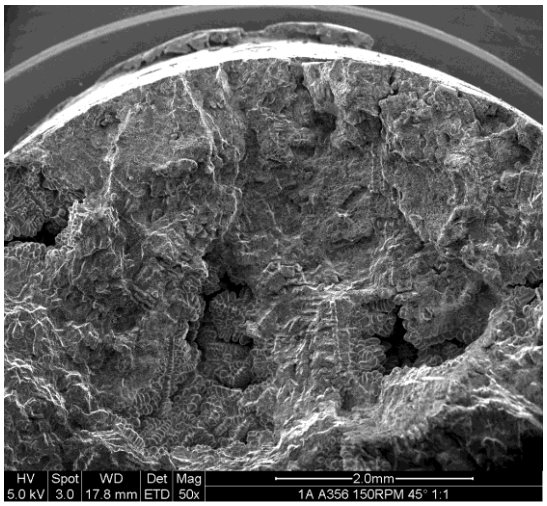

(a)

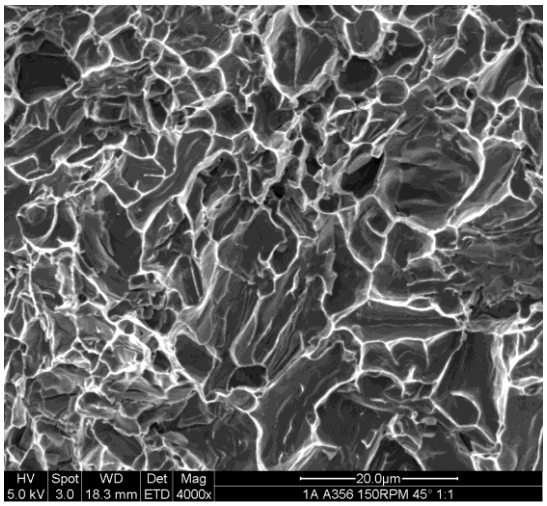

(b)

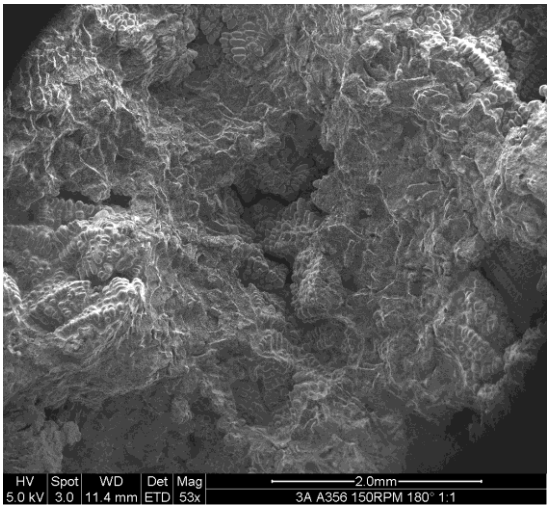

(c)

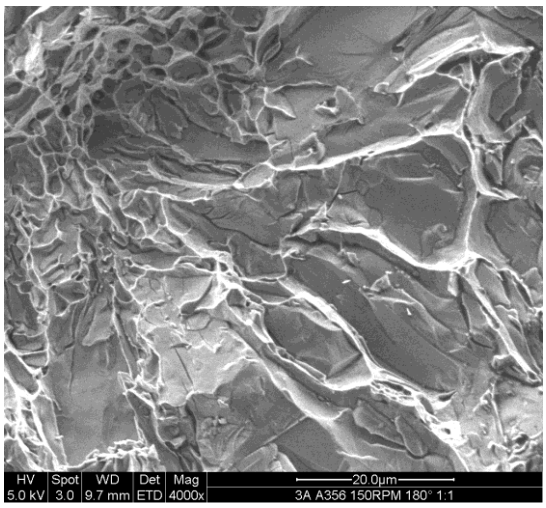

(d)

Figure C.4 SEM photographs of fractured centrifugal cast samples at (a & b) Trial 1 – 45°, 1:1 r/c ratio and (c & d) Trial 3 – 180°, 1:1 runner ratio (Magnifications shown on photographs).

300 RPM

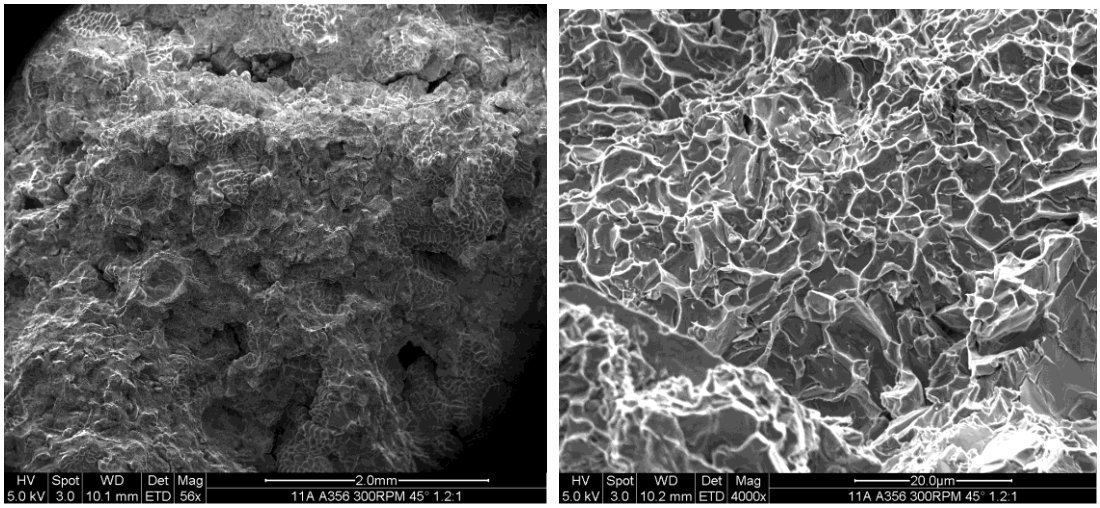

(a) **(b)**

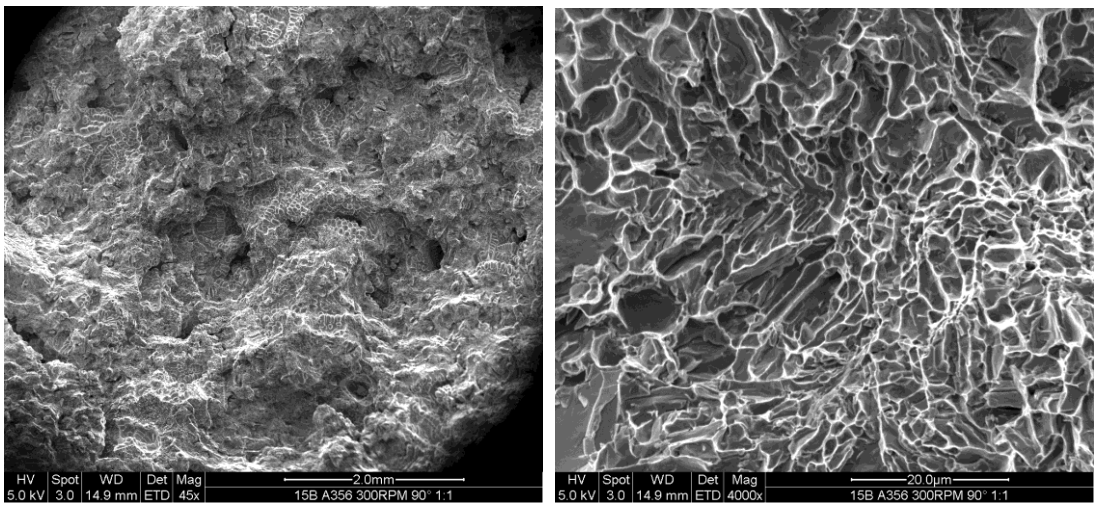

(c) **(d)**

Figure C.5 Fractured cast samples at (a & b) Trial 11 – 45°, 1.2:1 runner ratio and (c & d) Trial 15 – 90°, 1:1 runner ratio.

450 RPM

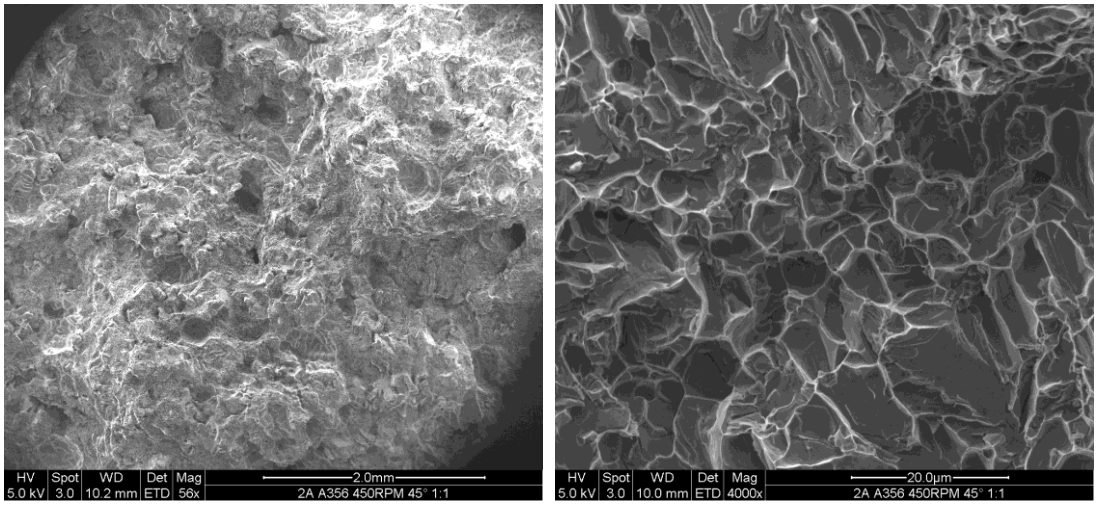

(a) **(b)**

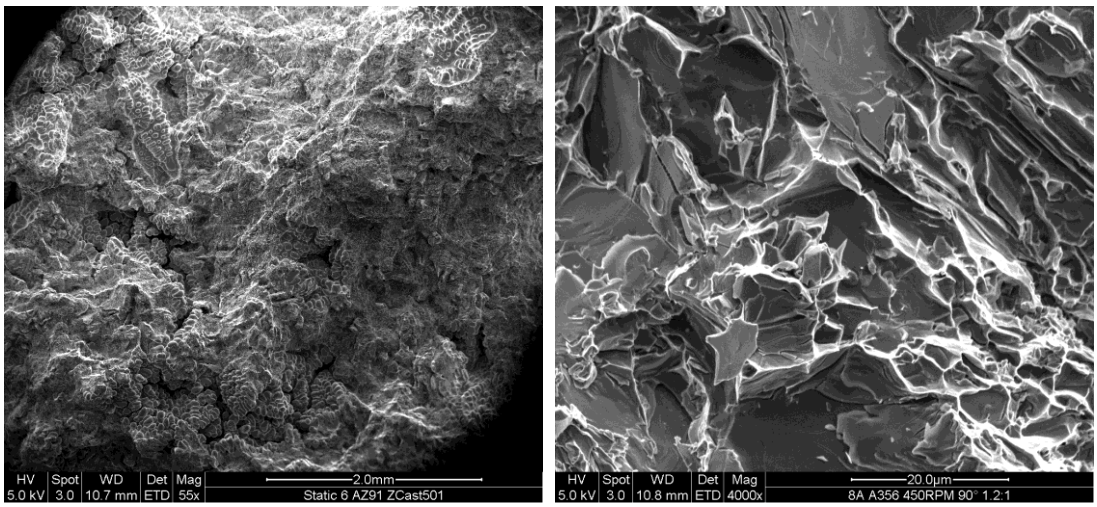

(c) **(d)**

Figure C.6 Fractured cast samples at (a & b) Trial 2 – 45°, 1:1 runner ratio and (c & d) Trial 8 – 90°, 1.2:1 runner ratio.

C.6 Die and Mould Design Drawings

To hold the plaster mould in position during the trials conducted at Centracast, a steel die was fabricated. Over the following pages, the overall die setup and individual part drawings are presented (all dimensions are in mm and scales are 1:3).

ITEM NO.	QTY.	PART NO.
1	1	Bolster spacer
2	1	Steel mould bottom
3	1	Steel mould top
4	1	Bolster
5	1	Spindal fitting

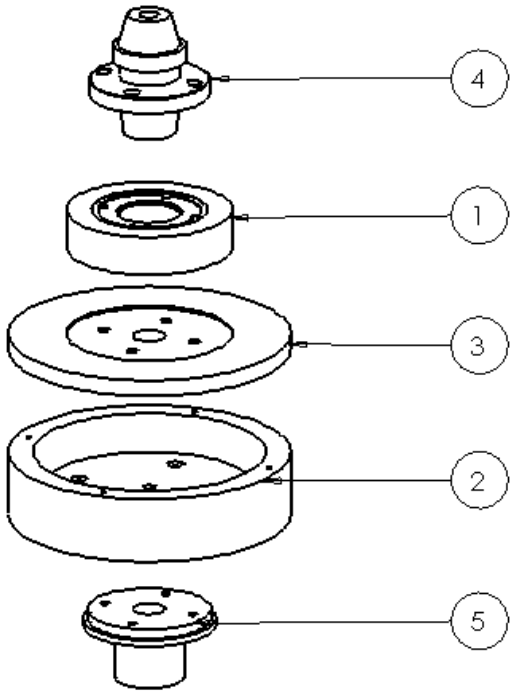

Figure C.7 Exploded view showing all die components used in the centrifugal casting trials

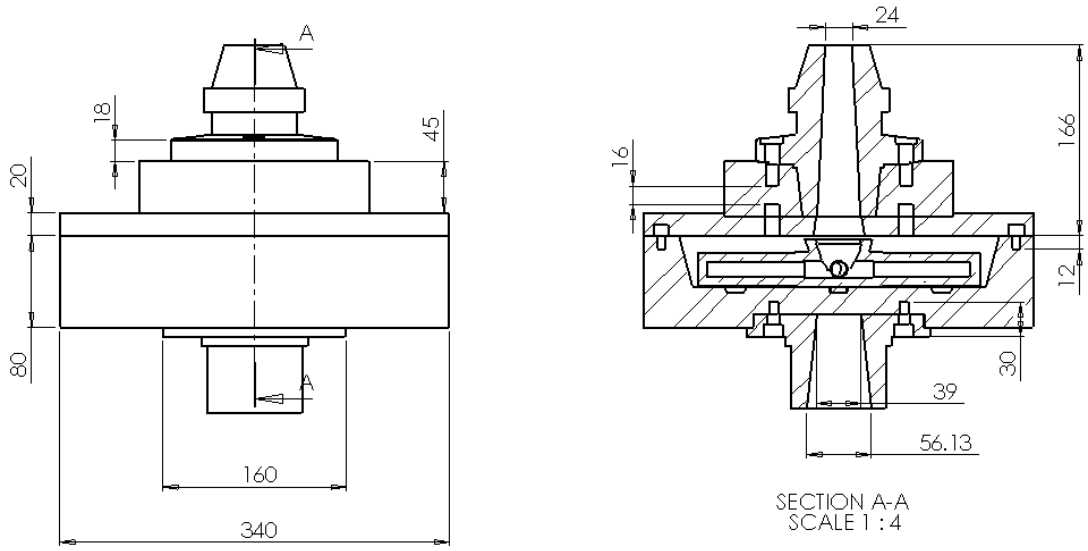

Figure C.8 CAD drawing and sectional view of the overall steel die, showing general part dimensions.

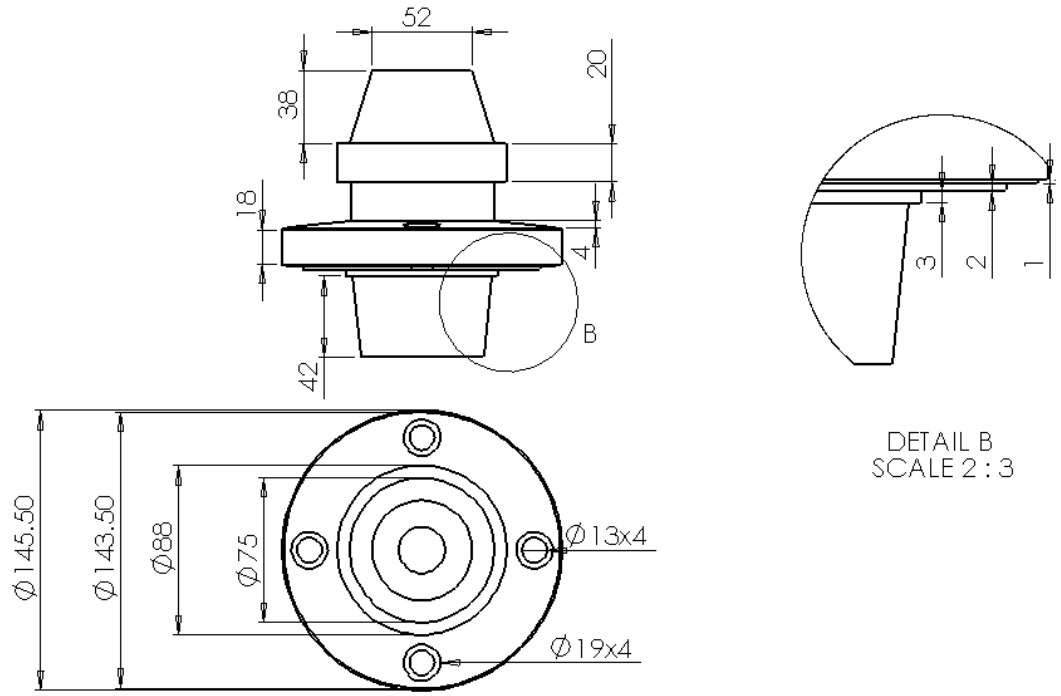

Figure C.9 CAD drawing of the Bolster

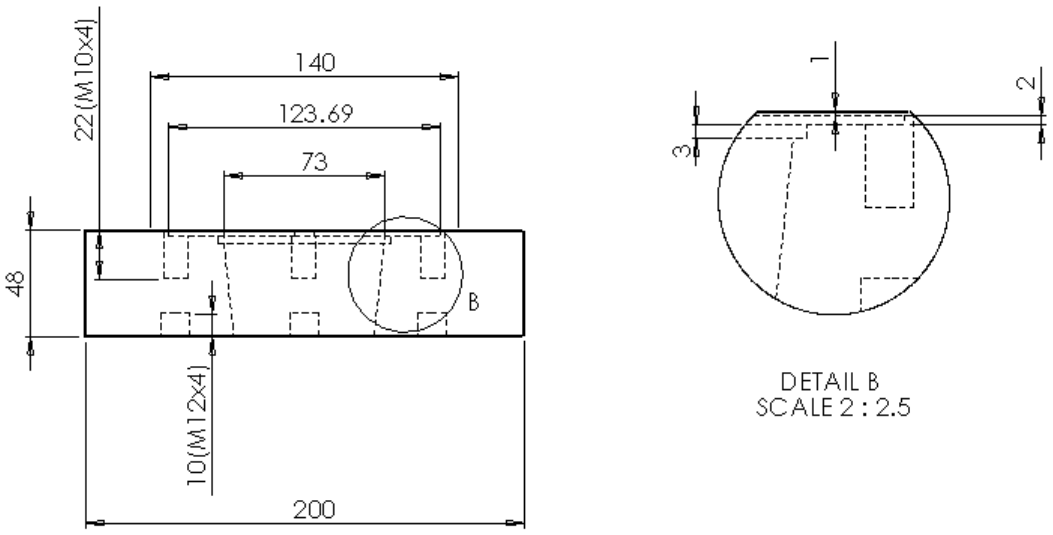

Figure C.10 CAD drawing of bolster spacer

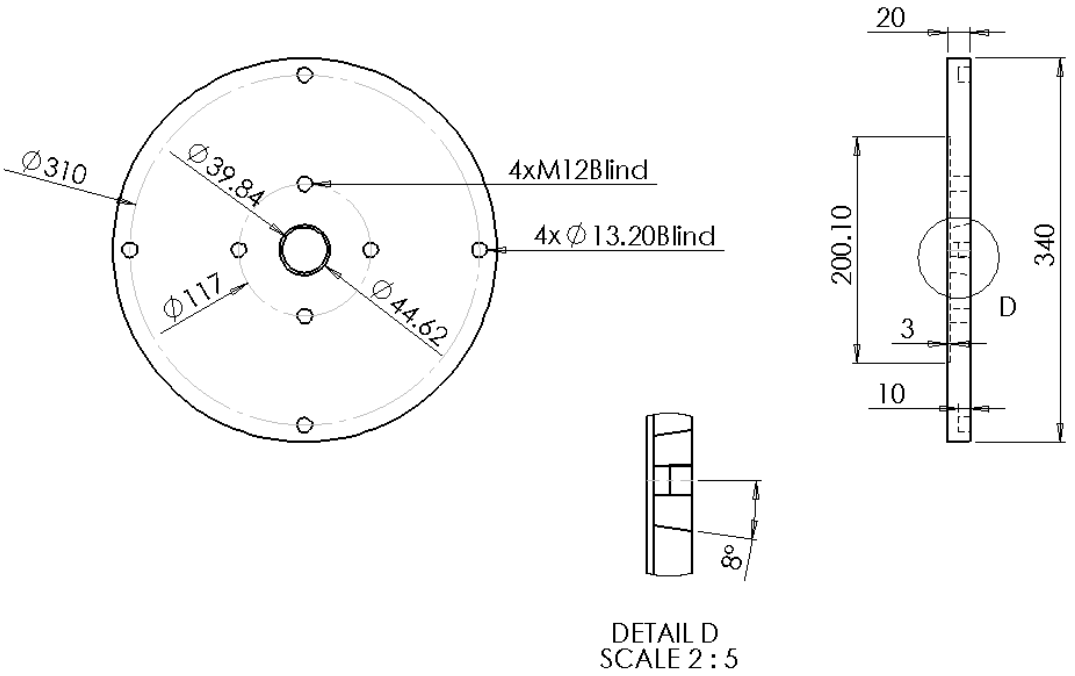

Figure C.11 CAD drawing of top steel die

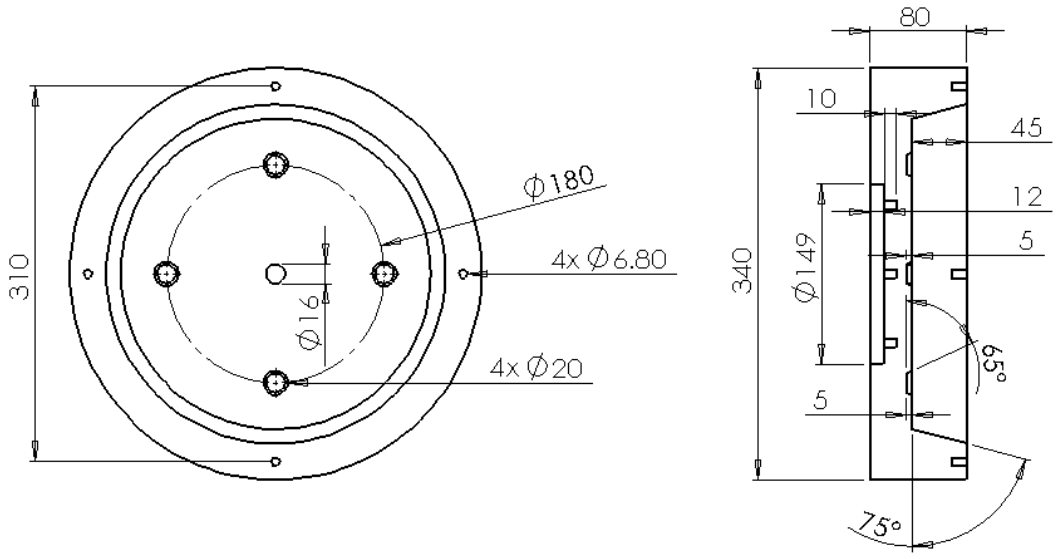

Figure C.12 CAD drawing of bottom, steel die.

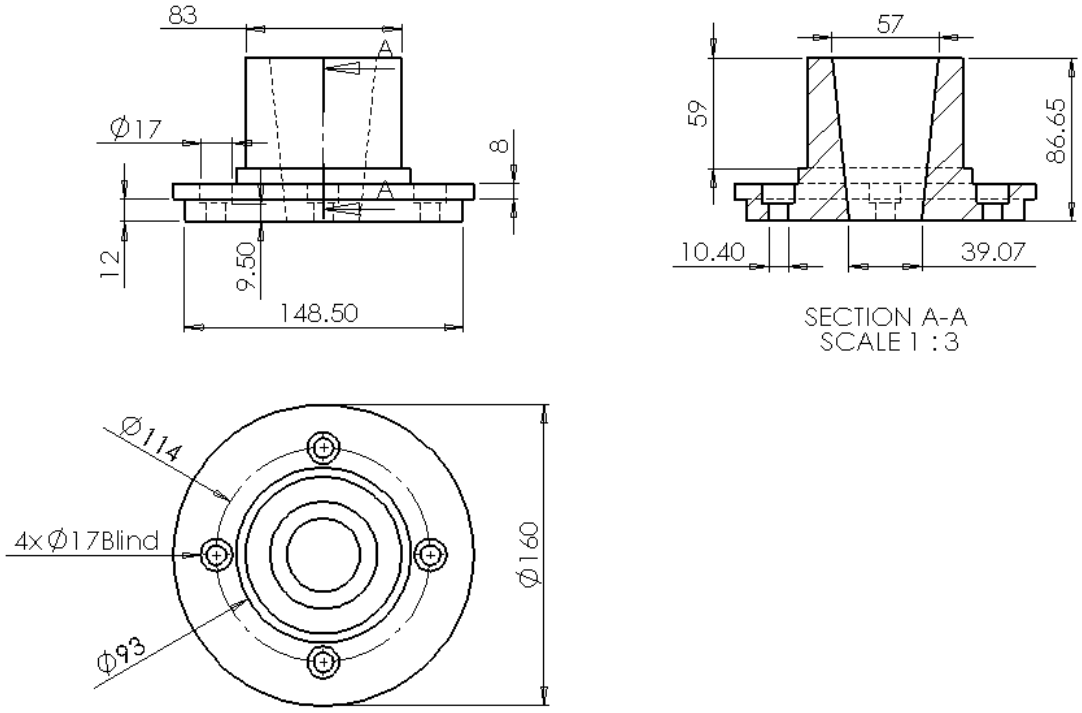

Figure C.13 CAD drawing of the spindle fitting between steel die and motor

C.7 Mould Design

During the centrifugal casting experiments two 3D printed mould configurations were used. These configurations differed in that the cylindrical cavities (from which the test parts were tested) were orientated at different angles. The first configuration comprised of cavities angled at 0 and 45° in relation to the cavity inlet, with the second design constituting of only cavities positioned 90° from the cavity inlet.

Overall, only ZP131 3D printed moulds were utilised in the centrifugal casting trials with the mould being 5mm in thickness at all points from the internal cavity. respectively detail the CAD drawings of the two pattern configurations which formed the cavity for the two respective 3D printed moulds.

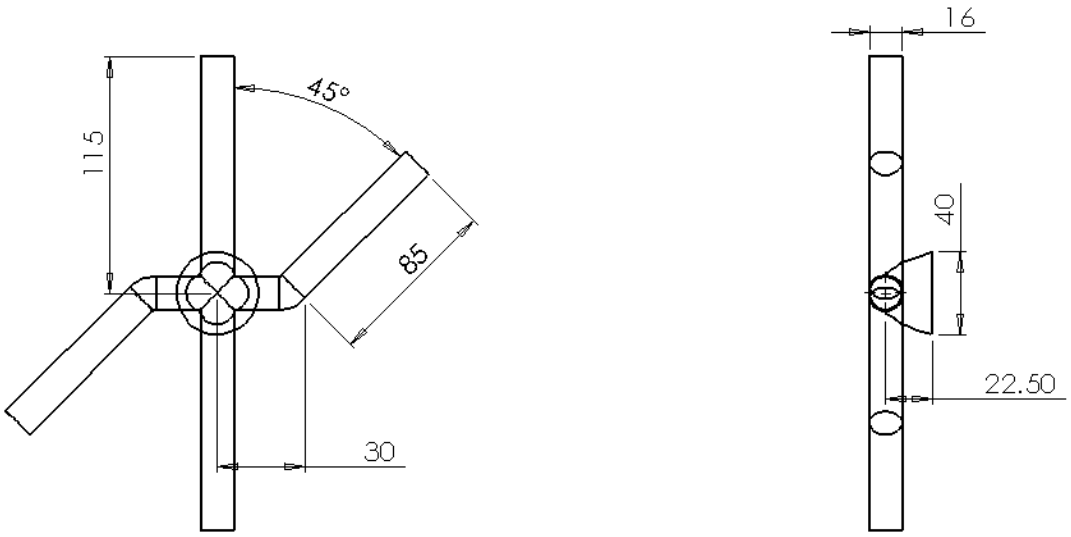

Figure C.14 CAD drawing of 0 and 45° mould pattern used in the 3D printed mould design.

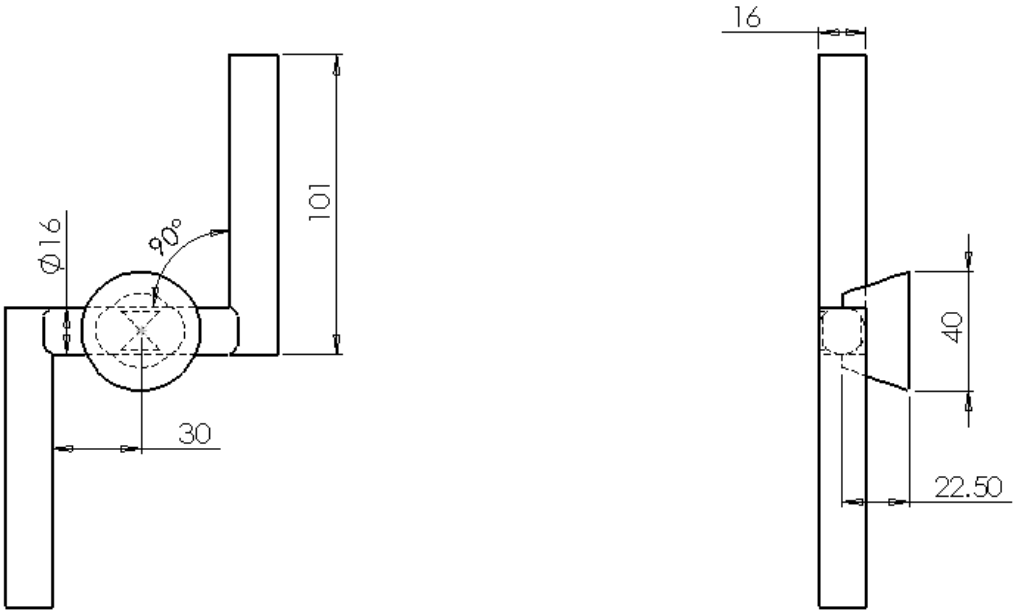

Figure C.15 CAD drawing of mould pattern with cavity at 90° to inlet.

C.8 Tensile testing part

The test part used for the tensile testing conducted on the centrifugally cast parts is shown below. The dimensions of this part adhere to the 10:002 1990 British Standard [108].

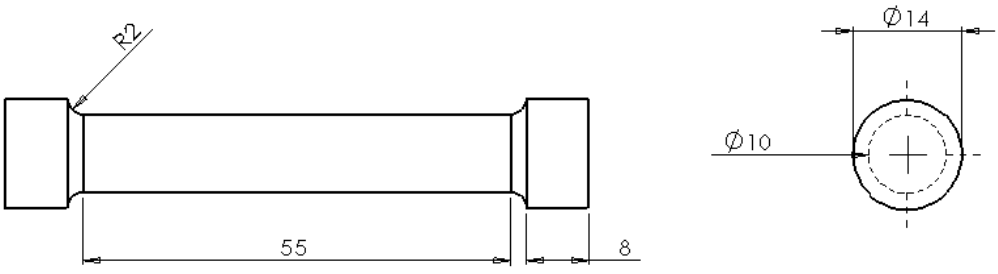

Figure C.16 CAD drawing of the Centrifugal tensile test specimen

C.9 Publications

Based on the results of this research, the following research papers were produced, in which the first two have already been published while the last two are currently pending:

Singamneni, S., McKenna, N., Diegel, O., Singh, D., Neitzert, T., St. George, J., Roy Choudhury, A, and Yarlagadda, P, “Rapid casting: A critical analysis of mould and casting characteristics,”, 2009, Australian Journal of Mechanical Engineering, Vol 7, No. 1, pp 33-41.

Singamneni, S.,McKenna, N., Olaf, D., Darius, S., Roy Choudhury, A., “Rapid manufacture in light metals processing,” 2009, Materials Science Forum, Vol. 618-619, pp 387-390.

Singamneni, S., McKenna, N., Diegel, O., and Singh, D., “Rapid casting of light metals: an experimental investigation using Taguch Methods,” Currently communicated to the International Journal of Metal Casting.

Singamneni, S., McKenna, N., and Singh, D., “Centrifugal casting in rapid prototyped moulds,” Currently communicated to the Proceedings of Institution of Mechanical Engineers UK, Part B, Journal of Engineering Manufacture.